

STUDIE ZUR SPEKTROSKOPIE, REAKTIONSKINETIK UND
ZUM MECHANISMUS DER IN DER ATMOSPHERE
RELEVANTEN I_2/O_3 PHOTOCHEMIE

SPECTROSCOPIC, KINETIC AND MECHANISTIC STUDIES
OF ATMOSPHERICALLY RELEVANT I_2/O_3
PHOTOCHEMISTRY

Vom Fachbereich für Physik und Elektrotechnik
der Universität Bremen

Dissertation zur Erlangung des Grades
Doktor der Naturwissenschaften (Dr. rer. nat)

von

Lic. Juan Carlos Gómez Martín

1. Gutachter: Prof. Dr. John P. Burrows
2. Gutachter: Prof. Dr. Richard P. Wayne

Eingereicht am: 20.04.2006

Tag des Promotionskolloquiums: 26.05.2006

Angesichts von Hindernissen
mag die kürzeste Linie
zwischen zwei Punkten
die Krümme sein.

"Leben des Galilei"
Berthold Brecht

A mis padres, Juan y Mercedes
A mis hermanas, Alicia y Carmen

CONTENTS

ABSTRACT	IX
OUTLINE	XIII
INTRODUCTION	1
1. HISTORICAL INTRODUCTION.....	3
2. ATMOSPHERIC IODINE CHEMISTRY.....	7
2.1. INTRODUCTION.....	7
2.2. IODINE SOURCES.....	7
2.2.1. <i>Open ocean sources</i>	9
2.2.2. <i>Coastal Sources</i>	11
2.3. FATE OF IODINE ATOMS	12
2.4. THE ROLE OF IODINE IN THE STRATOSPHERIC CHEMISTRY	13
2.5. THE ROLE OF IODINE IN THE TROPOSPHERIC CHEMISTRY	15
2.5.1. <i>Iodine catalysed ozone depletion</i>	15
2.5.2. <i>Impact of iodine monoxide chemistry upon MBL NO_x</i>	18
2.5.3. <i>Impact of iodine monoxide chemistry upon MBL HO_x</i>	20
2.5.4. <i>Interaction between iodine and sulphur cycles</i>	22
2.5.5. <i>Uptake of inorganic iodine compounds on sea salt aerosol. Halogen activation.</i>	24
2.5.6. <i>New particle formation</i>	25
3. OBJECTIVES	29
3.1. GENERAL STRATEGY.....	30
3.2. OBJECTIVES OF THIS WORK	33
THEORY	35
4. ELECTRONIC ABSORPTION SPECTRA	37
4.1. THE BEER-LAMBERT LAW	37
4.2. INTERACTION OF THE ELECTROMAGNETIC FIELD WITH MOLECULES.....	38
4.2.1. <i>Transition probability</i>	38
4.2.2. <i>Allowed and forbidden transitions</i>	43
4.2.3. <i>Types of transitions</i>	44
4.2.4. <i>Structure of an electronic band system</i>	47
4.2.5. <i>Intensity distribution of vibrational bands</i>	49
4.2.6. <i>Line profiles</i>	51
4.2.7. <i>Absorption continua</i>	52
4.3. ELECTRONIC SPECTRA OF DIATOMIC MOLECULES: THE CASE OF IODINE MONOXIDE (IO).....	54
4.4. ELECTRONIC SPECTRA OF ASYMMETRIC TRIATOMIC MOLECULES: THE CASE OF IODINE DIOXIDE (OIO)	56
5. FUNDAMENTAL PRINCIPLES OF GAS PHASE KINETICS.....	59
5.1. PHOTOCHEMICAL REACTIONS	59
5.2. BASIC KINETIC CONCEPTS	60

5.2.1. Empirical rate equations	60
5.2.2. Opposite reactions and chemical equilibrium.	62
5.2.3. Steady state treatment.....	64
5.3. THEORY OF REACTION RATES.....	64
5.3.1. Bimolecular reactions.....	64
5.3.2. Recombination and disproportionation reactions.....	67
5.4. THE PHOTOCHEMISTRY OF IODINE AND OZONE.....	71
5.4.1. Primary processes	71
5.4.1.1. Photolysis of I ₂	71
5.4.1.2. Photolysis of O ₃	72
5.4.1.3. Photolysis of IO	73
5.4.2. Secondary processes	74
5.4.2.1. Generation of IO radicals	74
5.4.2.2. Disproportionation of IO.....	74
5.4.2.3. Formation of higher iodine oxides	75
6. SEPARATION OF LINEARLY MIXED SIGNALS.....	77
6.1. INTRODUCTION	77
6.2. STATISTICAL REPRESENTATION OF DATASETS.....	78
6.3. BLIND SOURCE SEPARATION.....	81
6.3.1. Principal Components Analysis	81
6.3.1.1. PCA as a generative model: Decomposition and separation of sources.....	81
6.3.1.2. PCA for pre-processing: Dimension reduction and filtering	84
6.3.2. Independent Components Analysis.....	85
6.3.2.1. General: ICA as a generative model	85
6.3.2.2. Algorithm for ICA free of noise.....	87
6.3.2.3. Interpretation of the mixing matrix.	89
6.4. MULTIVARIATE LINEAR REGRESSION.....	90
METHODOLOGY.....	93
7. EXPERIMENTAL SET UP	95
7.1. DESCRIPTION	95
7.1.1. Generation of radicals	95
7.1.2. Detection	98
7.1.2.1. Multichannel Time-resolved Molecular Absorption Spectroscopy (MTRMAS).....	98
7.1.2.2. Atomic resonance absorption spectroscopy (ARAS).....	104
7.2. CHARACTERISATION.....	106
7.2.1. Lamp drift.....	108
7.2.2. Coarse resolution and binning.....	108
7.2.3. Diffusion and wall losses	109
7.2.4. Homogeneity in the cross axis.....	112
7.2.5. Photolysis of species by the analysis light	113
7.2.6. Photolysis of ozone.....	113
7.3. EXPERIMENTAL CONDITIONS.....	115
RESULTS AND DISCUSSION.....	123
8. PRINCIPAL AND INDEPENDENT COMPONENTS ANALYSIS OF MTRMAS DATA.....	125
8.1. INTRODUCTION	125
8.2. STATISTICAL PROPERTIES OF KINETIC TEST DATASETS.....	125

8.3. RESULTS	131
8.3.1. <i>Model requirements not fulfilled</i>	131
8.3.2. <i>Model requirements fulfilled</i>	136
8.3.3. <i>Model requirements approximately fulfilled</i>	142
8.3.4. <i>Validation of the method in a well known system</i>	144
8.4. DISCUSSION	145
8.4.1. <i>Physical meaning of uncorrelatedness and statistical independence</i>	145
8.4.2. <i>Advantages over 'classic' methods</i>	147
8.4.3. <i>First achievements of the method in the system under study</i>	148
8.4.4. <i>Outlook</i>	149
8.5. SUMMARY AND CONCLUSIONS.....	149
9. ANALYSIS OF MTRMAS DATA BY MULTIVARIATE MULTIPLE LINEAR REGRESSION.....	151
9.1. INTRODUCTION.....	151
9.2. RESULTS AND DISCUSSION.....	151
9.2.1. <i>Separation of the temporal behaviour of IO and other UV broad band absorbers</i>	151
9.2.2. <i>Separation of the temporal behaviours of IO($X^2\Pi_{3/2}$, $v'' > 1$), OIO and I₂</i>	155
9.2.3. <i>Separation of the temporal behaviour of IO($X^2\Pi_{3/2}$, $v''=1$)</i>	156
9.3. APPLICATIONS.....	157
9.3.1. <i>Separation of full range overlapping spectra</i>	157
9.3.2. <i>Determination of absolute absorption cross sections</i>	157
9.3.3. <i>Kinetic analysis</i>	159
10. KINETIC AND MECHANISTIC STUDY OF THE I ₂ /O ₃ PHOTOCHEMICAL SYSTEM.....	161
10.1. INTRODUCTION.....	161
10.2. CALIBRATION OF TEMPORAL BEHAVIOURS.....	161
10.3. DATA ANALYSIS.....	165
10.4. RESULTS.....	167
10.4.1. <i>Conventional kinetic analysis</i>	167
10.4.1.1. Overall rate coefficient of IO+IO→products.....	167
10.4.1.2. Branching ratios of IO+IO→products.....	171
10.4.1.3. Fate of OIO.....	172
10.4.1.4. Excited IO species.....	174
10.4.1.5. Formation of molecular iodine.....	176
10.4.2. <i>Complex kinetic modelling of the I₂/O₃ photochemistry</i>	177
10.4.2.1. Proposed Mechanism.....	177
10.4.2.2. Results obtained with the proposed mechanism.....	183
10.4.2.3. Sensitivity studies.....	190
10.5. DISCUSSION.....	198
10.5.1. <i>Excited IO species</i>	198
10.5.2. <i>Overall rate of the IO self reaction</i>	199
10.5.3. <i>Branching of the IO self reaction</i>	205
10.5.4. <i>Fate of OIO and link to the higher oxides</i>	211
10.5.5. <i>Higher iodine oxides</i>	213
10.5.6. <i>Atmospheric relevance</i>	215
10.6. SUMMARY AND CONCLUSION.....	219
DANKSAGUNG / ACKNOWLEDGEMENTS / AGRADECIMIENTOS.....	223

APPENDIX	225
A. STATISTICAL INDEPENDENCE AND COST FUNCTIONS	227
B. NOTATION IN PCA AND ICA	231
C. ABSORPTION CROSS SECTIONS OF IODINE OXIDES	233
D. PHOTOLYSIS RATES OF IODINE OXIDES	237
E. REFERENCES	241

ABSTRACT

Iodine is a key trace element for all vertebrate species as a result of its participation in the thyroid function. The development of the atmospheric sciences in the last century enabled the identification of the chemical mechanism which facilitates the transfer of iodine from the sea to the marine atmosphere and subsequently to the continents and the food chain. This mechanism comprises the photo-oxidation of organic or molecular iodine emitted by the marine biosphere to soluble inorganic compounds and the accumulation of the latter in marine aerosol, which grows further into cloud condensation nuclei. The branching point of this chemistry is iodine monoxide, IO, which can alternatively recycle iodine atoms back, by depleting ozone in some cases, or generate soluble inorganic compounds by interacting with itself or with key tropospheric oxidants like NO_x and HO_x . However, the IO self reaction appears to offer an alternative route for iodine to aerosol, such that iodine compounds are not only passively taken up in pre-existing aerosol, but rather are able to initiate their production by a nucleation mechanism.

This laboratory study tries to contribute to this open front of atmospheric research. A flash photolysis set up combining time-resolved molecular optical absorption spectroscopy and atomic resonance absorption spectroscopy has been employed to investigate the I_2/O_3 photochemistry, and in particular the overall rate coefficient and the branching ratios of the self reaction of IO and the fate of its products $-\text{I}$, OIO , I_2O_2- . The experimental set up has been accurately characterised with the objective of minimizing uncertainties in the kinetic analysis. Additionally, a novel application of state-of-the-art multivariate mathematical techniques to achieve the separation of overlapping absorptions presented in this study is shown to significantly improve the analysis of raw spectroscopic and kinetic data. The accurate separation of pure absorbance versus time curves for each absorber facilitated the determination of reliable

absolute absorption cross sections, which in turn enabled the scaling of the absorbance curves to concentration. A kinetic simulation and fitting software package based on modern algorithms for integration of stiff systems of differential equations and constrained non linear fitting has been developed and successfully applied to the analysis of the concentration versus time curves. The simultaneous recording and analysis of as many species as possible has been found to be critical in order to obtain a consistent picture of the chemical mechanism operating in complex chemical systems like the one studied here.

A pressure independent value of $k(\text{IO}+\text{IO}) = (7.6 \pm 1.1) \times 10^{-11} \text{ cm}^3 \text{ molecule}^{-1} \text{ s}^{-1}$ has been determined. The pressure dependence of the branching ratios for the I+OIO and IOIO product channels in the IO+IO reaction have been determined and have values of 0.45 ± 0.10 and 0.44 ± 0.13 at 400 hPa, respectively. The branching ratios for the 2I+O₂ and I₂+O₂ product channels are pressure independent with values of 0.09 ± 0.06 and 0.05 ± 0.03 , respectively. The sensitivity analysis indicates that the isomer IOIO is more thermally stable than predicted by theoretical calculations. A reaction scheme comprising OIO polymerization steps has been shown to be consistent with the temporal behaviors recorded in this study. For simplicity, the rate coefficient has been assumed to be the same for each reaction $(\text{OIO})_n + \text{OIO} \rightarrow (\text{OIO})_{n+1}$, $n=1,2,3,4$. The lower limit obtained for this rate coefficient is $(1.2 \pm 0.3) \times 10^{-10} \text{ cm}^3 \text{ molecule}^{-1} \text{ s}^{-1}$ at 400 hPa. Evidence for the participation of IO in the polymerization mechanism has also been found. The rate coefficient for IO attachment to OIO and to small polymers has been determined to be larger than $(5 \pm 2) \times 10^{-11} \text{ cm}^3 \text{ molecule}^{-1} \text{ s}^{-1}$ at 400 hPa.

The results obtained for the branching of the IO self reaction indicate that it might not have a large ozone destruction potential under atmospheric conditions, but that in turn its products, which seem to be relatively photostable, could enhance the formation of new particles in the marine boundary layer. It has been speculated that one of these products –iodine dioxide, OIO– could nucleate and be responsible for particle

bursts episodes observed at day time and low tide in the coasts. This work presents laboratory evidence for an OIO polymerization process, obtained by simultaneous kinetic analysis of all the relevant gas phase species. However, the results obtained indicate that the iodine monoxide itself could be directly involved in that process by recombination with OIO, which yields a thermally stable condensable species: I_2O_3 . The more important product of the IO self reaction under atmospheric conditions –the IO dimer–, which constitutes a major source of uncertainty of the iodine chemistry, has been found to be more stable than previously thought and it could be involved in the nucleation process as well. Anyway, if the lifetimes with respect to thermal dissociation of the IO and OIO dimers were not long enough to allow other sinks for these species to compete under atmospheric conditions, the ozone destroying potential of the I-atom photosensitised decomposition of ozone would be about one third of that of bromine, and the main candidate for causing iodine-driven nucleation events in the coastal marine boundary layer would be I_2O_3 . A mechanism consistent with these findings is proposed to explain the different stoichiometric compositions of particles reported in the literature.

OUTLINE

This thesis is structured in ten chapters. While chapters 1 to 6 deal with the necessary background to this work, chapters 7 to 10 present the original scientific content. Some of the latter have a range of applications and implications which transcend the line of thinking of this Doctoral Thesis, and therefore partial conclusions and outlooks have been included.

-Chapter 1 gives some brief notes about the discovery of iodine, its biological role, its applications and the history of the atmospheric iodine chemistry.

-Chapter 2 offers a review of the atmospheric iodine chemistry. General concepts are introduced whenever they are required for a better understanding of the particular role of iodine.

-Chapter 3 enumerates the objectives of this work on the background of the previous chapter.

-Chapter 4 provides some general theoretical background about electronic absorption spectra, in the context of the Born-Oppenheimer approximation and the Franck-Condon principle. An understanding of the interaction between molecules and light is required to explain the experimental techniques and the methodology employed in this work. The particularities of the electronic spectra of IO and OIO are summarised at the end of the chapter.

-Chapter 5 summarises the concepts of the gas phase kinetic theory required for the understanding of the chemical mechanism under study. The summary focuses on the empirical rate equation and on the theoretical explanation of the rate coefficient of radical recombination reactions. A brief summary about the photochemistry of I₂ and O₃ is also

given.

-Chapter 6 contains a brief theoretical introduction to the separation of linearly mixed signals and in particular to the separation of overlapping absorption spectra.

-Chapter 7 describes the experimental set up used for this investigation and the steps undertaken in the present study for its accurate characterization.

-Chapter 8 presents a novel application of Principal and Independent Components analysis to the treatment of spectroscopic and kinetic raw data. This chapter consists of a stand-alone methodological investigation, whose results are used in Chapters 9 and 10.

-Chapter 9 describes how is carried out the separation of the overlapping temporal behaviours of all relevant absorbers contained in the datasets. The applications of the separated temporal behaviours are briefly discussed.

-Chapter 10 contains the main results of this work, i.e. the kinetic study of the I_2/O_3 photochemical system, and a thorough discussion of its atmospheric consequences.

Equations, reactions, figures and tables are respectively denoted with the letters E, R, F and T followed by the chapter number and the number of appearance in the chapter. For clarity, the reaction numbering starts afresh with each new chapter. References are numbered according to the order of appearance in the text. The units used belong to the international system (SI) and follow the recommendations of the Commission of Atmospheric Chemistry of the International Union of Pure and Applied Chemistry (IUPAC), Applied Chemistry Division [1]. Exceptions are indicated and justified in foot notes.

Part I

INTRODUCTION

1. HISTORICAL INTRODUCTION

The discovery of iodine and of its relationship to human health at the beginning of the 19th century [2-4] contributed to trigger some of the pioneering scientific studies of atmospheric processes and to the earliest attempts to establish a “chemical climatology” [5]. The first investigations of the geographical distribution of iodine in rain and soils [6, 7] were able to unravel the correlation between the occurrence of endemic goitre [8, 9] among the populations of certain regions and an iodine-depleted environment. These findings helped to develop a bundle of valuable ideas, which finally enabled the discovery of the essential biological role of iodine [2, 10] and of other trace species by the end of the 19th century. In retrospective, these historic facts highlight the importance of the atmospheric research and the characterisation of geochemical mechanisms with an impact on human life and health.

In 1852 there was already evidence that the iodine available to the continental biosphere is released by the marine biosphere and transported from the oceans by the atmosphere to the continents [7]. However, significant improvements in the understanding of the atmospheric cycle of iodine and its importance had to wait until the middle of the 20th century. In the 1960's, several studies [11, 12] presented evidence for the accumulation of iodine in marine particles and rain, thus confirming that the carrier of iodine to the continental biosphere are atmospherically processed sea-salt aerosols, subsequent condensation nuclei (CNN) and rain droplets. In the 1970's some studies reported tropospheric observations of CH₃I [13]. It was also suggested that the major portion of iodine in marine atmospheres could be I₂ ([12] and references therein). Moyers and Duce [12] and Zafiriou [14] wrote the first general reports on atmospheric iodine chemistry, which pointed to the photolysis of biologically generated methyl iodide and/or

molecular iodine, both of marine origin, as the source of free iodine atoms in the atmosphere. These would be oxidised to inorganic iodine compounds, highly polar and easily hydrolysable, that are expected to hydrate spontaneously or be scavenged by droplets [14].

By the middle of the last century the atmospheric science also started to face new problems related to human activities rather than to natural mechanisms. The dispersion of radioactive material in the environment as a result of nuclear fallout indicated the need of an understanding of the behaviour of atmospheric iodine [15]. Because iodine easily enters the food chain and selectively deposits in the thyroid, the primary health hazard of radioiodine are thyroid tumours resulting from ionizing radiation [16]. The artificial isotope ^{131}I has a very short lifetime (8 days) and emits fairly high-energy beta particles and a number of gamma rays [17, 18]. The naturally occurring iodine isotope ^{129}I (lifetime of 15.7 million years), which originates from the spallation of ^{129}Xe in the upper atmosphere, can be used as tracer of nuclear waste dispersion into the natural environment. This isotope was used e.g. in rainwater studies following the Chernobyl accident [19].

The general interest in halogen-catalysed stratospheric removal of ozone [20-22] stimulated an important scientific effort to understand the atmospheric chemistry of halogen species in general. The information about atmospheric iodine obtained along in the 1970's was compiled and analysed by Chameides and Davis [23]. Their seminal paper identified IO as a major branching point in the tropospheric chemistry of iodine and suggested the potential impact of iodine in the oxidizing capacity of the troposphere by depleting O_3 and by influencing the partitioning of other critical tropospheric oxidisers like NO_x (nitrogen oxides) and HO_x (hydroxyl radical and hydroperoxy radical). However, at that time there were considerable uncertainties about rate coefficients and branching ratios and they observed that depending on the values of several key rate constants and the

source of inorganic iodine, it could be conceivable for example that iodine could temporally and locally control the ozone budget, causing sharp drops in $[O_3]$ tropospheric levels. This modelling study established the framework for the subsequent theoretical, laboratory, field and modelling investigations on tropospheric chemistry.

In the early 1990's, many physico-chemical laboratory studies had already provided a significant feed-back to atmospheric modellers, but the knowledge about iodine species still presented important uncertainties. The investigations of Chatfield and Crutzen [24] and Solomon et al. [25] provided a new impulse to the study of the kinetics and spectroscopy of key iodine containing species and to their detection in the atmosphere. Many of the open questions and uncertainties pointed out in these studies have been addressed in the last 10 years ([26-31] and references therein) by the determination of:

- a) rate constants for many reactions of atmospheric relevance, and
- b) absorption cross sections,
- c) photolysis rates,
- d) heterogeneous uptake coefficients and
- e) thermodynamical parameters of important iodine containing species.

A further particularly important result was the discovery of OIO in a study undertaken in the Institute of Environmental Physics, University of Bremen [32]. In the field, the improvement of measurement and analytic techniques (see [33] and references therein) facilitated a number of studies reporting the observation of several precursors for atomic iodine [34-39], IO [37, 38, 40-42] and OIO [36-39, 43]. The availability of absolute absorption cross sections for these species made possible the determination of atmospheric concentrations and photolysis rates. In turn, all these results have enabled further improved detailed modelling of the iodine chemistry [44, 45].

However, the understanding of the iodine geochemistry is far from being complete. The increase of the scientific knowledge and the improvement of the technical capacities in the last years have also raised new questions concerning the importance of iodine in the atmosphere. For atmospheric modellers there is still a continuous demand for key physical and chemical parameters from laboratory research groups. This thesis deals with the laboratory study of a chemical mechanism of potential atmospheric significance involving iodine containing species.

2. ATMOSPHERIC IODINE CHEMISTRY

2.1. Introduction

In the last years several authors have reviewed the tropospheric chemistry of iodine [46-49] as a result of the rapidly increasing knowledge accumulated, while the question of stratospheric iodine has lost the attention which was initially caused by the modelling study of Solomon et al. [25]. As a consequence of the low observed values of stratospheric IO, it is thought that iodine chemistry has a minor effect in the stratospheric ozone budget. This chapter integrates the contents of the reviews of von Glasow and Crutzen [46], Carpenter [47], Plane and Saiz-López [48], O'Dowd and Hoffmann [49], and of the monography of Seinfeld and Pandis [50], incorporating some of the last results of the NAMBLEX campaign published in 2005 [51] and other studies recently published (see F2.1 for a summary of the iodine chemistry). It also refers to the personal communications exchanged in the General Assembly of the European Geophysical Union (EGU) in Vienna (Austria) in 2005 like the draft of the "Halogens in the Troposphere" (HitT) White Paper [52], the Workshop of the "Atmospheric Composition Change European Network of Excellence" (ACCENT) in Urbino (Italy) in 2005 and the workshops and meetings in the framework of the European project "Tropospheric halogens: effect on ozone" (THALOZ) [53], which has also partly founded this work. The intention is not to offer a comprehensive review, but to highlight the topics of ongoing research to which the results of this Doctoral Thesis are relevant.

2.2. Iodine sources

Iodine atoms are released in the atmosphere by photolysis of molecular iodine and volatile iodocarbons. In general, iodine compounds are more photolabile than their chlorine or bromine counterparts and, once emitted, are quickly degraded by photolysis to release iodine atoms [54]. Due to its low electronegativity, iodine forms very weak

covalent bonds with carbon, hydrogen and nitrogen and as a result iodine compounds are easily photo-dissociated in the near UV and visible spectrum, having very short lifetimes of only a few days or weeks. The observation of iodine oxides at night also suggests the existence of a chemical source strongly correlated to I_2 . It has been proposed that reaction of I_2 with the nitrate radical (NO_3) could provide such a source [36, 38].

Many studies have reported the observation of a variety of alkyl iodides (CH_3I , C_2H_5I , CH_2ICl , CH_2IBr , CH_2I_2) in the atmosphere. Early works [20] recognised the importance of biogenic emissions of iodine in the form of CH_3I . However, high uncertainties about the individual contribution of iodocarbons to the global iodine budget remain. The relative amounts of alkyl iodides are highly variable (compare e.g. [34] and [55]). The photolysis lifetime calculated for methyl iodide is of 3-5 days [56], while for Bromo- and Chloroiodomethane is of about 1 hour [56, 57] and for di-iodomethane is of about 5 min [57]. Thus, even if the local mixing ratio of CH_3I were one order of magnitude larger than the mixing ratio of CH_2I_2 [34], the contribution of CH_3I to the overall flux of iodine atoms would be two orders of magnitude smaller than that of CH_2I_2 . Moreover, there is some evidence that the source strength of CH_2I_2 could be of the same order of magnitude as that of CH_3I [55, 58]. In general, the short lifetimes of these compounds make difficult the estimation of concentrations and as a consequence of fluxes and source strengths. A summary of observed mixing ratios and estimated emission rates and atmospheric lifetimes can be found in Plane and Saiz-López [48]. In addition to iodocarbons, evidence is accumulating that molecular iodine could be a major atmospheric source of iodine [36-39].

There is strong evidence indicating that macroalgae emit almost every kind of iodocarbons detected so far in the atmosphere. Due to their low solubility, the ocean water can become supersaturated in these compounds, causing a flux from the ocean to the

atmosphere [59]. Peak concentrations have been observed at low tide in coastal locations, indicating that direct macroalgae emissions may control the atmospheric concentrations of iodocarbons [34] and molecular iodine [35]. However, coastal areas occupy only a 0.5% of the ocean surface area. In contrast, phytoplankton is distributed in the entire ocean surface, and it has also been found to be a source of halogenated compounds. Global estimations of iodocarbons emissions by macroalgae are available, but not for phytoplankton. In so far, significant open ocean iodine sources remain uncertain. It must be emphasised that the global impact of the iodine chemistry on the oxidative capacity of the atmosphere depends on the existence of significant open ocean sources of iodine. If that is not the case, the impact of this chemistry is probably small, although locally important in coastal regions.

2.2.1. Open ocean sources

Little is known about the distribution of most iodocarbons in the open ocean marine boundary layer (MBL). The exception is methyl iodide, which has been recurrently observed both over the open ocean [13] and in coastal locations [34]. Its mixing ratios vary between 0.5 and 2 pmol mol⁻¹ in the open ocean. The source strength of phytoplankton seems to be not sufficient to explain such mixing ratios, and therefore the main oceanic source of CH₃I remains unknown.

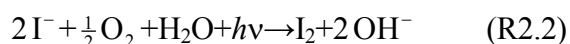
Moore and Zafiriou [60] showed that by irradiating seawater samples free of living matter with either sunlight or a solar simulator methyl iodide was produced. This was proved to be consistent with the recombination of photochemically produced methyl and iodine radicals:



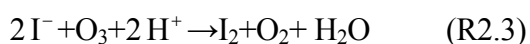
Surface seawater contains considerable amounts of iodide, which is readily oxidised by a variety of photochemical oxidants. Photolysis of biogenic iodocarbons also provides a source for iodine atoms. Methyl radicals are probably formed by the photolysis

of humic material. The process occurs at a rate which makes it potentially significant to the total production of methyl iodide in surface ocean waters and to the ocean supply of iodine in the atmosphere. However, it has been argued that maintaining a steady state concentration of CH_3I may be difficult because of rapid reaction with oxygen [47].

It is noticeable that the CH_3I source can not explain mixing ratios of IO observed in remote locations like Tenerife (Canary Islands, Spain) or Cape Grim (Tasmania, Australia), both representative of open ocean conditions [42]. Other iodocarbons might contribute to the iodine budget as well. Di-iodomethane has been observed in seawater but not yet in the open ocean atmosphere. Carpenter [61] suggests that evasion of CH_2I_2 into the atmosphere should occur, although some will be converted into the less reactive CH_2ICl in the surface ocean, which in contrast has been observed in the atmosphere. Also $\text{C}_2\text{H}_5\text{I}$ and $\text{C}_3\text{H}_7\text{I}$ have been observed both in air and seawater [62]. I_2 might provide the missing iodine source. Indeed, the 1974 halogen chemistry review of Zafiriou [14] considered both I_2 and CH_3I as the main precursors of atomic iodine in the atmosphere. Miyake and Tsungoai [63] demonstrated that by UV irradiated seawater releases molecular iodine. They suggested that photochemically produced molecular iodine could be the carrier species for the ocean to atmosphere transfer:



Garland and Curtis [64] proposed emission of I_2 in the presence of ozone, which is directly connected to dry deposition of ozone on the sea surface [49]:



However, it is not known whether I_2 can diffuse in significant amounts from the sea surface or not. According to Carpenter [61], in the open ocean environment, any production of I_2 is likely to be at least partly mitigated by rapid destruction in seawater, as a result of the rapid reaction of I_2 with organic matter. Molecular dynamics simulations for

the series of halide ions have shown that there is a trend for increasing availability at the interface for larger, more polarizable ions such as I^- . Therefore, iodide may be preferentially located at the interface and the volatilization of I_2 enhanced relative to its liquid phase reactions [49].

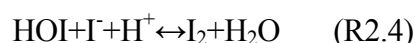
Data of transport and deposition of radioiodine following the Chernobyl fallout [19, 65] are consistent with significant deposition of gas phase iodine species from air masses after a transport time of about a week, suggesting that aerosol to vapour transfer of inorganic iodine is occurring. Halogen activation by iodine chemistry was proposed by Vogt et al. [44, 66]. Nevertheless, although halides in sea salt represent an important net flux of chlorine and bromine from the ocean to the atmosphere, sea salt particles act mainly to either remove or recycle gaseous iodine.

2.2.2. Coastal Sources

The current understanding is that CH_2I_2 constitutes the main form of organic iodine release in the coastal marine boundary layer, according to the production rate estimates reported by Carpenter [47], although many other iodocarbons have been observed whose atmospheric concentrations reach also peak values at low tide. Some species of macroalgae (seaweeds) tend to accumulate halide ions, which are subsequently used to get rid of the hydrogen peroxide produced as part of a defence mechanism against episodes of oxidative stress, originated by high temperatures, exposure to air as a result of low tide, etc (see [34, 35] and references therein). The formation of mono- and polyhalomethanes is initiated respectively by the enzymes halide ion methyl transferase and haloperoxidase, which catalyse the reaction between the accumulated halide ions and hydrogen peroxide, forming an electrophilic halogenating species. The latter can react with available organic material within the apoplast or outside the cell to form halogenated hydrocarbons, which are subsequently released to the surrounding water or air. Some laboratory studies suggest as

well the production of halocarbons by some species of phytoplankton, although at rates for unit of biomass smaller than in case of seaweeds [61, 62].

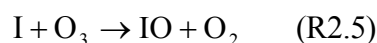
The photolysis of biogenic I_2 as source of atmospheric iodine has also been proposed by Saiz-López and Plane [36]. As a result of the haloperoxidase catalysed reaction of iodide and hydrogen peroxide, hipiodous acid is formed, and this species together with iodide establish an equilibrium with molecular iodine in aqueous solution:



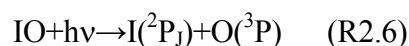
If the plant is exposed to air, covered only by a water film, the equilibrium is displaced towards the molecular iodine. I_2 is low soluble and relatively volatile, and will equilibrate between the liquid and the gas phase. Additionally, iodide can be oxidised by hydrogen peroxide, leading to direct iodine emission ([35, 61, 62] and references therein).

2.3. Fate of iodine atoms

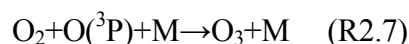
Unlike chlorine and bromine, which react with a range of organic molecules, iodine atoms do not react with organic compounds. As a result of the low electronegativity of iodine atoms they are unable to abstract H atoms from saturated hydrocarbons or add to double bonds of unsaturated species [50]. Therefore, reaction with O_3 , forming the iodine monoxide (IO) radical, is their major fate:



The regeneration of I atoms through IO photolysis is rapid. At daytime steady state exists between I and IO:



At atmospheric pressures recombination of $O(^3P)$ with O_2 is very rapid:



This cycle R2.5-R2.6-R2.7 has no net effect on ozone chemistry. It plays a dominant role in the IO chemistry, allowing a rapid interconversion of I and IO. Therefore

the behaviour of I and IO is coupled, and they may be collectively termed as 'IO_x'. However, a number of temporary soluble inorganic reservoir products are formed via self reaction of IO or reactions of I and/or IO with HO_x and NO_x [23]. These species facilitate the transfer of iodine from the gas phase to the aerosol phase. Iodine becomes concentrated in atmospherically processed sea-salt aerosol [11, 12] by heterogeneous uptake of soluble inorganic iodine compounds or by condensation of iodine oxides forming new particles [49, 67]. On the other side, reactions that convert IO back to iodine atoms without O atom formation lead to catalytic O₃ loss.

2.4. The role of iodine in the Stratospheric Chemistry

Ozone is the most important trace constituent of the atmosphere. Due to its strong absorption in the UV around 250 nm, it plays an essential role in screening the UV radiation emitted by the Sun. Ozone absorbs virtually all the UV radiation between 240 and 290 nm. Such radiation is harmful to unicellular organisms and to surface cells of higher plants and animals. Ozone also absorbs ultraviolet radiation in the range between 290 and 320, i.e. the UV-B. A reduction of stratospheric ozone leads to enhanced levels of UV-B radiation reaching the ground, which can increase the incidence of cancer skin. Most of the atmospheric ozone (about 90%) is found in the stratosphere, and stratospheric chemistry focuses on the chemical processes influencing the abundance of ozone.

Ozone is generated in the stratosphere by the Chapman cycle [50]. However, this photochemical mechanism is not capable to predict the observed ozone profiles of the stratosphere. It predicts too much ozone, thus indicating the existence of additional sinks. The effect on stratospheric ozone of chlorine released from man-made chlorofluorocarbons was predicted by Molina and Rowland [20]. Until 1994, only the chlorine and bromine had been considered among the halogens to play a role in stratospheric ozone depletion [21-23]. As a result of the rapid photo-dissociation of iodine compounds, it was generally

thought that they could never reach the stratosphere in significant amounts to have an impact upon ozone. Solomon et al. [25] suggested the necessity of re-evaluating the importance of iodine in the ozone depletion, as a result of:

- a) The observation of ozone trends in midlatitudes below 20 Km, where Cl and Br are not very effective for ozone depletion
- b) Evidence of fast convective transport of insoluble material in the tropics (short lived iodine compounds could be pumped up to the upper troposphere or the stratosphere). In fact, CH₃I has been observed in small but detectable concentrations in the lower stratosphere [59]
- c) Chain propagation for the iodine-catalysed ozone loss occurs most likely by the reaction of IO with ClO and/or BrO. Inter-halogen reactions involving iodine are exothermic and therefore rapid.

Solomon et al. [25] proposed that iodine chemistry in combination with trends in anthropogenic chlorine and bromine could be a factor in determining the depletion of lower stratospheric ozone in midlatitudes. By assuming $k(\text{IO}+\text{BrO}) = 10^{-10} \text{ cm}^3 \text{ molecule}^{-1} \text{ s}^{-1}$ and $k(\text{IO}+\text{ClO}) = 10^{-10} \text{ cm}^3 \text{ molecule}^{-1} \text{ s}^{-1}$, their model showed that 1 pmol mol⁻¹ of iodine and/or a trend in iodine could lead to much greater ozone losses. However, the current understanding [68] is that the stratospheric ozone loss enhancement by iodine is of minor importance as a result of low IO concentrations:

-Wennberg et al. [69]: upper limit of 0.2 pmol mol⁻¹ (ground-based spectra, 32°N)

-Pundt et al. [70]: upper limit of 0.2 pmol mol⁻¹ (balloon spectra, 44° and 68°N)

-Bösch et al. [71]: upper limit of 0.1 pmol mol⁻¹ (balloon spectra, 44° and 68°N)

On the other hand, Wittrock et al. [40] estimated an upper limit of 0.8 pmol mol⁻¹ (ground-based spectra, 79°N) that they suggest is in the stratosphere, based on SZA variation of slant column densities.

In addition, the rate constant for the IO+ClO reactions at $T < 210$ K is slower than originally predicted in the model of Solomon et al. $k(\text{IO}+\text{ClO}) = 1.6 \times 10^{-11} \text{ cm}^3 \text{ molecule}^{-1} \text{ s}^{-1}$ at 220 K [29, 72]. Although $k(\text{IO}+\text{BrO}) = 1.5 \times 10^{-10} \text{ cm}^3 \text{ molecule}^{-1} \text{ s}^{-1}$ at 220 K is high [29, 73, 74], with a mixing ratio of $0.1 \text{ pmol mol}^{-1}$ the loss of ozone at 16 km is too slow to affect mid-latitude ozone trends [68]. The large yields at 298 K reported for OClO and OIO from ClO+IO [29, 75] and BrO+IO [76] respectively do not favour iodine enhancement of the stratospheric ozone loss either. However, no data has been reported for lower temperatures. The quantum yield for the channel $\text{OClO}+h\nu \rightarrow \text{Cl}+\text{O}_2$ is less than 0.04 [31] and for $\text{OIO}+h\nu \rightarrow \text{I}+\text{O}_2$ less than 0.24 [77].

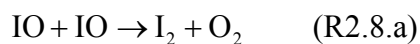
2.5. The role of iodine in the Tropospheric Chemistry

The modelling study by Chameides and Davies [23] suggested that iodine could play an important role in the tropospheric photochemical system. Recent observations of significant IO and OIO concentrations [36-43] support this hypothesis. Chameides and Davis speculated that, in contrast to the stratospheric chemistry, the chemical properties of iodine compounds resulting from the low electronegativity of iodine could make the iodine catalysed ozone depletion cycles more efficient in the troposphere than the chlorine and bromine cycles, and could even locally and temporally dominate the tropospheric ozone budget. However, Chameides and Davis also pointed out that any of these cycles could be short circuited by alternative reactions leading to cycles with no net impact on ozone. In addition, Chameides and Davis suggested that iodine can modulate the NO_x and HO_x balances. Finally, new ultra-fine particle formation events correlated to low tide and at day time observed in the coastal MBL have suggested a potentially important role of iodine in the formation of aerosol.

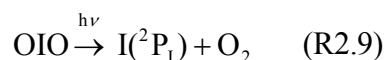
2.5.1. Iodine catalysed ozone depletion

The IO self reaction has been proposed [23] as one of the reactions leading to

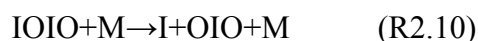
catalytic ozone destruction in the troposphere:



This reaction would have an important impact at high mixing ratios of IO ($> 2 \text{ pmol mol}^{-1}$) [70]. $\text{I}(^2\text{P}_1)$ atoms are generated directly by the IO self reaction, and in daytime by the photolysis of I_2 , resulting in additional consumption of O_3 , and IO being regenerated. The efficiency of O_3 destruction by the cycle comprising reactions R2.5 and R2.8 depends on the branching ratios of reaction R2.8, on the photo-stability of non iodine atom products and on the photo-fragments originated. There is evidence indicating that the dominating channels at atmospheric pressure are R2.8.c and R2.8.d [78, 79], restricting the ozone destroying potential of this cycle. I_2 is readily photolysed, but R2.8.a has been proved to be of minor importance, with an upper limit of the branching ratio of 0.05 [80]. The photolysis of OIO, if it occurs, proceeds via:

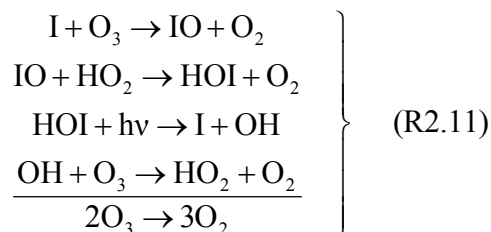


As photolysis of OIO to $\text{IO} + \text{O}(^3\text{P})$ has been ruled out (Ingham et al. [81], Ashworth et al. [82]), the cycle R2.5-R2.8-R2.9 has a larger chain length. The atmospheric fate of OIO is currently under discussion. A slow photolysis of OIO would result in a small ozone catalytic chain length. Recent studies report low upper limits for the I quantum yields from OIO photolysis: < 0.1 (562 nm) [83], < 0.05 (560 - 580 nm) [77] and < 0.24 (532 nm) [77]. Little is known about the properties of I_2O_2 . According to ab initio quantum calculations reported by Misra and Marshall [84] all the IO dimers thermodynamically accessible from R2.8.d are unstable. In particular, the more probable species IOIO would decay to $\text{I} + \text{OIO}$ in less than 1 ms under atmospheric conditions:

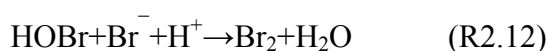


This would enhance the iodine destroying potential of the cycle comprising reactions R2.5 and R2.8. However, more recent estimations report lifetimes of about 100 ms [85].

At lower concentrations of IO, a photo-oxidation cycle becomes important:

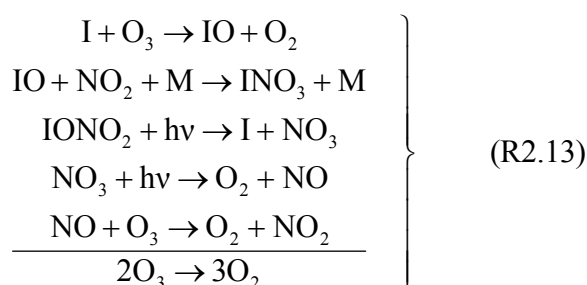


This cycle has a very long chain length and has been proposed to account for ozone depletion events in remote marine environments at sunrise, as a result of the photolysis of species that build up over night from halogen activation on sea-salt aerosol, i.e. volatilization of YX, where X,Y = Cl, Br and I (see [46] and references therein). The phenomenon known as ‘‘Bromine explosion’’, i.e. sudden and severe ozone depletion events observed in the cold seasons at sunrise in the Arctic and Antarctic MBL, occurs as a result of the bromine cycle analogous to R2.11. The aqueous phase reaction:



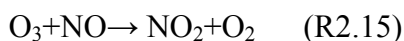
on brine-covered sea ice (frost flowers) [86] emits Br₂ to the gas phase, which is readily photolysed and initiate the cycle (R2.11) for bromine.

Finally, in semi-polluted environments, iodine nitrate formation can also lead to ozone depletion:



However, the efficiency of this cycle is reduced, because the photolysis of NO₃ yields NO₂+O rather than NO+O₂, leading to a null cycle in ozone via R2.7.

Once formed via reaction (R2.7), O_3 reacts with NO to regenerate NO_2 :



Since most of the NO_x emitted is in the form of NO , the concentration of ozone reached, if it were governed only by reactions R2.7, R2.14 and R2.15, would be far too low to account for the actual observed concentrations [50]. The reactions responsible for tropospheric ozone production are the so-called photooxidations. These reactions are discussed in section 2.5.3.

Chameides and Davis [24] proposed that in the presence of significant iodine concentrations the ratio NO_2/NO could be shifted towards NO_2 :



R2.14, R2.7, R2.16 and R2.5 constitute a null cycle for ozone, but they would have an indirect impact on the ozone production via photo-oxidation cycles (next section). However, during the night IO can also compensate the effect of R2.16 by removing NO_2 from the gas phase forming INO_3 , which is subsequently removed from the gas phase by recycling through sea salt aerosol:



This reaction provides an efficient route for denoxification of the MBL and conversion of NO_x to NO_3^- ions in the aerosols [46, 48]. During the day, the photolysis of INO_3 leads to a null ozone cycle, as indicated in the previous section.

One of the products of the IO self reaction, iodine dioxide (OIO), can also react with NO [87]:



This reaction would not have a large impact in NO_x . However, the slow OIO photolysis deduced from the latest laboratory studies [77, 83] could explain the low OIO mixing ratios observed at daytime, which normally remain under the detection limit [36-39].

As a result of the observation of IO and OIO at night time it has been proposed [36, 38] that I₂ reacts with NO₃:



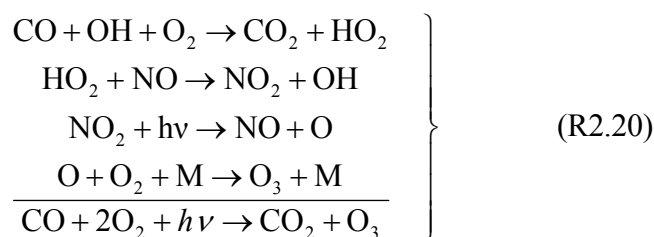
The nitrate radical is formed by oxidation of NO₂ by O₃. During the day, NO₃ photolyses rapidly both to NO+O₂ and NO₂+O, but during the night is available for reaction both with NO and NO₂, yielding respectively 2NO₂ and N₂O₅, the latter via third body recombination. In semi-polluted air masses, the loss of NO₃ is indirectly controlled by heterogeneous loss of N₂O₅, which occurs in aerosol particles or cloud droplets. Relatively high night time concentrations of NO₃ (tenths of pmol mol⁻¹) and I₂ (up to 93 pmol mol⁻¹ at night during low tide [37]) together with $k_{2.19} = 1.5 \times 10^{-12} \text{ cm}^3 \text{ molecule}^{-1} \text{ s}^{-1}$ [88] seem to be enough to provide the iodine source [38]. INO₃ decomposes thermally, yielding additional iodine, although heterogeneous uptake would occur at a similar rate and could compete as a sink for INO₃.

2.5.3. Impact of iodine monoxide chemistry upon MBL HO_x

The hydroxyl radical (OH) is the most important reactive species in the troposphere and indeed is the key to understand the reactions taking place on it. Unlike many molecular fragments formed from carbon containing molecules, OH does not react with O₂, and, as a result, it survives to react with virtually all trace gases, and among them most air pollutants and many gases involved in ozone depletion and the greenhouse effect. When reacting with trace species, OH is regenerated in catalytic cycles leading to relatively high sustained concentrations of about 10⁶ molecule cm⁻³ during day hours [50]. OH is formed in the troposphere by ozone photolysis and subsequent reaction of O(¹D) with water vapour, by photolysis of HONO and the reaction of hydroperoxy radicals with NO.

A example of the key role of OH as atmospheric oxidiser is its participation as

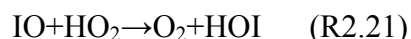
chain carrier in the carbon monoxide oxidation cycle. CO reacts with OH to produce CO₂ and a free hydrogen atom. The addition of the H to molecular iodine in an extremely fast third body recombination process weakens the O-O bond and the resulting hydroperoxy radical reacts more freely than O₂ itself. The subsequent reaction with NO is the most important sink of HO₂. The atmospheric cycle of oxidation of CO can be summarised as follows:



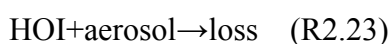
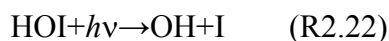
This mechanism exhibits many of the features of those involving much more complex organic species. The role of OH as the oxidizing species and the NO to NO₂ conversion by HO₂ are common to any atmospheric organic/NO_x mechanism (photooxidations), as well as the production of ozone (e.g. smog episodes in polluted urban environments). OH reacts with CH₄ and a range of Non Methane Hydrocarbons (NMHCs) to give a large number of organic peroxy radicals (RO₂), the most important of which is methyl-peroxy radical (CH₃O₂). The peroxy radicals react with NO to produce HO₂ and an alkoxy/acyloxy radical, which subsequently reacts with O₂ to yield HO₂ and thus close the OH-HO₂ cycle. Methane is the more abundant organic compound in the troposphere, and together with CO causes the major conversion rates between OH and HO₂, maintaining an steady state between these two radicals, and the catalytic ozone production cycle. A HO_x radical is recycled on average five times before it is removed by termination to form HNO₃.

Kanaya et al. [89] suggested that high levels of IO could explain the overestimation of measured HO₂ by up to 70% in atmospheric models. Recent evaluation of simultaneous measurements of halogen monoxides, NO_x and other related

species recorded during the NAMBLEX campaign at Mace Head [90, 91] has shown that under unpolluted conditions ($\text{NO}_x < 100 \text{ pmol mol}^{-1}$) the reaction:



can account for up to 40% of the hydroperoxy radical sink. The fate of the hypoiodous acid influences the HO_x abundance and partitioning:



At midday, the photolysis of HIO [92] could account of up to 15% of the total midday OH production rate [90]. Further, the production of a free iodine atom creates an ozone destructing cycle. Uptake of HOI upon aerosol leads to loss of HO_x from the gas phase system. Moreover, halogen oxides affect the O_3 loss and the NO_x partitioning, thus influencing indirectly the HO_x .

Similarly to NO, OH can also react with OIO:



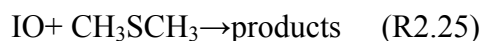
The rate coefficient predicted for this reaction by RRKM calculations [87] and the concentrations of OH observed in the MBL suggests that this reaction cannot control the OIO concentration, but it would provide a path for iodine to accumulate in the aerosol phase by heterogeneous uptake of the very stable HOIO₂ molecule.

2.5.4. Interaction between iodine and sulphur cycles

Dimethyl sulphide (DMS) CH_3SCH_3 emitted by phytoplankton in the oceans is the major contributor to the global sulphur flux. Once in the atmosphere, it reacts with OH or NO_3 to produce SO_2 and methane sulphonic acid (MSA). SO_2 reacts with OH to produce H_2SO_4 , which can generate particles with H_2O by binary homogeneous nucleation or condense on existing particles. SO_2 can also be adsorbed into existing droplets, where it can be heterogeneously converted to sulphate. By these processes,

sulphur emitted as DMS constitutes a major fraction of non-sea-salt sulphate and of marine CCN. It has been suggested that DMS is a prime regulator of marine CCN and that a climate feedback mechanism could exist in which temperature changes influence phytoplankton productivity and DMS emissions, thus affecting the marine cloudiness [50].

In 1990 Chatfield and Crutzen [24] analysed the consequences of a coupling between the iodine and sulphur cycles and their path to aerosols using a two dimensional model. They observed that if the reaction:



proceeded at the high rate coefficients ($\sim 10^{-11} \text{ cm}^3 \text{ molecule}^{-1} \text{ s}^{-1}$) which had been published in two studies published in 1987 (see [29] and references therein), it would be a principal sink for DMS in the MBL and would put a strong upper limit on IO concentrations of $2 \times 10^5 \text{ molecule cm}^{-3}$ ($0.02 \text{ pmol mol}^{-1}$). Their simulations suggested a better agreement with CH_3SOCH_3 concentration, the concentration and flux of sulphate and the diurnal variation of iodine species was obtained if the rate coefficient were below $10^{-12} \text{ cm}^3 \text{ molecule}^{-1} \text{ s}^{-1}$. The first observations of IO in the MBL were made years later, and mixing ratios of several pmol mol^{-1} were reported in remote marine locations [42], suggesting R2.23 is much slower. In subsequent laboratory studies [29] $k_{2.25}$ was found to be about $10^{-14} \text{ molecule}^{-1} \text{ s}^{-1} \text{ cm}^{-3}$, confirming that the iodine and sulphur cycles remain decoupled [29, 93]. The currently recommended value is $k_{2.25} = 1.5 \times 10^{-14} \text{ molecule}^{-1} \text{ s}^{-1} \text{ cm}^{-3}$ [29]. With this rate coefficient and the atmospheric mixing ratios of IO reported in the literature, reaction with IO is not an important sink for DMS. However, it could have locally some atmospheric relevance in iodine “hot spots”, e.g. at the coastal line, which are not detected in the DOAS field measurements as a result of integration over a path of several km.

2.5.5. Uptake of inorganic iodine compounds on sea salt aerosol. Halogen activation.

The enrichment on iodine of the aerosol with respect to seawater is well documented [11, 12, 94]. Duce et al. [11] observed I/Cl ratios in marine aerosol and precipitation samples 100-1000 larger than in seawater. The uptake of inorganic iodine compounds such as HI, HOI, HOIO₂, IONO₂, I₂O₂ and OIO together with iodine driven new particle formation (section 2.5.6) are thought to be responsible for such accumulation [95]. Therefore, aerosol appears to be a sink for I in the MBL. However, its distribution between the different possible chemical states is not clear. Variable proportions of iodate (IO₃⁻), iodide (I⁻), soluble organic iodine and insoluble iodine in aerosol have been reported [96]. This distribution is crucial, as it determines if iodine accumulates reversibly (I⁻) or irreversibly (IO₃⁻) in aerosol.

Depletion of aerosol in chlorine is known since the pioneering work of Cauer [97]. Vogt et al. [44, 66] have suggested that uptake of inorganic iodine on sea salt aerosols liberates chlorine and bromine into the gas phase, being also some iodine recycled back into the gas phase in this process. This would occur through acid-catalysed scavenging of HIO produced in R2.8:



where X = Cl, Br. Release of IX after interaction of HOI on salt surfaces has been observed in laboratory experiments [98]. IX molecules are readily photolysed at day time and both halogen atoms initiate ozone depleting cycles.

Accumulation of OIO and I₂O₂ has been assumed [95] as the main cause of irreversible enrichment of IO₃⁻ in aerosol (see F2.1). In the last years increasing photochemical information about OIO has been compiled [53, 77, 81-83], but few is known about I₂O₂ [53, 84]. The heterogeneous chemistry of this species is also

unknown. There are no data (accommodation coefficients, solubility, reactivity) on the interaction of OIO or I₂O₂ with e.g. sea-salt or sulphate aerosol [52].

2.5.6. New particle formation

Field observations

Condensation of condensable iodine vapours (CIVs) on pre-existing cluster embryos formed by H₂SO₄-H₂O-NH₃ nucleation and particle formation by homogeneous nucleation of iodine oxides have been proposed to explain bursts of ultra-fine particles in the coastal MBL. It is thought that particles generated in that way can contribute significantly to the background aerosol and further grow into condensation nuclei in the presence of additional CIVs, becoming important for cloud formation and radiative forcing [49, 67].

Strong evidence supporting the iodine oxides condensation mechanism is accumulating. Particle burst episodes have been observed at low tide and day time during the campaigns “New Particle Formation and Fate in the Coastal Environment” (PARFORCE) [67, 99-101], “North Atlantic marine Boundary layer Experiment” (NAMBLEX) [51, 102, 103] and “Quantifying coastal biogenic aerosol and gas flux” (BIOFLUX) [104, 105] in Mace Head. During these episodes high levels of iodocarbons and molecular iodine were detected, while the levels of sulphuric acid and ammonia were unable to explain condensational growth to observable particle size by ternary homogeneous nucleation H₂SO₄-H₂O-NH₃. Iodine has been observed in the freshly produced particles [106]. An inverse proportionality was found in early studies [16, 94] between particle size and iodine content, as one would expect from a gas phase condensable source of iodine [107]. The photolysis of mixtures of ozone and different precursors of atomic iodine, including samples of seaweed, in laboratory studies [35, 85, 108-113] has demonstrated the occurrence of iodine-driven rapid particle production.

Recently, it has been shown [35, 103, 112] that coastal particle bursts are more likely to result from molecular iodine photolysis than from di-iodomethane photolysis.

Laboratory studies

As a result of the significant electronegativity difference between iodine and oxygen, these atoms form very polar covalent bonds. Therefore, iodine oxides present large dipole moments ($\mu_{\text{IO}} = 2.5 \text{ D}$, $\mu_{\text{OIO}} = 3.9 \text{ D}^1$) [85] and are expected to condense as a result of long range intermolecular forces. Following the suggestion of Hoffman et al. [108], Burkholder et al. [110] simulated production of particles larger than 3 nm formed in a Teflon bag experiment by considering classical homogeneous homomolecular nucleation of OIO [50], consisting in multiple OIO condensation-evaporation steps leading to a thermodynamically stable iodine oxide cluster where particle growth starts:



Hoffman et al. [108] and Jiménez et al. [109], have proposed that $(\text{OIO})_n$ are polymeric chains or aggregates of polymeric branches containing the basic unit $-\text{I}-\text{O}-\text{IO}_2-$. The lack of hygroscopic growth in humid experiments observed by Jiménez et al. [109] supports this assignment.

Unfortunately, the experiments reported by Burkholder et al. [110] did not include the simultaneous measurement of IO, OIO and polymers, which would have been required to validate the mechanism. The OIO nucleation model, which successfully reproduced the particle formation observed, may oversimplify the chemistry by neglecting other nucleation paths. Similarly, the use of collision rates derived from classic kinetic theory in the first steps of the nucleation process is a simplistic approach to estimate the rate coefficients of the forward reactions of the equilibrium reaction (R2.27). Recent works [53, 83, 85] indicate that:

¹ The Debye (D) is the unit of dipole moment (μ) in the CGS system, although it is commonly preferred to the SI unit, the Coulomb \times meter (C \times m). 1 Debye = $3.33564 \cdot 10^{-30}$ C \times m

- a) The OIO radical could be involved in other reactions (i.e., other monomers could participate in the nucleation process),
- b) the rate coefficients for polymer formation may differ from those predicted by the kinetic theory,
- c) and that all iodine polymers may be thermally stable at ambient conditions from the beginning of the nucleation process ($n = 1$).

Recently, Pirjola et al. [111] have modelled ultra-fine particle formation from seaweed in chamber experiments by using a homogeneous nucleation model where all iodine clusters are assumed to be thermally stable. Their sensitivity studies indicate that the contribution of an extra CIV (I_2O_2 or I_2O_3) in the nucleation process is also likely. Unfortunately, no measurements of IO or OIO were made in these experiments either.

Several studies report the formation of higher iodine oxides in the form of aerosol or deposits (see Chase [31] and references therein). The composition of the deposits and aerosol collected varies between the different studies. For example, Vikis and McFarlane [114] and Sunder et al. [115] report the observation of a solid stoichiometrically and spectroscopically consistent with I_4O_9 . The study of Saunders and Plane [85] reports an O/I stoichiometric ratio of 2.5 for the particles produced in I_2/O_3 photolysis experiments and suggests an alternative path to the particles consisting in successive oxidation steps of I_2O_2 , I_2O_3 and I_2O_4 by ozone leading to I_2O_5 , which would subsequently condensate. In contrast, a recent study by Ristovski et al. [113] reports a O/I stoichiometric ratio of 2. The aerosol mass spectra recorded by O'Dowd et al. [101], Hoffmann et al. [108], Jiménez et al. [109] and McFiggans et al. [35] in different systems in the presence of O_3 are consistent with any of these iodine oxides.

Modelling studies

Recently published studies have incorporated iodine nucleation in atmospheric

models in an attempt to explain new particle formation in the MBL. The different approaches adopted indicate that further theoretical and experimental work is needed to study the thermal and photo-stability of I_2O_2 and the potential participation of other species than OIO in the nucleation. Saiz-Lopez et al. [103] consider a nucleation mechanism where the smallest “particles” formed can be either I_2O_2 , I_2O_3 or I_2O_4 , and demonstrate that the rate of formation of these species can be competitive with OIO photolysis if the concentration of iodine oxides is high. On the other hand, the model shows that the impact of the iodine chemistry on the ozone budget is small. In contrast, Pechtl et al. [116] consider in their model the parameterization of the homomolecular homogeneous OIO nucleation reported by Burkholder et al. [110] and ternary H_2SO_4 - H_2O - NH_3 nucleation. In this case I_2O_2 is assumed to be thermally unstable, in such a way that the IO self reaction proceeds effectively at 80% through the I+OIO channel. The amount of particles predicted by this model is sensitive to additional OIO sinks, like OIO photolysis.

As occurs with the rest of the iodine chemistry, the importance at global scale of iodine driven particle production depends on the existence of a significant marine source of iodine. The modelling studies of Saiz-López et al. [103] show that the iodine particles can grow to make an important contribution to CCN, at least on a regional scale. McFiggans et al. [117] proposed that the same nucleation mechanism may be partly responsible for the production of marine aerosol, which implies an additional source of iodine. O’Dowd et al. [113] claimed that the proposal of an additional source of CIVs being involved in marine aerosol formation is partly speculative, and argued that the amount of CIVs in the open ocean is not enough to allow nucleation in the absence of pre-existing nanometer-scale sulphate clusters.

3. OBJECTIVES

Together with field measurements and modelling, physical-chemical laboratory studies constitute the third column of atmospheric research. Apart from having an obvious value by themselves, they are required to supply valuable information both for analytic and for modelling and interpretation purposes. An example of the former is the well established detection of trace gases based in Differential Optical Absorption Spectroscopy (DOAS) (see [119] and references therein), which requires the determination of accurate absorption cross sections. Examples of the latter are the use of photolysis and reaction rates obtained in laboratory studies in models, which enable evaluating the importance of chemical processes in the atmosphere by comparison with the measured data.

The general objective of the laboratory studies on iodine chemistry conducted by the group of Molecular Spectroscopy and Chemical Kinetics in the Institute for Environmental Physics at the University of Bremen (IUP-UB) was a comprehensive characterization of the I_2/O_3 photochemical system with immediate application to the understanding of atmospheric phenomena. The initial aim was to reduce the uncertainties in the cycles involving the IO self reaction. In particular, expected results were:

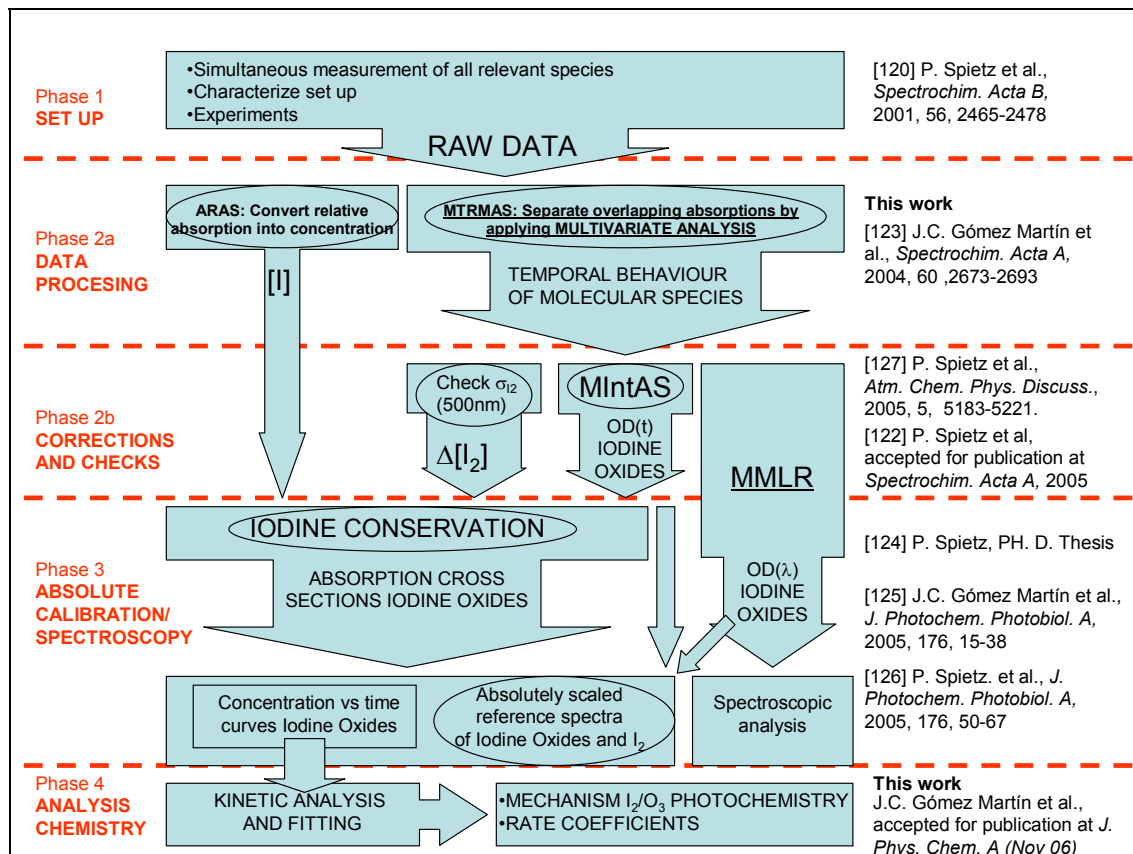
- a) a determination of the absolute absorption cross sections of relevant iodine containing species in the UV-visible spectral range independent of kinetic assumptions and
- b) a detailed description of the chemical mechanism involved, including determination of relevant rate coefficients and branching ratios.

As the investigation developed, new questions were raised, especially concerning the potential of iodine to induce new particle formation in the coastal MBL

3.1. General Strategy

The diagram in F3.1 indicates the strategy designed, the experimental and analytical techniques implemented and developed, the results obtained and the potential application in the atmospheric research. The initial phase of this project consisted in the development and characterisation of the experimental set-up and the identification of the main sources of uncertainties which could have affected previous spectroscopic and kinetic studies. In this phase it was decided to design an experimental set-up which enables to monitor simultaneously all relevant species involved in the primary chemical processes under study (I, IO, OIO, I₂). To implement this concept, a Charge Coupled Device (CCD) Camera was coupled to a Czerny-Turner spectrometer to perform Multichannel Time-resolved Molecular Absorption Spectroscopy (MTRMAS), using instrument resolutions which enable to monitor broad spectral windows of about 300 nm containing the spectral features of most relevant (known) absorbers. To monitor the atomic species of relevance (I), a synchronised detection apparatus based in Atomic Resonance Absorption Spectroscopy (ARAS) was included in the cross axis of the reaction vessel, perpendicular to the flow of the gas mixtures. A laboratory-made electrodeless iodine lamp was built in cooperation with the University of Riga (Latvia) and the ARAS set-up was carefully characterised [120]. With respect to the preliminary investigations performed in back to back experiments with single wavelength sampling using a photomultiplier tube (PMT) [121], this decision enabled to improve significantly the mutual consistence of the data recordings for each species, avoiding time drifts in concentrations and in other experimental conditions. In the last phase of the study, this also enabled to include more observational data in the kinetic fitting, reducing in that way the uncertainty associated with the analysis of a system of a complex kinetic behaviour as this one. The main drawbacks of such multichannel data recording, namely the effect of limited resolution on

narrow spectral features, was successfully tackled by developing a method (Multichannel Integrated absorption Spectroscopy, MIntAS)) with potential application in similar systems [122].



F3.1. Strategy, objectives and results of the laboratory studies on iodine chemistry conducted at the IUP-UB. Abbreviations: ARAS, Atomic Resonance Absorption Spectroscopy; MTRMAS, multichannel time-resolved molecular absorption spectroscopy; MMLR, Multivariate Multiple Linear Regression; OD: optical density.

A second phase comprised the analysis of the raw data recordings and required corrections and checks were carried out. It was found that a potential source of uncertainty in previous studies was the overlapping of spectral absorption features corresponding to different molecules. Optical density temporal behaviours of species like IO were definitely overlapped to optical densities resulting from unassigned UV absorbers. Similarly, I_2 and OIO were overlapped and the use of conventional deconvolution techniques was not a guarantee of success in the separation, mostly as a result of a lack of appropriate reference spectra. This issue was tackled dedicatedly by implementing a novel application of

Multivariate Analysis techniques like Principal and Independent Components Analysis (PCA and ICA) to the MTRMAS data recordings [123]. By selective application of these methods it was possible to obtain separated optical density time traces of absorbers to a high degree of accuracy and even the detection of new species.

In the third phase, the separated and resolution corrected temporal behaviours of the molecular species were used to carry out the spectroscopic analysis:

- 1) Determination of absolute absorption cross sections at selected wavelengths using an iodine conservation approach [124, 125].
- 2) Extraction of pure full range spectra of the different species by multivariate multiple linear regression [126].
- 3) Spectroscopic analysis of the IO improved spectrum and discussion of the origin of the featureless spectra observed [126].

Additionally, the VIS absolute absorption cross sections of I_2 were measured in parallel experiments to confirm the only reference value in which the determination of iodine oxides absorption cross sections by iodine conservation approach is based [127]. A by product of this work was the recording of I_2 reference spectra at column densities appropriate for atmospheric retrieval with DOAS.

The last stage of this project culminates the study of the I_2/O_3 photochemistry presented in the present work. The pure and resolution corrected time traces of the different species involved have been scaled to concentration by using the corresponding absorption cross sections determined in the previous phase, and they have been analysed by kinetic methods. Atmospherically relevant kinetic parameters have been obtained and a mechanism describing the chemistry involved has been proposed.

3.2. Objectives of this work

In this work an investigation of the I_2/O_3 photochemistry by multichannel time-resolved absorption spectroscopy and atomic resonance absorption spectroscopy is presented. The objectives are:

- i) To achieve methodological improvements in the analysis of spectroscopic and kinetic data by implementing multivariate techniques which enable to maximise the extraction of information from datasets and reduce the uncertainty introduced by overlapping absorptions.
- ii) To contribute to the clarification of the role of iodine on the atmospheric chemistry by investigating a chemical system with potential atmospheric relevance:
 - a. To study the overall rate coefficient and the branching of the IO self reaction at 298 K as a function of pressure.
 - b. To propose a plausible mechanism to explain the fate of OIO and I_2O_2 and their link to aerosol.

Part II

THEORY

4. ELECTRONIC ABSORPTION SPECTRA

4.1. The Beer-Lambert Law

The intensity of light $I(\nu)$ transmitted through a gas-phase homogeneous absorbing layer at a given frequency ν is given by an empirical relationship known as Beer-Lambert Law:

$$I(\nu) = I_0(\nu)^{-C\sigma(\nu)\Delta x} \quad (\text{E4.1})$$

where $I_0(\nu)$ is the intensity of the incoming radiation at the frequency ν , C is the concentration of the absorbing species (in molecule cm^{-3}), $\sigma(\nu)$ is the absorption cross section per molecule at the frequency ν and Δx is the thickness of an absorbing layer. The absorption cross section has dimensions of an area and can be regarded as the area of a disc of absorbing material that, placed at the right angles to the light beam, would absorb the same number of photons per second, each of energy $h\nu$, as the molecule under consideration. The link of the “empirical” absorption cross section to the transition probability between two given states of the molecules is explained in the next section. The usual mathematical expression of the Beer-Lambert Law is obtained by taking logarithms in both sides of E4.1. The resulting equation reads:

$$A(\nu, t) \equiv \log(I_0(\nu)/I(\nu)) = \sigma(\nu)C(t)\Delta x \quad (\text{E4.2})$$

where $A(\nu)$ is the absorbance or optical density. The absorbance could depend on time (t), because the concentration of the absorbing species could change as a result of a variety of phenomena, e.g. transport and chemical reactions. The quantities $I(\nu)$, $I_0(\nu)$, C and Δx can be directly measured and, thus, the Beer-Lambert Law enables to access experimentally the quantum-mechanical parameters linked to the transition probability between two states. In turn, this law enables the determination of the concentration of molecular species

provided that the absorption cross section for a given transition is known. Equation E4.2 constitutes the base of the methodology applied in this work, i.e. determining A with reduced uncertainty for different species in order to calculate their respective concentrations.

4.2. Interaction of the electromagnetic field with molecules

4.2.1. Transition probability

The Hamiltonian of a spinless particle of charge q and mass M in an electromagnetic field is given by:

$$H = \frac{1}{2M}(\mathbf{p} - q\mathbf{A})^2 + q\phi \quad (\text{E4.3})$$

where \mathbf{p} is the generalised momentum of the particle, and \mathbf{A} and ϕ are respectively the vector and the scalar potentials generating the electromagnetic field. In general, a linearly polarised pulse of radiation can be described by taking $\phi=0$ and representing $\mathbf{A}(\mathbf{r},t)$ as a superposition of plane waves $\mathbf{A}(\omega;\mathbf{r},t)$ having the same direction of propagation $\hat{\mathbf{k}}$:

$$\mathbf{A}(\mathbf{r},t) = \int_{\Delta\omega} A_0(\omega) \hat{\mathbf{e}} \left(e^{i(\mathbf{k}\cdot\mathbf{r} - \omega t + \delta_\omega)} + e^{-i(\mathbf{k}\cdot\mathbf{r} - \omega t + \delta_\omega)} \right) d\omega \quad (\text{E4.4})$$

where $\hat{\mathbf{e}}$ is the direction of linear polarisation, \mathbf{k} is the wave vector and ω the angular frequency ($\omega=2\pi\nu$). If the phases are distributed at random as a function of ω , the pulse of radiation is said to be incoherent.

Using the Coulomb gauge ($\nabla \times \mathbf{A} = 0$) and setting $\phi=0$ [128], the time dependent Schrödinger equation for a molecule with N electrons and N' nuclei in an electromagnetic field is given by:

$$\begin{aligned} i\hbar \frac{\partial}{\partial t} \psi(t; \mathbf{R}_1, \dots, \mathbf{R}_{N'}; \mathbf{r}_1, \dots, \mathbf{r}_N) = & \left[H_0 - \sum_{j=1}^N \left(\frac{i\hbar e}{m} \mathbf{A}(\mathbf{r}_j, t) \cdot \vec{\nabla}_j + \frac{e^2}{2m} (\mathbf{A}(\mathbf{r}_j, t))^2 \right) \right] + \\ & + \sum_{\ell=1}^{N'} \left(\frac{i\hbar Z_\ell e}{M_\ell} \mathbf{A}(\mathbf{R}_\ell, t) \cdot \vec{\nabla}_\ell + \frac{(Z_\ell e)^2}{2M_\ell} (\mathbf{A}(\mathbf{R}_\ell, t))^2 \right) \right] \psi(t; \mathbf{R}_1, \dots, \mathbf{R}_{N'}; \mathbf{r}_1, \dots, \mathbf{r}_N) \end{aligned} \quad (\text{E4.5})$$

where H_0 is the unperturbed Hamiltonian of the molecular system and the charges and masses of the nuclei are given by $Z_\ell e$ and M_ℓ respectively ($\ell=1, \dots, N'$). The solution of the unperturbed problem [128-132] yields the molecular wave functions and their corresponding energy eigenvalues. The configuration of energy levels for two bounding electronic states of the IO molecule is represented in figure F4.1.

In the case of a weak field the terms in \mathbf{A}^2 are small compared with the linear terms in \mathbf{A} , and therefore the former can be dropped and the sum of terms in \mathbf{A} can be treated as a small perturbation ($H'(t)$). This problem is solved by using time-dependent perturbation theory. The general solution of the time dependent Schrödinger equation is given by

$$\Psi = \sum_q c_q(t) \psi_q(\mathbf{R}_1, \dots, \mathbf{R}_{N'}; \mathbf{r}_1, \dots, \mathbf{r}_N) e^{-iE_q t / \hbar} \quad (\text{E4.6})$$

where ψ_q are the unperturbed molecular states. In the simplest approximation, the couplings between the electronic, the vibrational and the rotational motions in the molecule can be neglected. The complete molecular wave functions in two states a and b can be characterised respectively by the sets of quantum numbers $a \equiv (\nu_1'', \dots, \nu_{3N'-X}'', \mathfrak{S}'', M_{\mathfrak{S}}'', \Lambda'', S'')$ and $b \equiv (\nu_1', \dots, \nu_{3N'-X}', \mathfrak{S}', M_{\mathfrak{S}}', \Lambda', S')$ [128-132], with $X=5$ for linear molecules and $X=6$ for non-linear molecules. These quantum numbers are the vibrational ($\nu_1, \dots, \nu_{3N'-X}$), orbital angular momentum (\mathfrak{S}) and magnetic ($M_{\mathfrak{S}}$) quantum numbers of the nuclei, and the magnetic (Λ) and spin (S) quantum numbers of the electrons. If the molecule is initially in a well-defined bound state of energy E_a and a pulse of radiation is switched on at $t=0$ such that the initial condition is given by $c_k(t \leq 0) = \delta_{ka}$, then the coefficient $c_b(t)$ for the final state of energy E_b is given in first order of perturbation theory by:

$$\begin{aligned} c_b^{(1)}(t) &= (i\hbar)^{-1} \int_0^t \langle \psi_b | H'(t) | \psi_a \rangle e^{i\omega_{ba}t'} dt = \\ &= \int_0^t \langle \psi_b | -\frac{e}{m} \sum_{j=1}^N \mathbf{A}(\mathbf{r}_j, t) \cdot \vec{\nabla}_j + \sum_{\ell=1}^{N'} \frac{Z_\ell e}{M_\ell} \mathbf{A}(\mathbf{R}_\ell, t) \cdot \vec{\nabla}_\ell | \psi_a \rangle e^{i\omega_{ba}t'} dt \end{aligned} \quad (\text{E4.7})$$

where $\omega_{ba}=(E_b-E_a)/\hbar$. It is convenient to separate the electronic and the nuclear terms:

$$\begin{aligned} \langle \psi_b | -\frac{e}{m} \sum_{j=1}^N \mathbf{A}(\mathbf{r}_j, t) \cdot \vec{\nabla}_j + \sum_{\ell=1}^{N'} \frac{Z_\ell e}{M_\ell} \mathbf{A}(\mathbf{R}_\ell, t) \cdot \vec{\nabla}_\ell | \psi_a \rangle = \\ = \langle \psi_b | -\frac{e}{m} \sum_{j=1}^N \mathbf{A}(\mathbf{r}_j, t) \cdot \vec{\nabla}_j | \psi_a \rangle + \langle \psi_b | \sum_{\ell=1}^{N'} \frac{Z_\ell e}{M_\ell} \mathbf{A}(\mathbf{R}_\ell, t) \cdot \vec{\nabla}_\ell | \psi_a \rangle \end{aligned} \quad (\text{E4.8})$$

By inserting E4.4 in E4.7 and splitting the terms as in E4.8 results:

$$\begin{aligned} c_b^{(1)}(t) = -\frac{e}{m} \int_{\Delta\omega} d\omega A_0(\omega) e^{i\delta\omega} \left[\sum_{j=1}^N \langle \psi_b | e^{i\mathbf{k}\cdot\mathbf{r}_j} \hat{\boldsymbol{\epsilon}} \cdot \vec{\nabla}_j | \psi_a \rangle \int_0^t dt' e^{i(\omega_{ba}-\omega)t'} + \right. \\ \left. + e^{-i\delta\omega} \sum_{j=1}^N \langle \psi_b | e^{-i\mathbf{k}\cdot\mathbf{r}_j} \hat{\boldsymbol{\epsilon}} \cdot \vec{\nabla}_j | \psi_a \rangle \int_0^t dt' e^{i(\omega_{ba}+\omega)t'} \right] + \\ + \int_{\Delta\omega} d\omega + A_0(\omega) e^{i\delta\omega} \left[\sum_{\ell=1}^{N'} \frac{Z_\ell e}{M_\ell} \langle \psi_b | e^{i\mathbf{k}\cdot\mathbf{R}_\ell} \hat{\boldsymbol{\epsilon}} \cdot \vec{\nabla}_\ell | \psi_a \rangle \int_0^t dt' e^{i(\omega_{ba}-\omega)t'} + \right. \\ \left. + e^{-i\delta\omega} \sum_{\ell=1}^{N'} \frac{Z_\ell e}{M_\ell} \langle \psi_b | e^{i\mathbf{k}\cdot\mathbf{R}_\ell} \hat{\boldsymbol{\epsilon}} \cdot \vec{\nabla}_\ell | \psi_a \rangle \int_0^t dt' e^{i(\omega_{ba}+\omega)t'} \right] \end{aligned} \quad (\text{E4.9})$$

In general the duration of the pulse is much larger than the periodic time $2\pi/\omega_{ba}$. Thus, the first and third integrals over t' will be negligible unless $\omega_{ba} \approx \omega$, *i.e.* $E_b \approx E_a + \hbar\omega$. In this case the final state of the molecule has a greater energy than the initial state and one photon of energy $\hbar\omega$ has been absorbed from the radiation. On the other hand, the second and fourths integral over t' will be negligible unless $\omega_{ba} \approx -\omega$, *i.e.* $E_b \approx E_a - \hbar\omega$. In this case the final state of the molecule has a lower energy than the initial state and one photon of energy $\hbar\omega$ has been emitted. Since only one of these conditions can be satisfied for a pair of states a and b , it is possible to deal with the terms for absorption and emission in E4.9 separately. The following discussion will focus only in the absorption of radiation, *i.e.* the first integral over $\Delta\omega$. This is the phenomenon in which the detection technique used in this work is based.

The probability of finding the molecule in the state b is given by:

$$|c_b^{(1)}(t)|^2 = 2 \int_{\Delta\omega} d\omega [A_0(\omega)]^2 \left| -\sum_{j=1}^N \frac{e}{m} \langle \psi_b | e^{i\mathbf{k}\cdot\mathbf{r}_j} \hat{\boldsymbol{\epsilon}} \cdot \vec{\nabla}_j | \psi_a \rangle + \sum_{\ell=1}^{N'} \frac{Z_\ell e}{M_\ell} \langle \psi_b | e^{i\mathbf{k}\cdot\mathbf{R}_\ell} \hat{\boldsymbol{\epsilon}} \cdot \vec{\nabla}_\ell | \psi_a \rangle \right|^2 F(t, \omega - \omega_{ba}) \quad (\text{E4.10})$$

assuming that the pulse of radiation is coherent. The matrix element inside the integral in E4.10 is denoted usually $M_{ba}(\omega)$ and it is the so-called transition moment. The function $F(t, \omega - \omega_{ba})$ is a squared t -sinc function [128, 133]. For large t , this function presents a sharp maximum at $\omega = \omega_{ba}$, and therefore $\omega = \omega_{ba}$ can be set in the slow varying quantities $A_0^2(\omega)$ and $|M_{ba}(\omega)|^2$, so that these factors can be taken outside the integral and extend the integration limits on ω to $\pm\infty$. From these operations results the following expressions:

$$|c_b^{(1)}(t)|^2 = 2\pi [A_0(\omega_{ba})]^2 |M_{ba}(\omega_{ba})|^2 t \Rightarrow W_{ba} \equiv \frac{d|c_b^{(1)}(t)|^2}{dt} = 2\pi [A_0(\omega_{ba})]^2 |M_{ba}(\omega_{ba})|^2 \quad (\text{E4.11})$$

where W_{ba} is the transition rate for absorption, i.e., the transition probability per unit time and molecules in absorption. In terms of intensity per unit angular frequency range, $I_0(\omega)$, the transition rate for absorption can be written as follows:

$$W_{ba} = \frac{\pi}{c\epsilon_0} \frac{I_0(\omega_{ba})}{\omega_{ba}^2} |M_{ba}(\omega_{ba})|^2 = \frac{I_0(\omega_{ba})}{c} B_{ba} \quad (\text{E4.12})$$

where B_{ba} is the Einstein coefficient for absorption. The rate of absorption of energy from the beam per molecule is $(\hbar\omega_{ba})W_{ba}$. The absorption cross section for the transition between the states a and b is defined as the rate of absorption of energy per molecule divided by $I_0(\omega_{ba})$:

$$\tilde{\sigma}_{ba} = \frac{\pi \hbar}{c\epsilon_0 \omega_{ba}} |M_{ba}(\omega_{ba})|^2 = \frac{\hbar\omega_{ba}}{c} B_{ba} \quad (\text{E4.13})$$

The intensity of absorption, i.e. the energy absorbed from the incident beam per cm^2 , is given by:

$$I_{abs}(\omega_{ba}) = \frac{I_0(\omega_{ba})}{c} B_{ba} \hbar\omega_{ba} C_a \Delta x = I_0(\omega_{ba}) \tilde{\sigma}_{ba} C_a \Delta x \quad (\text{E4.14})$$

where Δx is the thickness of an absorbing layer, i.e. the path length, and C_a the concentration of molecules in the state a (in $\text{molec}\cdot\text{cm}^{-3}$).

Equation E4.14 enables to connect the quantum-mechanic description of the interaction between molecules and radiation fields with the phenomenological Beer-Lambert law. If in E4.1 the exponent $|\sigma C \Delta x| \ll 1$, the terms of order larger than 2 of the Taylor expansion of the exponential in E4.1 can be neglected:

$$I(\nu) = I_0(\nu)(1 - C\sigma(\nu)\Delta x) \quad (\text{E4.15})$$

This result can be expressed as well in terms of absorbed intensity:

$$I^{abs}(\nu) = I_0(\nu) - I(\nu) = I_0(\nu)C\sigma(\nu)\Delta x \quad (\text{E4.16})$$

As a result of the finite width of the absorption lines, the total intensity absorbed in a transition between a and b is given by the integral of the intensity absorbed over a given frequency interval. Therefore, by integrating E4.16, and assuming that I_0 is constant over the integration range, it can be written:

$$I_{ba}^{abs}(\nu_{ba}) = I_0 C \Delta x \int \sigma(\nu) d\nu \quad (\text{E4.17})$$

By comparing E4.14 and E4.16 the absorption cross section as defined in E4.13 can be related to the empirical quantity of E4.1:

$$\int \sigma(\nu) d\nu = \tilde{\sigma}_{ba} \quad (\text{E4.18})$$

Therefore, the Beer-Lambert Law enables to access experimentally the theoretical parameters related to the absorption transition probabilities between two states in the molecule. Note that the cross section σ is an experimental observable which depends both in the transition probabilities and in the physical phenomena causing broadening of the line width. This absorption cross section can only be related to the cross section for transitions between two states by integrating in the appropriate spectral interval.

4.2.2. Allowed and forbidden transitions

The transition moment M_{ba} can be simplified in many cases of practical interest by expanding the corresponding exponentials as a series of powers of $i\mathbf{k}\cdot\mathbf{r}_j$ and $i\mathbf{k}\cdot\mathbf{R}_\ell$ and retaining only the first term. The molecular wave functions and the internuclear distances can extend over small distances of several hundreds picometers, while the wavelengths associated with optical transitions are of the order of several hundreds nanometers, so that the corresponding wave number $k=2\pi/\lambda$ is of the order of 10^{-5} cm^{-1} . Thus, the quantities $k\times r$ and $k\times R$ are small for $r\sim 100 \text{ pm}$ and $R\sim 100 \text{ pm}$ respectively, and the exponentials can be replaced by unity. For the electronic matrix element it can be written:

$$\langle \psi_b | e^{i\mathbf{k}\cdot\mathbf{r}_j} \hat{\mathbf{e}} \cdot \bar{\nabla}_j | \psi_a \rangle \approx \hat{\mathbf{e}} \cdot \langle \psi_b | \bar{\nabla}_j | \psi_a \rangle = \hat{\mathbf{e}} \cdot \frac{i}{\hbar} \langle \psi_b | \mathbf{p}_j | \psi_a \rangle = \hat{\mathbf{e}} \cdot \frac{im}{\hbar} \langle \psi_b | \dot{\mathbf{r}}_j | \psi_a \rangle \quad (\text{E4.19})$$

The nuclear matrix element can be simplified in the same way by substituting in the last expression \mathbf{r}_j by \mathbf{R}_ℓ and m by M_ℓ .

This is the so-called *electric dipole approximation* and amounts to neglecting retardations across the molecule. The Heisenberg equation of motion for the dynamical variables \mathbf{r}_j and \mathbf{R}_j [128] enables to express the matrix element M_{ba} as a function of the dipole moment operator (\mathbf{D}) of the molecule:

$$\begin{aligned} M_{ba} &\approx -\hat{\mathbf{e}} \cdot \sum_{j=1}^N \frac{ie}{\hbar} \langle \psi_b | \dot{\mathbf{r}}_j | \psi_a \rangle + \hat{\mathbf{e}} \cdot \sum_{\ell=1}^{N'} \frac{iZ_\ell e}{\hbar} \langle \psi_b | \dot{\mathbf{R}}_\ell | \psi_a \rangle = \\ &= -\hat{\mathbf{e}} \cdot \sum_{j=1}^N \frac{e}{\hbar^2} \langle \psi_b | [\mathbf{r}_j, H_0] | \psi_a \rangle + \hat{\mathbf{e}} \cdot \sum_{\ell=1}^{N'} \frac{Z_\ell e}{\hbar^2} \langle \psi_b | [\mathbf{R}_\ell, H_0] | \psi_a \rangle = \\ &= -\hat{\mathbf{e}} \cdot \sum_{j=1}^N \frac{e}{\hbar^2} (E_a - E_b) \langle \psi_b | \mathbf{r}_j | \psi_a \rangle + \hat{\mathbf{e}} \cdot \sum_{\ell=1}^{N'} \frac{Z_\ell e}{\hbar^2} (E_a - E_b) \langle \psi_b | \mathbf{R}_\ell | \psi_a \rangle = \\ &= -\frac{\omega_{ba}}{\hbar} [\langle \psi_b | \hat{\mathbf{e}} \cdot \mathbf{D}_{elec} | \psi_a \rangle + \langle \psi_b | \hat{\mathbf{e}} \cdot \mathbf{D}_{nucl} | \psi_a \rangle] = \\ &= -\frac{\omega_{ba}}{\hbar} \langle \psi_b | \hat{\mathbf{e}} \cdot \mathbf{D} | \psi_a \rangle = -\frac{\omega_{ba}}{\hbar} \hat{\mathbf{e}} \cdot \mathbf{D}_{ba} \end{aligned} \quad (\text{E4.20})$$

where $\mathbf{D}_{\text{elec}} = -e \sum_{j=1}^N \mathbf{r}_j$ is the electric dipole operator of the electrons, $\mathbf{D}_{\text{nucl}} = e \sum_{\ell=1}^{N'} Z_{\ell} \mathbf{R}_{\ell}$ is the electric dipole operator of the nuclei and $\mathbf{D} = \mathbf{D}_{\text{elec}} + \mathbf{D}_{\text{nucl}}$ is the electric dipole operator of the molecule as a whole and $\mathbf{D}_{ba} \equiv \langle \psi_b | \mathbf{D} | \psi_a \rangle$.

The transition rate for molecular absorption in the electric dipole approximation is given by:

$$W_{ba} = \frac{\pi}{\hbar^2 c \epsilon_0} I(\omega_{ba}) |\hat{\boldsymbol{\epsilon}} \cdot \mathbf{D}_{ba}|^2 \quad (\text{E4.21})$$

The quantity $\hat{\boldsymbol{\epsilon}} \cdot \mathbf{D}_{ba}$ is the component of the dipole moment of the molecule in the polarisation direction, $\hat{\boldsymbol{\epsilon}}$, between the states a and b . If \mathbf{D}_{ba} is non-vanishing, i.e. if the dipole moment of the molecule changes between the states a and b , the transition is said to be allowed, and if vanishes the transition is forbidden. When a transition is forbidden, higher terms of the expansion of the exponential in E4.19 which correspond to the magnetic dipole, electric quadrupole, and so on, may be non-vanishing, but the transition rate will be much smaller than for allowed transitions. If M_{ba} in its exact form vanishes, the transition is said to be strictly forbidden. For unpolarised radiation the orientation of $\hat{\boldsymbol{\epsilon}}$ will be at random, and the transition rate can be written as follows:

$$W_{ba} = \frac{\pi}{3\hbar^2 c \epsilon_0} I(\omega_{ba}) |\mathbf{D}_{ba}|^2 \quad (\text{E4.22})$$

4.2.3. Types of transitions

Two different types of transitions can be distinguished [129]. This can be easily shown by separating the electronic and the nuclear parts of the molecular wave functions (*Born-Oppenheimer approximation*) [128-131] and further splitting the electronic part into an orbital (ϕ) and a spin function (χ), i.e. $\psi = \phi F \chi$. Introducing this wave function in the fourth line of E4.20, it follows:

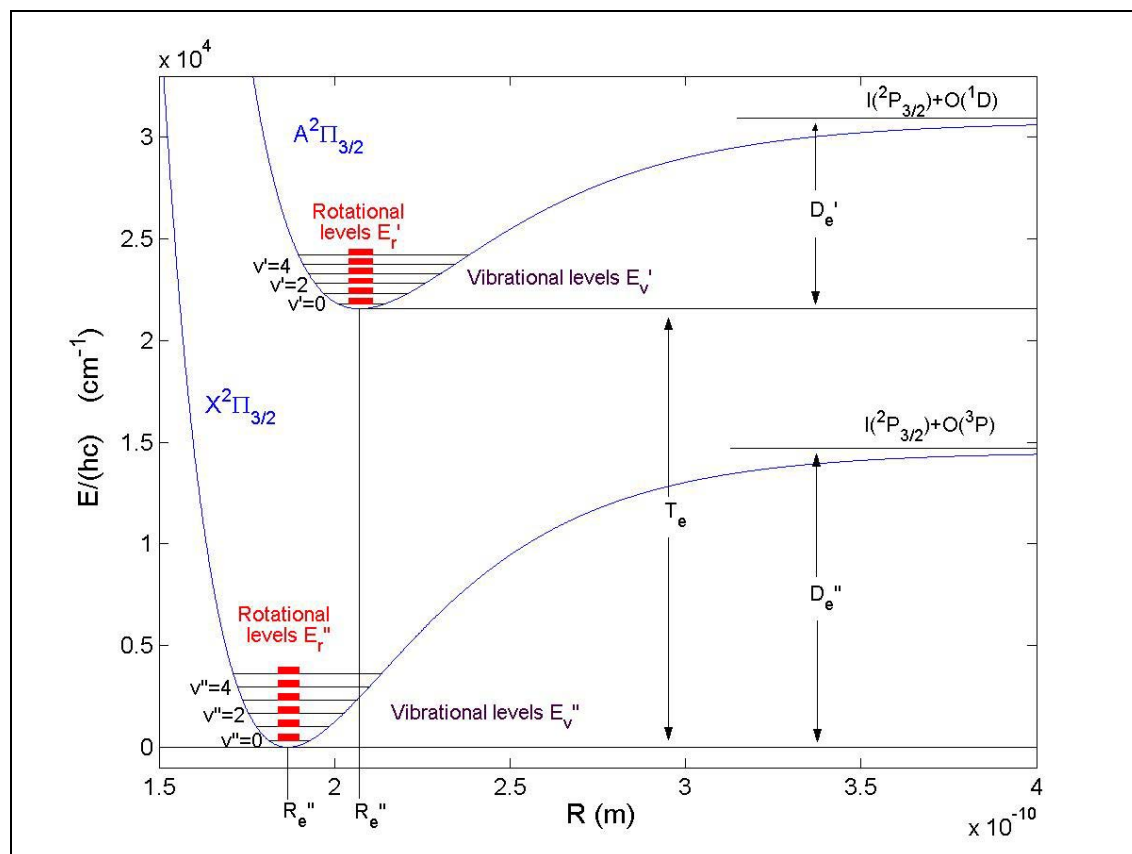
$$\begin{aligned}
 M_{ba} &= -\frac{\omega_{ba}}{\hbar} [\langle \psi_b | \hat{\mathbf{e}} \cdot \mathbf{D}_{elec} | \psi_a \rangle + \langle \psi_b | \hat{\mathbf{e}} \cdot \mathbf{D}_{nucl} | \psi_a \rangle] = \\
 &= -\frac{\omega_{ba}}{\hbar} [\langle F_b | \langle \phi_b | \hat{\mathbf{e}} \cdot \mathbf{D}_{elec} | \phi_a \rangle | F_a \rangle \langle \chi_b | \chi_a \rangle + \langle F_b | \hat{\mathbf{e}} \cdot \mathbf{D}_{nucl} | \phi_b \rangle | F_a \rangle \langle \chi_b | \chi_a \rangle] = \quad (E4.23) \\
 &= -\frac{\omega_{ba}}{\hbar} [\langle F_b | \hat{\mathbf{e}} \cdot \mathbf{D}_{ba}^{elec} | F_a \rangle \delta_{S'S''} + \langle F_b | \hat{\mathbf{e}} \cdot \mathbf{D}_{nucl} | F_a \rangle \delta_{\Lambda'\Lambda''} \delta_{S'S''}]
 \end{aligned}$$

As the electronic wave functions could depend to some extent of the internuclear distance, the matrix element $\mathbf{D}_{ba}^{elec} \equiv \langle \phi_b | \mathbf{D}_{elec} | \phi_a \rangle$ has been defined and kept inside the integral on the space of nuclear coordinates. In the second summand, the independence of \mathbf{D}_{nucl} of the coordinates of the electrons enables to use the orthonormality of the set of electronic wave functions. Thus, the transitions can be classified depending on the values of the quantum numbers of the final state b , as follows:

a) The transition takes place between the vibrational and rotational levels of the same electronic state: $(\nu_1', \dots, \nu_{3N-X}', \mathfrak{S}', M_{\mathfrak{S}}', \Lambda, S) \leftarrow (\nu_1'', \dots, \nu_{3N-X}'', \mathfrak{S}'', M_{\mathfrak{S}}'', \Lambda, S)$. The summand depending on \mathbf{D}_{nucl} in (E4.23) is in general non-vanishing ($\delta_{\Lambda'\Lambda''} \delta_{S'S''} = 1$). The first summand vanishes, because it comprises the integral of an odd function of the integration variables \mathbf{r}_j . Thus:

$$W_{ba} = \frac{\pi}{\hbar^2 c \epsilon_0} I(\omega_{ba}) |\langle F_b | \hat{\mathbf{e}} \cdot \mathbf{D}_{nucl} | F_a \rangle|^2 = \frac{\pi}{\hbar^2 c \epsilon_0} I(\omega_{ba}) \left| \langle F_b | \hat{\mathbf{e}} \cdot \left(e \sum_{\ell=1}^{N'} Z_{\ell} \mathbf{R}_{\ell} \right) | F_a \rangle \right|^2 \quad (E4.24)$$

Figure F4.1 shows a representation of two bound electronic states of the IO molecule. Vibrational and rotational levels are embedded in a “nested” configuration and give rise respectively to a “first and second order” splitting of the electronic energies [128]. Transitions between two vibrational levels within the same electronic state have energies $(E_b - E_a)/(hc)$ of the order of magnitude of 1000 cm^{-1} , and give rise to the infrared (IR) molecular spectra. Pure rotational transitions have energies of the order of magnitude of 100 cm^{-1} or less and therefore are placed in the far infrared and microwave ranges.



F4.1. Representation of two electronic states of iodine monoxide, IO, with their equilibrium internuclear distances (R_e' , R_e''), vibrational and rotational structure (v' and v'' up to 5, \mathfrak{J}' and \mathfrak{J}'' up to 30), dissociation energies (D_e' , D_e'') and transition energy (T_e). All energy levels are approximately to scale. The energy levels contained in the bundles of rotational levels (in red) are placed very close to each other and can not be resolved in the scale of energy considered. Electronic potentials (blue curves) have been calculated with the Morse potential [130] and experimental values of the vibrational constants [134-136].

However, not all transitions are allowed. Only those changes of the quantum numbers ($v_1, \dots, v_{3N-X}, \mathfrak{J}, M_{\mathfrak{J}}$) implying a change of the dipole moment, i.e. a non vanishing transition moment, are allowed. The selection rules depend on a number of factors, e.g. the polarisation state of the radiation and the symmetry properties of the angular part of the wave functions (spherical harmonics) of the states a and b .

It is worthwhile to recall that in case of homonuclear diatomic molecules $Z_1\mathbf{R}_1 = -Z_2\mathbf{R}_2$, so that they do not have a permanent nuclear dipole moment. Therefore all vibronic transitions within the same electronic state for homonuclear diatomic molecules are forbidden.

b) The transition takes place between different electronic states: $(\nu_1', \dots, \nu_{3N-X}', \mathfrak{S}', M_{\mathfrak{S}'}', \Lambda', S')$ \leftarrow $(\nu_1'', \dots, \nu_{3N-X}'', \mathfrak{S}'', M_{\mathfrak{S}''}', \Lambda'', S'')$. In this case the second summand vanishes ($\delta_{\Lambda'\Lambda''} = 0$) and the first one will be in general non-vanishing if the transition takes place between states with the same multiplicity ($S'' = S'$):

$$W_{ba} = \frac{\pi}{\hbar^2 c \mathcal{E}_0} I(\omega_{ba}) \left| \langle F_b | \hat{\mathbf{e}} \cdot \mathbf{D}_{ba}^{elec} | F_a \rangle \right|^2 \quad (\text{E4.25})$$

This type of transition imply spectral energies ranging from the vacuum ultraviolet (UV) to the near infrared, including the visible spectrum (VIS). In case of IO, the normalised electronic transition energy has a value of $2.15 \cdot 10^4 \text{ cm}^{-1}$, and therefore is situated in the middle of the VIS spectrum. The detection technique employed in this work is based in optical absorption spectroscopy, i.e. on the absorption of visible radiation by molecules in the VIS range.

4.2.4. Structure of an electronic band system

In spectroscopy is usual to express the energies in units of wavenumber, i.e to normalise the energy to hc . These normalised energies are referred to as ‘terms’. The so-called vibronic terms are the sum of the electronic term T_e corresponding to the minimum of the potential function (see F4.1) and the vibrational term $G(\nu_1, \dots, \nu_{3N-X})$. This vibrational contribution can be further spitted into the contributions of the $3N'-X$ *normal modes of vibration* of the nuclear configuration [129, 131, 137]. In the usual spectroscopic notation, the vibrational term is written as follows:

$$G(\nu_1, \dots, \nu_{3N'-X}) = \sum_{i=1}^{3N'-X} \omega_i \left(\nu_i + \frac{1}{2} \right) + \sum_{i=1}^{3N'-X} \sum_{j \geq i} x_{ij} \left(\nu_i + \frac{1}{2} \right) \left(\nu_j + \frac{1}{2} \right) + \dots \quad (\text{E4.26})$$

In this equation ω_i are the vibrational wave numbers (not to be confused with the angular frequencies used previously) and x_{ij} are the anharmonicity constants [132]. Equation E4.26

assumes that all vibrations are non-degenerate, as would always be the case for unsymmetrical molecules.

If the vibrational term values of the upper and lower states are $G(v_1', \dots, v_{3N-X}')$ and $G(v_1'', \dots, v_{3N-X}'')$ respectively and if the electronic term values are T_e'' and T_e' , the wave numbers of all possible vibrational transitions of a given electronic transition are represented by:

$$k = (T_e' - T_e'') + \sum_{i=1}^{3N'-X} \omega_i' \left(v_i' + \frac{1}{2} \right) + \sum_{i=1}^{3N'-X} \sum_{j \geq i} x_{ij}' \left(v_i' + \frac{1}{2} \right) \left(v_j' + \frac{1}{2} \right) + \dots - \sum_{i=1}^{3N'-X} \omega_i'' \left(v_i'' + \frac{1}{2} \right) - \sum_{i=1}^{3N'-X} \sum_{j \geq i} x_{ij}'' \left(v_i'' + \frac{1}{2} \right) \left(v_j'' + \frac{1}{2} \right) - \dots \quad (\text{E4.27})$$

For practical purposes is more convenient to refer the energies to the lowest vibrational level in each state:

$$k = k_{00} + \sum_{i=1}^{3N'-X} \omega_i^{0'} v_i' + \sum_{i=1}^{3N'-X} \sum_{j \geq i} x_{ij}^{0'} v_i' v_j' + \dots - \sum_{i=1}^{3N'-X} \omega_i^{0''} v_i'' - \sum_{i=1}^{3N'-X} \sum_{j \geq i} x_{ij}^{0''} v_i'' v_j'' - \dots \quad (\text{E4.28})$$

where :

$$\omega_i^0 = \omega_i + x_{ii} + \frac{1}{2} \sum_{i \neq j} x_{ij} \quad (\text{E4.29})$$

$$k_{00} = (T_e' - T_e'') + \frac{1}{2} \sum_{i=1}^{3N'-X} \omega_i' + \frac{1}{4} \sum_{i=1}^{3N'-X} \sum_{j \geq i} x_{ij}' - \frac{1}{2} \sum_{i=1}^{3N'-X} \omega_i'' - \frac{1}{4} \sum_{i=1}^{3N'-X} \sum_{j \geq i} x_{ij}'' \quad (\text{E4.30})$$

The quantity k_{00} is the wavenumber corresponding to the ($0 \leftarrow 0$) band.

For a diatomic molecule (only one normal mode) a progression consists of all possible transitions from v'' to the upper vibrational levels $v'=1, 2, \dots$. For an asymmetric triatomic molecule (three normal modes) a “progression of progressions” [132] is observed, which consists of all possible transitions from (v_1'', v_2'', v_3'') to the upper vibrational levels $(v_1'=1, 2, 3, \dots, v_2'=1, 2, 3, \dots, v_3'=1, 2, 3, \dots)$, .

4.2.5. Intensity distribution of vibrational bands

Assuming that no interaction between rotational and vibrational movement takes place, the nuclear part of the wave function can be expressed as a product of a vibrational and a rotational wave function:

$$F(\mathbf{R}) = \psi_v(\tau_v) \psi_r(\tau_r) \quad (\text{E4.31})$$

where \mathbf{R} is the general nuclear configuration, τ_v are the normal vibrational coordinates and τ_r the rotation coordinates (polar angles). By using E4.31, the vibrational and the rotational parts of the transition moment for electronic transitions can be split up as follows:

$$M_{ba} = \hat{\mathbf{e}} \cdot \int \psi_{vb}^* D_{ba}^{elec} \psi_{vb} d\tau_v \int \psi_{rb}^* \hat{\mathbf{d}} \psi_{ra} d\tau_r \quad (\text{E4.32})$$

where $\mathbf{D}_{ba}^{elec} = D_{ba}^{elec} \hat{\mathbf{d}}$, and $\hat{\mathbf{d}}$ is a unitary vector indicating the orientation of \mathbf{D}_{ba}^{elec} in a molecule-fixed coordinate system. The integral over the angular coordinates can be denoted as the matrix element $\mathbf{D}_{ba}^{rot} = \int \psi_{rb}^* \hat{\mathbf{d}} \psi_{ra} d\tau_r$. Each component of \mathbf{D}_{ba}^{rot} is a constant for a given $(\mathfrak{J}, \mathfrak{J}')$ combination [130]. Selection rules for the rotational quantum numbers in electronic transitions [128-132] arise by evaluating these integrals. The first integral is independent of \mathfrak{J} and can be treated separately.

The electronic wave function depends to some extent on the nuclear configuration, and therefore, for a given electronic transition, D_{ba}^{elec} depends also on τ_v . Assuming that the variation of D_{ba}^{elec} with τ_v is slow, it can be written:

$$M_{ba} = \bar{D}_{ba}^{elec} \left(\int \psi_{vb}^* \psi_{va} d\tau_v \right) (\hat{\mathbf{e}} \cdot \mathbf{D}_{ba}^{rot}) \quad (\text{E4.33})$$

where \bar{D}_{ba}^{elec} is an averaged value of the electronic transition moment. This approximation is known as *Franck-Condon principle*, and amounts to assume that the internuclear distances in a molecule keep approximately constant when a transition

between two electronic levels occurs, i.e. that the transition occurs instantaneously with respect to the vibrational motion of the nuclei, since the relative potential energy of both states has not changed. The rate of transition probability, assuming unpolarised isotropic radiation, is given by [129, 130]:

$$M_{ba} \approx \frac{\pi}{3\hbar^2 c \epsilon_0} I(\omega_{ba}) \left| \overline{D}_{ba}^{elec} \right|^2 \left| \int \psi_{vb}^* \psi_{va} d\tau_v \right|^2 \frac{\sum_{M_a', M_b'} |\mathbf{D}_{ba}^{rot}|^2}{2\mathfrak{J}'+1} \quad (\text{E4.34})$$

The Franck-Condon factor is defined as the square of the overlap integral of vibrational states:

$$f_{ba} = \left| \int \psi_{vb}^* \psi_{va} d\tau_v \right|^2 \quad (\text{E4.35})$$

Thus, the transition moment between the states a and b and, as a result, the intensity of absorption (E4.14), is directly proportional to f_{ba} . This means that the most intense transitions will be those for which the overlap between the vibrational wave functions in the lower and the upper electronic states is a maximum. If the potential functions of the two electronic states are nearly alike, and therefore the internuclear distances and vibrational frequencies are nearly the same, then the vibrational eigenfunctions with different vibrational quantum numbers in the upper and lower states are nearly orthogonal with respect to each other, and therefore M_{ba} will be different from zero only if $v_i''=v_i'$, $i=1, \dots, 3N'-X$. Thus only transitions with $(v_i''=v_i' \leftarrow v_i'')$ would be visible, whose relative intensities are determined mainly by the population of vibrational levels in the lower electronic state and given by the corresponding Boltzmann factors. On the other hand, if the equilibrium position of the nuclei changes from one electronic state to the other, and if this change is mostly represented by the vibrational mode v_i , bands with $\Delta v_i \neq 0$ will occur. If the change of equilibrium position is large, the maximum of intensity will no longer be at $v_i'=0$, as occurs for the $A^2\Pi_{3/2} \leftarrow X^2\Pi_{3/2}$ transition of IO (see F4.1 and F4.2)

The integration of experimentally determined absorption cross sections enables to determine successively the electronic, vibrational and rotational dependencies in E4.58, by means of the conservation of probability [130]. To determine Franck-Condon factors theoretically by calculation the overlap integral it is necessary to know the vibrational states ψ_v . For low values of the vibrational quantum number v , the approximation of harmonic oscillator is useful, because it enables an analytical solution of the nuclear wave equation [129-131, 137]. For diatomic molecules the potential well can also be approximated by the Morse potential [130]. A more accurate approach consists on obtaining an approximation of the potential well by applying the Rydberg-Klein-Rees method [138], to subsequently obtain the vibrational eigenstates by numerically solving the nuclear wave equation and finally calculate directly the overlap integral in E4.35. The Franck-Condon factors of the $A^2\Pi_{3/2} \leftarrow X^2\Pi_{3/2}$ transition of IO were calculated by Rao et al. [139] using this approach.

4.2.6. Line profiles

In summary, molecular electronic transitions resulting from absorption of radiation give rise to a band system, i.e. a group of bands corresponding to transitions from ro-vibronic states in the lower electronic state to ro-vibronic states in the upper electronic state. Normally, the vibrational states in the lower electronic state have low vibrational quantum numbers at room temperature as a result of the Boltzmann distribution. Therefore the progressions with $v_i''=0,1$ are the more intense. Inside each vibrational progression, the intensity is governed by the Frank-Condon factor. Inside a vibrational band, the intensity of the rotational lines is governed by the occupation of rotational levels in the lower levels, given by the Boltzmann distribution and the M -fold degeneracy, and the line strength, which is linked to the selection rules as well [130, 132].

However, in this discussion of the intensity of the bands only the transition probability is taken into account and the lines are assumed to be Dirac's δ functions. Actually, the frequency of the absorption is not strictly monochromatic. The intensity absorbed displays a distribution about an average frequency. The existence of a natural line width is a result of the uncertainty relationship for energy and time, which relates the energy and the lifetime of the state. The natural line shape is given by a Lorentz profile whose full width at half maximum (*FWHM*) is inversely proportional to the life time of the state [129]. Therefore, the shorter the life time the broader the rotational line. There are several phenomena which can decrease the lifetime of levels, for example pre-dissociation and pressure broadening. In addition, as a result of the fact that the velocities of the molecules are distributed according to the Maxwell distribution, which depends on the temperature, the Doppler Effect gives rise to a convolution of the natural line shape with a gauss curve, i.e a Voigt profile. Note that all these processes affect also the absorption intensity for a given frequency, although the integral over the band contour must remain constant at different conditions of pressure and temperature and governed only by the transition probability.

In the case that the lifetimes of rotational levels are strongly reduced, the rotational bands become very broad and overlap strongly. The resulting vibrational bands are diffuse, i.e smooth featureless functions of frequency.

4.2.7. Absorption continua

Continuous molecular spectra result generally from transitions between two states, one of which at least can be assumed to be a continuous range of energy values. For atoms, a continuous range joins on each series of electronic states and corresponds to the removal of an electron (ionization) or, conversely, to the capture of one electron by the ion (recombination), the corresponding wave functions being respectively outgoing or

incoming plane waves. For molecules, such continuous ranges corresponding to ionization are also possible. However, in addition, there are continuous ranges which correspond to a splitting of the molecule into fragments, that is, to dissociation. Dissociation continua join onto the series of vibrational levels of every electronic state and are the only feature present if the electronic state under consideration has no discrete vibrational levels (unstable state).

The Franck-Condon principle holds as well in the case of absorption continua, if it is applied to intensity per unit wave number interval. For the evaluation of the overlap integral in E4.35 a knowledge of the repulsive eigenfunctions of the unstable state is required. In the case of diatomic molecules, these functions resemble those of high vibrational excited states of bounded electronic states, although only in one side. At some distance from the classical turning point of the motion they behave like a simple sine wave of constant amplitude, whose wavelength is the smaller the higher the energy lies above the asymptote of the potential curve. In the neighbourhood of the classical turning point the amplitude and the wavelength of the wave are greater, and directly above the turning point there is a maximum which falls off exponentially to smaller values of the internuclear distance(s) [130]. For polyatomic non-linear molecules, the vibrational eigenfunctions ψ_{va} and ψ_{vb} of the upper and lower states depend on the $3N+X$ normal coordinates. The wave function in the initial state ψ_{va} is in first approximation a product of harmonic oscillator functions (E4.19), but ψ_{vb} is a more complicated function.

The most important case of absorption continua is that in which a transition takes place from a stable lower state to a continuous upper state. Absorption of a light quantum in the resulting continuous spectrum leads to photo-dissociation of the molecule under consideration. Frequently an approximation known as the reflection method is used to derive the intensity distribution of continuous spectra. The repulsive eigenfunction is

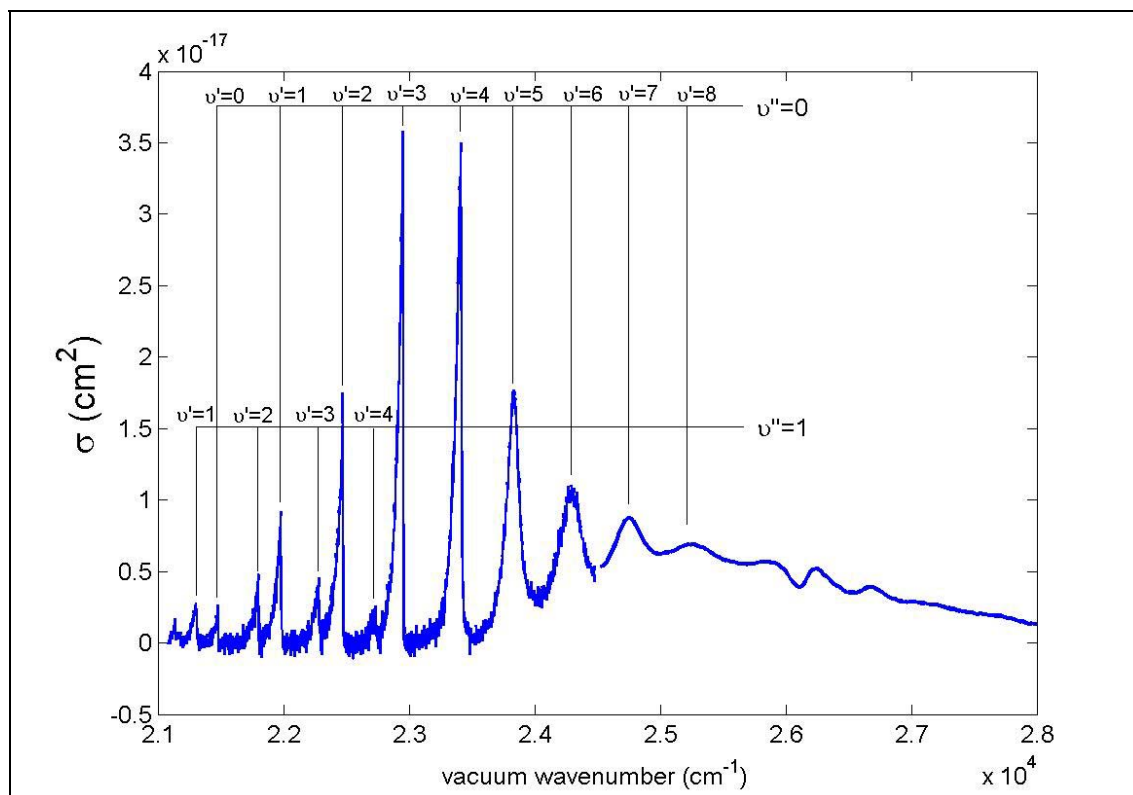
replaced by a δ function, which is different from zero only at the classical turning point. Thus, the Franck-Condon factor is obtained simply by reflecting the probability density distribution in the lower state ($|\psi_{\text{val}}|^2$) at the repulsive potential curve or surface. Conversely, an observed intensity distribution can be used to derive the course of the repulsive part of the potential curve or potential. This method would appear to be a very poor approximation for the repulsive eigenfunction. Actually, however, the results obtained with it for diatomic molecules deviate only very slightly from those obtained with the accurate repulsive functions. By using this method, the underlying continuum ranging from 23500 cm^{-1} to the UV (F4.2) has been resolved as resulting from transitions from $\text{IO}(X^2\Pi_{3/2}, v''=0)$ to two anti-bonding electronic states by Spietz et al. [126].

4.3. Electronic spectra of diatomic molecules: the case of iodine monoxide (IO)

The IO $A^2\Pi_{3/2} \leftarrow X^2\Pi_{3/2}$ subband system (F4.2) was first observed in 1937 by Vaidya [140] from its emission in a methyl iodide flame. In 1948 Coleman et al. [141] observed the same emission spectrum by using an oxyhydrogen flame to which iodine was added, thus supporting the assignment to IO. In 1958 Durie and Ramsay [134] recorded the first absorption spectrum of IO in flash photolysis experiments. Also Durie et al. [135] photographed the methyl iodide flame bands and carried out rotational and vibrational analysis, which confirmed the spectral assignment to IO. An interesting feature of the halogen monoxides and in particular of IO is that they fall within Hund's case (a) and possess inverted spin-orbit states, so that the $^2\Pi$ state with $\Omega=1/2$ is higher in energy than the $^2\Pi$ ground state with $\Omega=3/2$ [142, 143].

IO is a good example of different degrees of pre-dissociation of vibrational levels due to overlapping of electronic states. It presents diffuse bands like $(4 \leftarrow 0)$ and $(5 \leftarrow 1)$ [135, 144], together with bands with sharply structured rotational features like $(2 \leftarrow 0)$ and $(0 \leftarrow 0)$. The latter exhibit consequently laser induced fluorescence (LIF)

[145]. Different repulsive potentials correlating to the dissociation products $O(^3P)+I(^2P_{3/2})$ can be deduced from Wigner-Witmer correlation rules [144]. The bounded $A^2P_{3/2}$ state correlates to the more energetic dissociation products $O(^1D)+I(^2P_{3/2})$ (see F4.1). Therefore, the $A^2P_{3/2}$ overlaps to a number of repulsive states [126, 144, 146], leading to a rapid pre-dissociation of most vibrational bands of the IO electronic spectrum. Newman et al. [144] have suggested that the comparatively slow pre-dissociation of the $v'=2$ level is a result of fortuitous near cancellation of the pre-dissociation Franck-Condon factor at this energy.



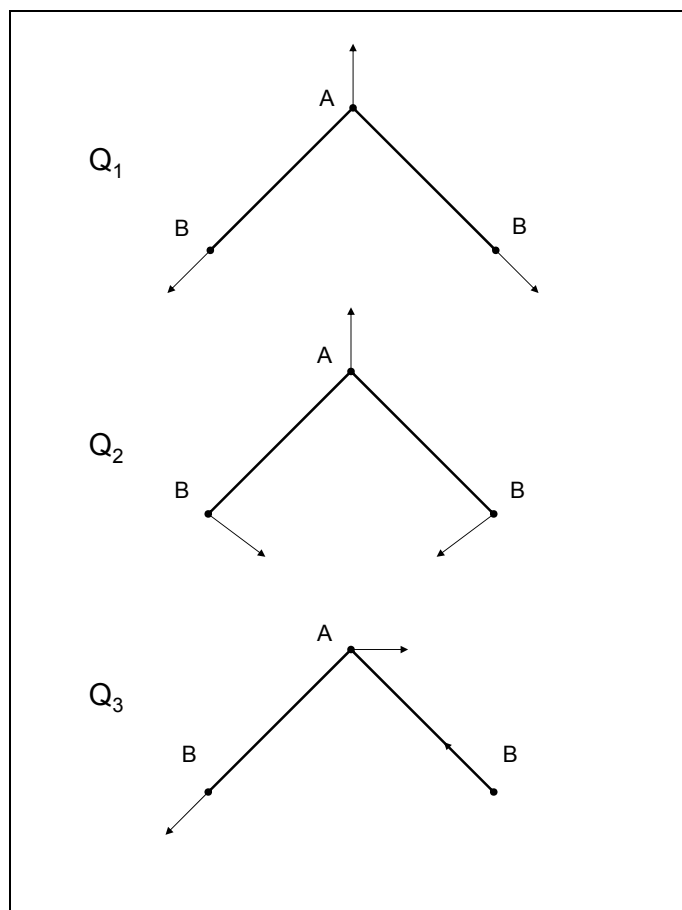
F4.2. $A^2\Pi_{3/2} \leftarrow X^2\Pi_{3/2}$ subband system of IO, recorded in the IUP Bremen laboratory at $FWHM=30 \text{ cm}^{-1}$ (0.07 nm) up to 24500 cm^{-1} , and $FWHM=565 \text{ cm}^{-1}$ (1.3 nm) from 24500 cm^{-1} to the UV [147]. Two progressions with $v''=0$ and $v''=1$ can be observed. The continuum arises most likely from the overlap of further bands of the $v''=0$ progression and transitions from $X^2\Pi_{3/2}$ to repulsive states [126, 144, 146]. The instrumental resolution is not sufficient to resolve the rotational structure of the $(0 \leftarrow 0)$, $(2 \leftarrow 0)$, $(2 \leftarrow 1)$, $(3 \leftarrow 0)$, $(3 \leftarrow 1)$ bands, although enables a good sampling of the diffuse bands $(4 \leftarrow 0)$, $(5 \leftarrow 0)$, $(6 \leftarrow 0)$, etc.

The electronic absorption spectrum of IO is habitually used to measure its concentration in the atmosphere by DOAS [37, 38, 40-42]. The existence of strong diffuse bands like those between 23000 and 25000 cm^{-1} facilitates the atmospheric retrieval,

because the spectrum is insensible to pressure changes and a high instrumental resolution is not needed. The field measurements require accurate scaling of the spectra to absolute absorption cross section.

4.4. Electronic spectra of asymmetric triatomic molecules: the case of iodine dioxide (OIO)

The OIO ($A^2B_2 \leftarrow X^2B_1$) [82, 148] band system (F4.7) was observed for the first time in 1996 by Himmelmann et al. [32, 149], who produced it in the same laboratory of the present work by flash photolysis of I_2 in the presence of O_3 . In 1997 Maier and Bothur [150] reported the spectrum of OIO isolated in a matrix.



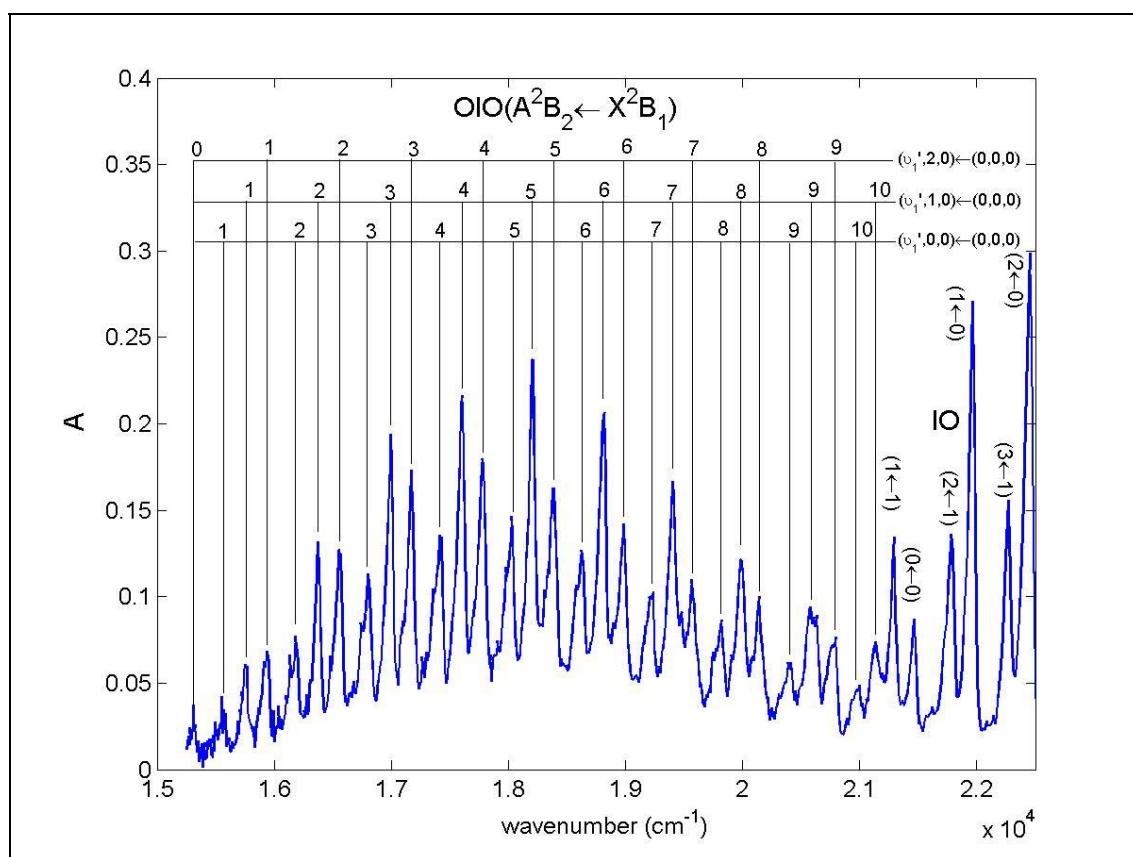
F4.3. Normal modes of vibration of an asymmetric triatomic molecule: Q_1 : symmetric stretch; Q_2 : bent, Q_3 : asymmetric stretch.

The generalised (geometric) coordinates q_j of an asymmetric triatomic molecule like OIO are given by the mass-weighted deviations from the equilibrium point of the bond

4.4. Electronic spectra of asymmetric triatomic molecules: the case of iodine dioxide (OIO)**Electronic spectra of asymmetric triatomic molecules: the case of iodine dioxide (OIO)**

distances and the angle between the bond directions. The normal modes of vibration are shown in figure F4.3. It can be appreciated that these coordinates are no longer geometric, but vectors with components (q_{j1}, q_{j2}, q_{j3}) describing the overall deviation of all nuclei from the equilibrium position.

The energy of each combination (ν_1, ν_2, ν_3) depends on the normal angular frequencies, which in turn depend on the masses and force constants involved. Usually the notation of vibrational quantum numbers for the vibrational states follows the pattern: (symmetric stretch, bent, asymmetric stretch).



F4.4. Vibrational assignments in the OIO ($A^2B_2 \leftarrow X^2B_1$) band system, according to Himmelmann et al. [32]. Groups with three equidistant peaks can be clearly distinguished. The first peaks in consecutive groups are separated by about 600 cm^{-1} . Within each group, the peaks are separated by about 180 cm^{-1} . The assignment was made by analogy to OClO and OBrO electronic bands. The spectrum presents a strong overlap of OIO and IO ‘hot’ bands from about 20000 cm^{-1} towards the blue side.

The OIO electronic spectrum presents a series of well defined triplets, consistent with transitions from the ground state $(0, 0, 0)$ to progressive ν_1' vibrational states $(0$ to

10), accompanied by transitions with upper state v_2' quantum number ranging from 0 to 2. The wave numbers of the observed transitions are well described by the following expression (see E4.28):

$$k = k_{00} + \omega_1^0 v_1' + x_1^0 v_1' + \omega_2^0 v_2' \quad (\text{E4.36})$$

The vibrational frequencies and the anharmonicity constants were reported by Himmelman et al. [32] and Maier and Bothur [150].

Ashworth et al. [82] published a high resolution cavity ring-down spectrum (CRDS) of OIO which does not exhibit rotational structure. In addition, they did not observe LIF by pumping the molecule between 540 nm and 605 nm, thus suggesting that the transition to the A^2B_2 state leads to prompt pre-dissociation. However, Ingham et al. [81] observed an insignificant yield of both $O(^3P)$ and $I(^2P)$ in OIO photolysis experiments. Prompt recovery of ground state OIO after photo-absorption has been observed by Joseph et al. [83] and Tucceri et al. [77], suggesting that the diffuse bands of OIO are a result of fast internal conversion from A^2B_2 onto high vibrational levels of X^2B_1 rather than pre-dissociation.

5. FUNDAMENTAL PRINCIPLES OF GAS PHASE KINETICS

5.1. Photochemical reactions

Visible and low frequency UV radiation can induce chemical reactions, which are referred to as photochemical. The process in which electromagnetic radiation is absorbed by a molecule, with the formation of species that undergo further reaction, is known as the photochemical primary process. Absorption of radiation leads initially to the formation of an excited species, which may in a subsequent step produce atoms and free radicals. These atoms and free radicals may be involved in subsequent reactions, which may involve chains. Such reactions are referred to as secondary processes.

As explained in the previous chapter, not all the incident radiation is absorbed by a molecule. The probabilities of transitions when light is absorbed are governed by the Frank-Condon principle and also certain selection rules must be satisfied. In addition, not all the absorbed radiation leads to chemical change. After an electronically excited molecule has been produced by the absorption of radiation, it can undergo a number of processes: fluorescence/phosphorescence, molecular dissociation, vibrational relaxation, collisional quenching and internal quenching. In the case of fairly simple gas molecules, the first two processes are generally the only ones that can occur.

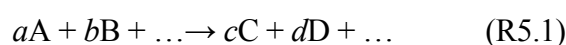
Fluorescence and phosphorescence imply the relaxation of the excited species to a lower state with subsequent release of electromagnetic radiation. In general, only molecular dissociation leads to chemical change. Molecular dissociation occurs e.g. when the frequency of the exciting radiation is within the range of the absorption continuum of the molecule (section 4.2.7). It also occurs when the excited electronic state of the molecule is crossed by one or more repulsive states, such that the system undergoes transitions to them and dissociates (predissociation, see sections 4.2.6 and 4.3).

On changing the frequency of the incident radiation there is usually a sharp transition from a region in which there is no chemical reaction, to one in which a considerable amount of reaction occurs. Reactions occur on the higher frequency side of the photochemical threshold.

5.2. Basic kinetic concepts

5.2.1. Empirical rate equations

A chemical reaction of known stoichiometry can be written in general as:



where the low case letters indicate stoichiometric coefficients. The rate of consumption of the species A is given by the negative time derivative of its concentration, while the rate of formation of the species C is equal to the positive time derivative of its concentration. The rate of reaction is given by the any rate of consumption or formation divided by the corresponding stoichiometric coefficient:

$$v_1 = -\frac{1}{a} \frac{d[A]}{dt} = -\frac{1}{b} \frac{d[B]}{dt} = \dots = \frac{1}{c} \frac{d[C]}{dt} = \frac{1}{d} \frac{d[D]}{dt} = \dots \quad (\text{E5.1})$$

For some reactions the rate of reaction can be expressed by the empirical equation:

$$v = k[A]^\alpha [B]^\beta \dots \quad (\text{E5.2})$$

where α , β ,... and k are independent of concentration and time. In such case, the rate of consumption of the species A is given by:

$$-\frac{d[A]}{dt} = k[A]^\alpha [B]^\beta \dots \quad (\text{E5.3})$$

This equation is known as empirical rate equation for the absorber A. The exponents α , β , ... are known as partial orders of reaction with respect to A and B respectively. The overall order of reaction n is given by the sum of exponents $\alpha + \beta + \dots$. These orders are purely

experimental quantities and are not necessarily integral. If $n = \alpha = 1$, the reaction is said to be of first order, and of second order if $n = \alpha + \beta = 2$. The constant k is known as rate coefficient, reaction rate or rate constant.

The molecularity of an elementary reaction is the number of reactant particles involved in each individual chemical event. Note that bimolecular reactions are not necessarily of second order. The order simply indicates how the rates depend on concentration.

An objective of chemical kinetic analysis is the determination of the concentration of the species involved in a chemical mechanism as a function of time. In elementary reactions the concentration of a given species is governed by a single reaction rate as E5.3. This equation is analytically integrable under some circumstances, i.e. depending on the partial orders and the reactants involved [151]. In the case of bimolecular reactions of second order, it is possible to force pseudo-first order behaviour of the concentration one of the reactants by increasing the initial concentration of the second in several orders of magnitude. This means that considering $\alpha = \beta = 1$ and $[B]_0 \gg [A]_0$, E5.3 can be easily integrated by assuming that $[B]$ is constant with respect to time. In this case an exponential decay of $[A]$ results, with time constant $(k[B]_0)^{-1}$. However, most practical problems deal with composite mechanisms, where a given species C may be involved simultaneously in several reactions and the concentration of other species may also depend on the concentration of A , thus resulting a system of coupled differential equations. Such system may be analytically solvable under some circumstances and assumptions. A typical case is the set of simultaneous and consecutive reactions:



The corresponding differential rate equations for the reactants A , C and F are:

$$\frac{d[A]}{dt} = -k_{5,2}[A][B] \quad (\text{E5.4})$$

$$\frac{d[C]}{dt} = k_{5,2}[A][B] - k_{5,3}[C][E] \quad (\text{E5.5})$$

$$\frac{d[F]}{dt} = k_{5,3}[A][C] \quad (\text{E5.6})$$

Under the assumption of pseudo-first order for both reactions, i.e. $[B]_0 \gg [A]_0$ and $[E]_0 \gg [C]_0$, the system of differential rate equations E5.4-E5.5-E5.6 is solvable and analytical expressions for the time dependence of the concentrations of A, C and F can be obtained [151] (see figure F5.1). However, chemical mechanisms are in general more complex and the corresponding systems of coupled ordinary differential equations (ODE) have not analytical solution. In such cases numerical integration techniques such as the Runge-Kutta method [152, 153] are required. The software package FACSIMILE [154], based in the predictor-corrector integration method, is the most commonly used tool for resolution of systems of differential equations in chemical kinetics.

5.2.2. Opposite reactions and chemical equilibrium.

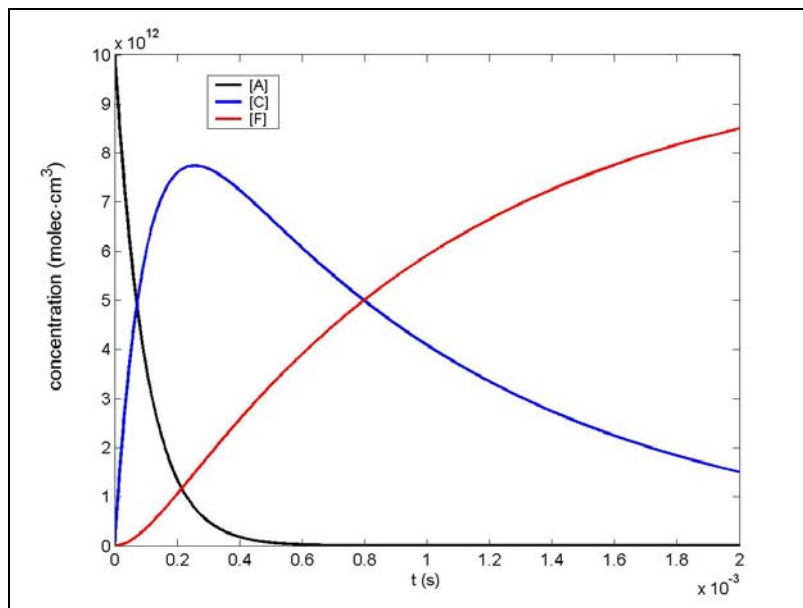
Most elementary reactions can be considered to be reversible. For example, for a reversible bimolecular reaction it can be written:



An elementary reaction and its inverse create a composite mechanism, whose rate equations are:

$$\frac{d[A]}{dt} = -k_{5,4}[A][B] + k_{-5,4}[C][D] \quad (\text{E5.7})$$

$$\frac{d[C]}{dt} = k_{5,4}[A][B] - k_{-5,4}[C][D] \quad (\text{E5.8})$$



F5.1. Analytical solution of the ODE system E5.4-E5.5-E5.6. [151], assuming pseudo-first order in both R5.2 and R5.3. Parameters used: $[A]_0 = 10^{13}$ molecule cm^{-3} , $[B]_0 = [E]_0 = 10^{15}$ molecule cm^{-3} , $k_1 = 10^{11}$ $\text{cm}^3 \text{molec}^{-1} \text{s}^{-1}$, $k_2 = 10^{12}$ $\text{cm}^3 \text{molec}^{-1} \text{s}^{-1}$.

Reaction R5.4 proceeds to a state of equilibrium that differs appreciably from completion. If the reaction is far from the equilibrium and $k_1 \gg k_{-1}$, the inverse reaction can be neglected, but as the reaction proceeds the latter must be taken into account. Finally, in the equilibrium the concentrations are in steady state, and thus:

$$0 = -k_{5.4}[A]_{eq}[B]_{eq} + k_{-5.4}[C]_{eq}[D]_{eq} \Leftrightarrow K_{5.4} \equiv \frac{k_{5.4}}{k_{-5.4}} = \frac{[C]_{eq}[D]_{eq}}{[A]_{eq}[B]_{eq}} \quad (\text{E5.9})$$

where $K_{5.4}$ is the equilibrium constant. This expression enables to relate experimentally accessible parameters as the concentrations at equilibrium to thermodynamic quantities.

The Gibbs free energy of reaction is related to the equilibrium constant K by:

$$\Delta G_r^0 = -RT \ln K \quad (\text{E5.10})$$

Further thermodynamical variables of interest which can be determined from the Gibbs free energy are the enthalpy of reaction and the enthalpies of formation of species involved in the reaction (see e.g. [75] for the enthalpy of formation of IO).

5.2.3. Steady state treatment

Apart from the chemical equilibrium in reversible reactions (E5.9), the steady state treatment can be used as well in the maxima of the concentration curves, e.g. in the peak concentration of the blue curve in figure F5.1, where the derivative of the concentration vanishes as well. This enables to obtain simple expressions relating experimental quantities which might be helpful in the determination of a concentration or a rate coefficient. In the case the mechanism R5.2 and R5.3, from equation E5.5 it follows:

$$0 = k_{5.2}[A]_{SSC}[B]_0 - k_{5.3}[C]_{SSC}[E]_0 \Leftrightarrow k_{5.2}[A]_{SSC}[B]_0 = k_{5.3}[C]_{SSC}[E]_0 \quad (\text{E5.11})$$

If $k_{5.3}$ were unknown, this expression would enable its determination given the values of all other parameters.

The steady state approach can also be used to obtain simplified expressions even when the steady state condition does not hold rigorously. Many composite reactions involve very reactive intermediate species such as free radicals, which, as a result of their high reactivity, are consumed virtually as rapidly as they are formed and consequently exist at very low concentrations. To deal with such intermediates, the pseudo-steady state approximation (PSSA) can be considered, which consists in assuming that the rates of formation and decay of the intermediate are equal [151]. That amounts to state that the intermediate is so reactive that reacts by one of its sinks as soon as it is formed [50].

5.3. Theory of reaction rates

5.3.1. Bimolecular reactions

Gas molecules can react only when they come close enough to one another for direct energy exchange that can lead to bond breaking. From elementary kinetic theory, the frequency of collisions per unit volume of molecules of type A with molecules of type B is given by [151]:

$$Z_{AB} = N_A N_B \pi \sigma_{AB}^2 \sqrt{\frac{8kT}{\pi\mu}} \quad (\text{E5.12})$$

where N_A and N_B are the respective concentrations, σ_{AB} is the collisional diameter and μ the reduced mass. According to the old hard-sphere collision theory, the collision number multiplied by the Arrhenius factor $e^{-E/(RT)}$ gives the rate of formation of the products of reaction, in terms of the number of molecules formed per unit volume and unit time. Thus, for reaction between two molecules A and B the rate is expressed as:

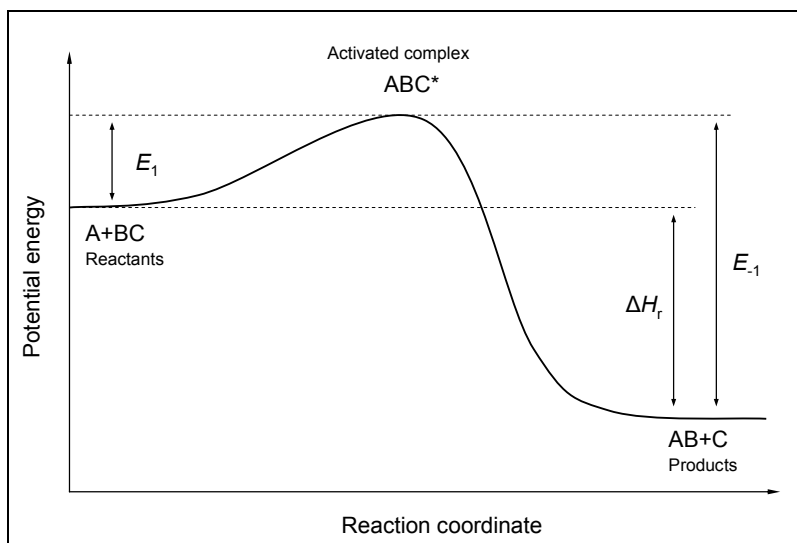
$$v = Z_{AB} e^{-E/(RT)} \quad (\text{E5.13})$$

If the reaction can be assumed to be of second order, division of the rate of production E5.13 between the product of concentrations gives the rate coefficient:

$$k = \pi \sigma_{AB}^2 \sqrt{\frac{8kT}{\pi\mu}} e^{-E/(RT)} \quad (\text{E5.14})$$

The pre-exponential factor in E5.14 is known as collision frequency factor. The maximum possible value of the rate constant of a bimolecular reaction is achieved if every molecular collision between molecules A and B results in reaction. This is called the gas-kinetic collision rate, and the corresponding value of the second order rate constant at room temperature is about $2 \times 10^{-10} \text{ cm}^3 \text{ molec}^{-1} \text{ s}^{-1}$. Most reactions have rates smaller than this. First, whereas the collision of two molecules is a necessary condition for reaction, sufficient energy must be available to break chemical bonds. The exponential factor in expression E5.14 gives the fraction of collisions involving energy greater than a required energy—the activation energy—. Second, molecules with complex geometry have to be aligned properly at the point of collision for reaction to take place and perfect alignment is not achieved in every collision. The old theory included an additional steric factor in the pre-exponential factor in order to account for this fact. However, the evaluation of these factors can not be done in a satisfactory manner. Only the development of a dynamical

theory, i.e the conventional transition state theory (CTST), offered a consistent physical picture about the reaction coefficient.



F5.2. Potential energy surface along the reaction coordinate for a bimolecular reaction. The relationship between the energies of the process is shown.

Figure F5.2 shows the potential energy surface for the bimolecular reaction:



As the two reactants approach each other, the energy of the reaction system rises. A point is reached, denoted by ABC^* , beyond which the energy starts to decrease again. The so-called activated complex ABC^* is a short-lived intermediate species through which the reactants must pass if the collision is to lead to reaction. By estimating the energy of this transition state the activation energies E_1 and E_{-1} may be estimated. This point is a saddle point in the potential energy surface of the system.

The figure shows the relationship between the activation energies of the forward and the reverse reactions. The enthalpy of reaction is given by:

$$\Delta H_r = E_1 - E_{-1} \quad (\text{E5.15})$$

The forward reaction sketched in F5.2 is exothermic ($\Delta H_r < 0$). The reverse reaction is endothermic and must have an activation energy at least as large as ΔH_r .

The rate equation for a bimolecular reaction $A+B \rightarrow \text{products}$, derived by the methods of CTST [151] is given by:

$$k = \frac{RT}{N_a h} \frac{q^*}{q_A q_B} e^{-E/(RT)} \quad (\text{E5.16})$$

where q_A , q_B and q^* are respectively the partition functions [155] of the reactants and the so-called activate complex (see below). In this expression R/N_a has been used in place of the Boltzmann constant to avoid confusion with the rate coefficient. The evaluation of partition functions starts with a separation of the different types of energy of the molecule under the assumption of its mutual independence. The Born-Oppenheimer approximation and the assumption of rigid rotator enable such separation. From this assumption, it follows that the partition function can be factorised in separated partition functions, one for each type of energy. For the translational, rotational and vibrational partition functions compact expressions can be obtained [151]. At ordinary temperatures the upper electronically excited states of the molecules are usually too high to make a significant contribution to the electronic partition function. Thus, this function comprises only the statistical weight of the lowest electronic state, take as having zero energy.

To apply E5.16 to practical cases it is necessary to estimate the structure of the activated complex, with its vibrational frequencies, and this is difficult for systems of any complexity.

5.3.2. Recombination and disproportionation reactions

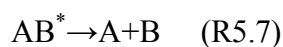
Reactions in which atoms and free radicals combine together to give an addition product play a very important role in chemical kinetics. Such reactions, for example, have a significant bearing on the course of many composite reactions. An example of combination reaction is the very important third-body ozone formation: $O_2 + O(^3P) + M \rightarrow O_3 + M$. Such reactions have zero activation energy and occur on

virtually every collision. Another type of process is disproportionation: the combination of two IO radicals, for example, may produce I_2+O_2 , $2I+O_2$ or $I+OIO$. Note that in the IO self reaction disproportionation and recombination (channel forming I_2O_2) are competing pathways.

At first sight such processes might seem to be straight forward examples of bimolecular reactions, showing second order kinetics. The recombination reactions are however the inverse of unimolecular dissociations and therefore must show special features. This may be seen from the fact that equilibrium expression must be the same under all conditions of pressure. Since at equilibrium the equilibrium constant is the ratio of the rate coefficients in the forward and the reverse reactions, it follows that if one of these coefficients shows some variation with total pressure, the other must show a parallel variation. Unimolecular reaction rates are theoretically explained on the basis of the Rice-Ramsperger-Kassel-Markus (RRKM) theory, which is an extension of the mechanism initially proposed by Lindemann-Christiansen [151]. For the dissociation of a molecule AB into two radicals A and B, the initial step is taken to be the process:

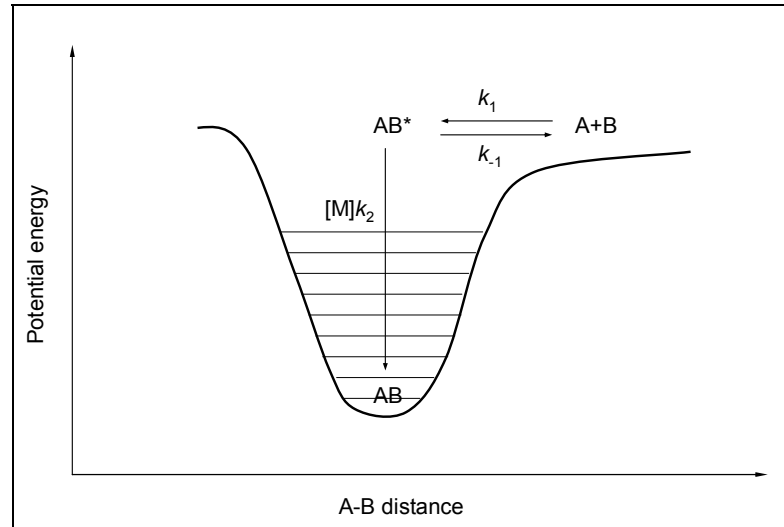


And the second step is taken to be the dissociation of the energised molecule:



In this scheme the energization has been brought about by a molecule M, which may be AB itself or may be a molecule of some added substance(s), commonly known as third body or chaperon. If this is the mechanism of dissociation, the reverse combination under the same condition is:





F5.3. Lindemann-Christiansen mechanism applied to radical recombination

The essential feature of this mechanism is that in R5.9 the energy of AB^* is transferred to the chaperon in a so called energy-transfer mechanism (see figure F5.3).

The application of the PSSA to this mechanism leads to:

$$\frac{d[AB^*]}{dt} = k_1[A][B] - (k_{-1} + k_2[M])[AB^*] = 0 \Leftrightarrow [AB^*] = \frac{k_1[A][B]}{k_{-1} + k_2[M]} \quad (\text{E5.17})$$

Therefore, the rate of removal of A is:

$$\frac{d[A]}{dt} = -k_2[M][AB^*] = \frac{k_1k_2[M][A][B]}{k_{-1} + k_2[M]} \Rightarrow k_{\text{rec}} = \frac{k_1k_2[M]}{k_{-1} + k_2[M]} \quad (\text{E5.18})$$

This expression for the recombination rate coefficient enables to explain qualitatively the fall-off of the k_{rec} versus pressure curve observed experimentally (F5.4) for the recombination of radicals.

At sufficiently low pressure the recombination reaction has third order. The pressure dependent effective rate coefficient is given by:

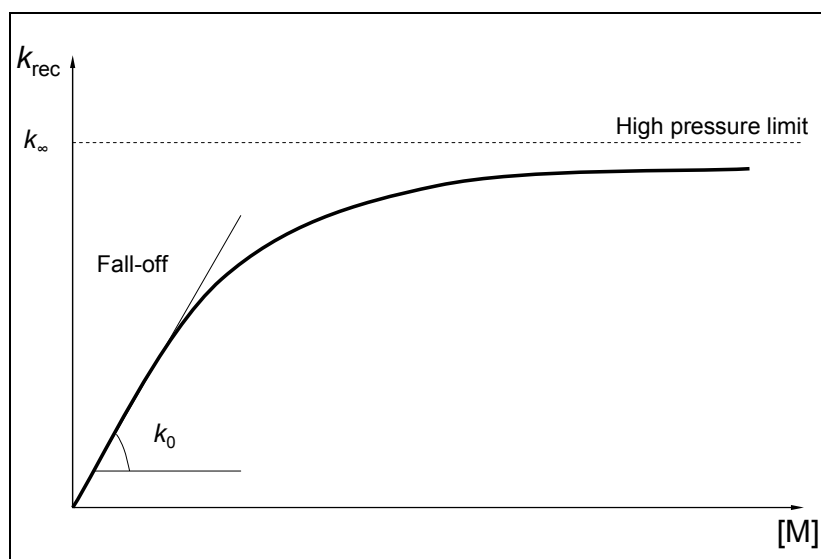
$$k_{\text{rec}} = \frac{k_1k_2[M]}{k_{-1}} \equiv k_0[M] \quad (\text{E5.19})$$

The rate coefficient k_0 is known as low pressure limit rate coefficient (see F5.4). When $[M]$ is sufficiently large, the recombination rate coefficient is controlled by the rate of

recombination of the radicals to form AB^* , which is very rapidly de-energised:

$$k_{\text{rec}} = k_1 \equiv k_{\infty} \quad (\text{E5.20})$$

The recombination reaction is therefore second order. The rate coefficient k_{∞} is known as high pressure limit rate coefficient. The combination of free radicals always occurs largely by this type of mechanism.



F5.4. Sketch of the observed pressure dependence of the recombination rate coefficient

The energy of the species AB^* is distributed among a number of modes of vibration, and there is a reasonable possibility that AB^* will be struck by a molecule M before it has time to dissociate. The more complicated the radicals A and B , the longer the lifetime of the complex AB^* , since its energy will be distributed among a larger number of vibrational modes, and more vibrations will have to occur before dissociation takes place. The combination of complex radicals therefore remains second order down to lower pressures than do the combination of simpler radical or atoms. It must be pointed out, however, that in atomic recombinations (like in the case of iodine) the rate coefficient depends on the chaperon. While the energy transfer mechanism holds for certain chaperons, there are also more efficient chaperons which can bring about atom recombination by an alternative mechanism known as the atom-molecule complex

mechanism [151].

The existence of different channels in a recombination reaction depends on two factors. First, for a reaction like R2.8 collision might occur is several surfaces, giving rise to excited complexes of different symmetry. This amounts to divide the mechanism into two different branches which can be treated separately. Second, the thermochemistry of products determines which of them are more favourable. This depends on their enthalpies of formation and in the existence of barriers resulting from symmetry constraints, i.e. in the rearrangement of bonds.

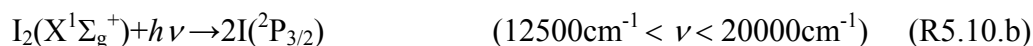
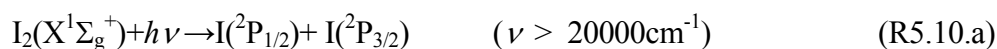
A more rigorous treatment of radical recombination in the context of the RRKM theory enables obtaining quantitative results and specifically to explain the behaviour in the transition between the low and the high pressure limits. In addition, this theory makes possible to incorporate recombination reactions presenting a number of channels. Rate coefficients are obtained by solving the master equation [156], which describes the time evolution of the population of the energy levels (grains) of AB^* . The bulk reaction coefficients are replaced by explicit microcanonic rate constants which treat each energy level of AB^* independently.

5.4. The photochemistry of iodine and ozone

5.4.1. Primary processes

5.4.1.1. Photolysis of I_2

The photolysis of molecular iodine has been used as primary process to initiate further secondary processes of interest [78, 80, 157]. It proceeds as follows [158, 159]:

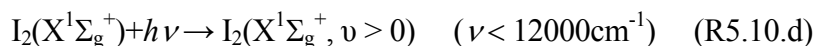


The number between parentheses indicate the thresholds for the fragmentations at 298 K when the parent molecule $I_2(X^1\Sigma_g^+)$ is excited from its vibrationless level ($v = 0$) [29].

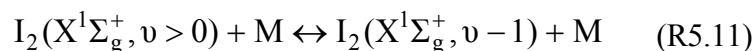
Additionally, $I_2(B^3\Pi(O_u^+))$ can be generated:



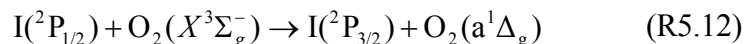
The overall pre-dissociation and fluorescence lifetimes in the $I_2(B^3\Pi(O_u^+))$ state are smaller than $2 \mu\text{s}$ [159]. The quenching of $I_2(B^3\Pi(O_u^+))$ proceeds to dissociation to $2I(^2P_{3/2})$ via $C^1\Pi_u$, with a lifetime of $\sim 1 \mu\text{s}$ at 10 hPa. Also vibrationally excited ground state I_2 can be generated:



Vibrationally excited $I_2(X^1\Sigma_g^+)$ is rapidly thermalised e.g. by collision with $M = O_2$ or N_2 [160]:



The quenching of metastable iodine:



is very effective due to resonance between energy levels of $I(^2P_{1/2})$ and O_2 [161].

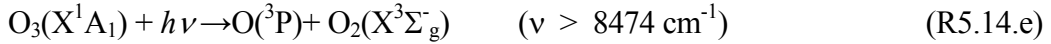
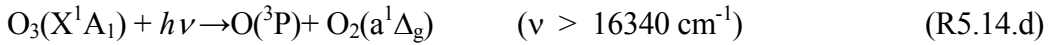
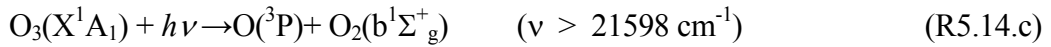
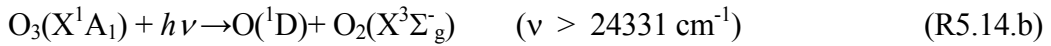
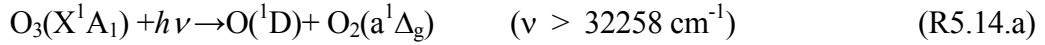
The quenching of metastable iodine has secondary effects, as a result of the regeneration $O(^3P)$ in the following reaction:



$O(^3P)$ contributes to subsequent IO formation and consumption, although depending on pressure it also recombines rapidly with O_2 to yield O_3 (R2.7). $O_2(a^1\Delta_g)$ has a long radiative lifetime of the order of 67 min [162] and it is slowly quenched by N_2 [28].

5.4.1.2. Photolysis of O_3

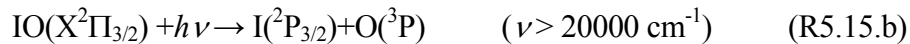
The photolysis of ozone has been also considered as primary process in the context of the iodine photochemistry [81, 163]. Ozone photolysis proceeds as follows [164]:



where the thresholds take as reference the vibrational ground state of $\text{O}_3(\text{X}^1\text{A}_1)$. Excitation to $\text{O}_3({}^1\text{B}_2)$ leads to immediate pre-dissociation (lifetimes of the order of 1 ps [165]).

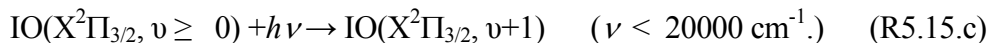
5.4.1.3. Photolysis of IO

IO photolysis proceeds as follows [29, 81]:

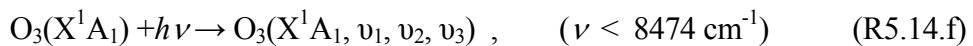


The vibrational levels of the $\text{IO}(\text{A}^2\Pi_{3/2})$ state are strongly pre-dissociated due to the crossing of a number of higher electronic states (see Chapter 4). Life times are smaller than 1 ns [144]. $\text{O}({}^1\text{D})$ is rapidly quenched by O_2 and N_2 [28].

Vibrationally excited $\text{IO}(\text{X}^2\Pi_{3/2})$ [125, 126, 134, 135, 166, 167] can be generated:



High vibrational levels of $\text{IO}(\text{X}^2\Pi_{3/2})$ could be reached if $\text{O}_3(\text{X}^1\text{A}_1)$ is vibrationally excited:

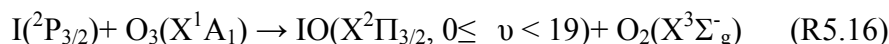


Vibrationally excited $\text{O}_3(\text{X}^1\text{A}_1)$ can be produced in reaction (R.2.5) as well. The quenching rates of vibrationally excited $\text{O}_3(\text{X}^1\text{A}_1)$ in the (100), (010) and (001) manifold are of the order of magnitude of $10^{-14} \text{ cm}^3 \text{ molecule}^{-1} \text{ s}^{-1}$ [168] both for N_2 and O_2 as deactivating gases.

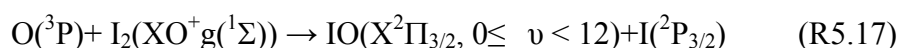
5.4.2. Secondary processes

5.4.2.1. Generation of IO radicals

The reaction of iodine atoms with ozone [28, 29, 80, 157, 163, 166, 169] is the major atmospheric source of iodine monoxide (see Chapter 2):



The photolysis of O_3 and of IO as well as reaction R5.13 generate $\text{O}({}^3\text{P})$, which can react with I_2 to produce iodine atoms and IO via reaction [28, 29, 157, 170]:



5.4.2.2. Disproportionation of IO

The IO self reaction :



is responsible for the removal of IO in the iodine-ozone or iodine-oxygen photochemical systems. Several studies have reported the value of the overall rate coefficient of this reaction [79-81, 163, 169-174]. The preferred value reported by the IUPAC review [29] is based in the results obtained in chemical systems such as $\text{N}_2\text{O}/h\nu/\text{I}_2$ in the absence of O_3 where second order kinetics of the IO decay were observed [79, 81, 170, 171]:

$$\frac{d[\text{IO}]}{dt} = -2k_{5.18}[\text{IO}]^2 \Rightarrow \frac{1}{[\text{IO}]} = \frac{1}{[\text{IO}]_0} + 2k_{5.18}t \quad (\text{E5.21})$$

Iodine atoms are regenerated by channels R5.18.b and R5.18.c. The photolysis of I_2 followed by reactions R5.16a, R5.18.b and R5.18.c produces a chain reaction destroying ozone. The branching mechanism of reaction R5.18 is uncertain and not yet well established. Iodine atom yields ($\alpha \equiv (k_{5.18,b} + 0.5k_{5.18,c})/k_{5.18}$) of 0.78 at 1.9-2.2 Torr [174] and 0.2 at 760 Torr [78] have been published. A pressure dependence of the yield

of non iodine atom products ($1-\alpha$) has also been reported [80, 171], indicating a pressure dependence of the branching ratios and the stabilization of an IO dimer. On the other hand, theoretical considerations seem to favour the pressure independence of the branching and a thermally unstable IO dimer [84, 174]. It is though that the IO self reaction is consistent with an energy-transfer mechanism in which R5.9 presents up to four different channels in competition [79, 84, 174].

5.4.2.3. Formation of higher iodine oxides

The disproportionation of IO (R5.18) is known to lead to the formation of higher iodine oxides of different stoichiometry [31, 35, 80, 85, 108-115, 169, 172, 173, 175]. OIO is a major gas phase product of R5.18 [32], but it decays rapidly [81, 83, 149]. In the absence of ozone, OIO is most likely removed by an excess of iodine atoms, leading to a reformation of I_2 [83]. In the presence of ozone, this rapid decay results most likely in the formation of higher iodine oxides. The specific mechanism responsible for the removal of OIO and the subsequent gas to particle conversion process remains to date unknown.

6. SEPARATION OF LINEARLY MIXED SIGNALS

6.1. Introduction

The principle of absorption spectroscopy is to measure the transmitted intensity (I) of an incoming light beam (with intensity I_0) after it has passed through a vessel containing reactive gases. These gases absorb part of the light depending on their respective absorption cross section $\sigma_j(\lambda)$, their concentration $c_j(t)$ and the geometric path length L of light. Incoming intensity I_0 and transmitted intensity I are monitored as a function of wavelength λ and time t . Both are linked by the Beer-Lambert Law:

$$I(t, \lambda) = I_0(\lambda) \times \exp(-L \times \sum_{j=1}^n c_j(t) \times \sigma_j(\lambda)) \quad (\text{E6.1})$$

or, equivalently:

$$A(t, \lambda) := \ln\left(\frac{I_0(\lambda)}{I(t, \lambda)}\right) = L \times \sum_{j=1}^n c_j(t) \times \sigma_j(\lambda) \quad (\text{E6.2})$$

where $A(t, \lambda)$ is called Optical Density (OD) and n is the number of different absorbing gasses present in the mixture. The values $A(t, \lambda)$ form a data array consisting of a time series of absorbance spectra covering the selected spectral window and time interval. The spacing of the data along the wavelength axis is defined by the linear dispersion and the sampling of the spectroscopic set-up. The spacing along the time axis is defined by the temporal resolution of the spectroscopic detection system. Data arrays recorded in this way allow the studying of chemical reactions by means of the characteristic absorption of radiation due to the reactants and products absorbing in the selected spectral window.

In both atmospheric and laboratory studies, molecular species of interest very often absorb in the same range of wavelength, presenting overlapping bands. In certain

cases it might be possible to find spectral sub-ranges containing characteristic features of only one absorber, but the problem of overlapping spectra comes up in many other cases when it is not possible to find such a separate window for each of the absorbers. This is, e.g., the case in ozone-halogen chemistry, where the spectra of the produced radicals are usually superimposed and the complexity of the overall reaction makes it difficult to modify the chemical system in such a way that selective minimisation of individual absorptions and thereby a separation of spectra could be achieved. The mixing of different absorbers in the kinetic data is a major source of uncertainty in kinetic and spectroscopic studies.

These facts suggest the use of multivariate statistical methods for source separation as it has been done in many other research fields dealing with multidimensional data arrays containing mixed signals: speech recognition (e.g. Lee et al. [176]), electroencephalographic analysis (e.g. Jung et al. [177]), mobile communication (e.g. Feng et al. et al. [178]), climatic research (e.g. Von Storch et al. [179], Aires et al. [180]), etc. This is an alternative to more ‘classical’ methods in spectroscopic analysis, e.g. trying to minimise individual absorptions by modification of the mixtures, looking for single-absorber spectral windows or iterative empirical calculation of residuals.

6.2. Statistical representation of datasets

Each dataset obtained from Multichannel Time-Resolved Molecular Absorption Spectroscopy (MTRMAS) can be seen as a $N \times M$ matrix with components $A(t, \lambda)$. Using standard statistic nomenclature and notation², a MTRMAS dataset is a set of N random variables, one for each time interval of observation (time label t_i , $i = 1 \dots N$), arranged in

² Usually, the realizations of a stochastic process take place in time. By analogy, a stochastic representation of a vector of absorbance is adopted here, in which the realizations of the process take place in wavelength, giving a ‘vector of spectra’ as a result of the sampling. It is useful to exploit the analogy between vibrational absorption spectra and time-dependent random variables to give an overview of the problem and to characterise the models presented here.

a random vector \mathbf{a} of dimension N . This vector³ is *sampled* over M wavelength values (wavelength label λ_k , $k = 1, \dots, M$). Thus, the dataset is given by a subset $\{\mathbf{a}(\lambda) \in \mathfrak{R}^N, \lambda = \lambda_1, \dots, \lambda_M\}$.

Following this vector notation, if $n \leq N$ different absorption spectra $\sigma_j(\lambda)$ are assumed to be mixed in such data recording, then their corresponding contributions in E6.2 can be written as follows:

$$\mathbf{a}_j(\lambda) = L \mathbf{c}_j \sigma_j(\lambda) \quad ; \quad j=1, \dots, n \quad (\text{E6.3})$$

where $\mathbf{a}_j(\lambda) = (A_j(t_1, \lambda) \dots A_j(t_N, \lambda))^T$ is the random vector corresponding to the OD of the molecular compound j –describing only the absorption of the single molecule j –, σ_j is its absorption cross section and $\mathbf{c}_j = (c_j(t_1) \dots c_j(t_N))^T$ is its concentration vector –or temporal behaviour.

For n simultaneous absorbers the superposition of all individual absorptions can be written as follows:

$$\mathbf{a}(\lambda) = \sum_{j=1}^n \mathbf{a}_j(\lambda) \quad (\text{E6.4})$$

Inserting E6.3 into E6.4, the following matrix expression can be written:

$$\mathbf{a}(\lambda) = \mathbf{C} \boldsymbol{\sigma}(\lambda) \quad (\text{E6.5})$$

where $\mathbf{a}(\lambda) = (A(t_1, \lambda) \dots A(t_N, \lambda))^T$ is the observed random vector of OD, $\mathbf{C} = (L\mathbf{c}_1 \dots L\mathbf{c}_n)$ is an $N \times n$ matrix whose columns are the temporal behaviours \mathbf{c}_j of the n absorbers multiplied by the path length L , and $\boldsymbol{\sigma}(\lambda) = (\sigma_1(\lambda) \dots \sigma_n(\lambda))^T$ is the absorption cross section vector, whose n components are the respective cross sections of the n absorbers. The vector-matrix representation of the Beer-Lambert law for a multi-component system is standard in ‘Chemometrics’ (see e.g. Brown et al. [181]).

A generative linear model like E6.5 can be expressed in the general form:

³ Standard lower and upper-case letters indicate scalars, bold lower-case letters indicate vectors, and bold upper-case letters indicate matrices. All vectors are understood as column vectors. Thus \mathbf{x}^T , or the transpose of \mathbf{x} , is a row vector. See notation appendix (B)

$$\mathbf{y} = \mathbf{B} \mathbf{s} + \boldsymbol{\varepsilon} \quad (\text{E6.6})$$

where $\mathbf{y} \in \mathfrak{R}^N$ is the observed random vector, $\mathbf{B} \in \mathfrak{R}^{N \times n}$ is the so-called mixing matrix, $\mathbf{s} \in \mathfrak{R}^n$ is the vector of source signals and $\boldsymbol{\varepsilon} \in \mathfrak{R}^N$ is a noise term. The observed random vector is sampled over M points: $\{\mathbf{y}_i \in \mathfrak{R}^N, i = 1, \dots, M\}$.

If the mixing matrix \mathbf{B} is known, the objective is to estimate the underlying signals \mathbf{s} . Assuming a Gaussian distribution of the residuals and linear independence of the columns of \mathbf{B} , the components of the vector \mathbf{s} can be estimated by using the Multiple Linear Regression (MLR) technique. The optimal solution is given by:

$$\mathbf{s} = (\mathbf{B}^T \mathbf{B})^{-1} \mathbf{B}^T \mathbf{y} \quad (\text{E6.7})$$

An example of this case is the determination of atmospheric concentrations from absorption spectra given the absolutely calibrated reference spectra of the species absorbing in the spectral range under study.

However, in some situations no other knowledge beside the observed data $\{\mathbf{y}_i \in \mathfrak{R}^N, i = 1, \dots, M\}$ is available, and the aim is to estimate *both* the mixing matrix \mathbf{B} and the underlying source signals \mathbf{s} for the given sample. The solutions to this problem are usually referred to as blind source separation (BSS) techniques. Note the ambiguity inherent in the problem, arising from the fact that both \mathbf{B} and \mathbf{s} are unknowns. It is not possible to determine the variances of the factors, because any scalar multiplier in one of the sources s_j can always be cancelled by dividing the corresponding column \mathbf{b}_j of \mathbf{B} by the same scalar. Their magnitudes must be arbitrarily fixed, it being common practice to constrain them to have unity variance: $E[s_j(\lambda)^2] = 1$. The ambiguity in the sign remains, but it is unimportant in most cases. The model E6.6 can be implemented using a number of different source separation techniques Principal Components Analysis (PCA) and Independent Components Analysis (ICA).

The use of such models in this context has been suggested by the comparison of the structure of vibrational energy levels of species with different atomic bonds and different molecular symmetry (Chapter 4, sections 4.2.4 - 4.2.6). Different physical processes tend to generate statistically independent signals, which under certain conditions can plausibly be assumed for transitions between vibrational states of different molecules. In principle, it could be also possible to treat the temporal behaviours of the different absorbers as the sources to be separated from each other, but there is a strong argument against using ICA to retrieve temporal behaviours as sources, given the relationship between them through the law of conservation of mass, which should imply statistical correlation.

ICA has not yet been used for component extraction in spectroscopy, although Aires et al. [182] proposed it as a more advanced statistical technique than PCA in compression and denoising of the observations obtained with the high spectral resolution Infrared Atmospheric Interferometer (IASI) instrument.

6.3. Blind source separation

6.3.1. Principal Components Analysis

6.3.1.1. PCA as a generative model: Decomposition and separation of sources.

PCA is a well known and widely used generative linear model (see Jolliffe [183] for a reference text) used to retrieve a source signal vector \mathbf{s} consisting on n uncorrelated components s_j (called principal components: PCs), given an observational vector \mathbf{y} with dimension N (in order to simplify the calculations \mathbf{y} is previously centred). These PCs are sorted accordingly to the amount of variability in \mathbf{y} that they are able to explain.

The strategy adopted to invert the linear model represented by E6.6 is the recursive calculation of the rows $(\mathbf{b}^\dagger)^T$ of the mixing matrix generalised inverse $\mathbf{B}^\dagger = (\mathbf{B}^T\mathbf{B})^{-1}\mathbf{B}^T$, by maximisation of the variance of linear combinations of the observed

signals $s = (\mathbf{b}^\dagger)^\top \mathbf{y}$ with the constraint of mutual uncorrelatedness and unity variance. In practice, only a finite sample with M realisations of the observational vector \mathbf{y} is available, and what can be calculated is an estimate source signal vector $\mathbf{z} = \hat{\mathbf{s}}$ consisting of n *sample* principal components⁴. For simplicity, the estimates of \mathbf{B} and \mathbf{B}^\dagger are denoted respectively as \mathbf{P} and \mathbf{Q} . Its rows \mathbf{q}_j^\top are obtained by maximisation with constraints of $Var(z(\lambda)) = E[(\mathbf{q}^\top \mathbf{y}(\lambda))^2]$, i.e. the sample variance of linear combinations of the observed signals. The wavelength label is used here as a sampling label to emphasise the connection of the model with the problem addressed in this work. A constraint of orthogonality accounts for the requirement of uncorrelatedness between sources. In case of centred vectors, orthogonality and uncorrelatedness are equivalent. The first row of \mathbf{Q} is obtained as follows:

$$\mathbf{q}_1^\top = \underset{E[\mathbf{q}^\top \mathbf{q}] = 1}{arg\ max} [\mathbf{q}^\top \hat{\Sigma} \mathbf{q}]$$

The subsequent rows of \mathbf{Q} are obtained using the following optimisation-orthonormalisation recursive expression:

$$\mathbf{q}_j^\top = \underset{\substack{E[\mathbf{q}^\top \mathbf{q}] = 1 \\ E[\mathbf{q}^\top \Sigma \mathbf{q}_i] = 0}}{arg\ max} [\mathbf{q}^\top \hat{\Sigma} \mathbf{q}]; \quad i = 1 \dots j-1; \quad j > 1 \quad (\text{E6.8})$$

where $\hat{\Sigma}$ is the estimate of the covariance of the observational random vector \mathbf{y} and the function *argmax* reads ‘the argument which maximises’ the function in brackets. Note that in order to take the sample expected value $E[(\mathbf{q}^\top \mathbf{y}(\lambda))^2] = \mathbf{q}^\top \hat{\Sigma} \mathbf{q}$, the scalar random variable $\mathbf{q}^\top \mathbf{y}(\lambda)$ is considered as a row vector, because the sampling is arranged in rows in the observed data array. The sample is assumed to be previously centred, that is, the average of all samples of the random vector was previously subtracted from each of its M realisations. It can be shown that the determination of the vectors \mathbf{q}_j^\top as written in E6.8 boils down to the diagonalisation of $\hat{\Sigma}$ [183]. The vectors \mathbf{q}_j^\top are the eigenvectors

⁴ See notation appendix (B)

of $\hat{\Sigma}$, and its corresponding eigenvalues inform about the amount of variance of the observed data explained by projecting them with the weights \mathbf{q}_j^T , being sorted in ascending order according to this criterion. It can also be proven that on each step of E6.8 a component is calculated such that the remaining variability (i.e. in the residuals) is minimised in the Least Squares (LS) sense. This means that if $\mathbf{B}_{(j)} = (\mathbf{b}_1 \dots \mathbf{b}_j)$ and $\mathbf{s}_{(j)} = (s_1 \dots s_j)^T$ are respectively the mixing matrix and the signals vector in the step j of PCA, then the square error $(\mathbf{y} - \mathbf{B}_{(j)}\mathbf{s}_{(j)})^2$ is minimised. A rigorous deduction of this and other optimal algebraic and geometric properties of PCA can be found in Jolliffe [183].

Normally only a limited number of PCs –those explaining the major amount of variability– contain physical information, the rest being only gaussian noise. This fact makes PCA useful in de-noising and dimension reduction (see below).

PCA efficiently extracts orthogonal, i.e. uncorrelated contributions. Note that, however, uncorrelatedness does not mean statistical independence. This is only true for gaussian sources. Therefore, source separation via PCA can be expected only if prior knowledge makes the following assumptions plausible:

- 1) The sources are non-gaussian (see the characterisation of PCA for Projection Pursuit in Bolton et al. [184])
- 2) The sources are mutually uncorrelated (orthogonality constraint in E6.8)
- 3) The weighting vectors are linearly independent. Therefore, a generalised inverse \mathbf{B}^\dagger of the mixing matrix exist, where \mathbf{B} contains a weighting column vector for each source.

If such conditions are not satisfied, the mixing of different physical phenomena remains in the principal components. But it can also happen that the conditions are too weak to describe the real nature of the sources. In particular, absorbance signals are not orthogonal in every wavelength range, but only in determined spectral windows, and even in these windows orthogonality does not characterise entirely the statistical

relationship between the sources. As a consequence of these two facts, a set of principal components obtained from MTRMAS datasets generally contains mixed spectra.

6.3.1.2. PCA for pre-processing: Dimension reduction and filtering

Apart from using PCA for source extraction as described before, this method has a quite general application as a pre-processing tool for nearly any kind of statistical data. In this respect, once the estimate \mathbf{P} of the mixing matrix \mathbf{B} has been obtained from the estimate \mathbf{Q} of its generalised inverse \mathbf{B}^\dagger , and the estimated PCs \mathbf{z} have been calculated, the sum of the matrix product \mathbf{Pz} can be truncated in order to reassemble the dataset by using only those components that explain a major amount of variance. Only the n vectors \mathbf{q}_j with the n largest eigenvalues are kept:

$$\mathbf{y}(\lambda) = \mathbf{P} \mathbf{z}(\lambda) = \sum_{j=1}^M \mathbf{p}_j z_j(\lambda) = \sum_{j=1}^n \mathbf{p}_j z_j(\lambda) + \sum_{j=n+1}^M \mathbf{p}_j z_j(\lambda) \approx \sum_{j=1}^n \mathbf{p}_j z_j(\lambda) = \tilde{\mathbf{P}} \tilde{\mathbf{z}}(\lambda) \quad (\text{E6.9})$$

where the sampling label λ emphasises the idea of a *sample* model, in contrast to the *population* model E6.6). $\tilde{\mathbf{P}}$ refers to the rectangular matrix resulting from removing the mixing weights of the low variance components and $\tilde{\mathbf{z}}$ indicates the vector of retained components. For any degree of truncation, PCA gives the optimal dimension of reduction, in the mean square sense.

In this way PCA can be used as a valuable pre-processing method, which can even be applied when the requirements of the model for source separation are not satisfied by the *real* sources. For example, a quick analysis of the possible stoichiometry of a given set of reactions reveals that the real dimension of the source vector (n spectra corresponding to n reacting absorbers) is much smaller than the dimension of the dataset under study (N mixtures of spectra –one for each time step– with $N \gg n$). The physically meaningful information can be summarised in a reduced number of so-called ‘whitened’ variables ($E[\mathbf{y}\mathbf{y}^T] = \mathbf{I}$), while gaussian noise is removed as indicated in E6.9. The number of parameters to be estimated in further analysis is dramatically reduced by

the dimension reduction of the problem ($n \ll N$). Note that these principal components are not forced to have any physical meaning, but contain mixed features of the real sources.

PCA pre-processing removes noise, reduces the dimension of the problem and produces a set of n ‘whitened’ observations ($E[\mathbf{y}\mathbf{y}^T] = \mathbf{I}$ is satisfied). This simplifies considerably the computational effort of the ICA algorithm.

It is important to note that a ‘blind’ quantitative variance criterion for the truncation of the sum in E6.9 is not enough to ensure a correct dimension reduction. It has to be checked that all the significant spectral features are contained in the retained components, and that the rejected ones contain nothing but noise or outliers.

6.3.2. Independent Components Analysis

6.3.2.1. General: ICA as a generative model

An introduction to ICA can be found in Hyvärinen et al.[185] or Cardoso [186]. This is a widely used method to perform blind source separation and feature extraction, developed in recent years and with a wide range of applications. The model is based upon three basic assumptions:

- 1) The sources have all a non-gaussian probability distribution function (pdf) with the possible exception of one of them.
- 2) The sources are statistically independent.
- 3) The generalised inverse \mathbf{B}^+ of the mixing matrix exist.

MTRMAS datasets only partially fulfil these conditions: absorption spectra are, in general, non-gaussian signals; statistical independence is suggested by the existence of different symmetries and bonds in the molecules and under certain chemical conditions temporal behaviours are linearly independent. However the condition of statistical independence might not be satisfied in every spectral range, and there might be some absorbers with linearly dependent temporal behaviours.

The ICA model free of noise⁵ (Hyvärinen [197]) consists in the estimation of the following generative model from the observational data:

$$\mathbf{y} = \mathbf{B} \mathbf{s} \quad (\text{E6.10})$$

The problem can be presented in the same terms as in the case of PCA. A source signal vector \mathbf{s} consisting of n independent components s_j (ICs) has to be retrieved, given an observational vector \mathbf{y} with dimension $N > n$. Note that PCA and ICA are treated up to now as different implementations of the same model E6.6).

The strategy for inverting E6.10 is the same as employed by PCA. The rows \mathbf{b}^\dagger of the mixing matrix generalised inverse \mathbf{B}^\dagger are calculated by constrained maximisation of a *cost* or *contrast* function $J(s)$ of linear combinations $s = (\mathbf{b}^\dagger)^\top \mathbf{y}$ of the observed signals. In the case of PCA the cost function is the variance. In ICA, a cost function able to quantify the quality of the linear combinations in terms of their statistical independence is required (see appendix A). Since statistical independence implies uncorrelatedness, the ICA method constrains the estimation procedure so that it always yields uncorrelated estimates of the independent components, simplifying the computation. As centred vectors are considered, the orthogonality constraint $E[\mathbf{s}\mathbf{s}^\top] = \mathbf{I}$ is imposed.

As it was pointed out in the case of PCA, in practice only a finite sample with M realisations of the observational vector \mathbf{y} is available, and what can be calculated is an estimated source signal vector $\mathbf{x} = \hat{\mathbf{s}}$ consisting of n *sample* independent components x_j . For simplicity, the estimate of \mathbf{B}^\dagger is denoted as \mathbf{W} . Its rows \mathbf{w}_j^\top are then obtained by maximisation with constraints of $J_G(x(\lambda)) = J_G(\mathbf{w}_j^\top \mathbf{y}(\lambda))$, that is, a cost function of linear combinations of the observed signals. Similarly to PCA, the first row of \mathbf{W} is obtained using the following expression:

⁵ Later it is assumed that the observation vector has been previously freed of noise using PCA. This supports the selection of the model free of noise.

$$\mathbf{w}_1^T = \underset{E[\mathbf{w}^T \mathbf{y} \mathbf{y}^T \mathbf{w}] = 1}{\arg \max} [J_G(\mathbf{w}^T \mathbf{y}(\lambda))]$$

and the subsequent rows of \mathbf{W} are obtained with the recursive formula

$$\mathbf{w}_j^T = \underset{\substack{E[\mathbf{w}^T \mathbf{y} \mathbf{y}^T \mathbf{w}] = 1 \\ E[\mathbf{w}^T \mathbf{y} \mathbf{y}^T \mathbf{w}_i] = 0}}{\arg \max} [J_G(\mathbf{w}^T \mathbf{y}(\lambda))]; \quad i=1, \dots, j-1; \quad j > 1 \quad (\text{E6.11})$$

where the constraints force the estimation procedure to yield uncorrelated (orthogonal) estimates of the independent components, simplifying the computation. Note that PCA pre-processing also simplifies the constraints ($E[\mathbf{y} \mathbf{y}^T] = \mathbf{I}$ is satisfied). Please also note that, in contrast to PCA, ICA does not use variance as cost function. As a consequence, it requires on the one hand other properties of the input data and on the other hand it produces results with different characteristics. Therefore, ICA is not to be confused with Least Squares methods maximizing explained variance (i.e. minimizing variance of the residual).

6.3.2.2. Algorithm for ICA free of noise.

This approach for ICA estimation is implemented in the *FastICA* algorithm (see [188] for further details), which can be downloaded from the web page of the Laboratory of Computer and Information Science of the Helsinki University of Technology (<http://www.cis.hut.fi/projects/ica/fastica/>.) The steps followed by this algorithm are the following:

- 1) The samples are centred
- 2) The image is whitened and its dimension reduced using PCA. To this end eigenvalue decomposition of the covariance matrix is performed.
- 3) The ICs are calculated using as observations the vector $\tilde{\mathbf{z}}$ of retained PCs:

$$\tilde{\mathbf{z}}(\lambda) = \mathbf{M} \bar{\mathbf{x}}(\lambda)$$

where the slash over the source vector \mathbf{x} emphasises the sample centring of the sources, which has to be undone later. For simplicity, the estimate of \mathbf{B} is denoted as \mathbf{M} . A fixed-point iteration scheme is used to solve the optimisation problem defined by E6.11). After each step j , the projections $\mathbf{w}_j^T \mathbf{w}_i \mathbf{w}_i, i = 1, \dots, j-1$, are subtracted from \mathbf{w}_j , and in this way decorrelation is achieved.

It is also possible to use a parallel decorrelation ([188]). The drawback of this approach is that the same cost function has to be used for all the independent components, because this implies the assumption of identically distributed sources and prevents selecting the cost function which better picks the relevant information of the distribution of a given component. In this case, if no prior knowledge is available, one of the ‘all purpose’ non-linearities proposed in [188] must be selected. Nevertheless, if only two sources are mixed in the observed data, the selection of the cost function only affects the retrieval of the first source, because once this is found, the second source is univocally defined by the orthogonality constraint. Thus, the symmetric approach can be used equivalently to the stepwise procedure in this case.

When \bar{x}_j has been calculated for each $j = 1, \dots, n$, the original dataset \mathbf{y} can be approximately reconstructed as follows:

$$\bar{\mathbf{y}}(\lambda) \approx \tilde{\mathbf{P}} \tilde{\mathbf{z}}(\lambda) = \tilde{\mathbf{P}} \mathbf{M} \bar{\mathbf{x}}(\lambda) = \mathbf{U} \bar{\mathbf{x}}(\lambda)$$

where $\mathbf{U} = \tilde{\mathbf{P}} \mathbf{M}$ is the *total* mixing matrix. Decentring is straightforward:

$$\mathbf{y}(\lambda) = \bar{\mathbf{y}}(\lambda) + \mathbf{E}[\mathbf{y}(\lambda)] \approx \mathbf{U} \mathbf{x}(\lambda) + \mathbf{E}[\mathbf{y}(\lambda)] \quad (\text{E6.12})$$

Note again that the recovered dataset is noise-filtered in the step 2. Therefore, the error of each row in the reconstructed image is given by the LS error criterion:

$$\{\mathbf{E}[(\bar{y}_i(\lambda) - (\tilde{\mathbf{p}}_i)^T \tilde{\mathbf{z}}(\lambda))^2]\}^{1/2}.$$

To recover the vertical position of x_j (decentring) the generalised inverse \mathbf{V} of the *total* mixing matrix \mathbf{U} is applied over the vector of observed means. For the source j , the standardised mean can be written as follows:

$$E[x_j(\lambda)] \approx \mathbf{v}_j^T E[\mathbf{y}(\lambda)]$$

where \mathbf{v}_j^T is a row of \mathbf{V} . Thus, the decentred source is given by:

$$x_j(\lambda) = \bar{x}_j(\lambda) + \mathbf{v}_j^T E[\mathbf{y}(\lambda)] .$$

Note that the algorithm depends entirely on the mathematical concept of statistical independence of the sources. No physical arguments of reasonable weighting vectors are included. Such arguments could e.g. be that temporal behaviours must always be non negative and smooth curves. Note also that the algorithm is invariant against any arbitrary permutation of rows and columns in the part of the MTRMAS dataset considered for the analysis. The physical meaning of wavelength and time coordinates is still not considered.

6.3.2.3. Interpretation of the mixing matrix.

In the particular case of the BLL linear model E6.6, the mixing matrix obtained with the method described above can be interpreted as follows. E6.12 can be rearranged and written for a single component j :

$$\bar{\mathbf{y}}_j(\lambda) = \mathbf{y}_j(\lambda) - E[\mathbf{y}_j(\lambda)] \approx \mathbf{u}_j \bar{x}_j(\lambda) \quad (\text{E6.13})$$

where \bar{x}_j is the standardised independent component and \mathbf{u}_j is the corresponding column of the total mixing matrix. On the other hand, rearranging E6.6 to write the BLL as a function of a spectrum centred and normalised to unity variance, it can be written:

$$\begin{aligned} \mathbf{a}_j(\lambda) - E[\mathbf{a}_j(\lambda)] &= L \mathbf{c}_j \sigma_j(\lambda) - L \mathbf{c}_j E[\sigma_j(\lambda)] = L \mathbf{c}_j (\sigma_j(\lambda) - E[\sigma_j(\lambda)]) = \\ &= L \mathbf{c}_j \bar{\sigma}_j(\lambda) = L \mathbf{c}_j \bar{\sigma}_j(\lambda) s_j s_j^{-1} = L s_j \mathbf{c}_j \hat{\sigma}_j(\lambda) \end{aligned} \quad (\text{E6.14})$$

where $s_j = \{E[\bar{\sigma}_j(\lambda)^2]\}^{1/2}$. The comparison between E6.13 and E6.14 allows

interpreting the mixing matrix columns as follows:

$$\left. \begin{array}{l} \bar{\mathbf{y}}_j(\lambda) = \mathbf{a}(\lambda) - \mathbb{E}[\mathbf{a}(\lambda)] \\ \bar{x}_j(\lambda) = \hat{\sigma}_j(\lambda) \end{array} \right\} \Rightarrow \mathbf{u}_j = L s_j \mathbf{c}_j \quad (\text{E6.15})$$

This means that the mixing matrix column is the concentration vector times the path length times the standard deviation of the spectrum. If the spectrum is previously known, its standard deviation in the selected spectral window can be calculated, and inserting it in E6.15, the absolutely scaled concentration time curve can be retrieved. Thus, this prior knowledge partially removes the ambiguity of the model. Obviously, this calculation is not possible for species with an unknown spectrum.

6.4. Multivariate Linear Regression

The equation E6.1 is a form of the Beer-Lambert Law for a multi-component gas with n different absorbers. The OD measured at a given wavelength and time $A(t, \lambda)$ is a mixture of the ODs corresponding to the different species present in the mixture at that time and absorbing in the same wavelength range. OD data arrays obtained by applying E6.2 to MTRMAS raw data consist of different absorptions, which are overlapped to each other at different degrees and in different spectral ranges and times. The matrix equation for *all wavelengths and time steps*:

$$\mathbf{Y} = \mathbf{BS} + \mathbf{E} \quad (\text{E6.16})$$

is a generalization of the single wavelength matrix form of Beer-Lambert Law E4.2. If the columns of the so-called mixing matrix (\mathbf{B}) are linearly independent, it is possible to separate the *mixed* data \mathbf{Y} into several *pure* components, i.e. the rows of \mathbf{S} , one for each absorber, using multivariate analysis techniques based on the inversion of \mathbf{B} . PCA and ICA can be applied to solve the problem when both \mathbf{B} and \mathbf{S} are unknown, if the data subset fulfils the requisites of these models. Alternatively, if \mathbf{B} is known the components of the matrix \mathbf{S} can be more easily estimated by performing a Multivariate Multiple Linear Regression (MMLR).

Let us assume that the absorption cross sections of each absorber as a function of wavelength are known, and that the column densities are not known. The matrix \mathbf{Y} – matrix of observations– contains on each column the spectral absorbance at a given time. The columns in matrix \mathbf{B} –the so-called mixing matrix– contain the absorption cross sections of each absorber as a function of wavelength. Finally, the rows of \mathbf{S} – unknowns– are the transient column densities of each absorber, i.e. transient concentrations multiplied by path length. \mathbf{E} is a matrix of prediction error. A MMLR consists in a simple linear Least Squares technique, whose optimal solution [191] is given by:

$$\mathbf{S}=(\mathbf{B}^T\mathbf{B})^{-1}\mathbf{B}^T\mathbf{Y} \quad (\text{E6.17})$$

Note that his procedure can be equally applied if the unknowns are the absorption cross sections. In that case, each columns of \mathbf{Y} is an absorbance as a function of time at a given wavelength, the columns of \mathbf{B} contain the transient column densities of each absorber and the rows of \mathbf{S} are the unknown absorption cross sections of each absorber as a function of wavelength.

The existence and the accuracy of the solutions of E6.16 by inversion of the mixing matrix depend on how good is the assumption of linear independence of the columns of the mixing matrix. The clearer the linear independence, the smaller the uncertainty in the estimated spectra. If two or more spectra (temporal behaviours) contained in the mixing matrix are to some extent linearly dependent, then the solution according to E6.17 is limited, if not impossible. Such dependences between columns of the mixing matrix are referred to as multicollinearities. If multicollinearities exist in the mixing matrix, this causes at least one of the eigenvalues of the normal matrix $\mathbf{B}^T\mathbf{B}$ to tend to zero, and as a consequence the condition number tend to infinity, i.e. the normal matrix is ‘ill-conditioned’. According to Dahlquist et al. [192], the errors in \mathbf{S} , which originate from errors in the observational data \mathbf{Y} and in the data which constitutes the

mixing matrix \mathbf{B} are amplified by the condition number of the normal matrix.

The problem of multicollinearity is particularly acute in the separation of spectra, i.e. when the corresponding temporal behaviours are known. The latter are normally featureless, smooth functions, which in addition are indirectly linked by the law of mass conservation and the differential rate equations of the chemical system. Thus, it is easy to find that one or more temporal behaviours can be expressed to a good approximation as linear combinations of the others. This is more difficult in the case of structured spectra, although it might also occur if the overlapping spectra are featureless continua.

Multicollinearity can to a certain degree be avoided by appropriate selection of a data subset. In case of known temporal behaviours and unknown spectra, this means to select an appropriate spectral window where collinear absorptions are zero, which amounts to remove the corresponding columns from the matrix \mathbf{B} .

Part III

METHODOLOGY

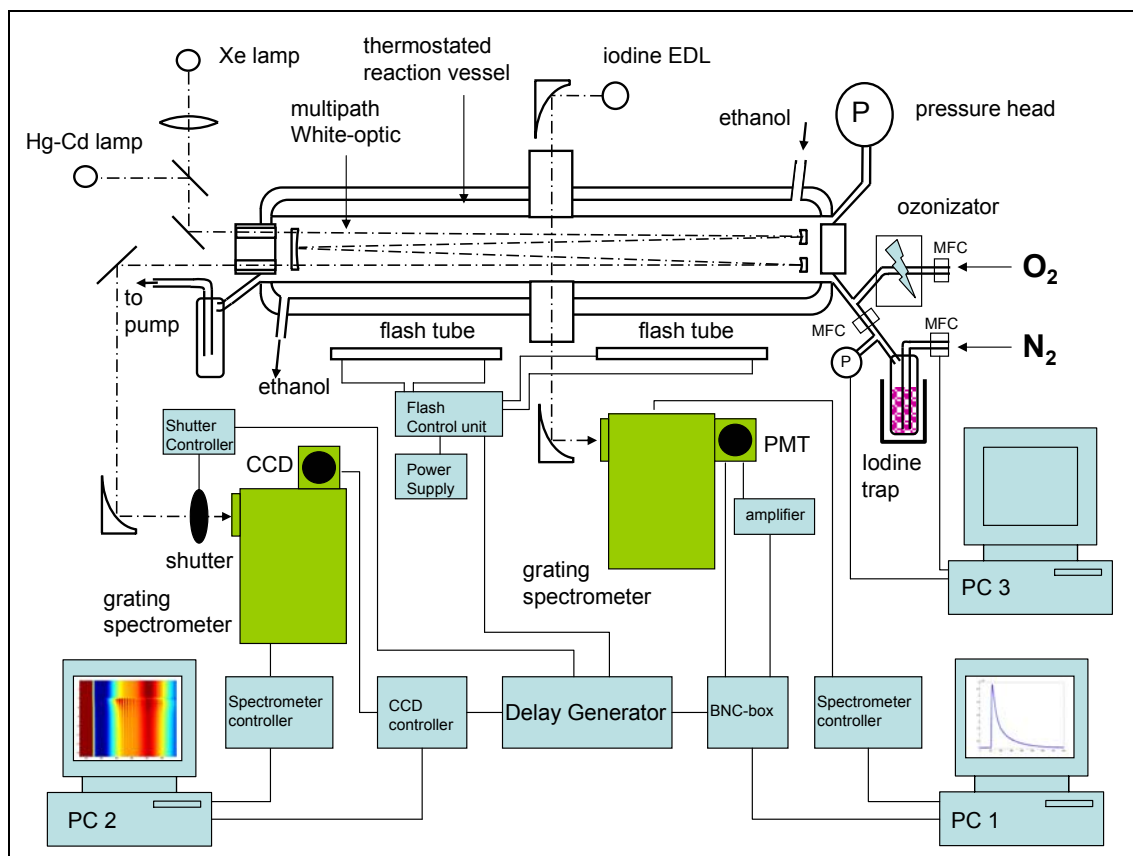
7. EXPERIMENTAL SET UP

7.1. Description

Flash photolysis is a well established technique employed in kinetic and spectroscopic studies [193, 194]. In the experimental set up used in the present study (F7.1), iodine oxides were generated by flashing upon a temperature stabilised quartz reaction vessel containing I_2/O_3 mixtures carried in a stable flow of N_2 and/or O_2 . The detection apparatus was designed to simultaneously monitor all relevant molecular and atomic species involved in the I_2/O_3 photochemistry. Ultraviolet-Visible (UV-VIS) molecular absorption of the analysis light was measured along the longitudinal axis of a White-type multipath reaction vessel by using a spectrometer and a CCD camera operated in kinetic mode. $I(^2P_{3/2})$ resonance absorption of radiation was measured simultaneously along a short path cross axis by using a spectrometer and a photomultiplier tube.

7.1.1. Generation of radicals

A standard IUP reaction vessel [32] with modifications for this type of synchronised experiments [124] was used. It consists of a 140 cm-long and 5 cm diameter double-jacketed quartz tube [32] with a cross probing axis. The experiments were performed at room temperature ($T = 298$ K) in flow mode. A stable flow of I_2 in N_2 was produced by passing a flow of N_2 through a thermostated and pressure stabilised glass trap ($T = 273$ K) containing I_2 . This flow could be diluted by an additional flow of pure N_2 . O_3 was produced by passing a stream of O_2 through a silent discharge. The N_2 and O_2 (grade 4.8) were obtained from Messer-Griesheim and the I_2 (resublimed p.a.) from ACROS organics. The flows were controlled by using calibrated mass flow controllers (MKS instruments) ranging from 1000 to 10000 standard cm^3 per minute (sccm). Calibrated capacitance barometers (MKS instruments) in the range of 100 and 1000 hPa were used to monitor the pressure.

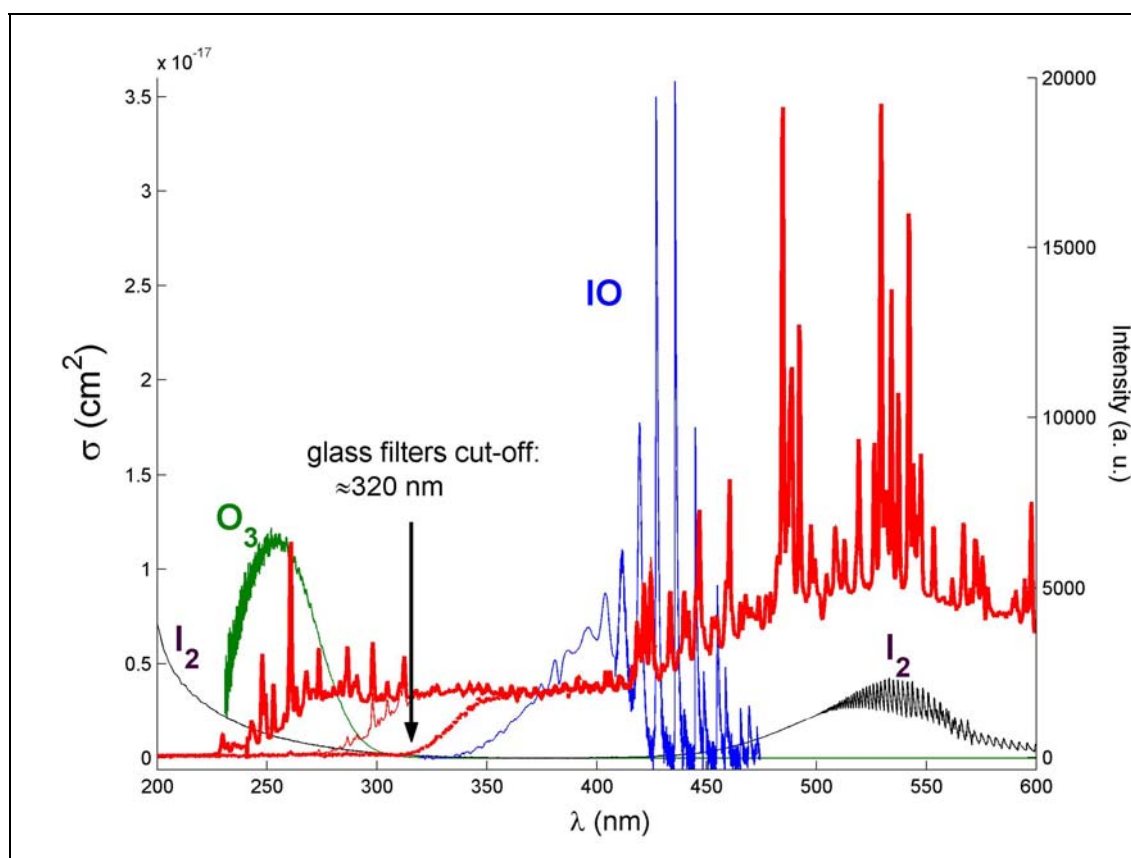


F7.1: Flash photolysis experimental set-up. It is conceived to perform synchronised multichannel time resolved absorption spectroscopy and atomic resonance absorption spectroscopy.

The photolysis flash system contains two 30 cm long Xenon flash tubes (Heimann, model HG9903) with a maximum output of 160 J per flash, charged by a 1500 V power supply (Converter Power Inc., RCS 1500) and two 145 μF capacitors (Siemens). These flash tubes emit a pulse of broad band radiation ranging from ultraviolet to visible and infrared. The spectral distribution corresponds to the radiation of a black body at ~ 7000 K with some superimposed broadened lines (red lines in figure F7.2). This radiation enabled the production of free I and O atoms by photolysis of I_2 and O_3 respectively. Optical filters (Tempax) between the flash tubes and the vessel were used to limit the wavelength of the photolysing radiation in the UV (compare the solid and the dashed thick red lines in F7.2). Specifically this enabled to eliminate the photolysis of O_3 in its Hartley and Huggins bands [164], thus minimising the reaction

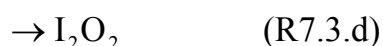


and leaving the as single source of IO the reaction:



F7.2. Raw transmitted intensity spectra (in arbitrary units) of the photolysis tubes (red) and wavelength dependence of the absorption cross sections of selected absorbers (indicated in the figure). The presence of ozone significantly reduces the transmitted intensity between 250 and 300 nm (compare thick red curve with dotted red curve). The introduction of glass filters establishes a cut-off for the photolytic radiation below 320 nm (note the difference between the solid thick curve and the dotted red curve) and practically suppresses the ozone photolysis. In these experiments, photolysis of I_2 is responsible for the release of free iodine atoms (R5.10), which react with ozone (R5.16) to produce IO (blue spectrum in the figure).

The main reaction under study is the IO self reaction:



IO is consumed in less than 30 ms for the mixing ratios of precursors considered (T7.1).

Such time scale is short with respect to the purging time of the vessel (~ 5 s, see T7.2).

This enabled the assumption of a static mixture to be made for analysis purposes.

7.1.2. Detection

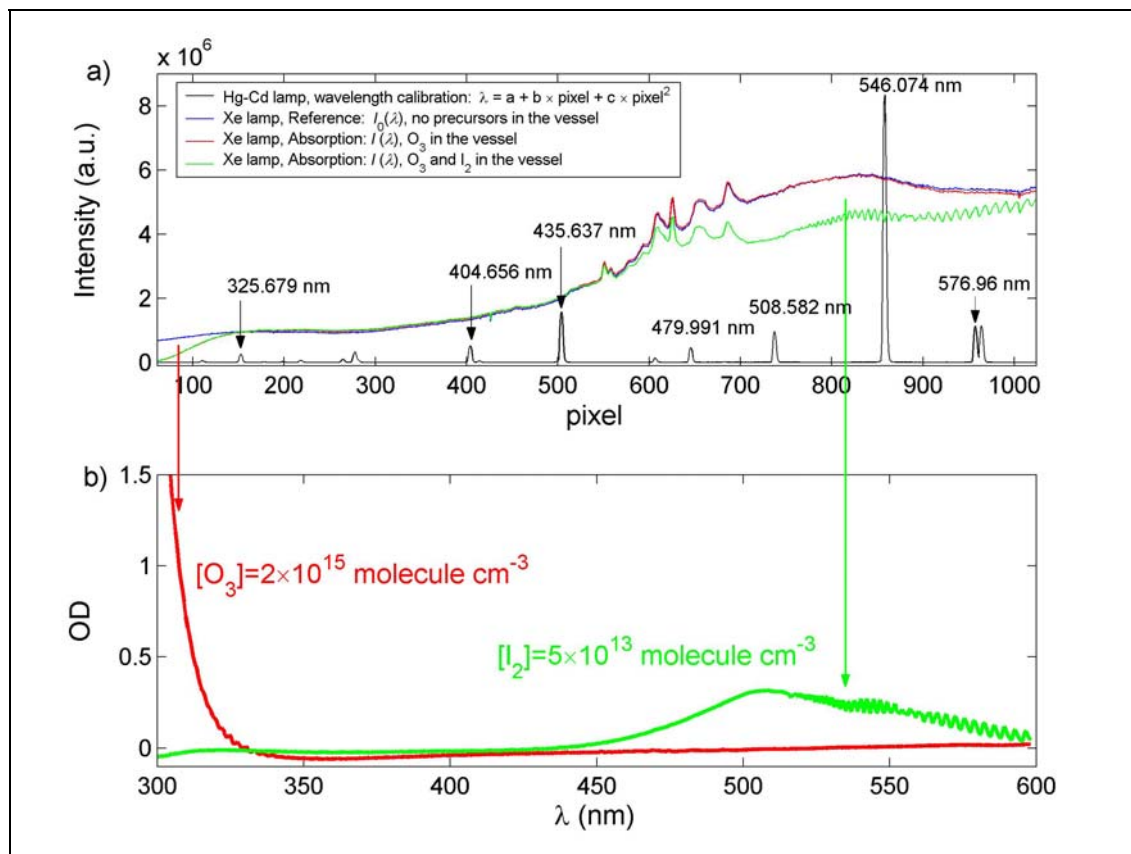
7.1.2.1. Multichannel Time-resolved Molecular Absorption Spectroscopy (MTRMAS)

A 150 W superquiet Xenon arc lamp (Hamamatsu) was used as absorption light source. This light could be passed through the reaction vessel by using double-walled, evacuated quartz optical windows. Molecular absorption was measured along the longitudinal axis of the reaction vessel with a multipath White optic system [195]. Aluminium and magnesium fluoride-coated spherical mirrors (Berliner Glas) were employed ($f=60\text{cm}$). By using the White optical arrangement the path length within the vessel could be varied in steps of 4.8 m to up to approximately 2880 cm (11 reflections). A path length of 2430.5 cm (9 reflections) enabled an optimal signal to noise ratio.

After having traversed the vessel, the analysis light was focused onto the entrance slit of a Czerny-Turner spectrometer (Acton Research, 0.5 m focal length), operated with a 150 gr/mm grating. A CCD camera (Roper Scientific) with a 1024×1024 silicon detector chip (SiTE, $26 \mu\text{m} \times 26 \mu\text{m}$) was used as detector. This enabled a “multiplexed” or “multichannel” monitoring of the absorption spectral features at each time step of the process under study. The combination of the $150 \text{ grooves mm}^{-1}$ grating with a slit width of $100 \mu\text{m}$, resulted in a spectral resolution of $FWHM = 1.3 \text{ nm}$.

The linear dispersion with this spectroscopic set up was $0.32 \text{ nm pixel}^{-1}$. This enabled a spectral window from roughly 300 nm to 600 nm to be measured in a single recording without changing the position of the grating (F7.3). Such window comprises the electronic absorption spectra (Chapter 4) of all molecular reactants and products involved in the reactions under study. The I_2 absorption was monitored in the $\text{B}^3\Pi(\text{O}_u^+) \leftarrow \text{X}^1\Sigma_g^+$ band system [127, 196, 197] between 500 nm and 600 nm. The O_3 absorption was monitored in the Hartley and Huggins bands [198, 199] around 260-320

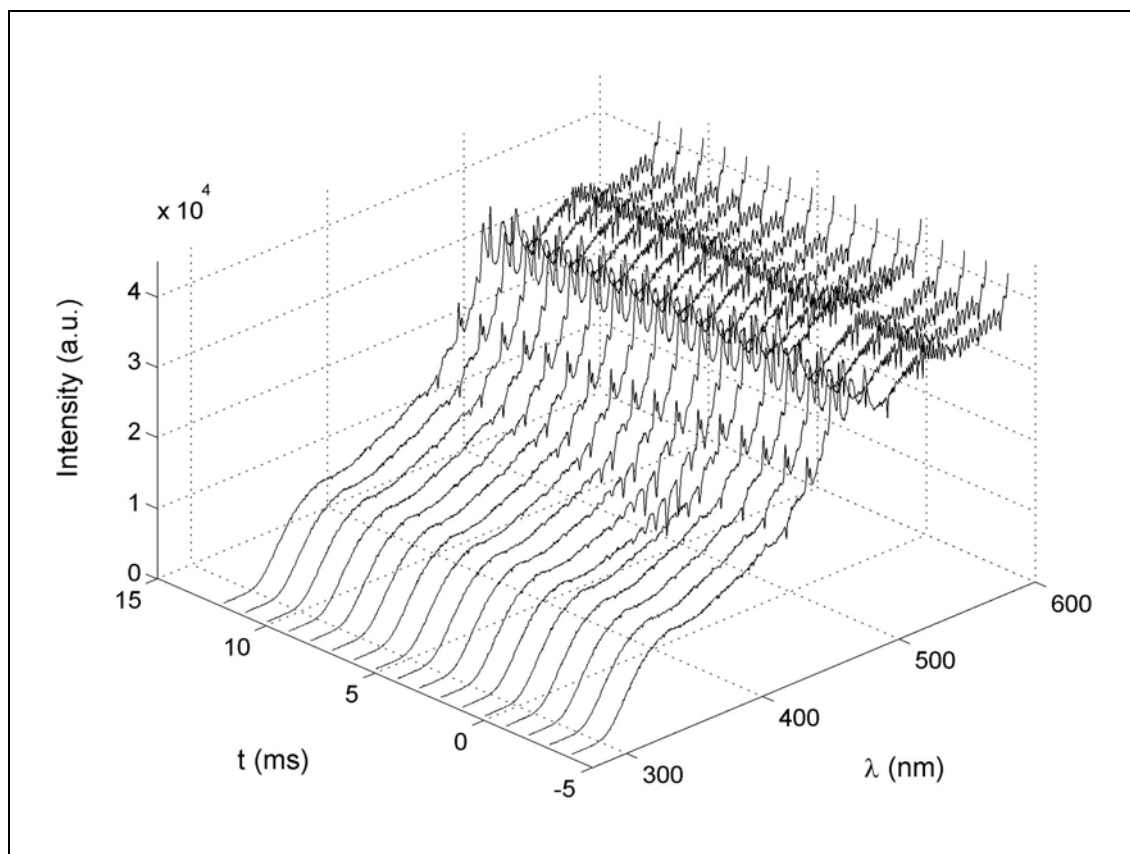
nm. IO was measured in the $A^2\Pi_{3/2} \leftarrow X^2\Pi_{3/2}$ subband system (Chapter 4, section 4.3) between 350 and 500 nm and OIO in the $A^2B_2 \leftarrow X^2B_1$ (Chapter 4, section 4.4) between 450 and 600 nm.



F7.3. Measurements performed in static mode. Panel F7.3.a shows raw data obtained with the CCD for both the Hg-Cd lamp (black line) and the Xe lamp (blue, red and green curves). The wavelengths of the lines used for the wavelength calibration of the pixel array of data are indicated in the graph. A second order polynomial was fitted to the wavelength versus pixel set of data. The difference between the blue curve (empty vessel) and the green and red curves (precursors inside the vessel) are caused by the selective absorption of radiation by O_3 and I_2 . Panel F7.3.b shows, in a calibrated wavelength axis, the optical density spectra obtained by processing the spectra in panel F7.3.a with the second term of E4.2. The application of the Beer-Lambert Law (third term of E4.2) enables to determine the concentration of these species. Wavelength calibration and determination of concentration of precursors were always performed previous to each series of kinetic measurements.

A brief summary of the main features of the CCD detection system in the context of chemical kinetic studies can be found in Rowley et al. [200]. The CCD was operated statically, recording individual spectra at pre-set times exactly like a photodiode array (PDA) (F7.3), and time resolved, recording sequences of full spectra at set time intervals (F7.4). In static mode the exposure time was defined by a shutter situated in front of the entrance slit of the spectrometer (see F7.1). Wavelength

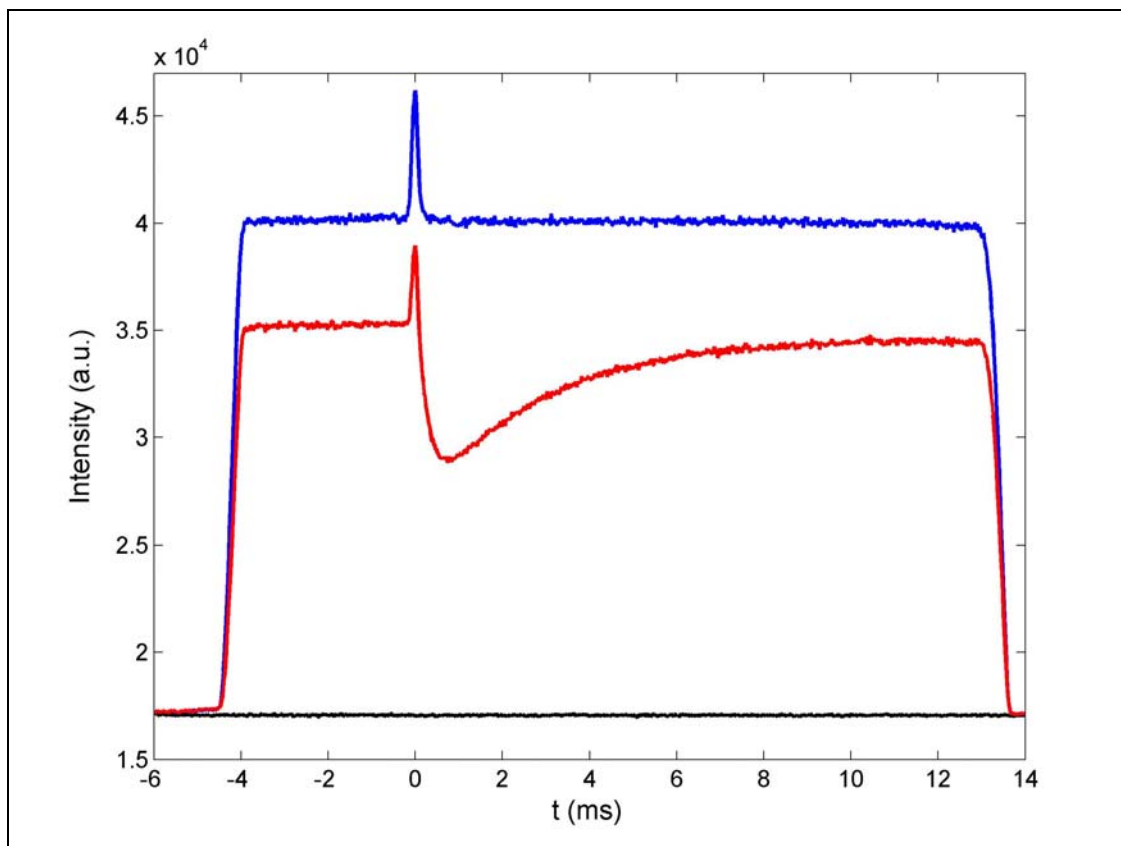
calibration was achieved by measuring spectra of a Hg-Cd line source (Osram Hg-Cd /10) in static mode and assigning to the observed lines the corresponding reference values (F7.3.a). The static mode was also used to measure absorption spectra of the chemical precursors I_2 and O_3 . This enabled to determine their concentrations previous to excitation by the flash tubes (F7.3.b), by applying the Beer-Lambert Law (E4.2).



F7.4. Time series of raw intensity spectra recorded with the CCD camera in kinetic mode. For clarity a reduced sequence of 17 spectra out of 1024 is shown. The time origin corresponds to the flash release. Absorption features belonging to IO are easily identifiable in the spectra recorded after the flash at about 400 nm. Each spectrum in this figure results from the sum of 100 spectra recorded in successive experiments under identical conditions.

In the time resolved mode the exposure time is not controlled by the electronic fast shutter (Oriel, 76995), whose fastest operating time (2 ms) would be too slow for the rapid reactions under study. Rather, the CCD is masked by a horizontal slit such that a few rows are exposed, and by shifting all rows stepwise from the exposed area down under the mask, time resolved recording of spectra is achieved. This is an important advantage with respect to a PDA, whose temporal sampling rate is severely limited by

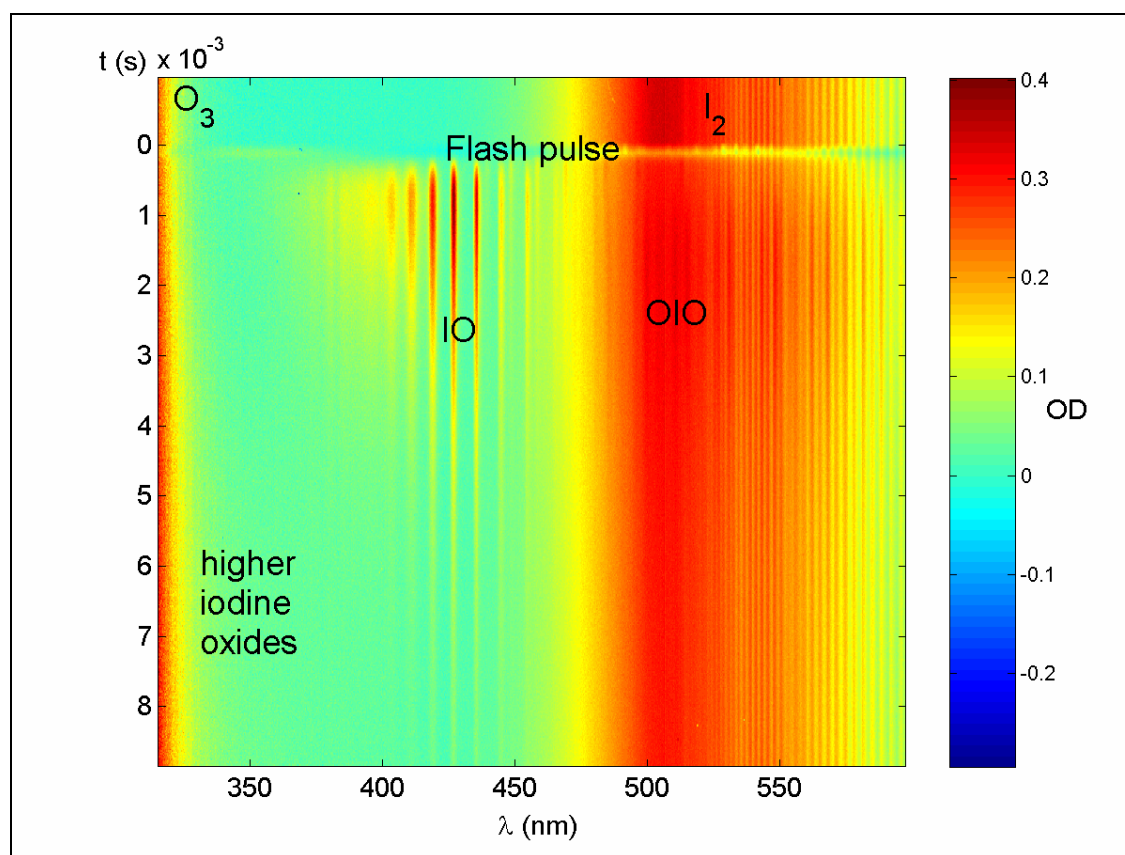
the readout and transfer time, typically in a time scale of milliseconds. In a CCD, the best sampling rate is equal to the fastest shifting rate, and the data is stored on chip and transferred to the PC at the end of the recording period. This transfer might take several seconds, but it does not limit any more the time resolution of the device.



F7.5. Example of raw data recorded for a single wavelength (427.2 nm) as a function of time. By flashing upon a gas mixture without chemical precursors (blue curve: $I_0(\lambda = 427.2 \text{ nm}, t)$) no difference between pre- and post-flash levels is observed. On the other hand, if a mixture containing the chemical precursors I_2 and O_3 is photolysed, the generation of the IO radical causes a decrease in the transmitted intensity at 427.2 nm (red curve: $I(\lambda = 427.2 \text{ nm}, t)$). The difference between the pre-flash levels of the red and the blue curves results from a drift of the lamp intensity between the reference and absorption measurements (see section 7.2.1). The left and right flanks of the curves correspond to the opening and closing of the shutter, which are defined by the timing of the delay generator and are synchronised to the release of the flash ($t=0$). The black curve is the background signal of the detection device.

In the CCD used in the present study roughly 5 rows are exposed and the fastest shifting time is 20 μs . By this mechanism each spectrum is exposed during 5 shift intervals and accumulates the temporal variation of signal during this time. This corresponds to a 5-point "moving-average" smoothing of the original temporal behaviour of optical density versus time. The shape of the smoothing kernel function is

not rectangular, but determined by the characteristic illumination function on the chip of the CCD. Without correction, the effective resolution in time is therefore limited to roughly $5 \times 20 \mu\text{s} = 100\mu\text{s}$. This is sufficient, if the observed structures change slowly in comparison to this effective temporal resolution. If faster processes had to be monitored, then a deconvolution in time would improve the effective temporal resolution slightly using a *measured* characteristic function of illumination. In the present work, however, all the relaxation processes were kept sufficiently slow to enable the direct usage of the time resolved signals recorded.



F7.6: Kinetic dataset: data points are plotted in a 2-dimensional grid of time versus wavelength, and the magnitude of the optical density is indicated by a colour code. Characteristic spectral features of O_3 and I_2 are visible in pre-flash and post-flash spectra, although a drop of I_2 absorbance due to photolysis can be appreciated. Immediately after the flash appear the IO bands and with a small delay those of OIO. The slight increase observed in the UV at longer reaction times is due to higher iodine oxides, and not to ozone, which remains constant as indicate a DOAS analysis of the Huggins bands.

Each kinetic data recording consists of a two dimensional array of intensities plotted on a grid of time steps versus detector pixels (wavelength) (F7.4). A delay

generator (Stanford Research Systems, DG535) was used to synchronise the flash photolysis to the time resolved measurement of molecular absorptions. The delay generator fixed the duration of the data recording and the position of the flash with respect to the beginning and the end of the measurement. The time interval covered by the measurement always comprised the photolysis flash itself and the subsequent relaxation reactions, as well as an interval before the flash (see F7.4 and F7.5). In order to improve the signal to noise ratio a large number of measurements recorded successively under identical conditions were averaged (typically 100).

Background measurements were obtained using the same procedure as in the recording of absorption datasets, but with the shutter in front of the spectrometer closed. By subtraction of this background signal from the measured intensities the effects of the detector characteristics and the dark current are corrected, yielding a data set of intensities $I(\lambda, t)$. The reference spectra, $I_0(\lambda, t)$, were obtained with the same procedure, but flashing mixtures of only N_2 and O_2 (F7.5). Any optical deformation within the vessel, by the mirror mounts, or the optical windows are thus identical in $I(\lambda, t)$ and $I_0(\lambda, t)$. This procedure also results in the removal of the majority of the scattered light coming from the flash and interfering with the analysis light (peaks in F7.5 at $t=0$).

The optical density (OD) arrays were obtained by using the first equality of equation E4.2:

$$A(\lambda, t) = \ln\left(\frac{I_0(\lambda, t)}{I(\lambda, t)}\right) \quad (\text{E7.1})$$

Figure F7.6 shows an OD array obtained by applying the procedure explained above. The calibration of the OD temporal behaviours to concentration was achieved by applying the second equality of equation E4.2 as follows:

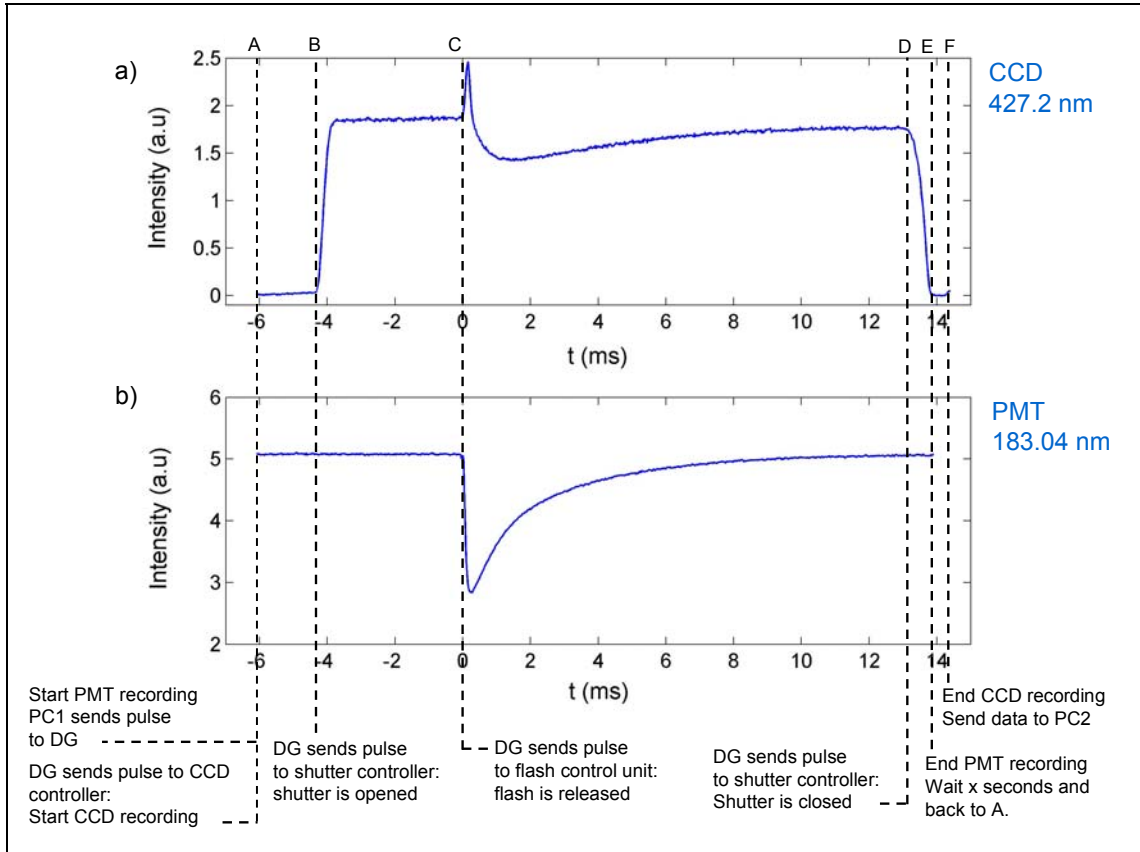
$$[\mathbf{R}](t) = \frac{a_{\mathbf{R}}(\lambda_0, t)}{L \sigma_{\mathbf{R}}(\lambda_0)} \quad (\text{E7.2})$$

where $[R](t)$, $a_R(\lambda_0, t)$ and $\sigma_R(\lambda_0)$ are respectively the concentration versus time curve, the OD temporal behaviour and the absorption cross section at the wavelength λ_0 of the species R, and L is the path length. In order to apply E7.2, the OD versus time curves for each “pure” molecular absorption, $a_R(\lambda_0, t)$, have to be retrieved first from the OD arrays $A(\lambda, t)$. A novel application of multivariate analysis techniques to such retrieval is explained in Chapters 7 and 8 of this thesis.

7.1.2.2. Atomic resonance absorption spectroscopy (ARAS).

An iodine electrodeless discharge lamp (EDL) [201] was used as light source for atomic resonance absorption spectroscopy. The measurements were carried out along a short path cross axis (5.5 cm), in order to compensate for the significantly larger absorption cross section of I atoms, compared to the molecular absorption cross sections. The cross probing axis of the reaction vessel was added by Spietz [120, 124] to the original design [32] in order to enable this type of synchronised MTRMAS and ARAS experiments.

After having traversed the reaction vessel the analysis light was focused onto the entrance slit of a Czerny-Turner spectrometer (Acton Research, 0.25 m focal length), operated with a 1200 grooves mm^{-1} holographic grating. With this grating it was possible to resolve the $I(^2[2]_{5/2}) \rightarrow I(^2P_{3/2})$ emission line at 183.038 nm (configurations: $5p^4(^3P_2)6s \rightarrow 5p^5$) [27] from neighbouring lines. A PMT (Hamamatsu, R955) was used as detection device. The detection of the emission line required to purge with N_2 in order to remove O_2 from the optical path, because O_2 absorbs strongly in this spectral region ($9 \leftarrow 0$ Schumann-Runge band, $\sigma(183.038 \text{ nm}) \approx 8 \times 10^{-21} \text{ cm}^2 \text{ molecule}^{-1}$ [30]). A decrease of the intensity of the 183.038 nm line transmitted through the cross axis is observed when ground state $I(^2P_{3/2})$ atoms are released by photodissociation of molecular iodine inside the vessel (F7.7.a). This is caused by the $I(^2[2]_{5/2}) \leftarrow I(^2P_{3/2})$ resonant absorption transition.



F7.7. Synchronisation of MTRMAS and ARAS. Panel F7.7.a: raw MTRMAS data for a single wavelength channel, like the red curve in F7.5. Panel F7.7.b: raw ARAS data. The $I(^2[2]_{5/2}) \leftarrow I(^2P_{3/2})$ resonant absorption transition causes a decrease of the intensity of the 183.038 nm line transmitted through the vessel. This enables to monitor the evolution of $I(^2P_{3/2})$ inside the reaction vessel. The PMT controller, governed by PC1 (see F7.1), acts as master: it starts the acquisition of data (A), gives the control to the delay generator within the recording period (A-D) and establishes a delay between consecutive measurements (E). This delay must be long enough to enable the complete transfer of data from the CCD chip to PC2 (F), and a 3-fold renewal of the gas mixture inside the reaction vessel.

The conversion of relative absorption curves for iodine atoms to concentration was achieved by calculating the relative difference between integrated emission and absorption Doppler and Voigt line profiles:

$$Q = \frac{I_0 - I}{I_0} = \frac{\int_{line} \Phi_0(\nu) d\nu - \int_{line} \Phi_0(\nu) \cdot \exp(-k(\nu) \cdot L) d\nu}{\int_{line} \Phi_0(\nu) d\nu} \quad (\text{E7.3})$$

were Q is the relative absorption, $\Phi_0(\nu)$ represents the emission Doppler profile and $k(\nu)$ designates the absorption Voigt profile. A relationship between the experimentally accessible relative absorption and the absorber concentration $[I]$ can be obtained by

substituting the explicit expression of the line profiles into equation E7.3 and using a series expansion ([120, 124] and references therein):

$$Q(t) = \sum_{n=1}^{\infty} C_n (\ell \sigma_I [I](t))^n \quad (\text{E7.4})$$

where ℓ is the path length of the cross axis of the vessel (0.055 m), σ_I is the absorption cross section of $I(^2P_{3/2})$ at 183.038 nm, $[I](t)$ is the concentration of iodine atoms. The coefficients C_n are given by:

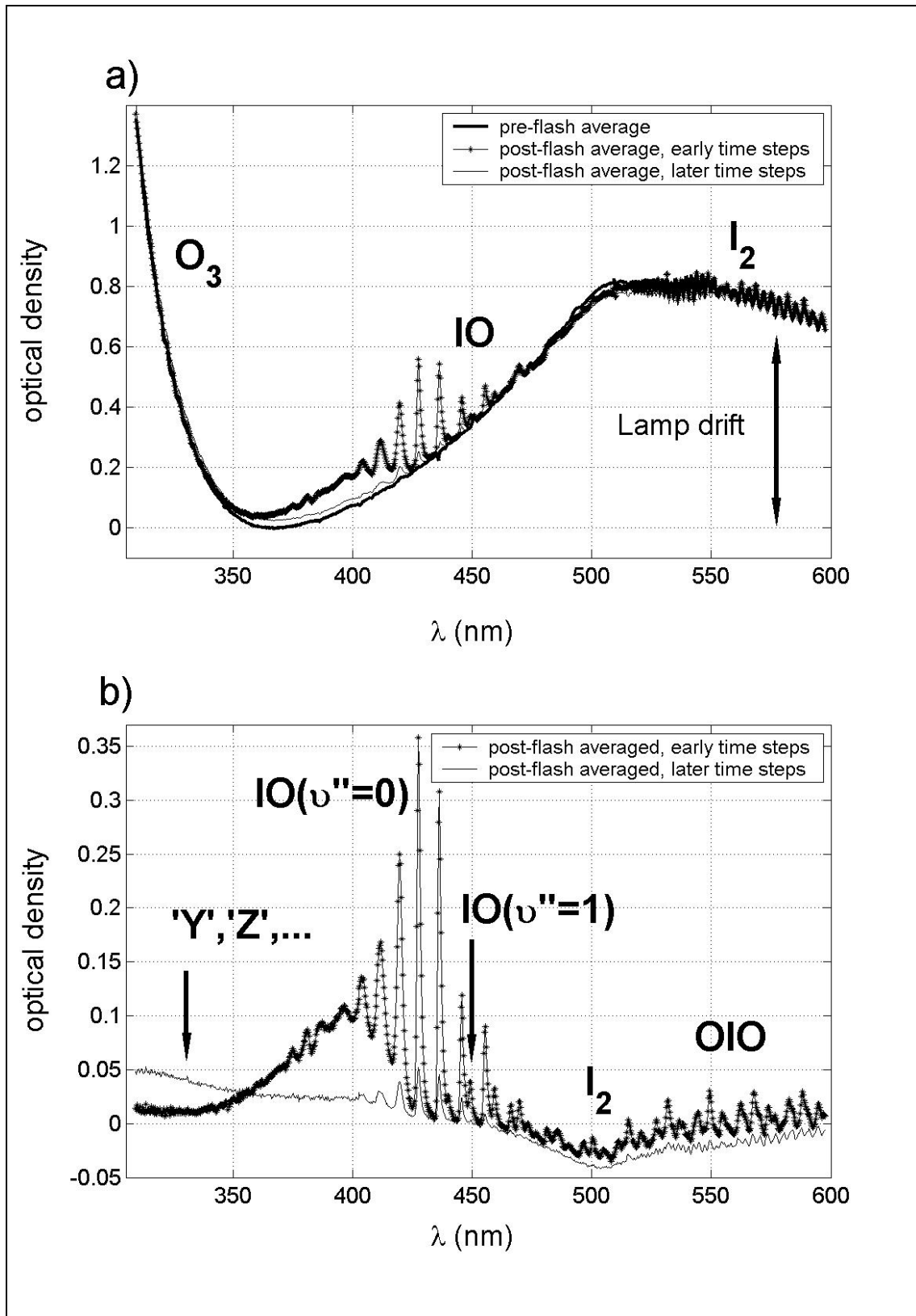
$$C_n = \frac{\int_{line} \Phi_0(\nu) \tilde{k}(\nu) d\nu}{\int_{line} \Phi_0(\nu) d\nu} \quad (\text{E7.5})$$

where $\tilde{k}(\nu)$ is a normalized Voigt profile. In order to calculate $[I](t)$, it is necessary to determine the appropriate order of truncation of the series and to find the real roots ($\ell \sigma_I [I](t)$) of the resulting polynomial.

Further details of the ARAS experimental set-up and data analysis can also be found in Spietz et al. [120, 124] and references therein.

7.2. Characterisation

The first problem tackled within the present work was the characterisation of the experimental set up. In order to reduce the uncertainties in the kinetic analysis it was necessary to quantify the influence in the concentrations of secondary processes like diffusion or inhomogeneous generation of radicals along the reaction vessel. If such quantification is not possible, it is necessary at least to estimate their contribution to the propagated uncertainties.



F7.8. Lamp drift correction of the kinetic datasets: pre-flash averaged spectral profile is subtracted from each spectral profile of the data recording. In F7.8.a the pre-flash spectrum and two spectra at different time steps are shown. After correction (F7.8.a), spectral features corresponding to different species can be better recognised. 'Y' and 'Z' refer to broad band UV absorbers, most likely higher iodine oxides.

7.2.1. Lamp drift

The pre-processing of the experimental data includes the elimination of spurious changes in OD caused by light source drift between $I(\lambda, t)$ and $I_0(\lambda, t)$ measurements (see F7.5). As no significant drift occurs within a single measurement (~ 20 ms) long term drift effects are corrected by subtracting from each dataset its own averaged pre-flash spectral profile. As a consequence, I_2 and O_3 temporal behaviours become relative to the initial concentrations. The pre-flash absolute absorption cross sections can be determined previously in static mode, or can be extracted from a pre-flash averaged profile (F7.8.a) by fitting the differential structure to reference I_2 and O_3 spectra. For I_2 the effect of low resolution must be carefully taken into account [127].

7.2.2. Coarse resolution and binning

A major draw back of the use of a coarse spectral resolution is the well known broadening of narrow spectral features as a result of low spectral resolution. In addition, integration of intensity on the CCD pixels also affects the observed optical density. For the absorption cross section of IO in the $4\leftarrow 0$ band ($\sigma_{IO}(4\leftarrow 0)$), Spietz et al. [122, 124] observed a clear dependence on the spectral resolution of the measured peak absorption cross section and its wavelength position. In order to take into account these effects, Spietz et al. derived an analytical relationship between $\sigma_{IO}(\lambda)$ obtained for low resolution/coarse binning experimental settings and $\sigma_{IO}(\lambda)$ obtained in high resolution/fine binning measurements. Using this relationship, a method to obtain the best approximation to the real peak OD of a vibronic-rotational absorption band from low resolved and coarsely binned measurements was developed and applied to the IO case. This method is called Multichannel Integrated Absorption Spectroscopy (MIntAS). It can be understood as an operation inverse to convolution, which does not require knowledge of the instrumental line shape, but relative reference spectra measured at a resolution such that the band shapes are not influenced by the instrument

function. These spectra, e.g. the spectrum of IO shown in F7.2, were measured with the same set-up by using a 1200 grooves mm^{-1} grating and 75 μm slit width ($FWHM = 0.12$ nm). In order to obtain concentration versus time curves free of instrumental effects, MIntAS has been applied to the OD versus time curves measured in this work (see Chapter 9).

7.2.3. Diffusion and wall losses

In the experiments performed for this study, the velocity of the gas mixture through the reaction vessel was about 0.4 m s^{-1} . Under these conditions, the distance travelled by a single particle due to the global motion of the gas on the time scale of the reactions (less than 30 ms) is negligible. As the vessel is temperature stabilised, no gradients are expected. Further, typical Reynolds numbers are below 600, enabling the assumption of a laminar flow. Under these circumstances, the movement of the molecules on the time scale of the experiment is dominated by Brownian motion.

The analysis volume (the inner volume of the reaction vessel illuminated with the analysis light) is separated from the walls by a distance of approximately 1 cm. To estimate the influence of diffusion towards an absorbing wall in the concentration of the relevant species contained in the analysis volume, it can be assumed that the distribution of molecular or atomic species inside the vessel can be described by the continuum diffusion equation with axial symmetry:

$$\frac{\partial n(r,t)}{\partial t} = D \left(\frac{\partial^2 n(r,t)}{\partial r^2} + \frac{1}{r} \frac{\partial n(r,t)}{\partial r} \right) \quad (\text{E7.6})$$

where r is the distance of the molecule or atom to the symmetry axis of the vessel, n is the concentration and D the diffusion coefficient of the species. Diffusion coefficients are estimated by using the Chapman-Enskog expression for binary diffusion under the assumption of hard spheres [50], considering a collisional diameter of 0.3 nm for O_2 and N_2 . Under the conditions of the experiments performed within the present work, typical

diffusion coefficients in a mixture of O₂ and N₂ for atomic iodine were in the range between 13 and 0.3 cm²s⁻¹ for the range of pressures considered in this work (10-400 hPa).

The initial and boundary conditions are:

$$n(r,0) = n_0 \quad (\text{E7.7})$$

$$n(R,t) = 0 \quad (\text{E7.8})$$

where R is the radius of the reaction vessel.

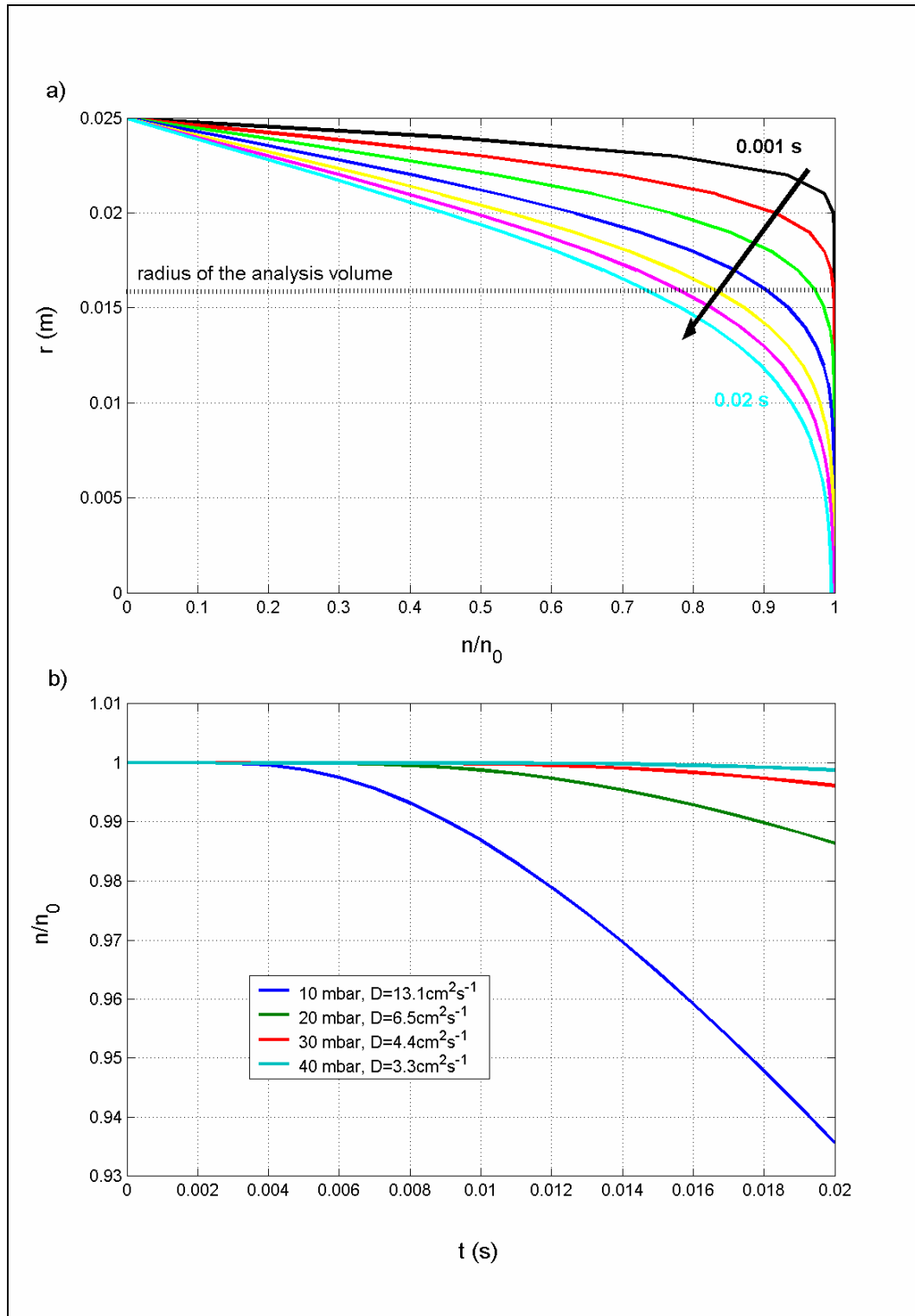
The initial condition given by E7.7 assumes that the molecules of the species are initially homogeneously distributed in space with concentration n_0 . The boundary condition given by E7.8 expresses the assumption that the wall acts as a perfect absorber, that is, the molecules adhere at every collision. The solution to the continuity equation (E7.6) with these conditions is [202]:

$$n(r,t) = \int_0^R n_0 \sum_{i=1}^{\infty} \frac{2\zeta}{(R J_1(\mu_n))^2} J_0(\mu_n r/R) J_0(\mu_n \zeta/R) e^{-D\mu_n^2 t/R^2} d\zeta \quad (\text{E7.9})$$

where μ_n are the positive zeros of the Bessel function, $J_0(\mu_n) = 0$.

The radial distribution of I atoms (the iodine species with larger diffusion coefficient) diffusing towards a perfectly absorbing wall in a stationary and non reactive mixture of N₂ and O₂ at 10 hPa is shown in F7.9.a As diffusion coefficients of IO and OIO are very close to those of I, the curves in F7.9 are also close to the corresponding curves for these species, while for larger molecules diffusion coefficients are smaller (in case of I₂O₂ by a factor of 3). The analysis volume is an inner cylinder of radius 1.75 cm, and therefore the relevant radii are those smaller than this value. The time scale of the experiments is smaller than ~ 25 ms. F7.9.b shows the averaged effect of diffusion inside the analysis volume as a function of time, for pressures between 10 and 40 hPa. Diffusion starts to have a measurable effect for diffusion coefficients larger than about 10 cm²s⁻¹ ($P < 10$ hPa). This is equivalent to the effect of a pseudo first order decay with a time constant

of $\tau = 300$ ms. However, this is a very small effect compared to the speed of the chemical sinks for I, IO and OIO.



F7.9. Solutions of the diffusion equation with axial symmetry for I atoms diffusing in a stationary mixture of N_2 and O_2 towards a perfect absorbing wall ($R = 2.5$ cm). Chapman-Enskog diffusion coefficients of iodine were calculated in the range of pressures considered in this study (T7.1). a) Evolution of the concentration profile at 10 hPa. b) Average effect for an inner volume with $r = 1.75$ cm

7.2.4. Homogeneity in the cross axis

I₂/O₂ photolysis experiments, i.e. without O₃, have been performed to check that the change in the concentration of iodine molecules due to photolysis ($\Delta[I_2]$) along the longitudinal axis corresponds to the concentration of iodine atoms ($[I]$) measured along the transversal axis. Under the hypothesis of homogeneous distribution of species, a relationship $2\Delta[I_2] = [I]$ was expected. However, the concentration of iodine observed was systematically smaller. This difference could result from screening of the flash by the joints of the transversal axis, which could reduce the photolysis of molecular iodine in this part of the vessel (a cylinder of 0.055 m diameter and 0.055 m length). As a consequence of the slow diffusion, no homogeneous mixing is achieved within the duration of the experiment. However, the large uncertainty of the oscillator strength (or the absorption cross section) of the 183.038 nm transition of I(²P_{3/2}) [120] could also explain such deviation.

In order to avoid the propagation of this uncertainty to the iodine atom concentration, an empirical calibration of the curves has been preferred. In the experiments performed without ozone, $\Delta[I_2]$ and Q were simultaneously measured. The observed relative absorption Q has been fitted to the calculated Q obtained by substituting $[I]=2\Delta[I_2]$ in equation E7.4. The free parameter is a scaling factor, which accounts for inhomogeneous distribution of I-atoms and/or error in the iodine atom absorption cross section. The combined uncertainty of the scaling factor and the raw data yielded a total estimated uncertainty at the maximum of the iodine atom concentration curves of ~8%. The detection limit was approximately 10^{11} atoms cm⁻³.

An inhomogeneous distribution of iodine atoms along the reaction vessel would have a non linear impact on that part of the $[I]$ curves, which depend on $[IO]^2$ as a consequence of iodine atom recycling through R7.3.b and R7.3.c. In order to quantify this effect, the difference between the spectroscopic and the empirical calibration has

been used. As stated above, such difference might result from a combination of the uncertainty in the oscillator strength and inhomogeneous distribution of iodine atoms. Assuming a worst case scenario, where the whole difference results from inhomogeneous distribution, and performing a series of kinetic simulations for the range of conditions considered in this work and using the largest iodine atom yield from reaction (2) reported in the literature [174], this effect has been found to be $\sim 6\%$ at the point where the peak IO concentration is reached. This results in an uncertainty of about 15% in the section of the I-atom curves affected by R7.3.b and R7.3.c.

7.2.5. Photolysis of species by the analysis light

Photolysis and activation due to the analysis lamp has been estimated to be negligible. Photolysis/activation rates can be calculated by using the expression:

$$k = \int_{\lambda} J(\lambda)\sigma(\lambda)\Phi(\lambda)d\lambda \quad (\text{E7.10})$$

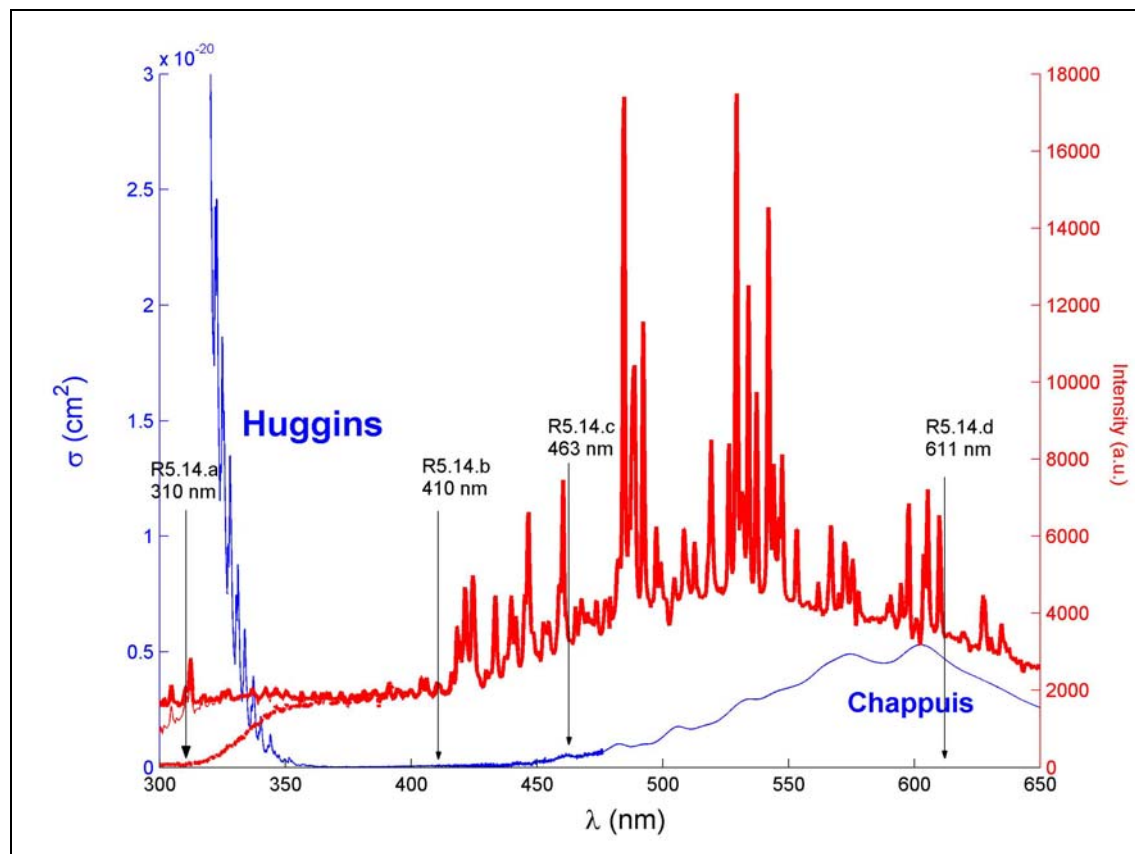
where $J(\lambda)$ is the incoming actinic flux from the Xe lamp, $\sigma(\lambda)$ the absorption cross sections of the species considered and $\Phi(\lambda)$ the quantum yield for dissociation/activation. Estimated photolysis rates related to the analysis lamp for I_2 and IO (assuming a unity photolysis quantum yield, see below) are $\sim 4 \times 10^{-3} \text{ s}^{-1}$ for IO and $\sim 4 \times 10^{-4} \text{ s}^{-1}$ for I_2 .

7.2.6. Photolysis of ozone

The glass filters establish a cut-off at 320 nm (31250 cm^{-1}), thus suppressing ozone photolysis (see 5.4.1.2) above this wavenumber, where the ozone spectrum presents substantial absorption cross sections. F7.10 shows that the absorption of ozone is important from about 320 nm to shorter wavelengths (thin red line), while by using glass filters no radiation of less than 320 nm reaches the reaction vessel (dotted red line).

The absorption cross sections of O_3 from 320 nm to the red are very low: in the Huggins band ($\sigma(320 \text{ nm}) \sim 3 \times 10^{-20} \text{ cm}^2 \text{ molecule}^{-1}$) and in the maximum of the Chappuis band ($\sigma(605 \text{ nm}) \sim 5.3 \times 10^{-21} \text{ cm}^2 \text{ molecule}^{-1}$). However, the photolysis of

ozone in the Huggins and Chappuis bands could still release a significant amount of ground state oxygen atoms. Note that $O(^1D)$ is collisionally quenched in an excess of N_2 and O_2 in less than $0.2 \mu\text{s}$ at 10 hPa [28].



F7.10. FTS Spectrum of O_3 [194] (blue curve) compared to different flash profiles (red curves). The threshold for R5.14.a is on the left hand side of the cut-off. Absorption of radiation by O_3 is significant only in this region (compare thin and thick red lines). Therefore the suppression of channel R5.14.a amounts to the practical suppression of O_3 photolysis. The dotted red line corresponds to the filtered flash profile.

Kinetic experiments without I_2 have been undertaken in order to estimate the extent of ozone photolysis. The signal to noise ratio was significantly improved by averaging up to 1000 flashes. However, no change in the O_3 curve has been observed by photolysing O_3/O_2 mixtures with glass filters over the detection limit. In these experiments the detection limit for ozone was of 0.05% of the initial O_3 concentration, implying an upper limit for the concentration of $O(^3P)$ released of 10^{12} molecule cm^{-3} .

A crude estimation of the photolysis rate of O_3 has been obtained by comparing the averaged absorption cross sections of I_2 and O_3 in the spectral interval between 320 and 750 nm. Assuming unity quantum yields, using averaged absorption cross sections and

taking into account that the integrated actinic flux is the same for both molecules, the dissociation rate of O₃ can be estimated as being in the same ratio to that of I₂ than the respective averaged absorption cross sections:

$$\frac{k_{\text{O}_3}}{k_{\text{I}_2}} = \frac{\int_{\lambda} J(\lambda) \sigma_{\text{O}_3}(\lambda) \Phi_{\text{O}_3}(\lambda) d\lambda}{\int_{\lambda} J(\lambda) \sigma_{\text{I}_2}(\lambda) \Phi_{\text{I}_2}(\lambda) d\lambda} \approx \frac{\bar{\sigma}_{\text{O}_3} \int_{\lambda} J(\lambda) d\lambda}{\bar{\sigma}_{\text{I}_2} \int_{\lambda} J(\lambda) d\lambda} = \frac{\bar{\sigma}_{\text{O}_3}}{\bar{\sigma}_{\text{I}_2}} \quad (\text{E7.11})$$

According to E7.7, about 0.02% of the initial amount of ozone is photolysed, producing $\Delta[\text{O}] = \Delta[\text{O}_2] \sim 5 \times 10^{11} \text{ atom cm}^{-3}$. This estimation is in agreement with the upper limit determined experimentally.

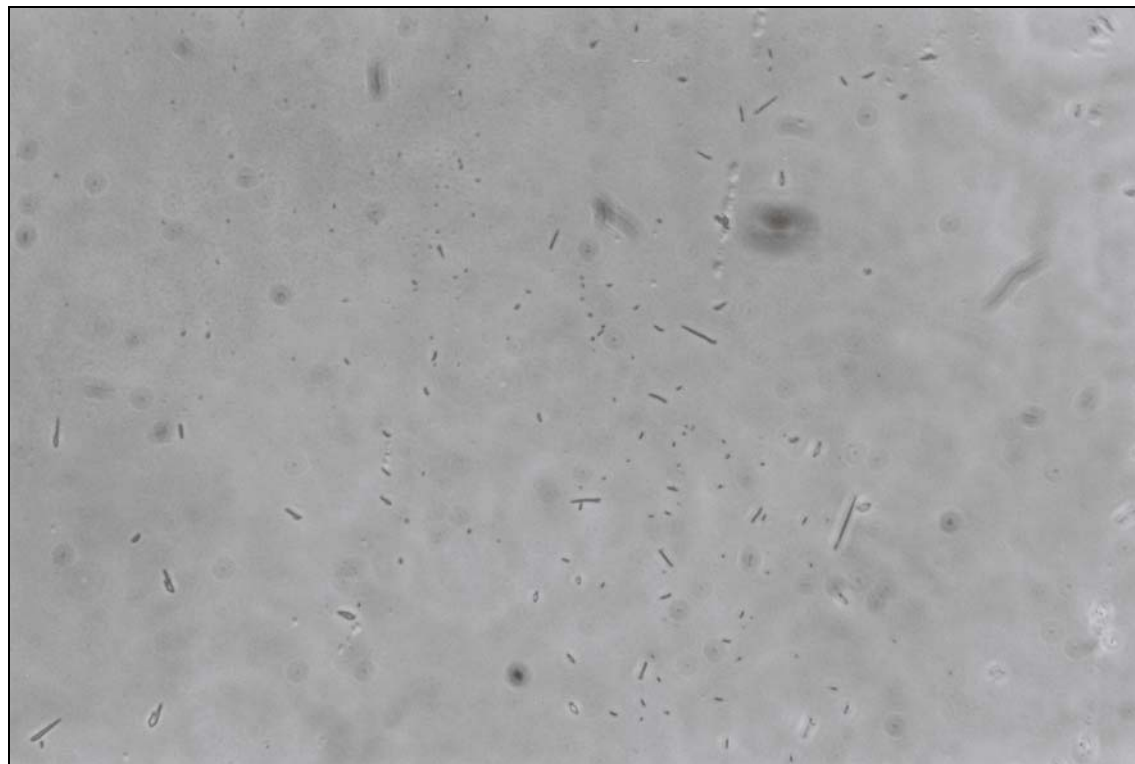
It can be concluded that the use of the filters reduces the ozone photolysis drastically, such that $[\text{O}^3\text{P}]_0$ is only 3%-10% of the maximum concentration of IO (see T7.1). The generation of such an small amount of free ground state oxygen atoms might have an influence on $[\text{IO}]_0$, but is irrelevant for the study of the removal of IO and OIO, because O^3P is instantaneously consumed in an excess of I₂ (R7.1).

Photolysis experiments of O₃/O₂ mixtures without glass indicate that the fraction O₃ photolysed was about 5%. In these experiments, an instantaneous production of IO via R7.1 was observed. However, the series of experiments carried out without glass filters have not been considered in the kinetic analysis as a result of the potentially complex chemistry associated to O₂(a¹Δ_g), apart from the fact that the use of two sources of IO makes difficult the analysis of the measured concentration curves and that the uncertainty of the photolysis rate is rather large.

7.3. Experimental conditions

Eight series of experiments were performed (T7.1). No attempt was made to search for optimal mixtures appropriate for simple kinetic modelling of the IO temporal behaviour. Rather, the concentrations of precursors were set to maximise the amount of radicals produced in order to achieve an excellent signal to noise ratio for spectroscopic

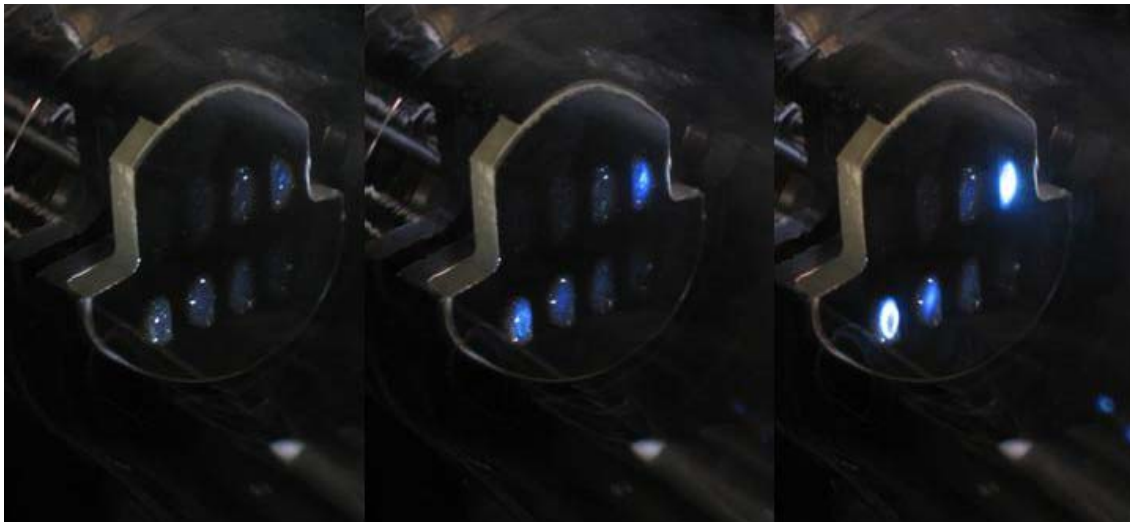
studies. This turned out to be an advantage as well in the study of the secondary gas phase chemistry. On the other hand, this resulted in the well known formation of solid phase products [80, 165, 170].



F7.11. Microscopic photography ($75\ \mu\text{m} \times 112.5\ \mu\text{m}$) of a deposit formed on the walls of the reaction vessel after a series of experiments. The characteristic needle-shaped crystals with a length of several μm are easily identifiable.

After several kinetic experiments deposits on the mirrors and walls of the reaction vessel were observed. Figure F7.11 shows a 320-fold augmented photography of a sample of a deposit formed inside the reaction vessel. Characteristic needle shaped crystal can be distinguished. Based on the IR spectrum, colour, crystal shape and hygroscopic behaviour (F7.12), Himmelmann [149] identified this solid as being I_2O_5 . These deposits were responsible for a progressive decrease of the transmitted intensity in the UV region, impeding the measurement of the ozone concentration and the monitoring of other unidentified gas phase UV absorbers. In addition, transient absorptions were observed by flashing upon the empty vessel after long series of kinetic experiments, indicating that part of these deposits were released from the walls or from the mirrors, and that they could

interfere chemically and spectroscopically. To minimise these interferences, it was necessary to clean regularly the vessel and the optics and to keep the series of experiments as short as possible.



F7.12. After a set of experiments, the room air was allowed to enter the reaction vessel. This series of pictures shows the evolution of a deposit formed on the main mirror of the White Optic arrangement. The mirror acquires a white colour as a result of the hygroscopicity of the deposit.

The range of pressures used ensured rapid thermalisation of a potential non-equilibrium population of the vibrational levels of ground state I_2 generated by the flash, as well as the quenching of metastable iodine by O_2 (R5.12) previous to observation (less than $4 \mu s$ at 4 hPa of O_2). $O(^1D)$ produced by photolysis of IO or O_3 , if any, would be collisionally quenched in an excess of N_2 and O_2 in less than $0.2 \mu s$ at 10 hPa. A summary of the kinetic experiments at different conditions recorded for this study can be found in T7.1.

For series 1-5, the initial amounts of I_2 and O_3 in the vessel were kept constant, while the pressure was varied by increasing the flow of the diluting gas, according to the following expression:

$$\frac{f_{N_2+I_2} + f_{O_2+O_3} + f_{buffer}}{f_{N_2+I_2} + f_{O_2+O_3}} = \frac{P_2}{P_1} \Rightarrow f_{buffer} = (f_{N_2+I_2} + f_{O_2+O_3}) \left[\frac{P_2}{P_1} - 1 \right] \quad (E7.7)$$

where $f_{N_2+I_2}$ and $f_{O_2+O_3}$ are respectively the flows of nitrogen and oxygen carrying I_2

and O_3 , and f_{buffer} is the flow of buffer gas added in order to increase the pressure in the vessel while maintaining the concentration of precursors constant. Constancy of $[I_2]_0$ and $[O_3]_0$ at different pressures was verified to be generally better than 10%. Table T7.2 shows the flows employed in series 1-5. The “reference” mixture (that with the lowest pressure and $f_{\text{buffer}} = 0$) determined the residence time in the reaction vessel (see T7.2), which is given by the expression:

$$\frac{P^0 f_{FC}}{T^0} = \frac{Pf}{T} = \frac{PV}{Tt} \Rightarrow t = \frac{P}{P^0} \frac{T^0}{T} \frac{f_{FC}}{V} \quad (\text{E7.8})$$

where P^0 and T^0 are the standard pressure and temperature, f_{FC} the flow through the flow controller, P , T , V and f are respectively the pressure, temperature, volume and flow in the reaction vessel, and is t the residence time of the gas mixture in the reaction vessel. In order to remove secondary products, which might interfere in the reactions under study, it is convenient to flush the vessel up to three times before the next flash. This implied a delay of 15 seconds between consecutive flashes (T7.2). This time was also enough to enable the transfer of data from the CCD chip to PC2 (~ 7 s). For each experiment 100 flashes were averaged. Thus, each dataset required 25 minutes to be completed.

Series 1 and 2 were performed between 60 and 360 hPa. They were carried out in order to check the effect of blocking the photolytic pulse below 320 nm with glass filters. Series 3-5 were run with glass filters between 40 and 400 hPa. Series 3 and 5 were performed with N_2 and series 4 with O_2 as diluting gas. Series 4 was run in order to check a potential influence of the third body on the chemistry under study. Series 5 was intended to check possible dependencies on the initial $[O_3]$. In this series, the concentration of ozone was reduced by reducing the O_2 pressure in the silent discharge from 1000 hPa to 650 hPa.

T7.1: Experimental conditions of kinetic datasets (concentrations in molecule cm^{-3})

Series	N_{exp}^a	Class Filter	P_{vessel}^b (mb)	$[N_2]^b \times 10^{18}$	$[O_2]^b \times 10^{18}$	$[O_3]^{10^c} \times 10^{15}$	$[I_2]^{10^c} \times 10^{13}$	$[I]_{\text{max}}^d \times 10^{13}$	$[IO]_{\text{max}}^e \times 10^{12}$	Use ^f
1	6	No	60-360	0.07-5	1.3-1.4	2	0.7	0.25	0.25	met
2	10	Yes	60-360	0.07-5	1.3-1.4	2	0.7	0.25	0.25	Met
3	7	Yes	40-400	0.5-10	0.4-1	2	5.4	1	7.5-8	met-kin
4	6	Yes	100-400	0	2-10	2	5.4	1	6.5-7	met-kin
5	8	Yes	40-400	0.5-10	0.4-1	9.2	4.4	1	5	met-kin
6	11	Yes	10-40	0	0.2-1	0.5-2	1-6	3-9	2-8	met-kin
7	6	Yes	10-40	0.1-0.6	0.1-0.4	0.5-2	0.3-1	2-6	1.5-5.5	met-kin
8	4	Yes	40	0.5	0.4	2	5.4	1	8	Met

^{a)}Experiments without O_3 were also carried out before each series in order to determine the photolysis rate of I_2 . ^{b)} N_2 and O_2 concentrations have been estimated from the total pressure in the vessel and the readout of the flow controllers. Uncertainty $\sim 10\%$. ^{c)} I_2 and O_3 concentrations are obtained either by measuring pure I_2 and O_3 spectra in static mode previous to the kinetic series and/or by using optical densities recorded in kinetic mode after the photolysis flash. Error estimates ($< 15\%$) take into account random noise of the detection device as well as for drifts of $[I_2]$ and $[O_3]$ along the experiment and lamp drifts. ^{d)} The uncertainties ($< 10\%$) are obtained as the standard error estimation of the least squares fits applied in the re-calibration. ^{e)} Calculated using σ_{10} reported in [125]. The uncertainties ($< 10\%$) consider the uncertainty in σ_{10} , as well as the estimated error of the time behaviour of IO. ^{f)} Indicates the use given to the datasets: met = methodology (separation of absorbers), kin = kinetics (study of the I_2/O_3 photochemical system).

In addition, two further series of experiments (6 and 7) were conducted at lower pressures (10 - 40 hPa). In this case the pressure was changed by varying the aperture of the valve in the exhaust of the vessel. Thus, the initial concentrations of the precursors changed within the series, although their relative concentration was kept constant. Series 7 was run to investigate the potential effect of varying the initial I_2 concentration. To this end, the flow of N_2 through the iodine trap was reduced from 750 to 250 sccm.

The settings of the detection apparatus (exposure time and delays), which determined the length of each measurement, were selected taking into account the effect of changing pressures and concentrations on the temporal behaviours of the species of interest. An important requirement was to register the complete temporal behaviour of OIO on each dataset. Therefore, the exposure time of the CCD was set accordingly to register the major part of the OIO in the data recordings. For all series of experiments undertaken with fixed $[I_2]$ and $[O_3]$ the duration of the experiments was about 10 ms, and a nominal exposure time of 20 μ s was appropriated to obtain data recordings of this duration. For the series of experiments with variable precursor concentrations, the duration of the experiments changed between 10 and 30 ms and the length of the data recordings is 20 ms (nominal exposure time of 40 μ s).

T7.2. Flows employed to change the pressure in the vessel without changing the concentrations of precursors.

Series	$f_{N_2+I_2}$ (sccm)	$f_{O_2+O_3}$ (sccm)	P (hPa)	f_{buffer} (sccm)	Residence time (s)
1-2	100	2000	60	0	4.7
			100	1400	
			150	3150	
			200	4900	
			250	6650	
			356	10360	
3-5	750	500	40	0	5.2
			100	1875	
			150	3438	
			200	5000	
			250	6563	
			300	8125	
			350	9688	
400	11250				

All data recordings were used for spectroscopic analysis (Chapter 8). However, only experiments with glass filters (series 3-8) have been considered for kinetic analysis, as a result of the difficulties found to evaluate accurately the photolysis rate of O₃ signalled in the previous section. From these, 38 datasets fulfilled the requirements of full coverage of absorbers and high signal to noise ratio.

Part IV

RESULTS AND DISCUSSION

8. PRINCIPAL AND INDEPENDENT COMPONENTS ANALYSIS OF MTRMAS DATA

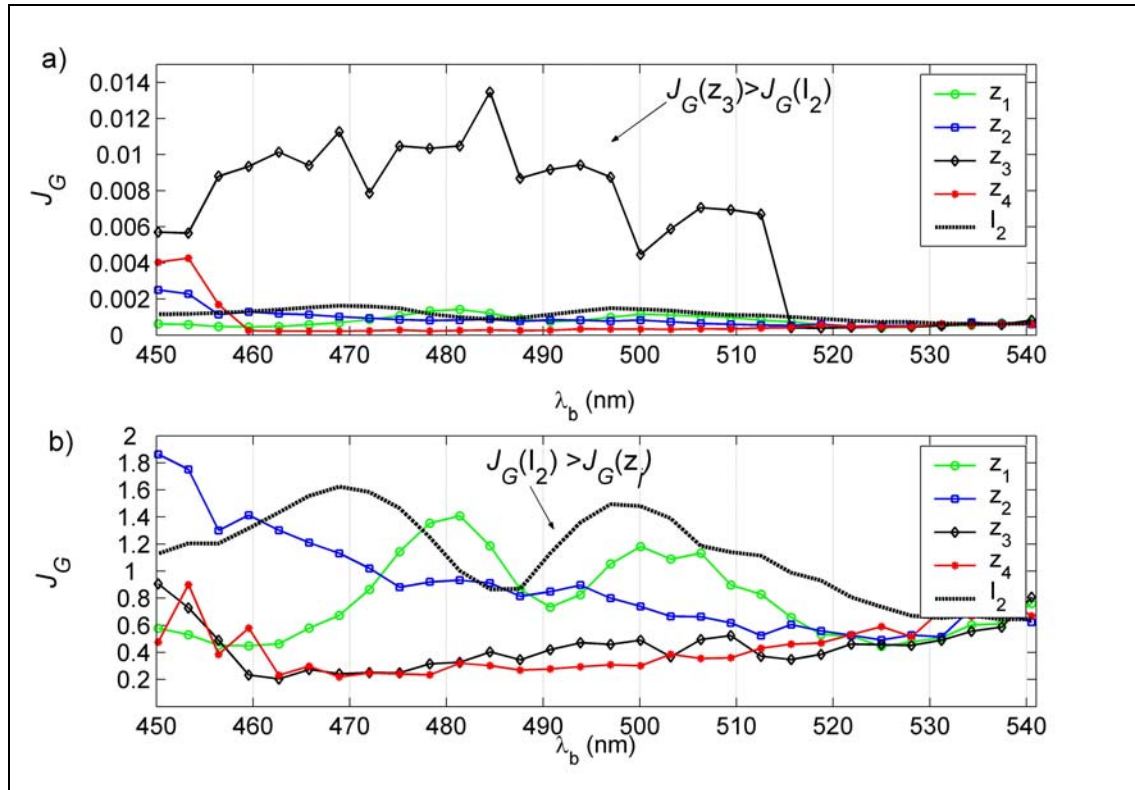
8.1. Introduction

The objective of this chapter is to describe a novel application of a recently developed source separation method known as Independent Components Analysis. It is shown how this mathematical tool (Chapter 6) can be used to scan the MTRMAS data recordings searching for different absorbers, and to obtain the separated optical density temporal behaviours of individual absorbers. These are a necessary condition for any subsequent study which tackles the task of obtaining absolute absorption cross-sections and reaction rates. A main by-product is the obtaining of separate qualitative spectra of the different absorbers observed.

8.2. Statistical properties of kinetic test datasets

Absorbance spectra are non stationary signals in the statistical sense, that is, they do not keep their statistical properties when the origin of the sampling variable λ is translated. Molecular species absorb in limited spectral windows, and even in these windows, spectral features like broad band continua introduce strong non-stationarity (see Chapter 4). This implies that the conditions for source separation with PCA and ICA can be satisfied by some samples and not satisfied by others. PCs and/or ICs obtained in a given spectral window are rigorously speaking sample PCs and ICs.

A simple and intuitive argument is used to check to which extent the data recordings fulfil the requirements of source independence in a given window. It makes use of the Central Limit Theorem, which states that the linear combination of statistically independent sources produces mixtures whose pdfs are closer to a gaussian distribution than the pdfs of the sources.



F8.1. Example of how a non-gaussianity index J_G can aid in the recognition of an appropriate spectral window. A set of different spectral ranges containing features of the known absorber (I_2) is considered. The red end is fixed and the UV border is subsequently shifted towards the red end to obtain spectral windows with decreasing size. In each of these windows PCA is applied to the original mixtures $\mathbf{a}(\lambda)$, retaining 4 components $z_j(\lambda)$. J_G is calculated for each $z_j(\lambda)$ ($j = 1, \dots, 4$) and for the I_2 reference spectrum, and is plotted against position in the wavelength axis of the UV border of the corresponding window. The comparison of the values of J_G for $z_j(\lambda)$ and the I_2 reference spectrum indicates which spectral windows could be appropriate for a separation. In the panel 7.1.a the complete time series of spectra $\mathbf{a}(\lambda)$ is considered and the necessary condition is not fulfilled in most of the windows. In the panel 8.1.b the first 50 time steps were not considered, and the necessary condition is fulfilled in many more windows.

For each MTRMAS dataset a full ranged reference I_2 spectrum –that is, a source– measured at the same conditions of concentration and temperature is available. Therefore it is possible to estimate its deviation from gaussianity and compare it to that of the mixtures. To this end, a non-gaussianity index J_G can be used. In the present work, J_G has been obtained by substituting $G(x) = \log(\cosh(x))$ in EA.3 (see the recommendations about the practical choice of the measuring function G in [188]). It is a necessary condition for source independence that the mixtures are closer to gaussianity than the I_2 spectrum. Note that ICA works with PCA pre-processed

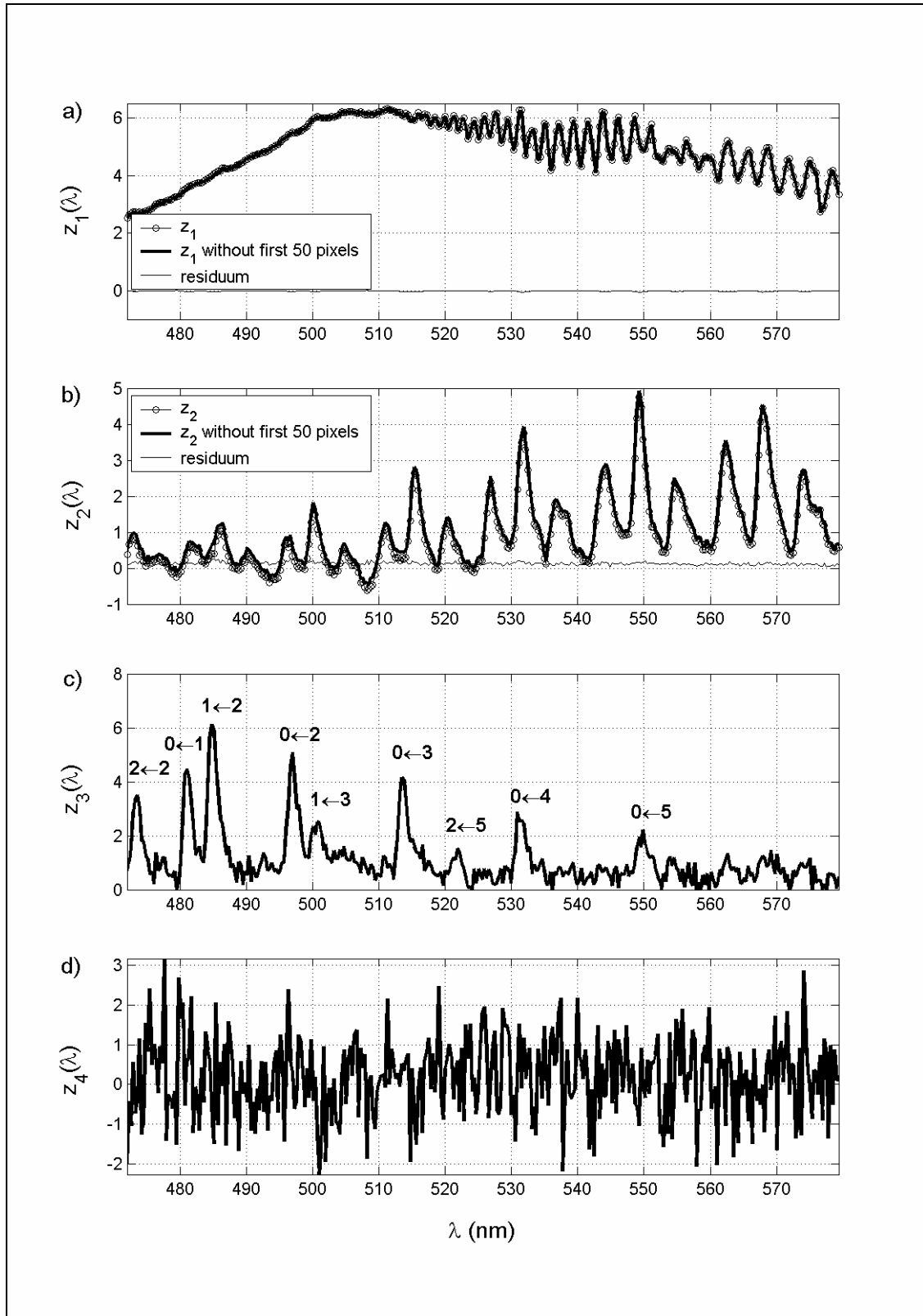
mixtures, and therefore the non-gaussianity index J_G of I_2 must be compared to that of the PCs $z_j(\lambda), j = 1 \dots n$.

F8.1 shows how J_G can help to recognise appropriate spectral windows. A MTRMAS dataset obtained at a pressure of 40 hPa in the vessel (therefore vibrationally excited $IO(X^2P_{3/2})$ with $v'' > 1$ can be observed) is analysed to illustrate the procedure. A set of different spectral ranges containing features of the known absorber (I_2) is considered. First, the red side λ_r is fixed and the blue border is placed at a given λ_b and afterwards subsequently shifted towards the red side in regular steps to obtain spectral windows with decreasing size. On each of them PCA is applied to the original mixtures $\mathbf{a}(\lambda)$, retaining 4 components $z_j(\lambda)$ (low variance components must be also inspected to check that they contain only noise). The deviation from gaussianity J_G is calculated for each $z_j(\lambda)$ ($j = 1, \dots, 4$) and for the I_2 reference spectrum, and plotted against position on the wavelength axis of the UV border of the corresponding window. The analysis can be repeated moving the red side λ_r to another value.

F8.1a shows an example in which λ_r was fixed at 579,7 nm and different windows were obtained by shifting λ_b to the red in successive steps of 3.1 nm, starting with $\lambda_b = 450.1$ nm. First, it is important to remark that the informational content of each principal component varies as the window is reduced, affecting the values of $J_G(z_j)$. Principal component $z_4(\lambda)$ contains relevant spectral features up to a window with $\lambda_b = 462.7$ nm, and becomes just noise when the last transition from $IO(X^2P_{3/2}, v''=0)$ (the $0 \leftarrow 0$ band at 466.1 nm) is excluded ($J_G(z_4)$ takes a low almost constant value from this point). In the following windows (F8.2 shows an example with $\lambda_b = 472.0$ nm) only three absorbers remain, which appear mixed in the first three principal components. The comparison with the band assignments in the $A^2P_{3/2} \rightarrow X^2P_{3/2}$ emission system of IO (Durie et al. [135]) and the absence of dominating features of OIO or I_2 indicate that

component $z_3(\lambda)$ in F8.2 is an almost pure spectrum of $\text{IO}(X^2P_{3/2}, \nu'' > 0)$ (from here on ground state $\text{IO}(X^2P_{3/2})$ will be denoted as IO and vibrationally excited $\text{IO}(X^2P_{3/2})$ as $\text{IO}(\nu'' > 0)$). This component contains spectral features relevant in terms of variance up to the window with $\lambda_b = 512.5$ nm. In the next window the $0 \leftarrow 3$ (513.1 nm) band is excluded and the absorption of $\text{IO}(\nu'' > 0)$ becomes negligible according to the PCA variance criterion. From this point on only features of two absorbers (I_2 and OIO) are detected and $z_3(\lambda)$ is just noise ($J_G(z_3)$ is closer to zero).

In F8.1.a it is remarkable that both $J_G(z_1)$ and $J_G(z_2)$ are below $J_G(\sigma_{I_2})$ in many spectral windows, while the component with major content of $\text{IO}(\nu'' > 0)$ (z_3) is impeding the fulfilment of the necessary condition up to $\lambda_b = 512.5$ nm. In F8.1b the non gaussianity analysis is repeated with the same limits and step, but excluding the first 50 time steps immediately after the flash (about 1ms). In this case, the component having lower variance ($z_4(\lambda)$) is noise from the first window ($\lambda_b = 450.1$ nm), because $\text{IO}(\nu'' > 0)$ can not be detected. Excited IO with $\nu'' > 0$ is quickly de-activated by quenching and with the chemical conditions of the system its absorbance can only be detected in the 50 time steps, which is not considered in this second analysis. In F8.1b $z_3(\lambda)$ behaves approximately like $z_4(\lambda)$ in the first case, being reduced to noise at about 459.5 nm, when the $0 \leftarrow 0$ band of IO is excluded. $J_G(z_1)$ and $J_G(z_2)$ are also below $J_G(\sigma_{I_2})$ in many spectral windows. In fact $J_G(z_1)$ and $J_G(z_2)$ take similar values in both analysis. Now the necessary condition $J_G(I_2) > J_G(z_j) \forall j$ is satisfied in many more windows than in the previous case. The reason is that the mixture less gaussian than the known source between $\lambda_b = 450.1$ nm and $\lambda_b = 512.5$ nm is no longer present.



F8.2. PCA results for a window between 472.0 nm and 579.7 nm. PCs obtained with and without $\text{IO}(\nu''>0)$ in the dataset are compared in order to estimate the residual IO contained in the first two components. Principal Component 3 can be considered as a good first approximation to the true $\text{IO}(\nu''>0)$ spectrum.

It is interesting to analyse what happens in the window with $\lambda_b = 472.0$ nm. For a given j ($j = 1, 2$), the difference of $J_G(z_j)$ is slight (changes of 0.2% and 8% respectively). In fact, if the respective $z_j(\lambda)$ ($j = 1, 2$) obtained in both analysis with $\lambda_b = 472.0$ nm are subtracted, the residual $IO(\nu'' > 0)$ absorbance present in the PCs of the first analysis is very small. The amount of $IO(\nu'' > 0)$ remaining absorbance in $z_2(\lambda)$ goes from 16% on the $1 \leftarrow 2$ band at 484.8 nm (maximum of $IO(\nu'' > 0)$) to 0.8% on the $0 \leftarrow 5$ band at 549 nm (maximum of OIO). In $z_1(\lambda)$ the mixing of $IO(\nu'' > 0)$ is in any case less than 1%. This means that the mixing of $IO(\nu'' > 0)$ in the first two principal components is low. Thus, it is understandable why $z_3(\lambda)$ is less gaussian than any of the other mixtures. PCA has been successful in obtaining a close approximation to the source $IO(\nu'' > 0)$, and it does not make sense to consider it any longer as a mixture in the input of ICA for $\lambda_b = 472.0$ nm. The corresponding temporal behaviour takes reasonable non-negative values; it is free of OIO and I_2 contributions and it can be used as a first approximation to the true temporal behaviour. This issue will be discussed later on this work.

When two absorbers are known, or at least good approximations of their spectra are available, it also makes sense to analyse their correlation in different windows (uncorrelatedness is another *necessary* condition for source separation). In the present studies, an OIO spectrum obtained by taking differences of averages is also available, although it can be considered to be pure only from 472 nm to the red due to the overlap with IO bands. Fixing again λ_r , the correlation coefficient between the two spectra was calculated in spectral windows with different λ_b . For $\lambda_r = 579.7$ nm, the results suggest selecting a window around 520 nm, where the values of the correlation coefficient are closer to zero.

If there is no prior information about at least one of the overlapping spectra, the previous analysis can not be done, and therefore the search for appropriate windows is

somehow blind. In this case only a qualitative criterion about the shapes of the spectra and their corresponding pdfs in a given interval can help to find spectral windows suitable for separation. Such a qualitative criterion is based on the possibility of uncorrelatedness (orthogonality) given the guessed shape of the overlapped absorbers.

From this analysis it becomes clear that the test datasets do not generally fulfil the requirements summarised in section 6.3.2.1. Therefore, three different cases are considered in the following section: a spectral window where the requirements for source separation are not fulfilled (8.3.1), a spectral window where they are fulfilled (8.3.2) and a spectral window where they are approximately fulfilled (8.3.3).

8.3. Results

8.3.1. Model requirements not fulfilled

To check how ICA performs in a spectral window in which the necessary condition is not fulfilled, a broad spectral range containing features of the main absorbers involved is analysed. The same procedure shown in F8.1 was performed for this spectral range and it was checked that the non-gaussianity of the known I_2 spectrum was smaller than many of the mixtures z_j . Thus, mixtures of physical components are expected in the independent components extracted, and in this sense, the analysis can be considered inadequate, because it does not lead to a separation of *all* the absorbances. Nevertheless, it is worthwhile to do ICA in this range, because interesting information can be obtained from it, and even the extraction of this information can be optimised.

This full range treatment comprises most of the spectral range covered in the experiments summarised in T3.1. A spectral window of about 50 nm from the UV side is not included, because the signal to noise ratio is not optimal due to the low light source intensity in this region.

Instead of using as contrast functions log-densities of well known distributions, contrast functions based on numerically determined pdfs of the sources are considered to enhance the extraction of information. These pdfs are obtained using prior knowledge about the main spectra. A pdf of I_2 can be calculated directly from the histogram of a reference spectrum. In case of IO and OIO, their pdfs are computed using spectra out of a mixture with approximately stationary concentration of I_2 after the flash. Firstly, I_2 and other absorbers are removed with the classical method of calculating differences between different spectral profiles. Then, a guess of the pdf of IO is obtained with the smoothed histogram of the signal resulting from setting all values to zero from about 470 nm to the red. For OIO all values are set to zero from the blue border to about 470 nm, and the pdf is calculated in the same way⁶.

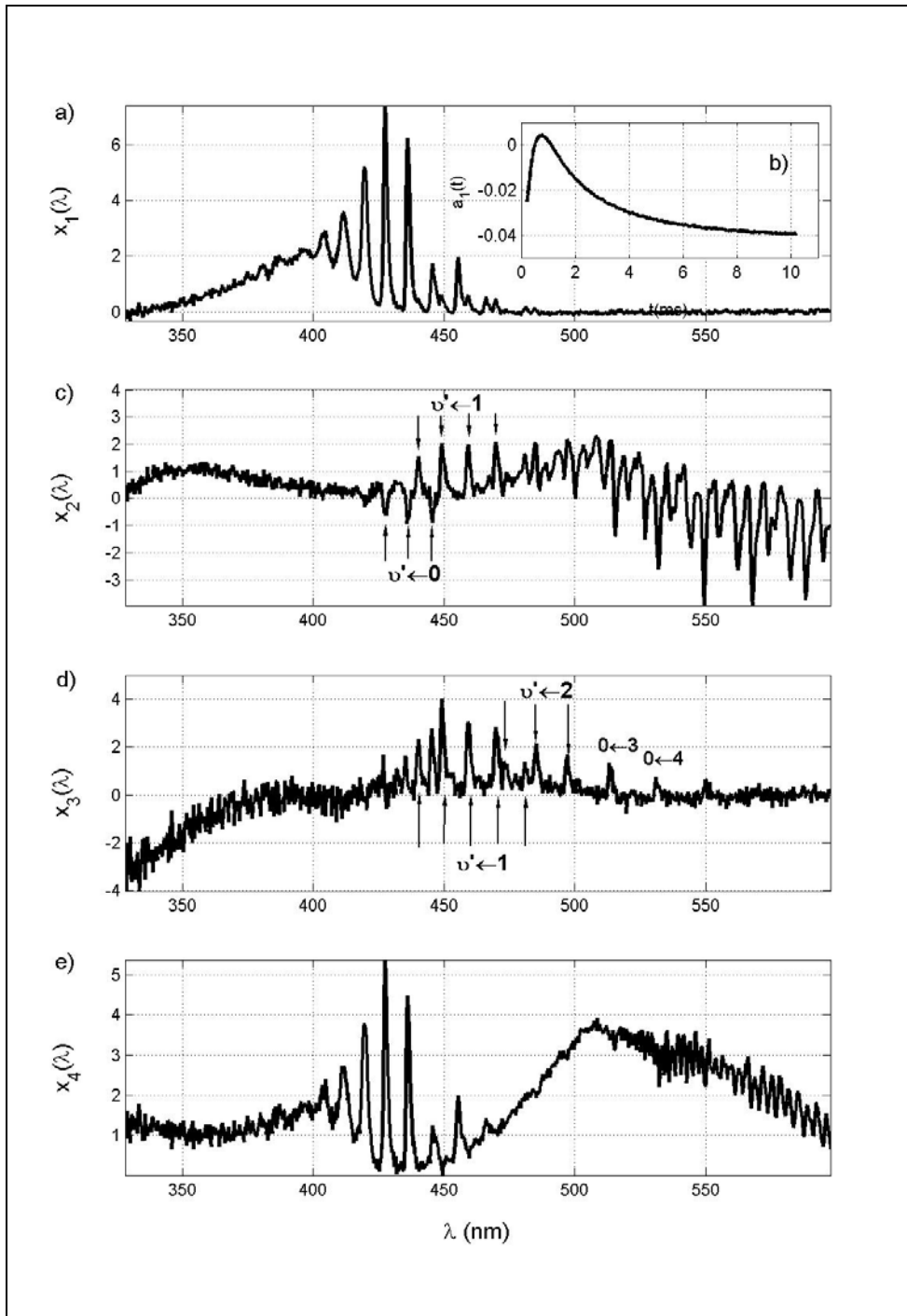
An example of ICA results between 328 nm and 600 nm is shown in F8.3. In pre-processing of the datasets, PCA found 4 components containing spectral features, explaining among them the 99.21% of the total variance in the dataset. Further PCs were inspected to check that they contain nothing but noise. The retained PCs were used as input for the noise-free ICA model. Instead of using for each component a standard non-linearity in the contrast function, respective estimates of the pdfs of the spectra of IO and OIO were used to build one step contrast functions. Then, the PCA/ICA algorithm was used. An approximation to the IO spectrum is achieved (F8.3.a) when IO is retrieved as first independent component. The spectra contained in a full window are not orthogonal, and therefore decorrelation (orthogonalisation) causes mixing between spectra in the remaining 3 components, even if cost functions based on guesses of the pdfs of further absorbers are used. Components 2, 3 and 4 show mixtures of the main absorbers present in the chemical system: IO, I_2 , OIO, and possibly higher order

⁶ ICA using guesses of the pdfs of the sources is equivalent to Maximum Likelihood Estimation (see [185,187]).

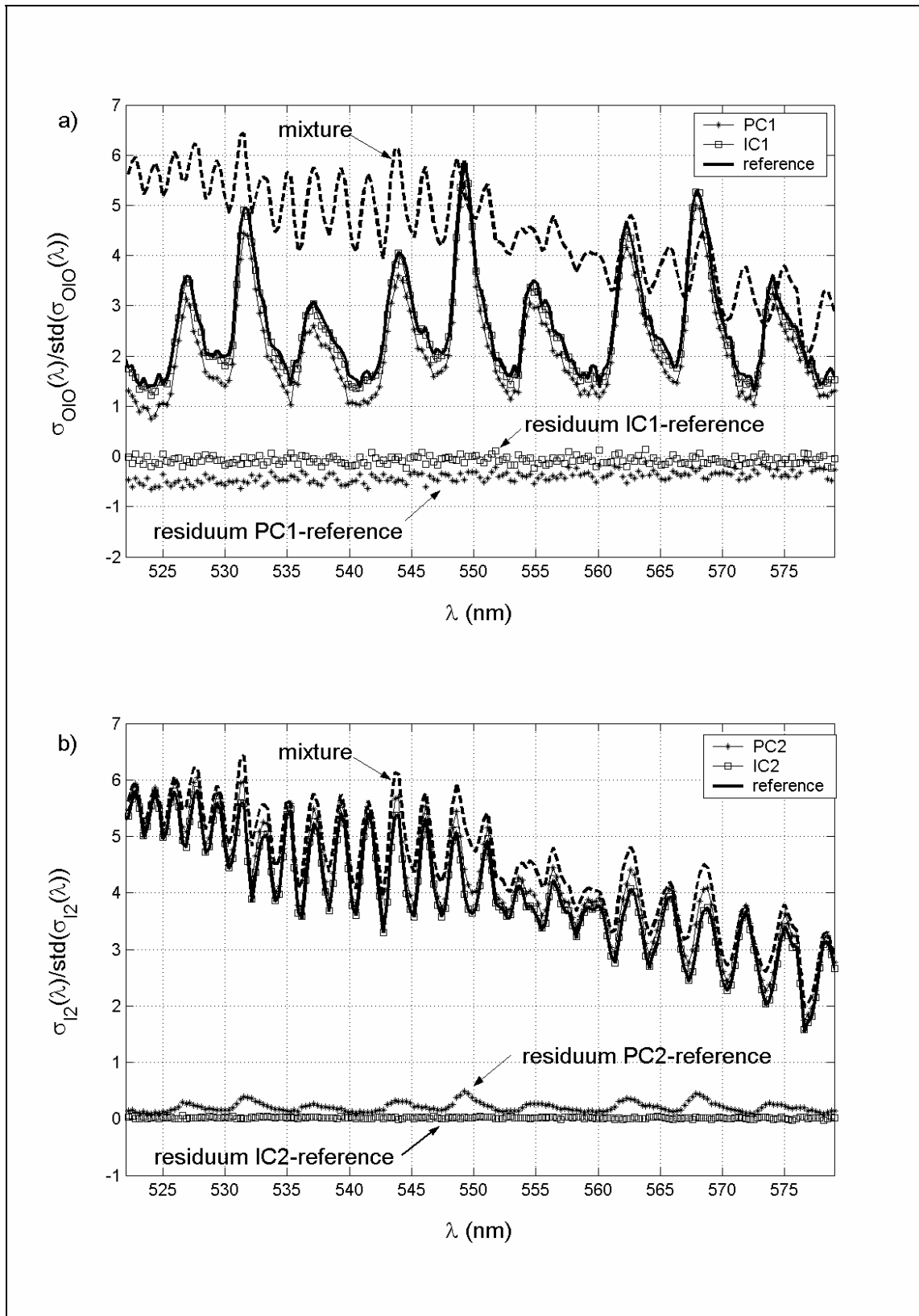
absorbers (UV side). The difference between IO and IO($\nu'' > 0$) is also noticeable. IO($\nu'' > 0$) bands appear in component 2 (F8.3.c) inverted with respect to IO bands, which proves that IO and IO($\nu'' > 0$) behave differently in time. Also the IO($\nu'' > 0$) bands are stronger than IO in component 3 (F8.3.d). It has been checked that all the peaks marked in component 3 really belong to excited IO absorption series (band assignments in [133]). The main advantage of using the log-density of the guessed pdf of the IO spectrum as cost function is the extraction of the IO spectrum (F8.3.a) as independent component. The information concerning different behaviour of IO and IO($\nu'' > 0$) can also be obtained when standard log-densities are considered.

Even though a reasonably well separated IO spectrum is obtained, the corresponding temporal behaviour (F8.3.b) reveals that using ICA without fulfilling the necessary conditions is inadequate in achieving separation of components. The temporal behaviour retrieved takes negative values and this, in terms of physics, does not make sense. As a consequence of the theory, if the physical sources are independent, the mixing matrix must give the correct temporal behaviours directly, without modification. It might be tempting to think that decentring can solve the negative shift in the temporal behaviour. But it has to be pointed out that decentring applies only to the sources, and not to the mixing matrix. It follows from this argument that the temporal behaviour shown in F8.3b can not be mathematically corrected. In spite of this strong argument, an empirical procedure was used in order to check the validity of the curve. The maximum absorption of IO at 427.3 nm (corrected for background absorbers) was taken directly from the raw data as the best approximation to the temporal behaviour of IO (this curve is plotted with a different scaling in F8.8b). If the shape of the ICA result were correct, only an additive constant and a multiplicative factor should be between this and the IO

temporal behaviour. A comparison of the two using LS clearly showed their disagreement and proved the incorrectness of the ICA temporal behaviour result.



F8.3. Results of ICA when a broad spectral range (340-600 nm) is considered. a) A numerical guess of the pdf of the IO spectrum is used to get in the first place a good approximation to it. IO and IO($v'' > 0$) bands are contained in this spectrum. b) Temporal behaviour corresponding to the first IC. It takes negative values, therefore it has no physical sense. The correct profile is plotted in F8.8.b. c)-d) Uncorrelatedness causes mixing of spectra in the following components. The different behaviour of IO and IO($v'' > 0$) in c) is detectable.



F8.4: a) ‘Raw’ profile of OD (‘mixture’) when [OIO] reaches its maximum, principal component (‘first guess’), independent component (‘source’) and reference spectrum of OIO between 521.9 nm and 579.4 nm. The respective differences between the PC and the IC and the reference spectrum are also plotted to show the improvement of the ICA solution with respect to the first guess provided by PCA. b) The same for I₂.

Nevertheless the spectrum of IO obtained as first IC is quite pure, especially in the blue side up to 433 nm, where it is well in agreement with a LS retrieved IO spectrum. On closer inspection weak mixing with other sources becomes apparent. Also –and reflecting the incorrect temporal behaviour– further IO contributions remain mixed in components 2 and 4 as a consequence of the physically unfulfilled uncorrelatedness constraint.

Note that the analysis of the complete spectral range is interesting in any case, even if the conditions for source separation with ICA are not fulfilled. Qualitative information about the system can be inferred from the components extracted, like the number of absorbers and differences in temporal behaviour, and therefore also assignments of bands.

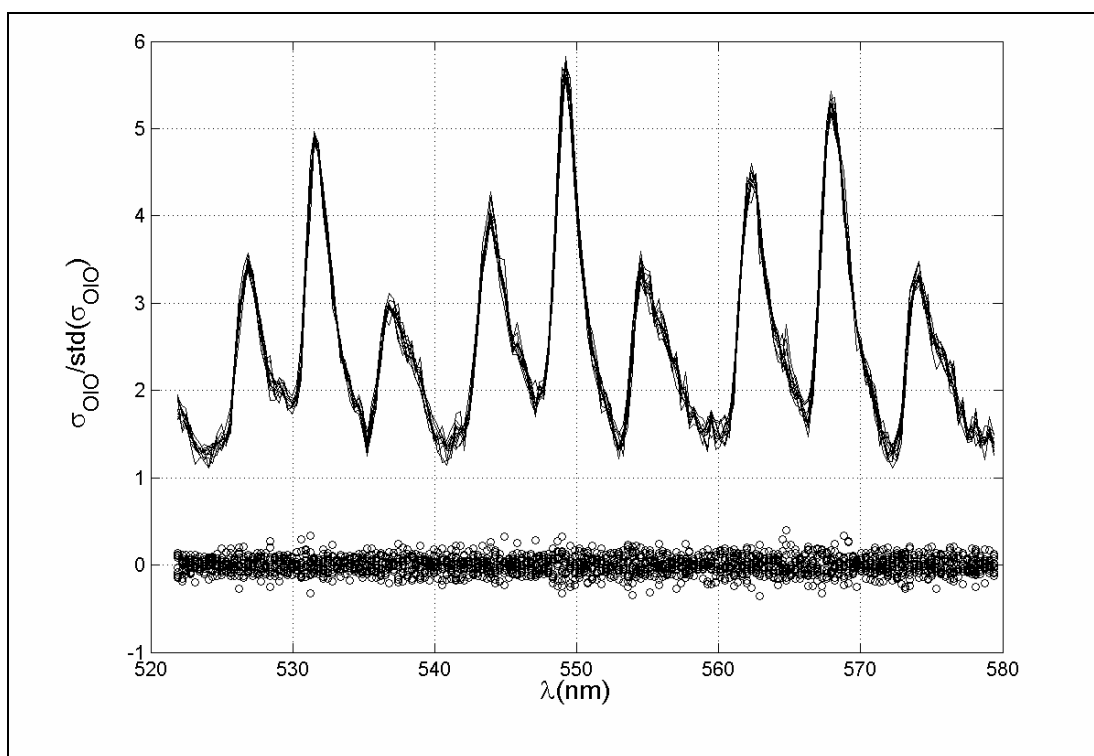
8.3.2. Model requirements fulfilled

After PCA pre-processing, ICA was applied over one of the spectral ranges suggested by the analysis of non-gaussianity and uncorrelatedness, and excellent results were achieved. Reference spectra obtained using conventional techniques were used to validate the results.

An example is shown in F8.4. ICs (separated spectral features of I₂ and OIO) extracted from the two first PCs in a window between $\lambda_b = 521.9$ nm and $\lambda_r = 579.4$ nm are shown, along with the PCs, the respective reference spectra and a mixture of spectra in the time step in which [OIO] reaches its maximum. The difference between the reference spectrum and the IC is compared to the analogous difference between the PC with major content of I₂ absorption and the same reference spectrum, to determine and emphasise the improvement of ICA with respect to PCA. It can be observed that spectral features remaining in the I₂ PC, which could be attributed to OIO, are

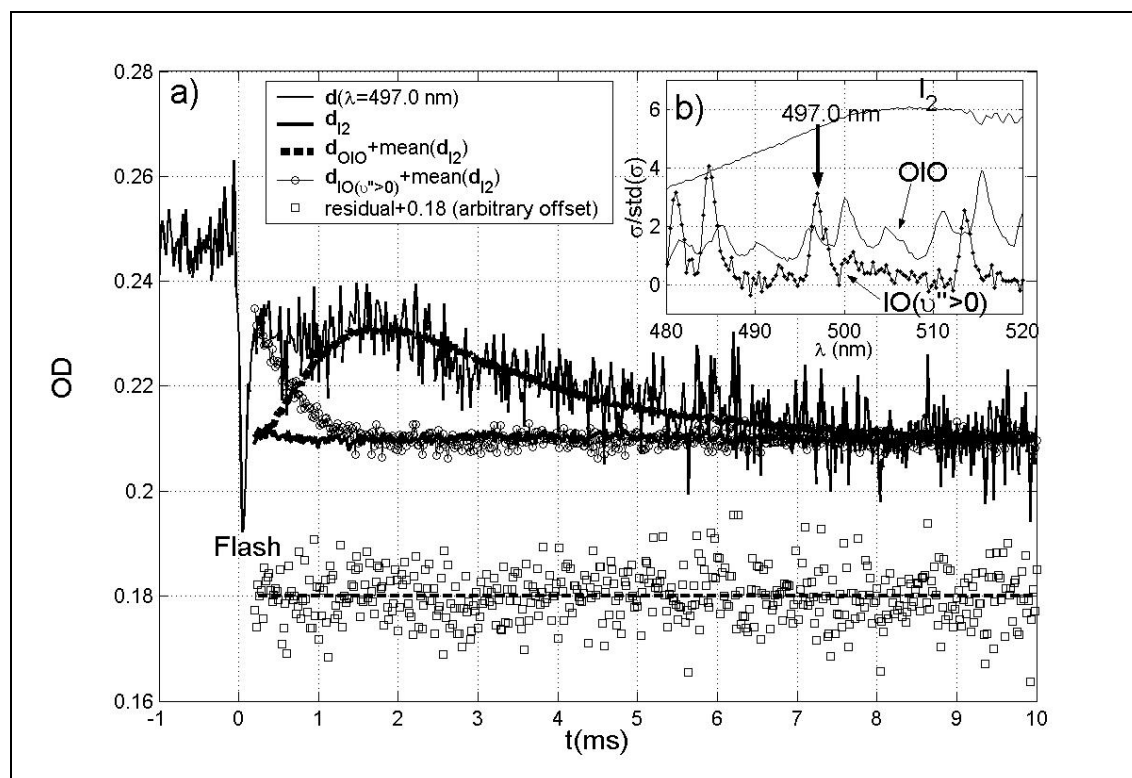
significantly reduced in the ICA result. Thus, PCA obtains a good first approximation, and ICA operates over it to improve the separation.

In order to quantify the quality of the PCA/ICA analysis, 20 datasets showing different temporal behaviours of the species involved were analysed. To obtain these datasets, the mixing ratio of precursors ($[I_2]/[O_3]$) was kept constant, and the differences in the chemistry were forced only by changing the pressure in the reaction vessel. F8.5 shows a set of 10 normalised decentred OIO spectra, each one extracted by PCA/ICA from one of these datasets in a spectral window between 521.9 nm and 579.4 nm, along with their corresponding residuals with respect to the averaged OIO profile. The reproducibility of the result is clear. No dependence on pressure was observed. The uncertainty on top of the $(5,1,0) \leftarrow (0,0,0)$ band of OIO at 549.1 nm can be estimated to be less than $\pm 2\%$.



F8.5: Set of 10 normalised and decentred OIO spectra separated using PCA/ICA between 521.9 nm and 579.4 nm from datasets obtained under different conditions, along with the residuals with respect to the averaged OIO profile. The spectra do not show dependence of the variation of the chemistry.

Mixing matrix columns scaled to the optical density at 497.0 nm, of OIO and I_2 are shown in F8.6. The temporal behaviour of I_2 can be easily re-scaled to yield absolute concentration according to the procedure indicated in section 6.3.2.3. The comparison with the time profile taken directly from the dataset shows the importance of the separation and the improvement of the signal to noise ratio. By contrast to the previous case (8.3.1), these temporal behaviours even on first sight fulfil the boundary conditions and criteria for physically reasonable temporal behaviours, although no previous knowledge about the type of curves to be expected is used. The [OIO] curve starts and ends at zero, which seems to be reasonable (note that in the figure this curve is plotted with an offset). The [I_2] curve is a constant or a slightly ascending slope in the time interval considered, which is in accordance to the low branching ratio assigned to R5.18.a [28, 80] and the slow recombination of iodine atoms $I+I+M \rightarrow I_2+M$ [203].

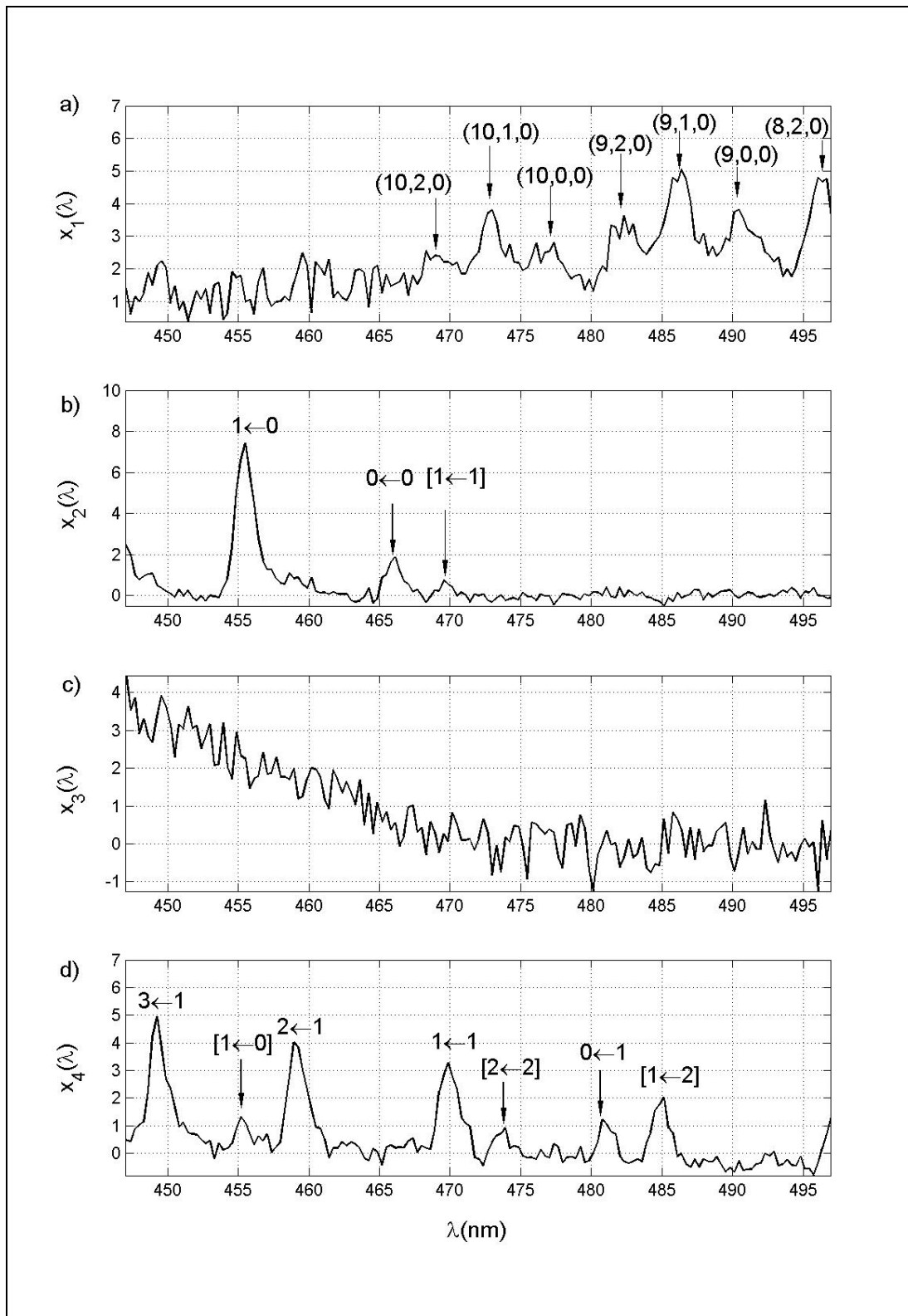


F8.6: Separated OD temporal behaviours at $\lambda = 497.0 \text{ nm}$ for I_2 , OIO, and $IO(v''>0)$ (F8.6.a). To compare, a temporal behaviour taken directly from the MTRMAS dataset at the same wavelength is also shown. F8.6.b shows the coincidence of bands of OIO and $IO(v''>0)$ at $\lambda = 497.0 \text{ nm}$.

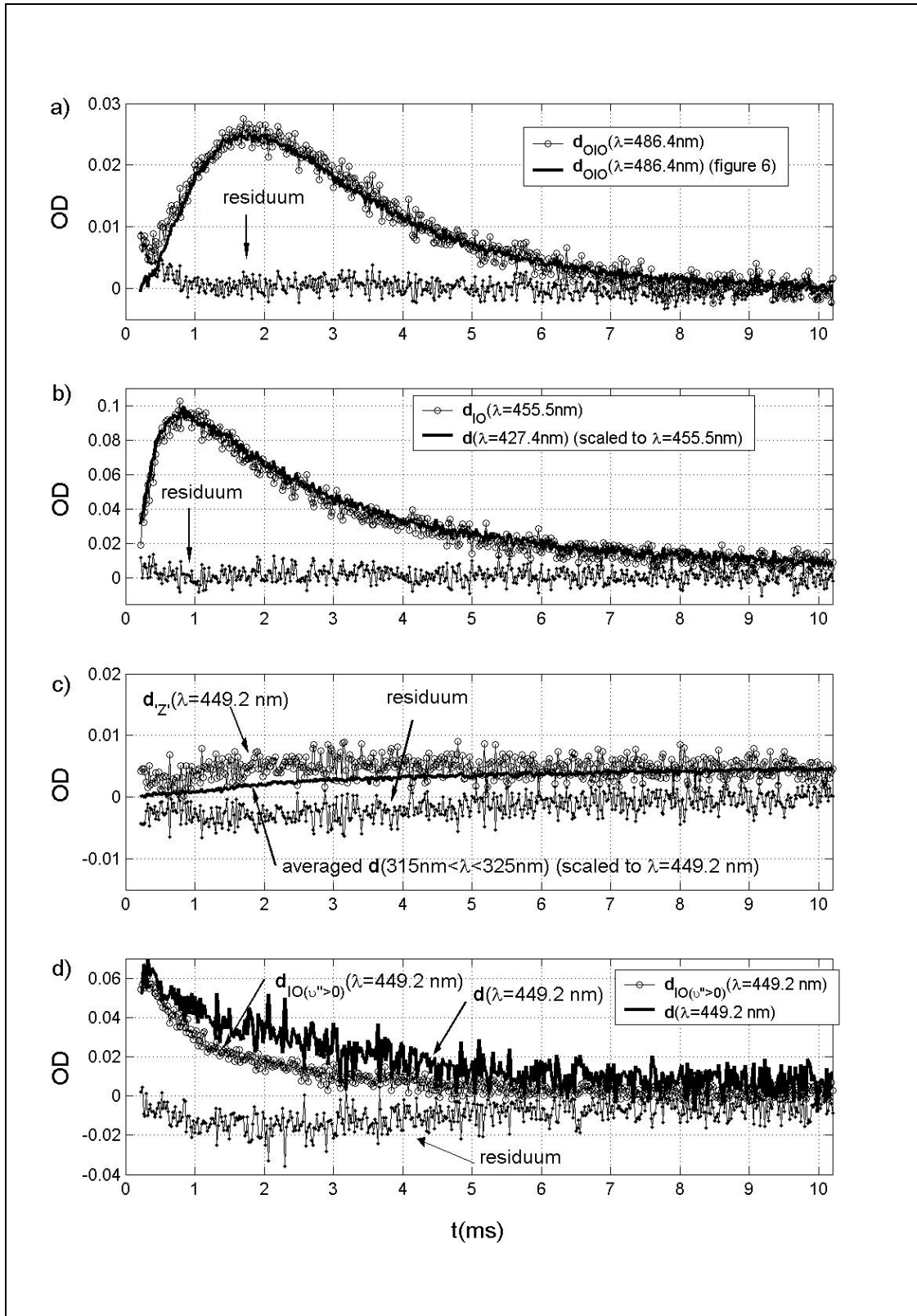
It is worthwhile to note the difference between the classical method used to obtain a pure OIO spectrum and the method described here. To obtain the reference spectrum shown in F8.4a different mixtures of precursors were studied. The observed temporal behaviours at 479 nm, where a minimum of OIO occurs, were compared. Thus it was possible to get an idea of the behaviour of $[I_2]$ in each dataset. An optimal $[I_2]/[O_3]$ mixing ratio to get post-photolysis stationary concentration of I_2 in the period of observation was found. The OIO absorbance spectrum was obtained from datasets recorded with this mixing ratio by subtracting averaged spectral profiles from different observational time intervals. $[I_2]$ is constant and its absorbance is removed in this subtraction. Assuming that there were no further absorbances in the spectral range under study, this OIO spectrum can be considered as pure. In contrast, PCA/ICA enables the extraction of the OIO spectrum under any chemical conditions, independently of the temporal behaviour of I_2 , which in many experiments is far from being constant. In F8.4a the results for OIO obtained with both methods in the same dataset are well in agreement (difference of 2% at 549 nm). Thus, they are mutually validated. The OIO spectrum obtained with ICA for this dataset is plotted as well in F8.5 along with another 9 results from datasets recorded under different conditions.

The OIO validated spectrum in the spectral window under study, along with a reference I_2 spectrum recorded at the appropriate pressure and column density [127], can be used to obtain the corresponding temporal behaviours in later analysis very easily. Given a dataset obtained at a give P and a given I_2 column density, if no additional absorbances are present –which can be checked by PCA–, the reference spectra mentioned above can be considered as the only two columns of the mixing matrix, and the model E8.6 can be solved by Least Squares. If there were evidence for

other overlapping absorbers, it would be necessary to repeat the analysis done previously in order to find a window in which ICA separation is possible.



F8.7: Partial separation of OIO (panel a), IO (b), 'Z' (c) and IO($\nu'' > 0$) (d). Traces of absorption bands of mixed absorbers are shown between brackets.



F8.8. Temporal behaviours of OIO (a), IO (b), ‘Z’ (c) and $\text{IO}(v''>0)$ (8d). In figures a), c) and d) they are scaled to the value of pure OD at the maximum of absorbance in the current window. Profiles at the same wavelengths obtained from a dataset without I_2 absorbance are also shown in b), c) and d) for validation purposes (denoted with $a(\lambda)$). The pure temporal behaviour of OIO reported in section 8.3.2 (F8.6) is also plotted in a) to show the consistency between the analysis in the two windows.

8.3.3. Model requirements approximately fulfilled

In some cases important absorbers are overlapped in such a way that the necessary conditions for ICA separation are not fulfilled in any spectral window, or only partially fulfilled. Nevertheless, in many of these cases it is possible to obtain a first guess of the overlapping spectra using PCA/ICA. As an example, this method was used between 447.06 nm and 497.0 nm, and the spectra in F8.7 were separated. In order to simplify the calculations and allow a better fulfilment of the conditions of the model, the I_2 absorbance $\mathbf{a}_{I_2}(\lambda)$ was previously calculated (E8.3) using the reference spectrum and the temporal behaviour showed in section 8.3.2, and removed from the dataset $\mathbf{a}(\lambda)$ in the complete spectral range. To simplify the notation in this section, $\mathbf{a}(\lambda)$ will denote the I_2 -corrected dataset.

PCA found four relevant components containing mixed features of the absorbances of IO, $IO(\nu''>0)$, OIO, and 'Z'. The absorber denoted as 'Z' is not identified and its assignment is discussed in Chapters 8 and 9. A further significant component was expected, as a consequence of the different temporal behaviour of $IO(\nu''=1)$ and $IO(\nu''>1)$, but it was not found. In F8.7, the first independent component (F8.7.a) contains two complete triplets of OIO ($(9, \nu_2, 0) \leftarrow (0, 0, 0)$ and $(10, \nu_2, 0) \leftarrow (0, 0, 0)$). There are also some traces of IO in this component. The second IC (F8.7.b) shows two $\nu' \leftarrow 0$ bands of IO ($\nu' = 1, 0$), with a trace of the $1 \leftarrow 1$ band. The third IC (F8.7.c) is a broad band absorber which extends from the UV up to 470 nm [79, 80]. The last IC (F8.7.d) contains $\nu' \leftarrow 1$ bands ($\nu' = 3, 2, 1, 0$) and $\nu' \leftarrow 2$ bands ($\nu' = 2, 1$) of IO. The corresponding temporal behaviours scaled to significant values of OD are plotted in F8.8, along with useful OD profiles for validation purposes. F8.8a compares the OD temporal behaviour obtained for OIO on top of the $(9, 1, 0) \leftarrow (0, 0, 0)$ band with the analogous *pure* temporal behaviour obtained in section 8.3.2 (PCA/ICA window to

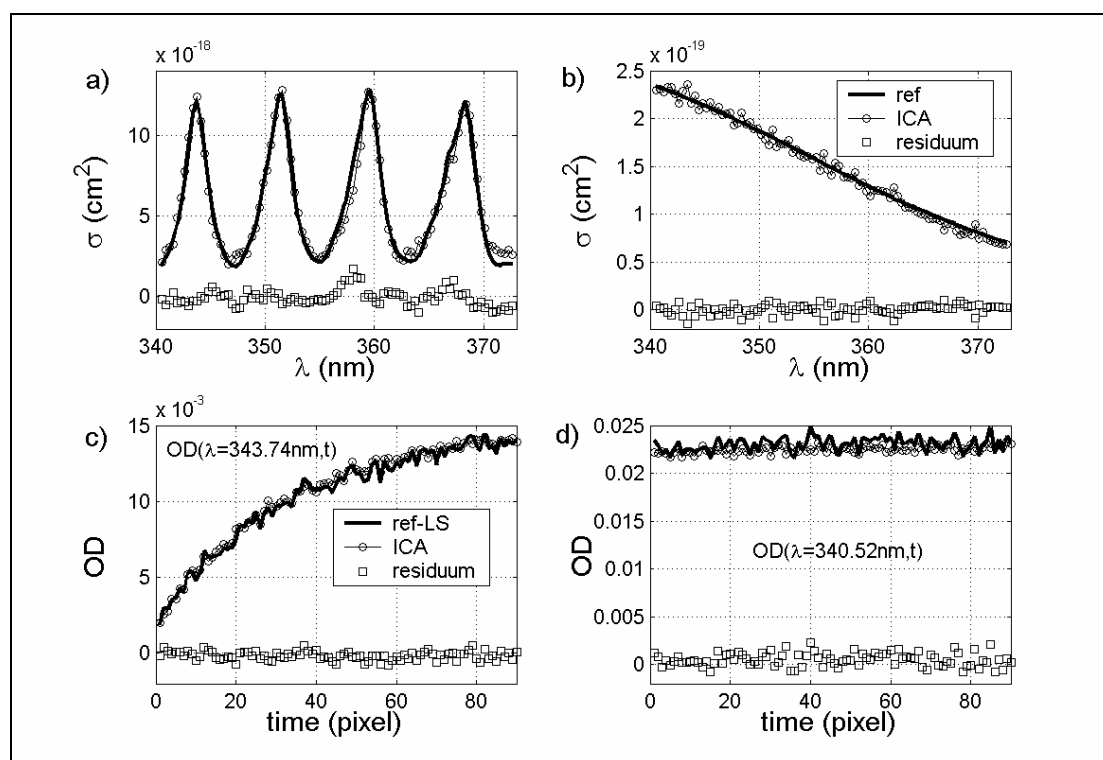
window validation). There is an excellent agreement between the two curves from 1 ms to 10 ms. In the first millisecond the residuum contains traces of $\text{IO}(\nu''>1)$. F8.8b compares the OD temporal behaviour obtained for IO on top of the $1\leftarrow 0$ band to $\mathbf{a}(\lambda = 427.4 \text{ nm})$ scaled at the maximum of [IO]. The vector $\mathbf{a}(\lambda = 427.4 \text{ nm})$ is considered usually as a good approximation to $\mathbf{a}_{\text{IO}}(\lambda = 427.4 \text{ nm})$ (PCA/ICA window to original data validation). The agreement between these two curves is very good. F8.8c shows the temporal behaviour of 'Z' at 449.2 nm (the $3\leftarrow 1$ band of IO is located at this wavelength) along with a scaled temporal behaviour obtained by averaging $\mathbf{a}(\lambda)$ between 315 nm and 325 nm, where the absorbance of 'Z' dominates over those of O_3 , IO and further iodine oxides (PCA/ICA window to original data validation). The disagreement between these curves is quite strong up to 6ms. The residuum shows a structure similar to the temporal behaviour of OIO. Finally, F8.8d compares the OD temporal behaviour obtained for $\text{IO}(\nu''>0)$ on top of the $3\leftarrow 1$ band ($\lambda = 449.2 \text{ nm}$) to $\mathbf{a}(\lambda = 449.2 \text{ nm})$. The residuum shows clearly that the absorption at 449.2 nm results from contributions of $\text{IO}(\nu''>0)$, 'Z' and OIO individual absorptions. Therefore $\mathbf{a}_{\text{IO}(\nu''>0)}(\lambda = 449.2 \text{ nm})$ is the better approximation to be used in any subsequent spectroscopic or kinetic analysis.

It is worthwhile to note that PCA/ICA in this window does not allow the separation of $\text{IO}(\nu''=1)$ and $\text{IO}(\nu''>1)$. PCA is unable to find a further relevant component, which implies that the primary problem in this case is not correlation or statistical dependence of the spectra, but linear dependence of the temporal behaviours, and therefore it is impossible to find the generalised inverse of a mixing matrix containing separate temporal behaviours of $\text{IO}(\nu''=0)$, $\text{IO}(\nu''=1)$, $\text{IO}(\nu''>1)$, OIO and 'Z'. In fact, it is easy to demonstrate that a linear combination of four of the former temporal behaviours gives a good approximation to the remaining one. To this end, some of the

temporal behaviours shown in this section ($IO(v''=0)$, $IO(v''=1)$, 'Z') and the former ($IO(v''>1)$, OIO) can be used.

8.3.4. Validation of the method in a well known system

In order to validate the method in a system with less uncertainty, the methods discussed in this chapter were also applied to data recordings obtained for OCIO photolysis supplied by J. Orphal (personal communication, 2002). This photolysis leads to an immediate formation of Cl_2 , and afterwards a slow recovery of OCIO can be observed. The spectra of OCIO and Cl_2 are overlapped, and ICA was used to separate them and to obtain the corresponding temporal behaviours. An example is shown in F8.9.



F8.9. Spectra and temporal behaviours obtained with PCA/ICA in an appropriate spectral range of a OCIO photolysis data recording. Reference spectra are plotted along the retrieved ones in panels a and b. Pure optical density temporal behaviours of OCIO (c) and Cl_2 (d) obtained by least squares fitting to the reference spectra are compared to the corresponding curves retrieved with PCA/ICA.

The retrieved OCIO spectrum is plotted in F8.9.a along with a reference spectrum, which was obtained from a static measurement of a pure and stable sample

and validated with the spectrum of Wahner et al. [204]. The discrepancies between the reference and the ICA retrieved spectrum indicate differences in the population of excited states between the stable sample and the post-photolysis recovery. The Cl₂ reference spectrum E8.9.b can be found in Maric et al.[205]. F.7.9.c and F8.9.d show respectively pure optical density temporal behaviours of OCIO and Cl₂ at a given wavelength. In each case, the profile obtained by applying LS to the data recording with the reference spectra as design matrix is plotted along the ICA result.

8.4. Discussion

8.4.1. Physical meaning of uncorrelatedness and statistical independence

The use of ICA is justified if the independence of the sources can be assumed as a good approximation. The approach considered in this work uses the hypothesis of statistically independent absorption spectra. This hypothesis links E8.6 with the properties of the physical sources. Different physical processes tend to generate statistically independent signals, and under certain conditions this can be plausibly assumed in the case of transitions between vibrational states of different molecules. If the absorbers under study have different kinds of bonds between atoms and they do not have the same symmetry, their series of vibrational bands can be considered statistically independent signals as it is the case for example of I₂ and OIO.

On the other hand, the spectra of different molecules have a number of common properties which reflect general characteristics of the phenomenon of molecular absorption. These common properties correlate the spectra. It is important to remark that in some cases overlapping absorbers have the same kind of atomic bonds (in spite of having different molecular symmetry), which could imply a quite similar vibrational structure (e.g. IO and OIO). Furthermore, sometimes species have the same symmetry (e.g. IO and IO($\nu'' > 0$)), and their spectral progressions are simply shifted, the only

difference being the absolute and relative intensity of the bands (different Franck-Condon factors.). Other common properties are the existence of continua, and broad spectral ranges in which absorbance is zero. An experimental aspect is sampling, which is common to all vibrational bands. If two absorbers show dominant broad band features in the region of overlapping, cancellation of terms in the scalar product is generally not possible. The selection of the window decorrelates the sources by excluding common features like broad band continua. In the case of I_2 and OIO the selection of the window reduces the importance of the OIO continuum in such a way that the vibrational structure determines the statistical properties of this source. By avoiding having a strong slope in both overlapping absorbers, it is possible to find finally a window in which uncorrelatedness is a good assumption. In case of IO and $IO(\nu''>0)$, the selected window avoids the inclusion of the complete progressions in such a way that the relative positions of bands is no longer a determinant correlation factor.

It is worth commenting on the PCA extraction of the $IO(\nu''>0)$ spectrum. The correlation between the component showed in F8.2.c, corresponding to an almost pure $IO(\nu''>0)$ spectrum, and pure spectra of I_2 and OIO is found to be low. The first two PCs shown in F8.2.a and F8.2.b are mixtures of I_2 and OIO. This particular mixing is a consequence of using variance as cost function. The spectra of I_2 and OIO are the most significant contributions in the mixtures from the point of view of variance, and have low correlation to the spectrum of $IO(\nu''>1)$, which presents significantly lower variance than the former. Thus, any linear combination of the first two PCs in this spectral window is approximately orthogonal to the centred spectrum of $IO(\nu''>1)$. This explains why $IO(\nu''>1)$ is retrieved using the uncorrelatedness constraint. It is possible to validate finally this spectrum by fitting the observed data to linear combinations of this and the former spectra using Least Squares. Temporal behaviours for I_2 and OIO

are identical to those obtained using ICA in an appropriate window, and the corresponding one for $IO(\nu''>0)$ is identical to that obtained by PCA. It is worth to mentioning that further ICA of the components found by PCA plotted in F8.2 leads again to mixed components, because independence is not a valid assumption for the spectra of $IO(\nu''>0)$ and OIO.

8.4.2. Advantages over ‘classic’ methods.

Multivariate analysis methods like PCA and ICA provide a general approach to systematic analysis of multidimensional data arrays in the context of MTRMAS. Classic methods are generally not optimal in extracting information from such datasets.

To get pure spectra, averaged OD profiles from the dataset are sometimes considered, and iterative empirical procedures based on intelligent differencing are used as well. These procedures are nevertheless dependent on the particular chemical conditions of the system. As an example, the OIO spectrum used here as reference for validation purposes was obtained by simple subtraction of two averaged profiles in datasets containing no more than two overlapping absorbances (I_2 and OIO) from 472nm to the red, where I_2 was constant time. In many other cases (like for example for IO) the overlapping absorbers are more than two and/or do not have constant temporal behaviours, and iterative procedures are required (see for example the procedure followed in [10] to separate IO and a broad band UV absorber). Different results can be found in the literature for the spectral shape of IO, proving the inconsistency of such approaches. In any case, the separation of full ranged spectra with these methods is difficult. Opposed to that it is possible to use temporal behaviours (like those showed in F8.6) retrieved from selected windows to obtain the respective pure spectra in the complete range of work by using Multivariate Linear Regression (see Chapter 8).

Pure time curves are also required in calculating absolute cross sections and

reaction rate coefficients. To obtain the temporal behaviours, it is common to look for assumed single absorber spectral windows. Sometimes it is even possible to manipulate the chemical conditions in order to minimise one determined absorbance and therefore make the former assumption plausible. The inconvenience of such procedure is again the possibility of neglecting overlapping absorptions. The extraction of unmixed temporal behaviours using PCA-ICA will allow the obtaining of more accurate calculations of rate constants and cross sections. A further advantage of such multivariate techniques lies in the possibility of analysing *all* the information contained in a dataset. With this approach it is possible to obtain a good signal to noise ratio of the temporal behaviours of the different absorbers. The reason for this is the inclusion of a significantly larger amount of data than if just a single appropriate profile is extracted from the dataset, which would be equivalent to a single wavelength measurement like e.g. a photomultiplier tube measurement.

8.4.3. First achievements of the method in the system under study

A first interesting result of the analysis presented in section 8.3.1. is the separation of the $IO(\nu''>1)$ absorbance. The complete spectrum obtained for $IO(\nu''>0)$ is the first reported in absorption measurements. Previous absorption spectra of IO clearly contain $IO(\nu''>0)$ [134, 170, 171], but bands with $\nu''>1$ are not reported. In general $IO(\nu''>0)$ is treated as an integral part of the IO absorbance, assuming identical temporal behaviour. In this work, the analysis of the complete spectral window demonstrates that IO and $IO(\nu''>0)$ must be treated as different species, which will be particularly important in the determination of absolute absorption cross sections of IO.

PCA also underlines the importance of considering the overlap of the $0\leftarrow 5$ absorption transition of IO with the $(5,1,0)\leftarrow(0,0,0)$ transition of OIO at 549.1 nm. The time profile corresponding to this band is usually selected to calculate the absolute cross

section. In case of strong absorbance of $IO(\nu''>0)$, and if a linear decomposition like the one shown in this work is not possible, it would be recommendable to select another band which does not coincide with any $IO(\nu''>0)$ transition (e.g. the $(4,2,0)\leftarrow(0,0,0)$ band at 567.7 nm).

8.4.4. Outlook

The method described in this work allows the extraction of true and separated optical density temporal behaviours of individual absorbers. In particular, the temporal behaviours of I_2 and OIO obtained here have been used by Spietz et al. [126] in an LS based extraction of full ranged spectra of the absorbers under study. The spectra obtained in this way display a high reproducibility and fulfil the non-negativity condition to a high degree. The temporal behaviours have also been used in a study of the absolute absorption cross sections [125] of the absorbers involved and observable in the I_2/O_3 photochemistry (Chapter 10).

Apart from laboratory studies, ICA can be used as well for feature detection and source separation in the analysis of satellite data analysis. In the context of atmospheric observations, the detection of further species currently hidden in the observational data seems likely with the use of these multivariate techniques. Also, the detection of temporal cycles and developments of concentrations in the atmosphere promises to be a field which can be tackled successfully with PCA and ICA.

8.5. Summary and conclusions

PCA and ICA have good prospects in the treatment of multidimensional spectroscopic datasets, both in laboratory and in atmospheric contexts. The present studies have shown how a combination of PCA and ICA can be used to find linear decompositions of MTRMAS datasets into physically meaningful components, where the linear decomposition is justified by the Beer-Lambert Law. Firstly, PCA is used to

remove noise, recognise patterns and reduce dimension. PCA pre-processing allows decomposing the observed dataset into a limited number of orthogonal structures, which are sorted according to their variance. Secondly, ICA is used when its requirements are satisfied to enhance this separation towards independence of the contributions.

The problem of independence of sources has been tackled by selecting spectral windows in which this assumption of uncorrelatedness is at least approximately correct. The general properties of the phenomenon of molecular absorption in many cases introduce correlation between the overlapped spectra and, as a consequence, dependence between them. By reducing the spectral window considered in each analysis, the vibrational structure becomes more important from the statistical point of view and common features are partially avoided. Thus, uncorrelatedness and independence are more plausible. However, further work about how to exclude the common features without losing the characteristic information content is required.

9. ANALYSIS OF MTRMAS DATA BY MULTIVARIATE MULTIPLE LINEAR REGRESSION

9.1. Introduction

In the previous chapter it has been shown that the application of Blind Source separation methods helps to maximise the information extracted from MTRMAS datasets, and that under some circumstances it can be used to separate overlapping absorptions. It has been shown that the success of these techniques depends on the spectral range of application, and that a simultaneous separation of all overlapping ODs in the complete spectral range by applying PCA/ICA is not possible at the current stage of knowledge.

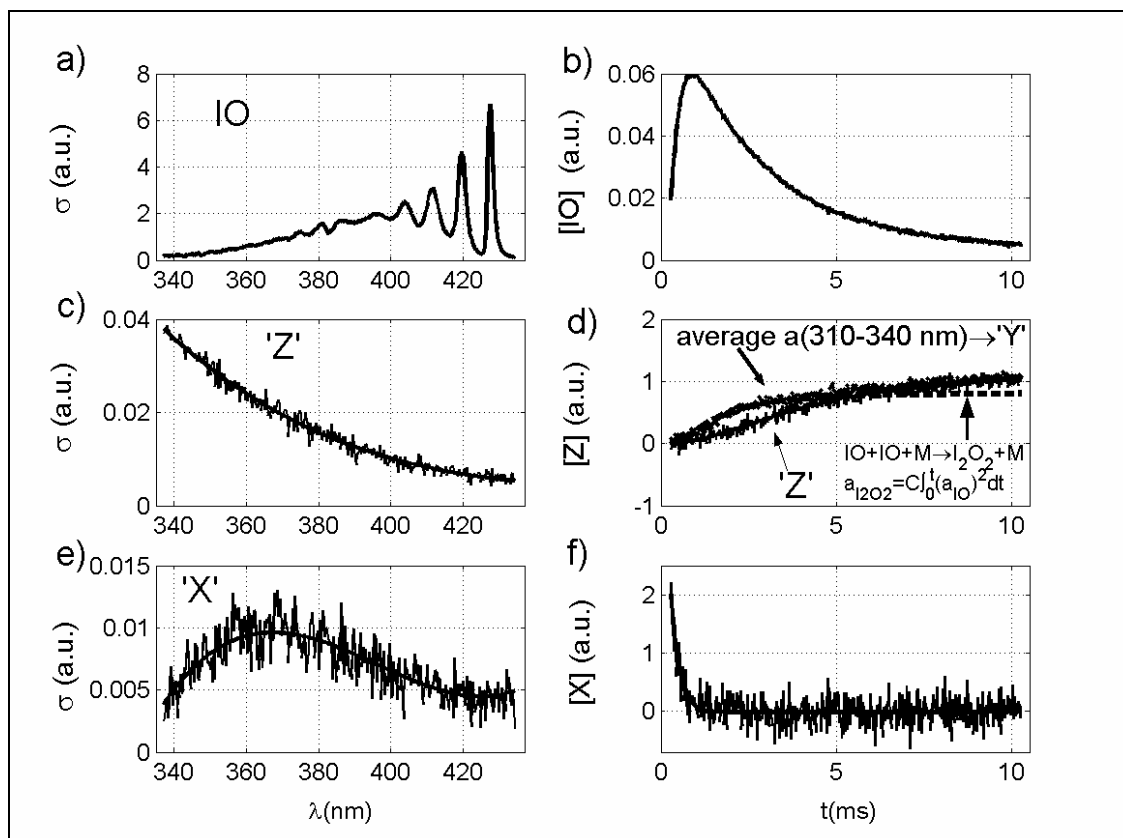
In this Chapter the separation of the temporal behaviours of all relevant species is described. In the case of I_2 , OIO and $IO(X^2\Pi_{3/2}, \nu''>1)$, the techniques explained in the Chapter 8 have been used, but in the case of $IO(X^2\Pi_{3/2}, \nu''>1)$ and the unidentified broad band UV-VIS absorbers, it has been necessary to use more ‘conventional’ linear Least Squares techniques together with some pieces of prior information.

9.2. Results and Discussion

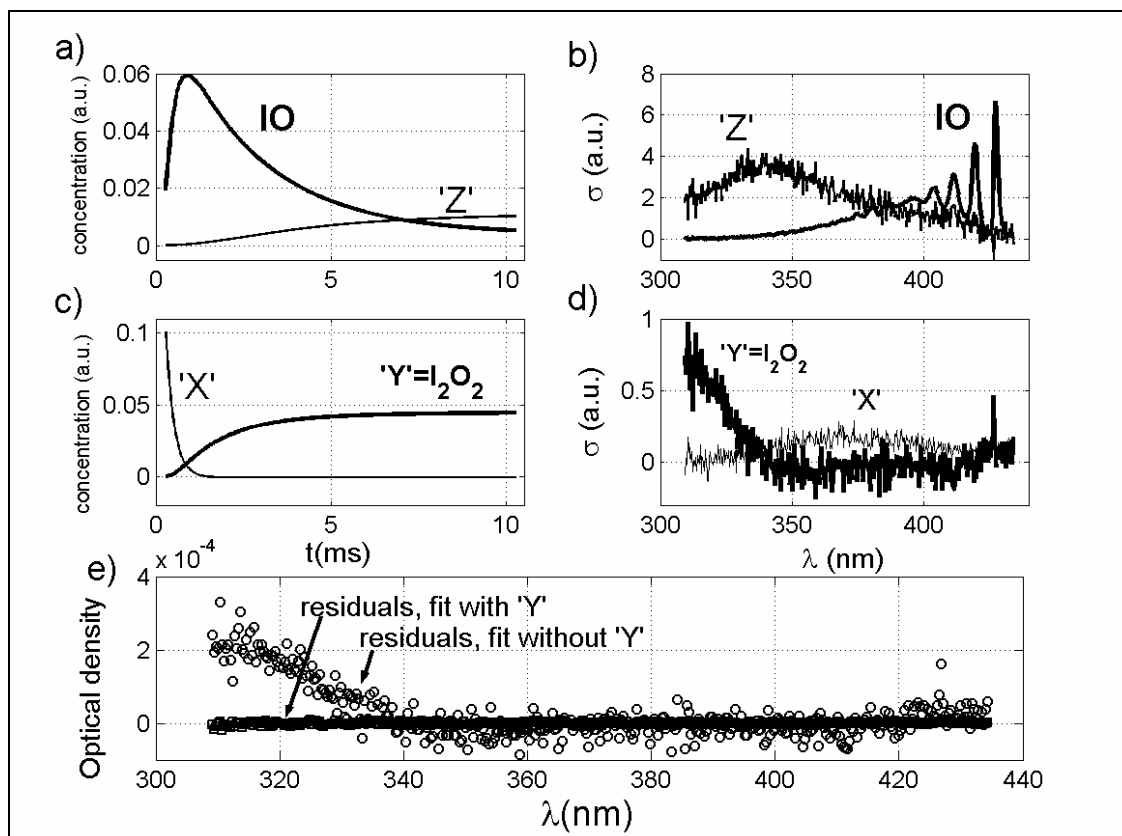
9.2.1. Separation of the temporal behaviour of IO and other UV broad band absorbers.

First the attention is focused on a wavelength region between 340 nm (chosen to avoid complications due to further UV absorbers, see below) and 435 nm (chosen to avoid complications derived from $IO(X^2\Pi_{3/2}, \nu''>0)$ and I_2). From knowledge of the kinetic behaviour of the different chemical species and/or by applying DOAS, the differences between spectra obtained at different time steps are generated. These yield separated relative spectra of IO and an unassigned species labelled as ‘Z’. A second broad band spectrum (labelled as ‘X’) is retrieved by fitting a polynomial underneath

the IO spectrum in a spectral profile averaged in a time interval of about 0.25 ms immediately after the flash. A MMLR is performed, accounting for the reference IO spectrum and the two spectra of 'X' and 'Z' as independent variables. Arbitrarily scaled temporal behaviours of the absorptions of IO, 'X' and 'Z' result. Results are shown in F9.1. The analysis can also be applied in such a way that the temporal behaviours obtained by MMLR, as indicated above, are used as independent variables in a further MMLR, in order to retrieve spectra. Provided that the fit is performed in the same spectral range, the retrieved spectra are in good agreement with the initial input.



F9.1: Results of separation of overlapping spectra between 340 nm and 435 nm. Spectra of IO (a), 'Z' (c) and 'X' (e) are obtained by combination of different techniques. The measured OD in the spectral range 340-435 nm is regressed against them, and temporal behaviours are subsequently obtained (panel b, d, and f respectively). Panel d shows the disagreement between the temporal behaviour of 'Z' and the modelled I_2O_2 concentration curve (dash line) obtained by using E9.1. The kinetic assignment of I_2O_2 to a further absorber observed from 310 to 340 nm is more plausible



F9.2: Results of separation of overlapping spectra between 310 nm and 435 nm (panels b and d). OD between 310 and 435 nm is regressed against the temporal behaviours (panels a and b) of IO, 'X', 'Z' and the modelled temporal behaviour of I₂O₂. The spectrum of a further absorber is retrieved (panel d). In panel e residuals of the same regression fit with and without the modelled temporal behaviour of I₂O₂ are compared. Note that in the second case the residual contain a similar spectral feature to that retrieved in the first one. Kinetic assignation of this spectrum to I₂O₂ is therefore plausible.

It was observed that if the fitting spectral window is enlarged down to approximately 310 nm, some systematic features appear in the residuals (F9.2.e), indicating the presence of a further UV absorber, labelled as 'Y'. The OD time profiles averaged between 310 and 340 nm show different behaviour to that of 'Z' (F9.1.d). Similarly the temporal curves obtained disagree with those used as input.

The strong spectral overlap of 'Y' and 'Z' and the absence of vibrational features impede the use of the mathematical techniques explained above to separate them. The experimental approach used in this work is not suitable for an unambiguous identification of the higher iodine oxides, and as a result the conditions of the mathematical models used for optimal extraction of information are not fulfilled. To

gain some knowledge about ‘Y’ from the data available it is necessary to use some prior information. One of the important products of the IO self reaction is expected to be the IO-dimer, I_2O_2 . Some broad band absorptions, similar to ‘Z’, have been previously assigned tentatively to I_2O_2 (see Bloss et al. [79]). In the present study, the temporal curve corresponding to ‘Z’, which has been attributed to a gas phase species in a previous publication [125], does not follow the expected second order formation (see F9.1.d), as argued by Bloss et al. [79]. Even if different sinks are considered (dissociation, I_2O_2+I , etc.) the temporal behaviour of the absorption ‘Z’ can not be modelled by the kinetics of the IO-dimer. It can be concluded therefore that ‘Z’ is not I_2O_2 . In contrast, the averaged time profile between 310 and 340 nm, containing the OD due to ‘Y’, (see F9.1.d) does show a rate of formation having an apparent second order dependence on IO. From its temporal behaviour ‘Y’ is tentatively assigned to be I_2O_2 . The ‘Y’ spectrum is fitted, by using the result of numerically integrating the branch differential equation corresponding to R5.18, that is:

$$[I_2O_2](t) - [I_2O_2]_0 = k_{5.18,d} \int_0^t ([IO](t'))^2 dt' = C \int_0^t (a_{IO}(t', \lambda_0))^2 dt' \quad (E9.1)$$

where $C = k_{5.18,d}/(L\sigma_{IO}(\lambda_0))^2$ and $[I_2O_2]_0 \approx 0$. The constant C is unknown, because whether the rate constant of the IO self reaction (R5.18) nor $\sigma_{IO}(\lambda_0)$ are known a priori. Nevertheless, the scaling of the temporal behaviour is unimportant in the separation procedure because the only objective is to obtain a pure optical density. Therefore, no assumption on the branching ratio is needed. By numerically integrating the squared absorption of IO at a given wavelength a normalised concentration is obtained (F9.2.c), and the corresponding spectrum obtained by MMLR (F9.2.d) is automatically scaled such that the product of both quantities gives the true pure optical density.

The results obtained are shown in F9.2. The panels F9.2.a and F9.2.b show the time curves used as input in E9.1, and the panels F9.2.b and F9.2.c the resulting spectra.

F9.2.e compares the residuals of the MMLR when ‘Y’ is and is not included on it, and demonstrates that the assignment of I_2O_2 to ‘Y’ is plausible. It must be remarked that in applying E9.1 it has been assumed that no significant sinks for I_2O_2 exists within the observation time and that ‘Y’ is a single absorber. The assignments of ‘X’, ‘Y’ and ‘Z’ are further discussed in Chapters 9.

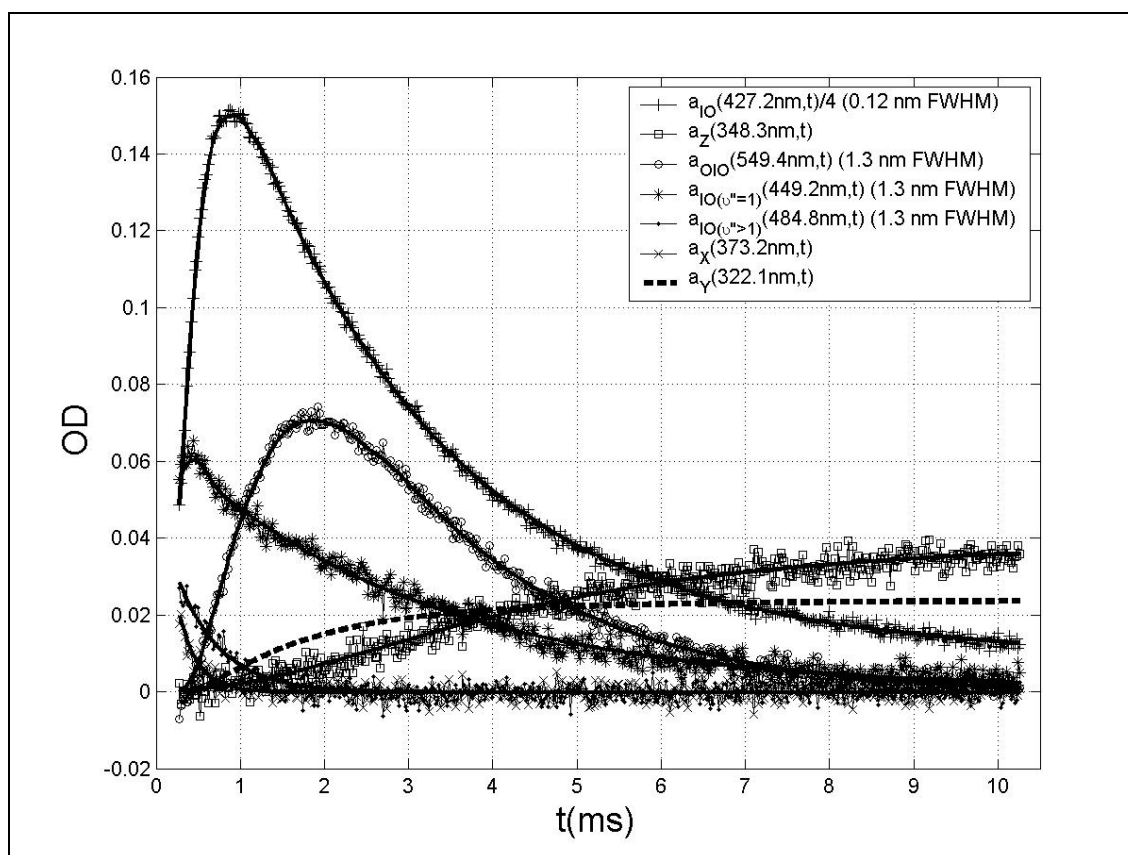
The formation of a deposit on the mirrors and the windows of the vessel together with the strong absorption of O_3 reduce the transmission of the analysis light in the UV dramatically, such that after two or three experiments the signal below 320 nm reaching the detector has decreased significantly and the signal to noise becomes poor. Thus only selected experiments are suitable for the identification of the spectrum attributed to I_2O_2 . It was therefore not possible to establish a systematic dependence of this absorption on pressure or on the mixing ratio of the precursors.

9.2.2. Separation of the temporal behaviours of $IO(X^2\Pi_{3/2}, v'' > 1)$, OIO and I_2 .

The multivariate methods explained in Chapter 8 have been used to separate the spectra and temporal behaviours of I_2 and OIO in the ‘optimal ICA window’ (520 nm - 580 nm). This analysis was performed for each dataset, because no reference spectra of I_2 at the different pressures considered were available. As a result of the relatively long lifetime of the rotational levels of $I_2(B^3\Pi(O^+_u))$ [159], the I_2 spectrum presents a very rich rotational structure which is sensible to the changes of pressure [127], in such a way that a reference spectrum recorded at a given pressure is not valid for all pressures. PCA has been also used to obtain an estimate of the spectrum and the time trace of $IO(X^2\Pi_{3/2}, v'' > 1)$ (see F8.2). The temporal behaviours obtained in that way have been used in equation E6.17 to obtain the corresponding spectra between 470 nm and 580 nm. Finally, these spectra have been used in a new MMLR to obtain pure temporal behaviours for the

three species with enhanced signal to noise ratio. This enhancement results from the inclusion of more data in the 470 nm - 580 nm with respect to the optimal ICA window.

The curves resulting from this analysis are shown in F9.3. In particular, the temporal behaviour of OD for I_2 at 500 nm yields the concentration from knowledge of the absolute absorption cross section of I_2 at 500 nm. In this study a value of σ_{I_2} (500 nm) = $(2.191 \pm 0.020) \times 10^{-18} \text{ cm}^2 \text{ molecule}^{-1}$ (see [127] and references therein) has been used.



F9.3: OD temporal behaviours of the different species observed at the wavelengths selected for the determination of their absorption cross section. The 'Y' temporal behaviour was calculated by using E9.1., i.e. it is assigned to I_2O_2 .

9.2.3. Separation of the temporal behaviour of $IO(X^2\Pi_{3/2}, v''=1)$

Absorptions of 'Z' and I_2 are not negligible in the spectral range where $IO(X^2\Pi_{3/2}, v''=1)$ is observed. Therefore, their contributions were subtracted from the total absorption and the resultant attributed to $IO(X^2\Pi_{3/2}, v''=1)$ during the time interval

where it is present. The I_2 optical density can be readily calculated by multiplying the I_2 temporal behaviour, obtained as explained in the previous section, with a reference I_2 spectrum, measured with the same experimental setup in static conditions. Note that the pressure effects in this case are not important, because the IO bands ($v' \leftarrow 1$) are not overlapped to the I_2 ro-vibrational structure. Similarly, the OD attributed to 'Z' is reconstructed by multiplying its spectrum with its temporal behaviour, both obtained as explained in section 9.2.1. When the spectral window selected is free of I_2 and 'Z', IO($X^2\Pi_{3/2}$, $v''=1$) the temporal behaviour is obtained from the maximum OD at 449.3 nm ($3 \leftarrow 1$). Separated temporal behaviours of all absorbers monitored are shown in F9.3.

9.3. Applications

9.3.1. Separation of full range overlapping spectra

By regressing the observational matrix \mathbf{Y} against the corresponding set of curves (F9.3) it would be possible, in principle, to retrieve the full range spectra of the species contained in the mixture. However, as explained above, the necessity of avoiding multicollinearity imposes the selection of appropriate data subsets. Spectra of full coverage can be obtained by joining the partial spectra from the individual spectral windows. Improved spectra of iodine oxides obtained using the curves reported here have been published by Spietz et al. [126].

9.3.2. Determination of absolute absorption cross sections

The application of the concept of conservation of iodine enables the retrieval of the absorption cross sections of IO($X^2\Pi_{3/2}$, $v''=0,1,2$), OIO, I_2O_2 , 'X' and 'Z' from the corresponding temporal behaviours shown in F9.3 [124, 125]. The mathematical procedure consists of a *single* multivariate linear regression, i.e. the observations are contained in a vector and the unknowns form a vector (see Appendix C).

T9.1: Results of MIntAS.

Species	<i>FWHM</i>		Correction/scaling	Non-linearity
	Lo-Res	Hi-Res		
IO(4←0)	1.3 nm	0.12 nm	(correction applied before iodine conservation) Average scaling: 1.64 ± 0.04	5%
IO(1←3)	1.3 nm	0.35 nm	1.82 ± 0.21	1%
IO(1←2)	1.3 nm	0.35 nm	1.82 ± 0.21	1%
OIO(1,5,0←0,0,0)	1.3 nm	0.35 nm	1.14 ± 0.05	0.1%

Previous to application of the iodine conservation, the influence of spectral resolution on the apparent optical density was characterised. The non linearity in IO(4←0) was judged to be large enough to justify the application of MIntAS *before* iodine conservation. In all the other cases a simple scaling factor is applied *after* iodine conservation. The uncertainties have been defined elsewhere [122].

However, before the determination of absorption cross sections, these temporal behaviours still requires a last correction. The analysis technique MIntAS [122] has been applied to the IO bands (4←0), (3←1), (1←2) and the OIO band (5,1,0)←(0,0,0), which are used for the iodine mass balance cross section retrievals. Results are summarised in T9.1, where the average scaling factors between spectrally low and high resolved optical densities are shown. In general the instrumental resolution causes a small, significant and non-linear dependence of the apparent optical density on concentration. In the case of the IO(4←0) band, the deviation from Beer-Lambert law represents a change of about 5% with respect to the mean scaling factor.

As a result of the above, the IO time traces have been corrected for this non-linear instrumental resolution effect. For the IO absorption bands (3←1) and (1←2), the non-linearity is less than 1% and for OIO is less than 0.1%. Therefore, the non linear correction is assumed negligible and a constant correction factor is applied. ^

9.3.3. Kinetic analysis

The separated curves of the different gas phase species detected in the I_2/O_3 photochemical system have been used for the kinetic analysis of the chemistry involved, i.e. for the determination of rate coefficients and branching ratios of relevant reactions (Chapter 10). A pre-requisite for this analysis is that the absorbance versus time curves shown in F9.3 must be converted into concentration versus time curves. This can be achieved by applying the Beer-Lambert law and using the corresponding absorption cross sections.

10. KINETIC AND MECHANISTIC STUDY OF THE I₂/O₃ PHOTOCHEMICAL SYSTEM

10.1. Introduction

In this chapter a study of the gas phase I₂/O₃ photochemistry in a system where O₃ is in excess over all other species is presented. The mixtures of I₂ and O₃ employed result in the formation of a significant amount of OIO and the higher iodine oxides. Although no specific measurements of particles have been performed, the formation of aerosol at longer time scales has been observed (F10.1). An important objective is to gain a better understanding of the gas phase chemistry of IO and OIO and the reactions producing higher oxides of iodine. In particular, the aims are:

- a) to investigate the branching of the IO self reaction at 298 K, and
- b) to generate a plausible mechanism to explain the fates of OIO and I₂O₂.

These objectives address the need to assess the ozone destroying potential of the iodine chemistry and the significance and extent of the formation of ultra fine iodine containing particles in the MBL (Chapter 2).

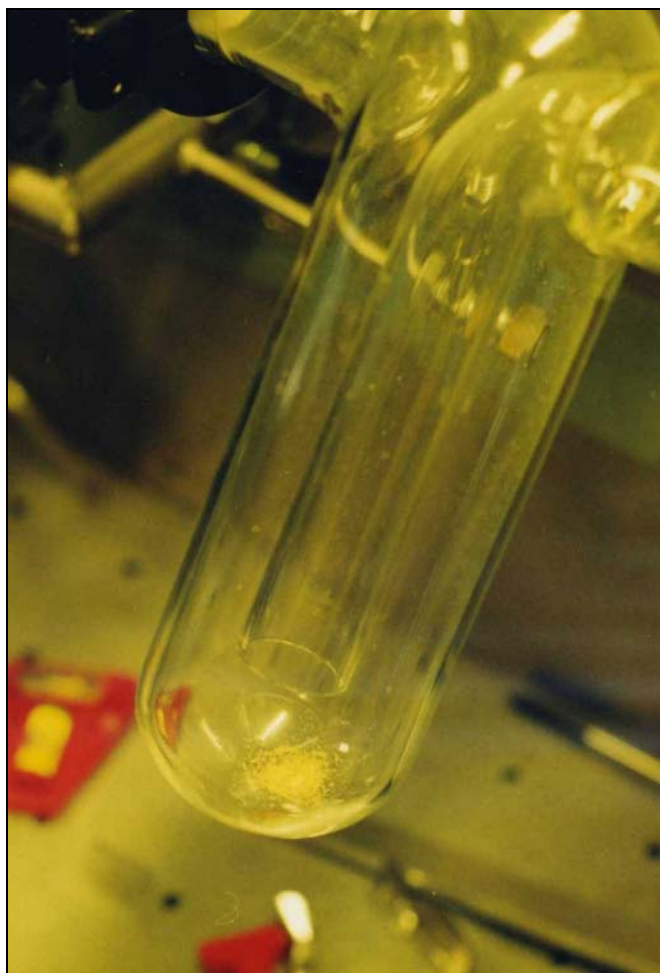
10.2. Calibration of temporal behaviours

The calibration of the OD temporal behaviours of molecules and radicals (F9.3) is achieved by applying the Beer-Lambert law as follows:

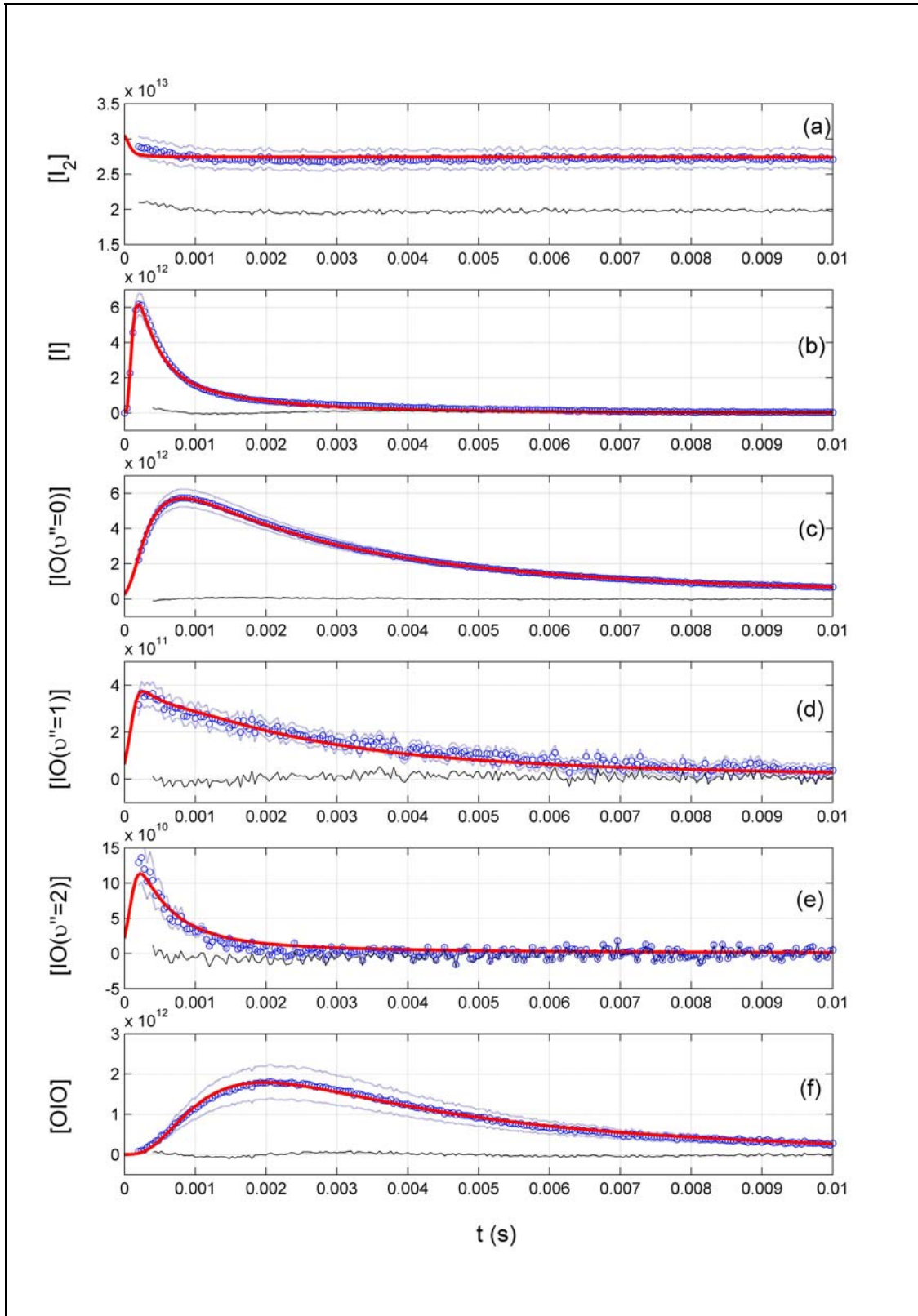
$$[\text{R}](t) = \frac{a_{\text{R}}(\lambda_0, t)}{L \cdot \sigma_{\text{R}}(\lambda_0)} \quad (\text{E10.1})$$

where $[\text{R}](t)$, $a_{\text{R}}(\lambda_0, t)$ and $\sigma_{\text{R}}(\lambda_0)$ are respectively the concentration versus time curve, the OD temporal behaviour and the absorption cross section at the wavelength λ_0 of the species R, and L is the path length. The vacuum wavelengths selected for calculating the concentrations of the different relevant species as a function of time are: 427.2 nm for IO($v''=0$), 459.3 nm for IO($v''=1$), 484.9 nm for IO($v''=2$), 500 nm for I₂ and 549.3 nm

for OIO (F9.3). The cross sections at these wavelengths have been reported in previous publications [124, 125] (see appendix C). Each of the 38 datasets comprises concentration curves of I₂, IO, IO(*v*'=1) and OIO (F10.2). Additionally, concentration curves of IO(*v*'=2) are available for measurements at low pressures ($P \leq 40$ hPa). Concentration versus time curves of two higher iodine oxides ('X', and 'Z') are also available (see F9.3) However, these data have not been used in the kinetic analysis, because of their high uncertainty and ambiguous chemical assignment. The concentration curves corresponding to 'Z' have been compared to the simulated curves of higher iodine oxides and polymers to check the plausibility of a kinetic assignment

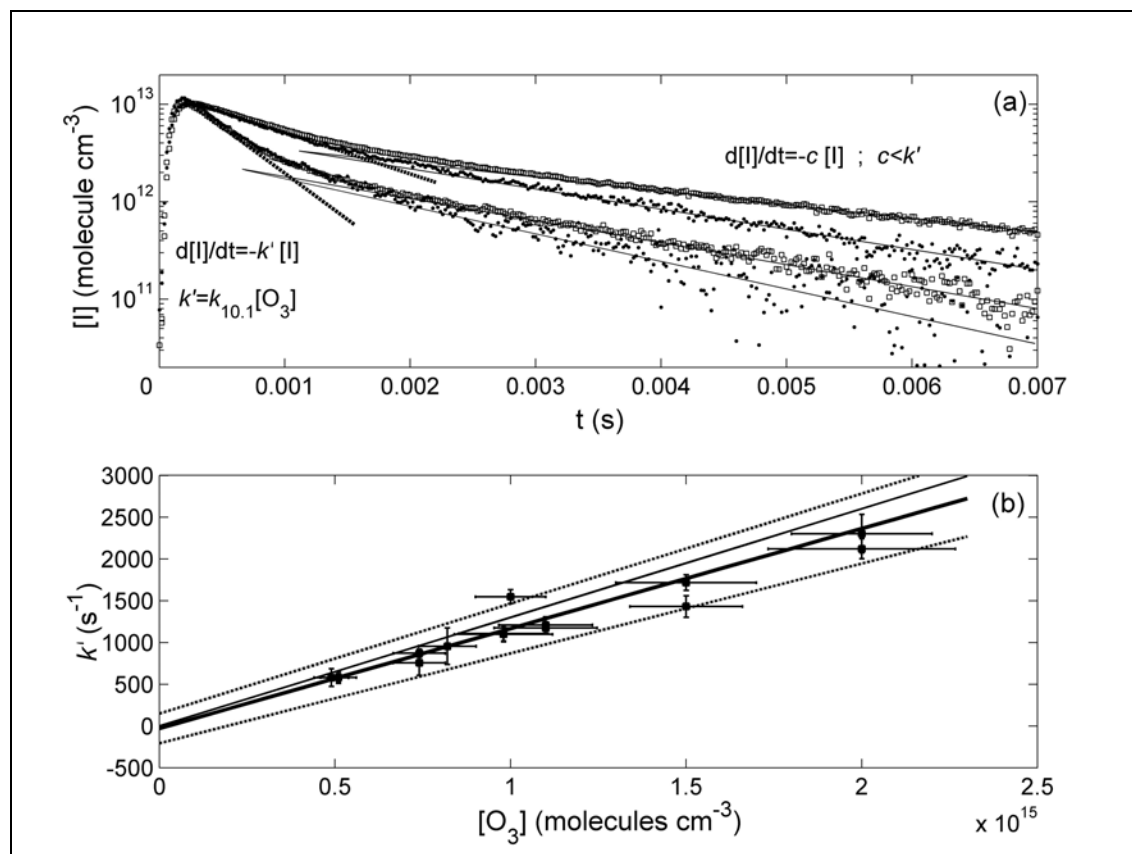
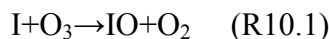


F10.1. Glass trap situated after the exhaust of the reaction vessel (left arm of the trap). A pale yellow powder accumulates on its bottom, thus indicating significant formation of aerosol after photolysis of I₂/O₃ mixtures. The colour suggests that the stoichiometry of the iodine oxide could be I₄O₉ [18, 173, 206].



F10.2. Group of concentration versus time curves (in molecule cm^{-3}) measured in a typical experiment at 40 hPa with $[\text{O}_3] = 2 \times 10^{15}$ molecule cm^{-3} and $[\text{I}_2] = 3 \times 10^{13}$ molecule cm^{-3} (blue circles). Red curves are the results of a simulation using the base kinetic model (T10.1). As a result of the application of techniques for reduction of noise and separation of overlapping absorbers [123, 125], the observational error (dotted blue lines) arise mainly from uncertainties in the concentrations of the precursors or in the reference absorption cross sections used to scale the curves. In case of the $[\text{I}]$ curve, the error estimation considers the effect of an inhomogeneous distribution of iodine atoms (Chapter 7, section 7.2.3).

Along with the concentrations of molecules, iodine atom curves are available for all datasets (F10.2.a). The conversion of relative absorption curves for I atoms to concentration is achieved by calculating the relative difference between integrated emission and absorption Voigt line profiles and by using the oscillator strength reported by Spietz et al. [120, 124]. A recalibration of the curves has been necessary, to take into account an inhomogeneous distribution of iodine atoms in the reaction vessel caused by a partial screening of the flash by the joints of the cross axis (see 7.2.4). The decay of iodine atoms shown by the ARAS curves is caused by the reaction:



F10.3. Panel (a) shows logarithmic plots of $[\text{I}]$ as a function of time for 40 hPa (squares) and 400 hPa (points). The O_3 concentrations are 2×10^{15} molecule cm^{-3} (fastest decays) and 7×10^{15} molecule cm^{-3} (slowest decays). Two linear sections can be observed in all curves. The first section (dashed line) is pressure independent and consistent with R10.1. The second linear section results from iodine atom recycling by R10.2. The pressure dependence of the slopes suggests a pressure dependence of the iodine atom yield of reaction R10.2. Panel (b) shows a plot of pseudo first order decay coefficients k' versus $[\text{O}_3]$. The slope of the regression curve (black thick line) is in agreement with the well established rate coefficient of R10.1 [29] (black thin line). The dashed lines indicate the 95% confidence region.

Pseudo first order fitting of the iodine atom decays has been performed in order to check the reliability of the calibration of the ARAS curves (figure F10.3). The rate coefficient $k_{10.1}=(1.24\pm 0.20)\times 10^{-12}$ cm³ molecule⁻¹ s⁻¹ has obtained, in good agreement with the well established IUPAC recommendation for R10.1 at 298 K [29] within the error limits

10.3. Data analysis

Figure F10.2 shows a group of curves measured in a typical experiment at 40 hPa. The red curves are the results of an optimised simulation by using a complex kinetic model. In spite of the complexity of I₂/O₃ photochemistry, classical kinetic analysis of the concentration curves of I, IO and OIO has been carried out first in order to gain some insights into the chemical mechanism.

Chemical simulations have been performed by numerical integration of the set of ordinary differential equations (ODE) resulting from the chemical mechanism:

$$\begin{aligned} \frac{dc_i(t)}{dt} &= f_i(c_1, \dots, c_n; k_1, \dots, k_m; t) \quad ; \quad i = 1, \dots, n \\ c_i(0) &= 0; \end{aligned} \quad (\text{E10.2})$$

where k_1, \dots, k_m are the rate coefficients and photolysis rates on which the concentrations c_1, \dots, c_n depend. This ODE system is stiff, as a result of the existence of rate coefficients of different orders of magnitude. A numerical integration algorithm based in the so called Numerical Differentiation Formulae [207] has been used to solve this problem.

A moving average smoothing of the simulated intensity versus time curves is required to model the finite (4-5 pixel wide) temporal characteristic function of the CCD chip [79, 125, 200]. Illumination experiments undertaken in this laboratory have shown that a 5 point square temporal averaging function is enough to take into account this effect. Thus, the concentration curves obtained as output of the kinetic simulation for species monitored with the CCD camera are converted to intensity by using an

arbitrary constant reference intensity, smoothed with the rectangular moving average function, and converted back to concentration

The determination of rate constants and assessment of reaction mechanisms based on fitting of a single concentration versus time curve for complex chemical systems is error prone, because the non linear system of equations to be solved by the fitting algorithm is often mathematically ill-determined and prior knowledge of non observed constituents is then required. Rather, it is advisable to fit simultaneously the concentration versus time curves of as many species as possible. Therefore, after simulation and smoothing, the relevant simulated curves are concatenated in a single vector, which is fitted to the analogous vector of observations by allowing selected reaction rate coefficients of the model to vary. A constrained non-linear minimization algorithm has been used [153] to solve a least squares problem with known covariance (experimental error, mainly arising from the uncertainties of the absorption cross sections used to scale the temporal behaviours). This means that the uncertainty of the measured curves determines how much each observation in the data set influences the final parameter estimates. For example, from figure F10.2 it is clear that the influence of the I₂ curves on the fitted parameters will be much smaller than those of the iodine atom and IO curves.

The photolysis rates are time dependent, because of the finite duration of the photolysis pulse (~ 0.1 ms). Therefore, a parameterisation of the observed flash intensity time profiles must be included in the simulating module, in a similar fashion to a prescribed concentration curve. The absolute scaling of the time dependent photolysis rate of I₂ can be determined from measured iodine atom curves obtained in photolysis experiments without O₃. These observations are fitted with the curves obtained by numerically solving the following differential equation:

$$\frac{d[\text{I}]}{dt} = 2\tilde{f}(t; t_{\max}, FWHM)k_{\max}[\text{I}_2] \quad (\text{E10.3})$$

where $\tilde{f}(t; t_{\max}, FWHM)$ is the parameterised time dependence of the photolysis rate, normalised to unity at the maximum, and k_{\max} the maximum photolysis rate.

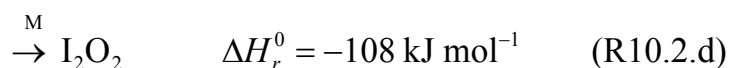
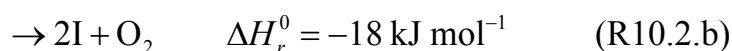
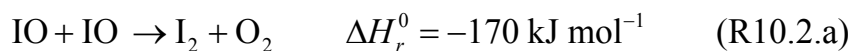
The finite duration of the photolysis flash also affected the freshly produced IO. Unfortunately it was not possible to generate IO in a steady concentration. In order to estimate its photolysis rate, a simplified simulated chemical scheme has been fitted to the first part (excluding the OIO decay) of the observed curves of I_2 , I, $\text{IO}(X^2\Pi_{3/2}, v''=0)$ and OIO. The curves used for this purpose were only those obtained at 400 hPa, to avoid possible complications related to vibrationally excited IO generated by the flash (the equilibrium distribution is considered). The activation rates for $\text{IO}(X^2\Pi_{3/2}, v''=1)$ and $\text{IO}(X^2\Pi_{3/2}, v''=2)$ were obtained in a similar way in experiments at low pressure by assuming that the non equilibrium distribution of IO is directly generated by the photolysis flash.

10.4. Results

10.4.1. Conventional kinetic analysis

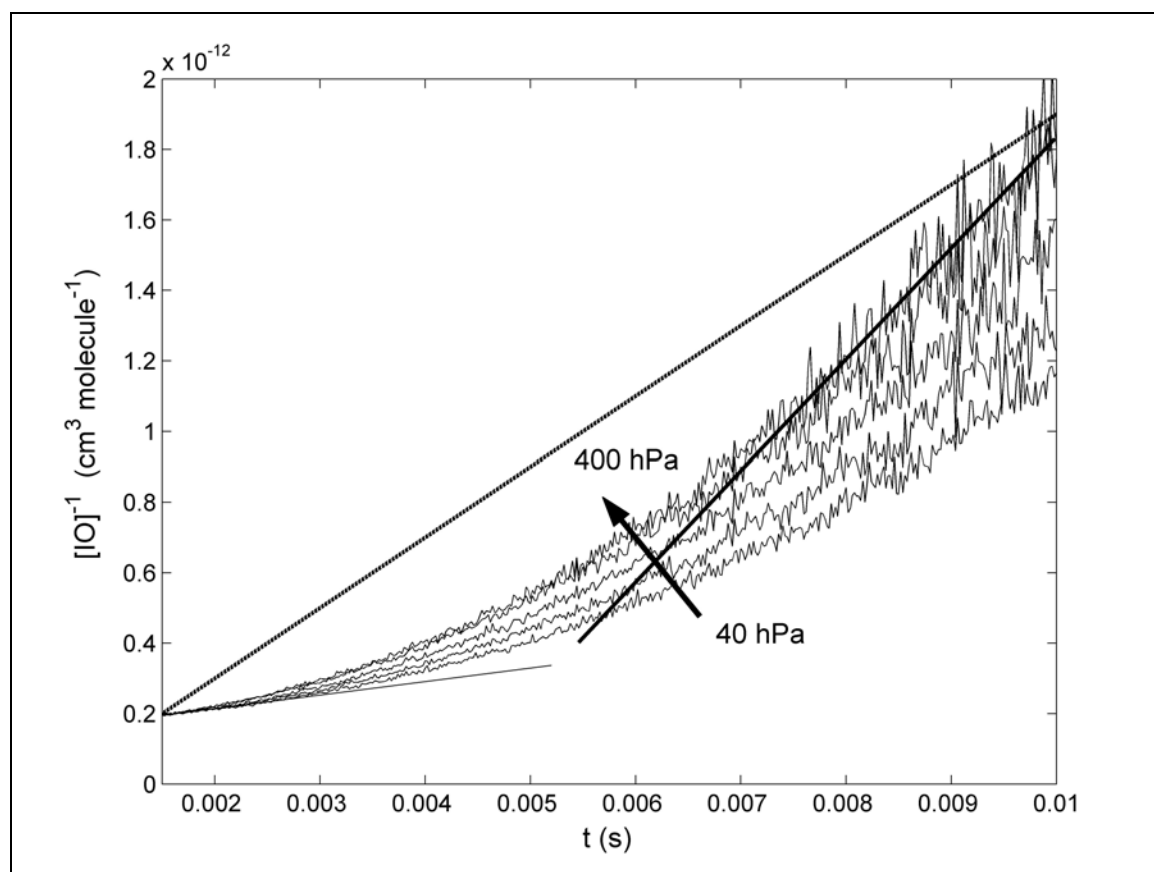
10.4.1.1. Overall rate coefficient of $\text{IO}+\text{IO}\rightarrow\text{products}$.

In systems where O_3 is in large excess over I, second order decays of IO have been reported for low concentrations of iodine [80, 171]. It has been argued that in this system the rate coefficient of the IO self reaction obtained by second order fitting is effectively reduced, due to fast I atom recycling through one of its channels:

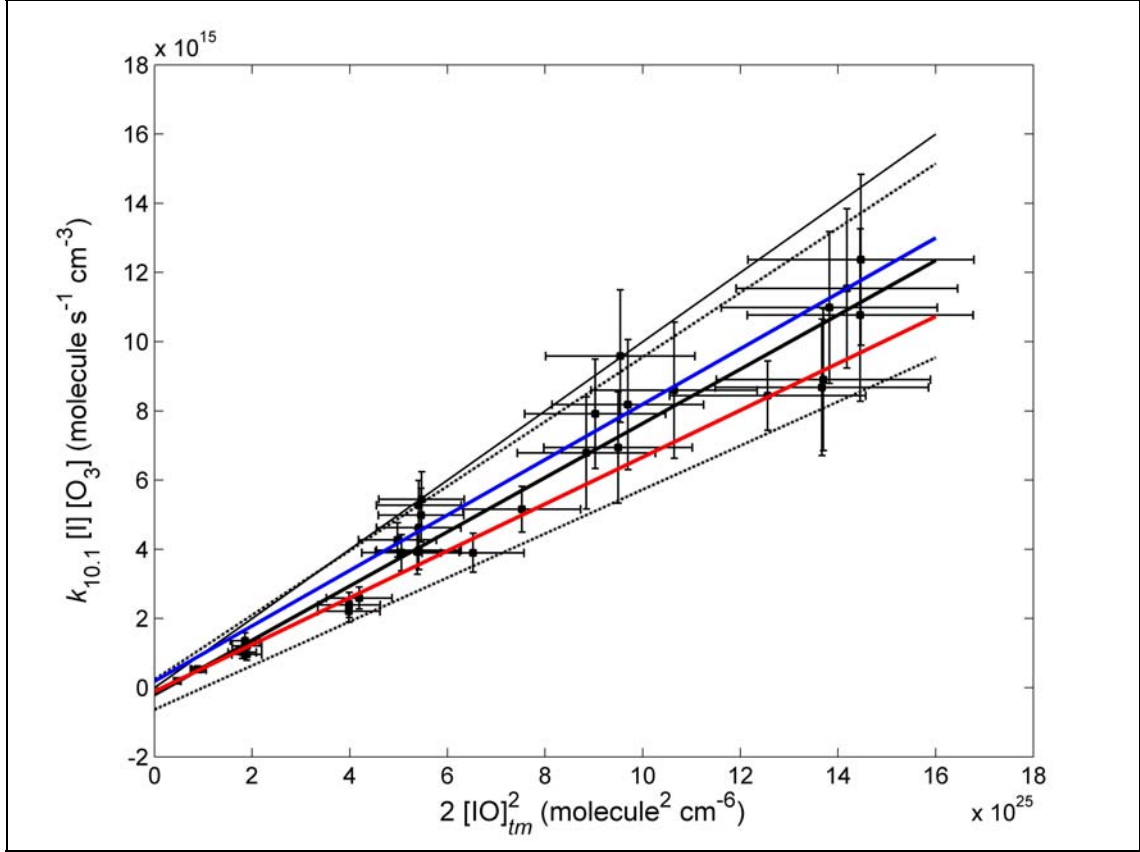


In the present study, such an effective reduction is not expected because the

observed iodine atom curves are taken into account in the kinetic analysis. The curvature of $[\text{IO}]^{-1}$ indicates that IO does not decay in a simple second order manner. Rather, a loss in addition to R10.2 and a production of IO are identified as being active during the decay (F10.4). In general, the IO decays are well described by combining a first and a second order loss processes. However, the minima of the Least Squares cost function are not well defined for the two free parameters considered, and in addition the source of IO cannot be accounted for. These fits yield pseudo first order rate coefficients for the secondary loss of about 100 s^{-1} . To avoid these uncertainties and estimate the rate coefficients, a steady state analysis of the maxima of the $[\text{IO}]$ versus time curve (Figure 2c) has been carried out by considering reactions R10.1 and R10.2.



F10.4 Plots of $[\text{IO}]^{-1}$ as a function of time for different pressures, showing non-second order behaviour of IO. The dashed line indicates the linear behaviour expected for $[\text{IO}]^{-1}$ when IO decays in second order (rate coefficient recommended by the IUPAC [29]). The recycling of iodine atoms through the IO self reaction and subsequent IO reformation are responsible for the smaller slope in the initial steps (thin solid line). In the final steps, further sinks of IO cause an increase of the slope (thick solid line) with respect to the second order rate coefficient.



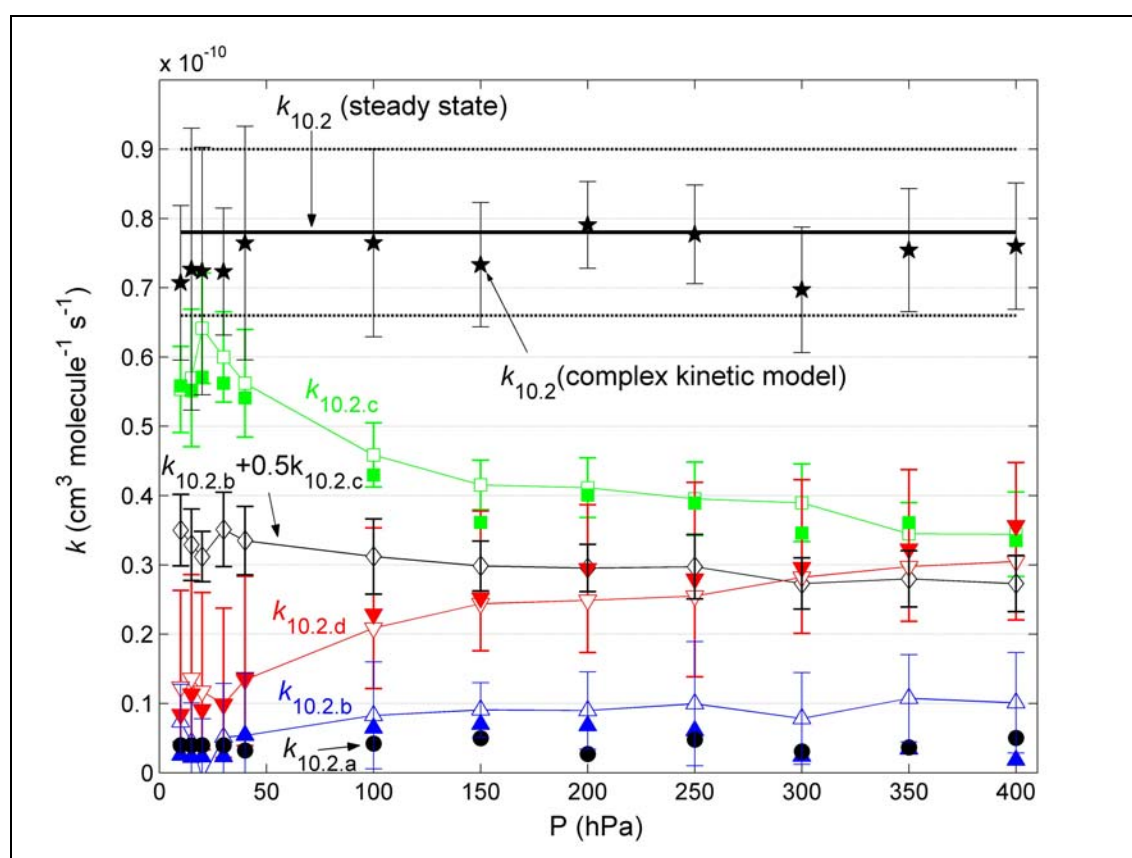
F10.5. Steady state analysis of the [IO] versus time curves. At the time where [IO] reaches its maximum (t_m), the rates of production and consumption of [IO] are equal, and an estimation of $k_{10,2}$ can be obtained by regressing one against the other if only reactions R10.1 and R10.2 are considered. The result for $k_{10,2}$ obtained by linear regression with error in both coordinates (solid thick black line) is smaller than the IUPAC recommended value (indicated by a thin solid line). The correlation coefficient of the fit was $R^2 = 0.94116$. The dashed black lines indicate the 95% confidence region. The blue line is the linear fit to experimental points with $P \geq 100$ hPa. At lower pressures ($P \leq 40$ hPa) the fit (red line) yields a slightly smaller slope.

At the maximum of [IO] (reaction time t_m) the rate of change of IO concentration is zero:

$$0 = \left. \frac{d[\text{IO}]}{dt} \right|_{[\text{IO}](t_m) = \max([\text{IO}])} = k_{10,1}[\text{O}_3]_{t_m}[\text{I}]_{t_m} - 2k_{10,2}[\text{IO}]_{t_m}^2 \Rightarrow 0.5k_{10,1}[\text{O}_3]_{t_m}[\text{I}]_{t_m} = k_{10,2}[\text{IO}]_{t_m}^2 \quad (\text{E10.4})$$

A plot of the rate of production of IO, $k_{10,1}[\text{O}_3]_{t_m}[\text{I}]_{t_m}$, by reaction (1) versus $2[\text{IO}]_{t_m}^2$ is shown in Figure F10.5. $k_{10,2}$ is determined from the slope of the plot of $y = k_{10,1}[\text{O}_3]_{t_m}[\text{I}]_{t_m}$ as a function of $x = 2[\text{IO}]_{t_m}^2$ and estimated by a least squares fitting procedure taking experimental error in both coordinates into account [152]. The error in the knowledge of the dependent variable y comprises of the errors in $[\text{O}_3]$ and $[\text{I}]$, which

are <15%, and the knowledge of the rate coefficient $k_{10.1}$, which has a literature value $k_{10.1} = (1.30 \pm 0.05) \times 10^{-12} \text{ cm}^3 \text{ molecule}^{-1} \text{ s}^{-1}$ [29], whilst that of the independent variable x includes an 8% uncertainty in the IO absorption cross section [125] (see also Appendix C). The rate coefficient obtained for reaction R10.2 in this manner is $k_{10.2} = (7.8 \pm 1.2) \times 10^{-10} \text{ cm}^3 \text{ molecule}^{-1} \text{ s}^{-1}$, the error interval given being the 95% confidence level. No pressure dependence can be discerned outside the 95% confidence region by fitting separately the data obtained at low and high pressures.



F10.6. Overall rate coefficient (solid thick line) with its corresponding uncertainty (thin dotted line), rate coefficient of iodine atom producing channels (diamonds), and rate coefficients of individual channels of reaction R10.2 (circles: R10.2.a, triangles up: R10.2.b, squares: R10.2.c, triangles down: R10.2.d). Open symbols connected by a thin line correspond to conventional kinetic analysis and filled symbols to optimized simulations. For clarity, only the uncertainties of the conventional kinetic analysis for the different channels are shown. Five pointed stars with error bars indicate the values of $k_{10.2}$ obtained by adding the rate coefficients of the individual channels obtained from optimized simulations.

The potential inhomogeneity within the White-Optic path (see Chapter 7, section 7.2.4) makes unfeasible an alternative approach to determine simultaneously $k_{10.1}$ and

$k_{10,2}$, which consists of the linear regression of the observed $[\text{IO}](t)$ curve against the cumulatively integrated curves of $[\text{I}]$ and $[\text{IO}]^2$. The residuals of these fits both to experimental and simulated data show systematic features as a result of the accumulation of systematic error due to cumulative integration.

10.4.1.2. Branching ratios of $\text{IO}+\text{IO}\rightarrow\text{products}$.

In Figure F10.3.a, two separate linear regions in the plot of $\log [\text{I}]$ versus time are identified. The slowing down of the loss rate provides evidence for a source of $[\text{I}]$. The temporal behaviour of this part of the decay of I atoms combines loss through R10.1 and production via R10.2.b and R10.2.c. The slopes of these regions of the logarithmic plots of $[\text{I}]$ versus time are shown in F10.3.a and are pressure dependent. This implies that reactions R10.2.b and R10.2.c are pressure dependent. Assuming that the only processes relevant for iodine atoms are reactions R10.1, R10.2.b and R10.2.c, the rate coefficient of the sum of iodine producing channels $k_{10,2,b}+0.5k_{10,2,c}$ can be estimated by regression as follows:

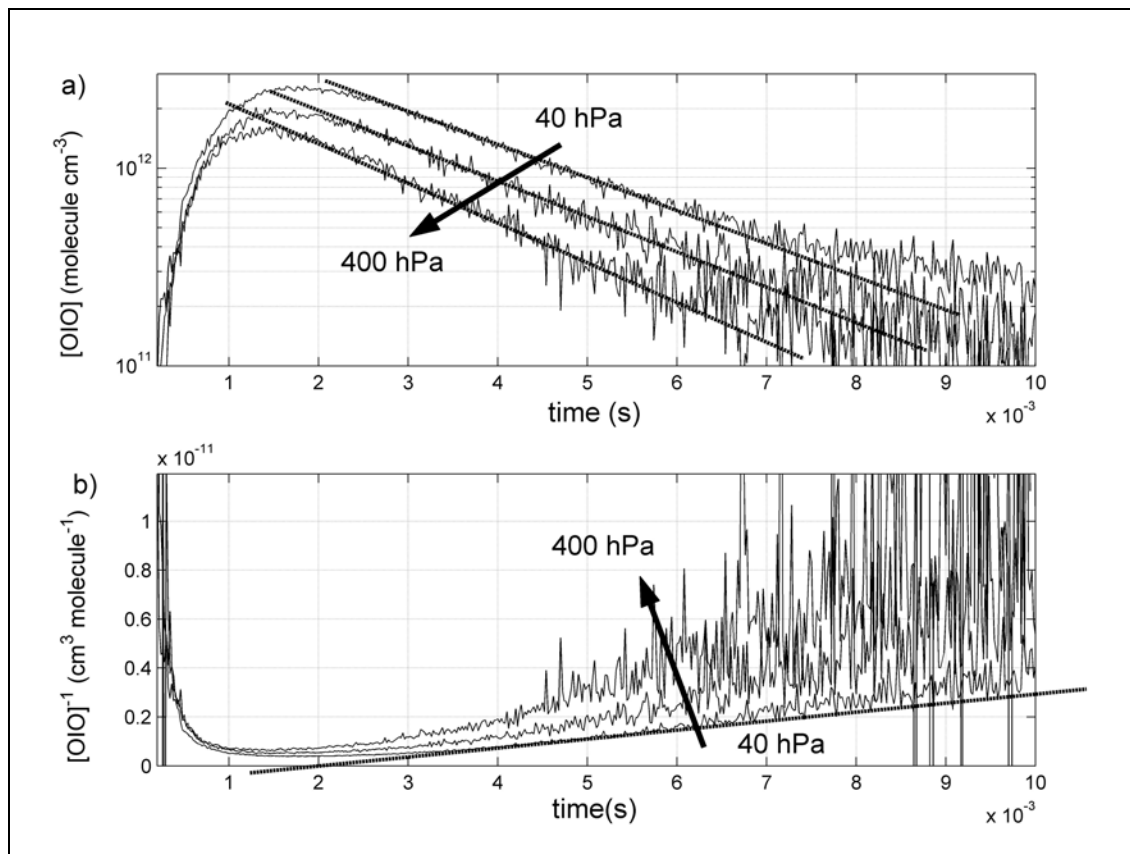
$$-c[\text{I}] = \frac{d[\text{I}]}{dt} = -k'[\text{I}] + 2(k_{10,2,b} + 0.5k_{10,2,c})[\text{IO}]^2 \Rightarrow (k'-c)[\text{I}] = 2(k_{10,2,b} + 0.5k_{10,2,c})[\text{IO}]^2 \quad (\text{E10.5})$$

where $k'=k_{10,1}[\text{O}_3]$ and c are the observed slopes of the $\log [\text{I}]$ curve (see F10.3.a). The values of $k_{10,2,b}+0.5k_{10,2,c}$ obtained with this method are pressure dependent and decrease by about 20% from 10 hPa to 400 hPa (Figure F10.6).

To investigate the order of the rate of loss of OIO, plots of $\log [\text{OIO}]$ and $[\text{OIO}]^{-1}$ versus time were made and are shown in F10.7. The decay of OIO in time is much closer to first order than second order. This implies that the disproportionation of OIO alone cannot explain the decay of OIO in the system. A regression analysis of the $[\text{OIO}]$ versus time curve utilizing the cumulative integral of $[\text{IO}]^2$ and $[\text{OIO}]$ has been undertaken to obtain estimates of the rate coefficient of R10.2.c and the effective pseudo first order loss rate coefficient for OIO:

$$[\text{OIO}](t) - [\text{OIO}]_0 = k_{10.2.c} \int_0^t ([\text{IO}](t))^2 dt - k'_{\text{OIO} \rightarrow \text{loss}} \int_0^t [\text{OIO}](t) dt \quad (\text{E10.6})$$

As shown in F10.6, the results of the analysis indicate that $k_{10.2.c}$ is pressure dependent. The values of $k_{10.2.b}$ can be determined by combining the results obtained for $k_{10.2.b} + 0.5k_{10.2.c}$ and $k_{10.2.c}$. Channel R10.2.b appears to be of minor importance in the IO self reaction under the condition studied.

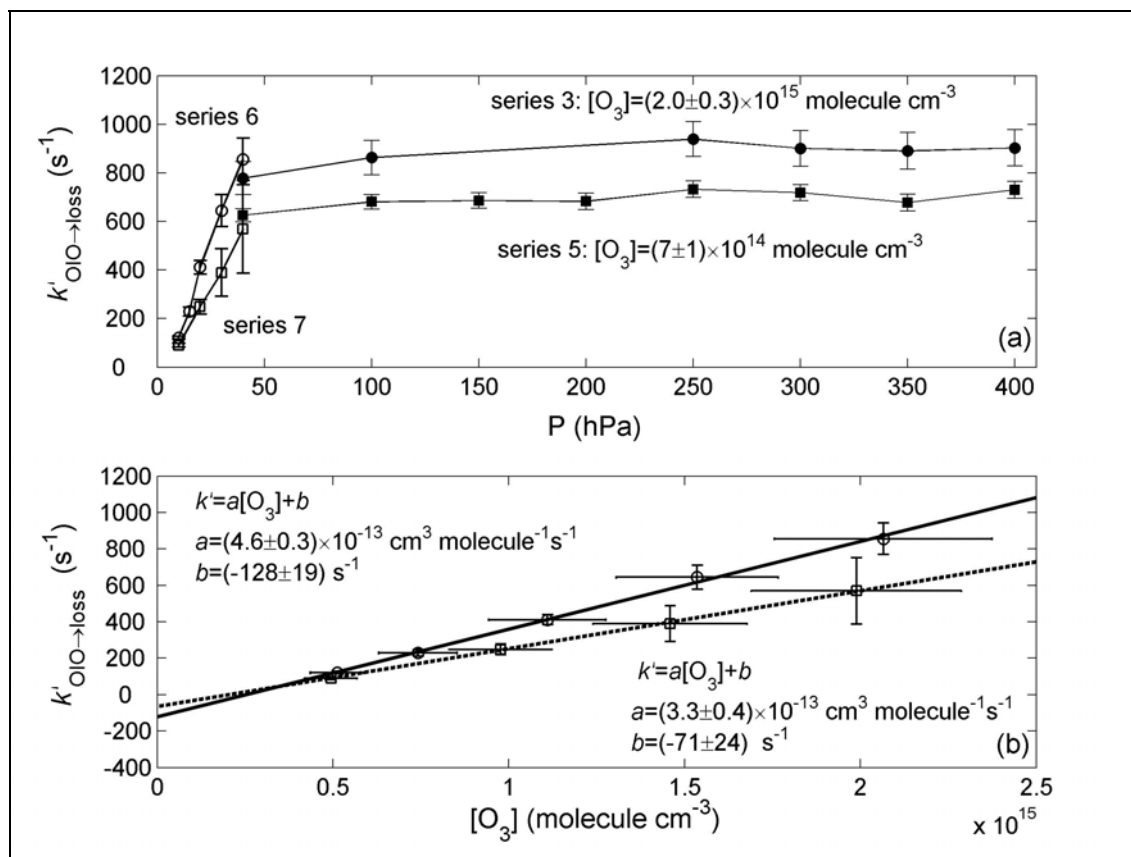


F10.7. Plots of $\log [\text{OIO}]$ (panel a) and $[\text{OIO}]^{-1}$ (panel b) against time for OIO time behaviours. The decay of OIO adjust in a large section to a direct proportionality of $\log[\text{OIO}]$ rather than to a direct proportionality of $[\text{OIO}]^{-1}$ to time. As shown in the panel b, the OIO self reaction alone does not explain the decay of OIO. It decays more rapidly than second order, indicating a multi-step mechanism in which OIO reacts with secondary products of its self reaction.

10.4.1.3. Fate of OIO

The pseudo-first order decay rate coefficient $k'_{\text{OIO} \rightarrow \text{loss}}$ has a small pressure dependence between 40 and 400 hPa (F10.8.a) and takes values around 800 s^{-1} . If a single bimolecular reaction were responsible for the removal of OIO, assuming a collision rate of $2 \times 10^{-10} \text{ cm}^3 \text{ molecule}^{-1} \text{ s}^{-1}$ as the upper limit for the rate constant, then

the reaction partner is required to have a concentration larger than about 4×10^{12} molecule cm^{-3} and to persist for at least 10 ms after the photolysis flash. Of the reactants and products excluding O_2 and N_2 , only I_2 and O_3 fulfils these conditions (see F10.2 and T7.1).



F10.8. Panel (a) shows the apparent pseudo first order decay rate coefficient (in s^{-1}) of OIO obtained from equation (E10.6). Individual results for four series of measurements are shown (T7.1, filled circles: series 3; filled squares: series 5; empty circles: series 6; empty squares: series 7). Series 3 and 5 were run with constant concentrations of precursors, but with a 3-fold difference in $[\text{O}_3]_0$ between them. A factor 3 difference in the pseudo first order rate coefficient is not observed, indicating that the reaction of O_3 with OIO is not primarily responsible for the removal of OIO. Panel (b) shows linear fits of $k'_{\text{OIO} \rightarrow \text{loss}}$ against $[\text{O}_3]$ for series 6 (circles, solid line) and 7 (squares, dashed line). Direct proportionality is not observed (non-zero slopes). A 6-fold drop of $[\text{I}_2]$ (series 7) causes a 40% decrease of the slope, suggesting that speed of the OIO consumption depends on the amount of iodine oxides generated.

A direct proportionality between $k'_{\text{OIO} \rightarrow \text{loss}}$ and $[\text{O}_3]$ is not observed. The 3-fold change in $[\text{O}_3]_0$ does not result in a 3-fold smaller value for $k'_{\text{OIO} \rightarrow \text{loss}}$ (see F10.8, series of experiments 1 and 3) and therefore reaction with O_3 is discounted as the explanation of the pseudo first order behaviour of OIO. The decrease of $k'_{\text{OIO} \rightarrow \text{loss}}$ for $P < 40$ hPa can not be directly interpreted as a pressure dependence, because the concentration of the

precursors in the experiments recorded at these pressures also varied. F10.8.b show linear fits of $k'_{\text{OIO} \rightarrow \text{loss}}$ against $[\text{O}_3]_0$ for experimental sets 4 and 5. In both cases the intercepts are significantly different from zero, indicating again that $k'_{\text{OIO} \rightarrow \text{loss}}$ is not directly proportional to $[\text{O}_3]_0$.

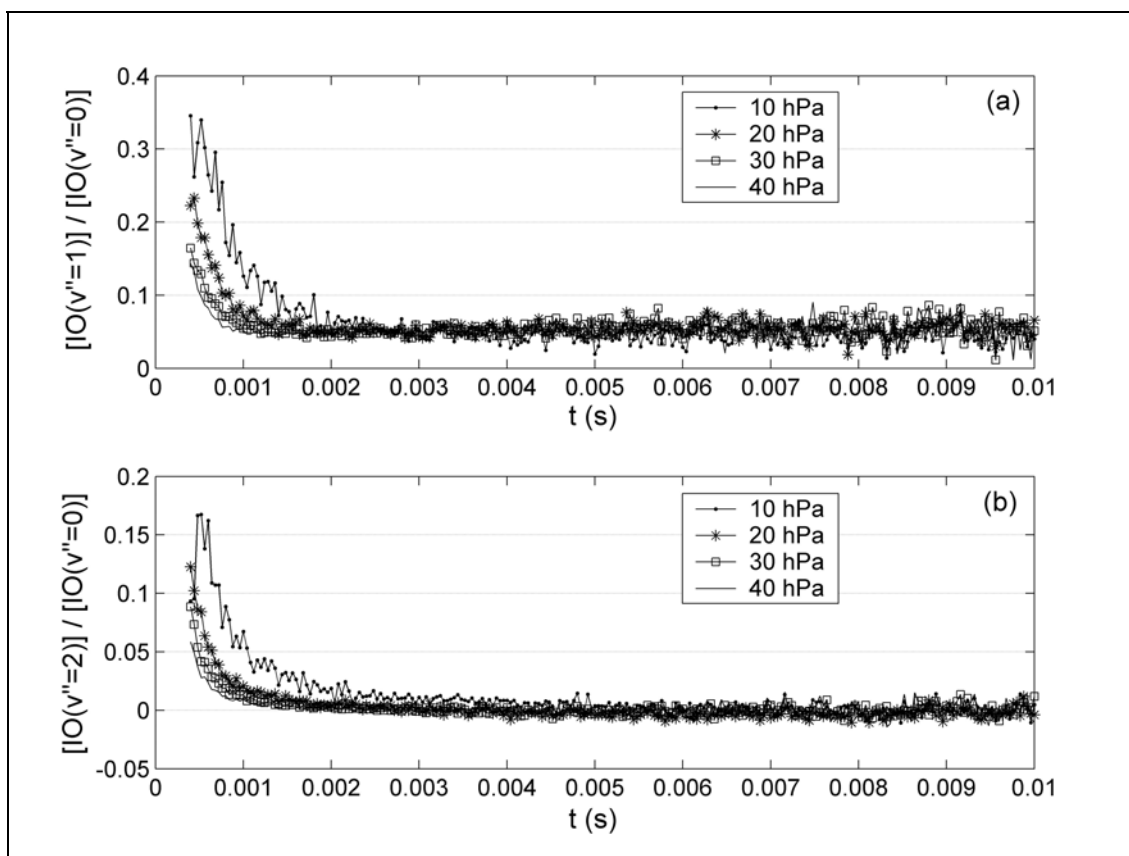
A 6-fold decrease of $[\text{I}_2]_0$ causes a significant, but not proportional decrease of $k'_{\text{OIO} \rightarrow \text{loss}}$ (F10.8.b). It is assumed that I_2 does not react with OIO and the observed decay of OIO is therefore attributed to be dependent on the concentrations of iodine oxides generated at higher I atom concentrations.

10.4.1.4. Excited IO species

In the experiments performed at pressures lower than 100 hPa, vibrational bands of IO corresponding to transitions $v' \leftarrow v''$ with v'' up to 7 have been observed [126]. Figure F10.2.d and F10.2.e show respectively the temporal behaviours of $\text{IO}(X^2\Pi_{3/2}, v''=1)$ and $\text{IO}(X^2\Pi_{3/2}, v''=2)$, recorded at 40 hPa. The temporal behaviours of the three IO species are clearly different. The peak concentrations of vibrationally excited IO occur immediately after the flash, and relaxation to thermal equilibrium takes about 3 ms. After thermal equilibrium is established at 298 K, the observed optical densities corresponding to transitions from levels $v'' > 1$ are below the detection limit and the ratio of $\text{IO}(X^2\Pi_{3/2}, v''=1)$ to $\text{IO}(X^2\Pi_{3/2}, v''=0)$ is constant and about 0.05. Assuming a Boltzmann distribution of the IO population, the ratio calculated, using the vibrational constants reported by Bekooy et al. [136] is ~ 0.04 . As the pressure is increased, the peak concentration of $\text{IO}(X^2\Pi_{3/2}, v'' > 0)$ decreases and thermal equilibrium is more rapidly achieved. For pressures above 100 hPa, the thermal equilibrium is achieved within the first time step of the experiment. These facts suggest that the source of the non-equilibrium population is related to the flash and that the most important sink for $\text{IO}(X^2\Pi_{3/2}, v'' > 0)$ is collisional quenching:



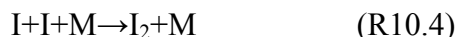
The observed exponential decays of $\text{IO}(X^2\Pi_{3/2}, v''=2)$ (F10.2.e) are consistent with R10.3. Assuming that collisional quenching is the dominating process, the rate coefficient of R10.3 with $v''=2$ can be estimated by regression analysis of the time constants of the observed decays and $[\text{M}]$. As a result, $k_{10.3, v''=2}$ is estimated to be $(2.2 \pm 0.5) \times 10^{-15} \text{ cm}^3 \text{ molecule}^{-1} \text{ s}^{-1}$. The non-zero intercept of the regression, which could be indicative of de-excitation by emission, is statistically not significant. The value obtained for $k_{10.3}$ is a lower limit, because relaxation of $\text{IO}(v''=3)$ to $\text{IO}(v''=2)$ has been neglected.



F10.9. Ratios $[\text{IO}(v''=1)]/[\text{IO}(v''=0)]$ (panel (a)) and $[\text{IO}(v''=2)]/[\text{IO}(v''=0)]$ (panel (b)) for experiments carried out at different pressures. Non-equilibrium populations can be observed in the initial time steps, suggesting a source of vibrationally excited IO species related to the photolysis flash. The concentrations of these species at the lowest pressures are significant compared to the concentrations of $\text{IO}(v''=0)$, indicating a substantial contribution of collisional deactivation of the excited species to the formation of ground state IO. Relaxation to thermal equilibrium ratios $[\text{IO}(v''=1)]/[\text{IO}(v''=0)] \sim 0.05$ and $[\text{IO}(v''=2)]/[\text{IO}(v''=0)] \sim 0.001$ occurs after about 3 ms.

10.4.1.5. Formation of molecular iodine

The half time for rise of I₂ from termolecular recombination of I, i.e. reaction:



is about 500 ms for $[I]_0=10^{13}$ molecule cm⁻³ and 400 hPa [29, 199]. With a typical ozone concentration of 10¹⁵ molecule cm⁻³, the lifetime of free iodine atoms is about 2 ms. Therefore, third body iodine atom recombination does not occur. Indeed, the concentration versus time curves of I₂ recorded in the present work are nearly constant within the observation interval (F10.10).

The uncertainties of the I₂ concentration curve, which originate mainly from spectral separation (Chapters 8 and 9), are small with respect to the absolute concentration level (about 3%), but large compared with potential changes caused by the chemistry under study. Nevertheless, the small reformation of I₂ observed seems correlate with the rate of production of the IO self reaction [29, 80, 170]. A regression analysis of the [I₂] versus time curve utilizing the cumulative integral of [IO]² enables to obtain an estimate of the rate coefficient of R10.2.a:

$$[I_2](t) - [I_2]_0 = k_{10.2.a} \int_0^t ([IO](t))^2 dt \quad (\text{E10.7})$$

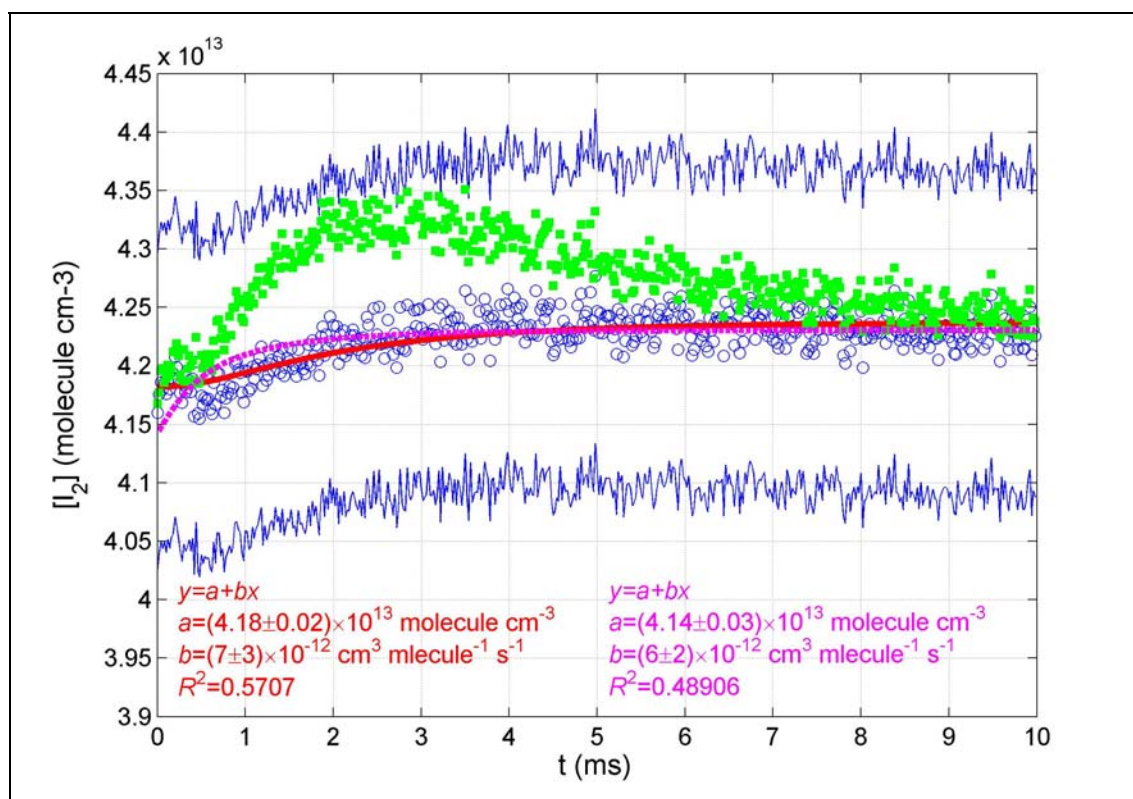
According to this analysis, the small contribution of channel R10.2.a to the overall rate coefficient takes a value about 5×10^{-12} molecule cm⁻³.

On the other hand, in previous experiments performed in this laboratory, different degrees of fast I₂ recovery had been observed for smaller [I₂]₀/[O₃]₀ ratios. Enhanced I-atom recombination would result from a molecule-complex mechanism:



with I-R designating iodine oxides with a protruding iodine atom at one end [83, 84, 170, 171]. If this mechanism were responsible for the early increase of I₂, the most

plausible chaperon R would be IO. However, enhanced iodine atom recombination fits worse to the observed data (see F10.10).



F10.10. Concentration versus time curve of I_2 (circles) from an experiment of series 3 ($P = 200$ hPa). The corresponding error intervals (solid blue lines) are larger than the OIO concentrations recorded in the same experiment (green squares, offset for clarity), indicating that the potential changes in the I_2 curve resulting from reaction R10.2.a would be under the uncertainty level ($\sim 3\%$). Nevertheless, some degree of correlation can be found between the I_2 curve and the cumulatively integrated $[IO]^2$ curve. Enhanced iodine atom recombination (magenta line) fits worse the data. Note that the effective recombination rate coefficient obtained from this fit ($6 \times 10^{-12} \text{ cm}^3 \text{ molecule}^{-1} \text{ s}^{-1}$) is two orders of magnitude faster than the effective rate coefficient of R10.4 at 200 hPa ($5 \times 10^{-14} \text{ cm}^3 \text{ molecule}^{-1} \text{ s}^{-1}$, see [29, 199])

It can not be completely discarded that the small increase of the I_2 concentration is totally or partially caused by residual overlapping of absorptions in the separated temporal behaviours (Chapter 8).

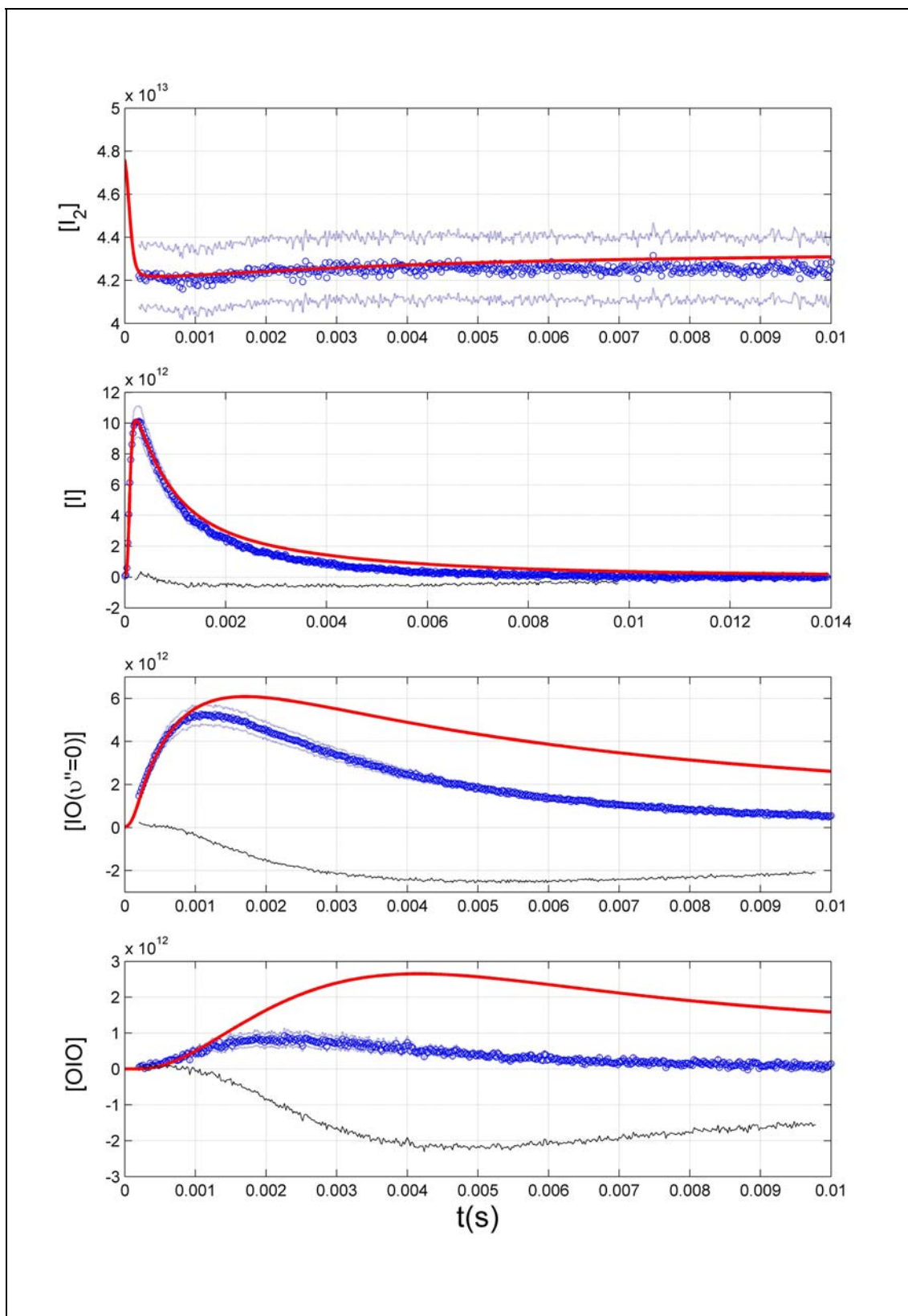
10.4.2. Complex kinetic modelling of the I_2/O_3 photochemistry

10.4.2.1. Proposed Mechanism

The conventional kinetic analysis described previously illustrates the complexity of the I_2/O_3 photochemical system. Many of the reactions are poorly characterized or even unknown, e.g. the dissociation of the IO dimer and the consumption of OIO. In

order to investigate the mechanism, simulations of the chemical constituents derived from chemically plausible reaction schemes have been mathematically compared with the observations. In this manner a mechanism able to reproduce the experimental data, whose reaction steps are listed in Table T10.1, was identified.

Ground state iodine atoms are generated by photolysis of molecular iodine. In the presence of an excess of ozone, sinks for iodine atoms other than R10.1 have been judged to be unimportant. In addition, no enhanced I₂ re-formation has been observed, which could indicate a molecule complex mechanism [151] resulting in an enhanced I-atom recombination. The major source of IO in the system is R10.1. Reaction R10.2 is the primary sink for IO. At the lowest pressures under study, the initial amount of vibrationally excited IO is comparable to ground state IO (F10.2). Therefore, activation and deactivation of IO vibrational states have been considered. It has been assumed that the quenching of all vibrational states proceeds at the same rate ($k_{10.3, v''=2}$). A small fraction of ozone (< 0.05%) could be photolysed. Some photolysis of newly formed IO may also occur as a result of the relatively long pulse of photolytic radiation. Ozone would be subsequently regenerated by combination of O(³P) with O₂ and IO would be formed by reaction of O(³P) with I₂. As a result of the large excess of I₂ over O(³P), this minor source of IO has only an influence on the value of [IO] in the initial time step of the data recordings. It is essentially impossible to distinguish between both sources of O(³P). For the conditions of this study, O₃ photolysis can be assumed to be insignificant.



F10.11. Blue circles: experimental data recorded at 400 hPa, with $[O_3] = 2 \times 10^{15}$ molecule cm^{-3} and $[I_2] = 6.3 \times 10^{13}$ molecule cm^{-3} . Dotted blue lines: experimental error intervals, obtained as explained for F10.2. Solid red lines: simulated concentrations obtained with a mechanism considering exclusively OIO addition steps (R10.7) with $n=1\dots 4$. Rate coefficients for R10.7 are approximated by collision frequency factors from kinetic theory. The lifetime with respect to re-dissociation for both IOIO and I_2O_4 is assumed to be 0.2 ms. The rate coefficients of R10.2 are those obtained by conventional kinetic analysis.

The information provided by conventional kinetic analysis and the OIO addition steps mechanism proposed in previous studies [108-111], have suggested the following set of reactions:

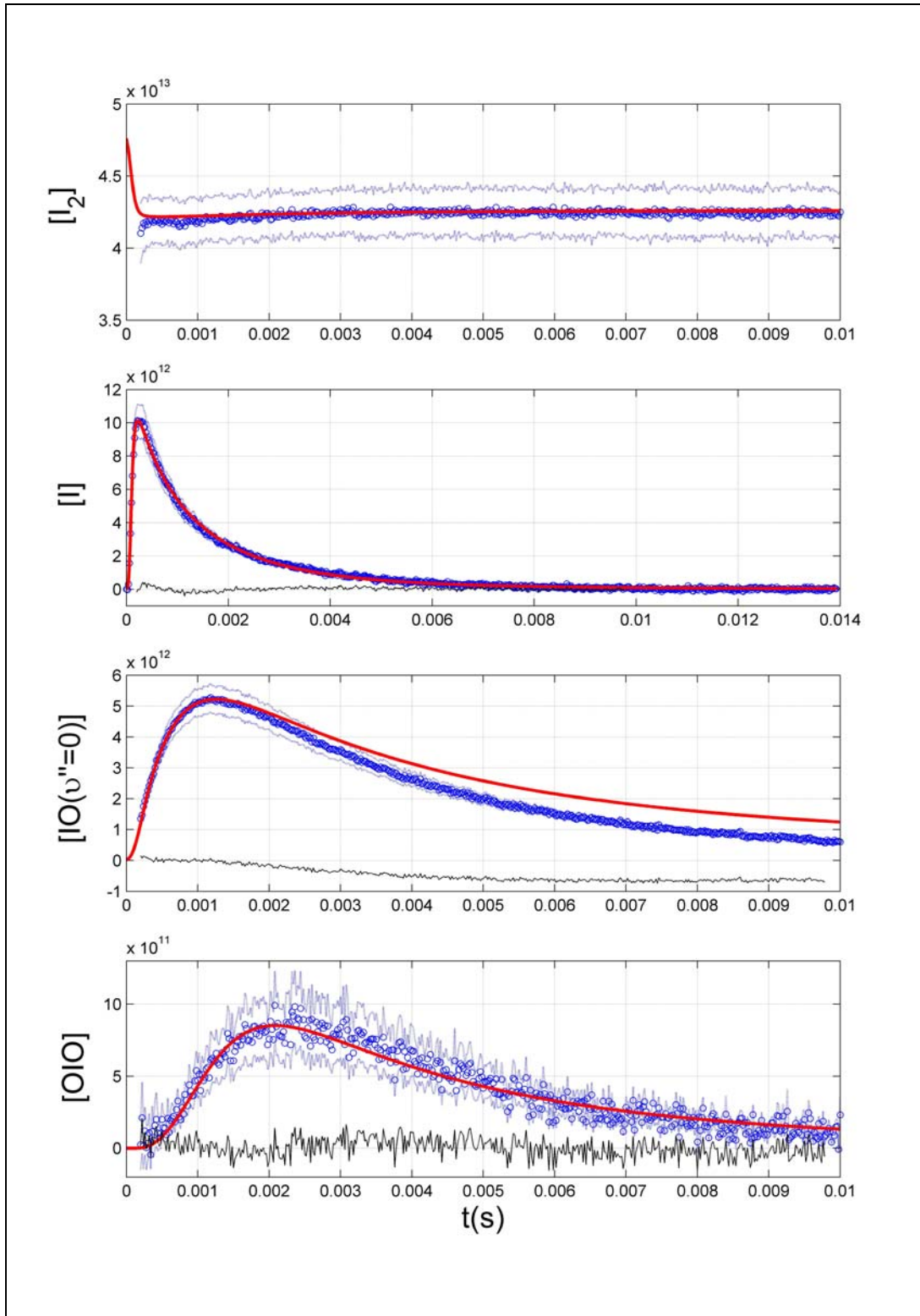


where $(\text{OIO})_n$ are polymeric structures [108]. However, by using forward and backward rate coefficients derived from kinetic theory for the set of reactions R10.7 and considering rapid dissociation of the IO dimer, the experimental data is not properly reproduced (see F10.11). Therefore, it can be concluded that the commonly accepted mechanism [110] is not able to account for the gas phase chemistry at short reaction times. In order to find a mechanism, which is able to reproduce the observations, it has been first assumed that backward reactions are slow. This assumption and its consequences are the subject of a sensitivity study presented below. In addition, the use of a common rate coefficient for all the reactions encompassed in reaction R10.7 [208] has been preferred against fixed collision frequency factors derived from kinetic theory, to avoid the large uncertainties in the geometry and density of these molecules. The collision rate coefficient, assuming spherical size, is given by [151]:

$$k = d^2 \sqrt{\frac{8 \pi k_B T}{\mu}} \quad (\text{E10.7})$$

where d is the collisional diameter and μ the reduced mass of the colliding molecules. The rather simplistic assumption of a common value of $k_{10.7}$ recognizes that one of the steps might be rate limiting and is also supported by the following arguments:

- a) Independently of the density assumed for the $(\text{OIO})_n$ clusters, the differences between the collision rate coefficients for $n=1, \dots, 4$ are small
- b) The high dipole moment of OIO [85] suggests that the rate coefficients could be dominated by long-range interaction.



F10.12 Result obtained for a mechanism considering only OIO addition steps (R10.7) with $n = 1 \dots 4$. The blue circles are the measured data, corresponding to an experimental run at 300 hPa, with $[\text{O}_3]_0 = 7 \times 10^{14}$ molecule cm^{-3} and $[\text{I}_2]_0 = 4.7 \times 10^{13}$ molecule cm^{-3} . The solid red lines are the simulated concentrations for the optimal rate coefficients. The solid blue lines are the error intervals, obtained as explained for F10.2. The optimal value of $k_{10.7}$ obtained from this fit was 4.8×10^{-10} cm^3 molecule $^{-1}$ s $^{-1}$, much larger than the collision rate coefficient ($2\text{--}3 \times 10^{-10}$ cm^3 molecule $^{-1}$ s $^{-1}$, depending on the density assumed). An additional sink for IO is clearly missing.

The set of reactions R10.7 reproduces reasonably the observed OIO decay with $n_{\max} \geq 4$. However, the common rate coefficient for R10.7 obtained in these preliminary fits is larger than the collision frequency factors by a factor 2-3. In addition a late sink for IO is missing (see F10.12). The rather large pseudo first order rate coefficients estimated for this loss process by simple kinetic analysis ($k' \sim 100 \text{ s}^{-1}$, see previous section) indicate that the reaction of IO and O₃ can not be responsible for such sink [209]. These facts have suggested the attachment of IO and OIO units to form complex polymeric adducts:

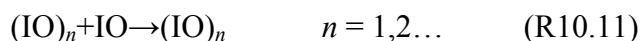


A common rate coefficient has been assigned to all reactions consisting on the attachment of IO to oligomers (R10.8 and R10.9) and another for the attachment of OIO (R10.7 and R10.10). This assumption builds on the knowledge of the different dipole moments of IO and OIO [85] The inclusion of these reactions enables to reproduce all experimental curves, and values for the reaction coefficients near the collision rates are calculated. It has been observed that $n_{\max}=4$ and $m_{\max}=2$ are enough to reproduce the data and that by increasing this value no further improvement in the correlation coefficient or significant changes in the optimal values for the rate constants is obtained. The rate coefficient of the reaction IO+OIO (R10.8, $n = 1$) was considered initially as an independent free parameter, but the results obtained were essentially equal to those obtained for $k_{\text{IO}+\text{X}}$ and the quality of the fits was not improved. In addition, the error estimates for $k_{\text{IO}+\text{X}}$ and $k_{\text{OIO}+\text{X}}$ were larger, thus indicating a redundancy between $k_{\text{IO}+\text{X}}$ and $k_{\text{IO}+\text{OIO}}$. On the other hand, the inclusion of IO+OIO in the group of reactions R10.10 ($n = 0, m = 1$) resulted in smaller values of $k_{\text{OIO}+\text{X}}$ and negligible values of $k_{\text{IO}+\text{X}}$,

with poor reproduction of the experimental OIO concentration curve and larger values of the χ^2 cost function in the multi-parameter fitting algorithm. Therefore, the reaction IO+OIO has been finally included in the group of reactions R10.8.

The observed temporal behaviours are successfully reproduced by neglecting thermal dissociation. This suggests that the IO and OIO dimers could be stable at least on a time scale < 30 ms. However, the forward and backward reactions could be encompassed in single effective forward reactions, as a result of undefined minima of the χ^2 function. This possibility is further discussed below.

Finally, the potentially slow dissociation of the IO dimer suggests its attachment to other species. Therefore, the following set of reactions has been included in the mechanism [25, 79]:



This, together with:



leads to a co-polymerization mechanism. To minimize the number free parameters, the rate coefficients of (R10.11) have been assumed to be equal to those of R10.8 and R10.9, and the rate coefficients of (R10.12) are equal to the rates of R10.7 and R10.10.

10.4.2.2. Results obtained with the proposed mechanism

The mechanism contained in T10.1 has been tested by fitting simulated concentration versus time curves to 38 full datasets at different pressures and initial mixing ratios of the precursors. The six free parameters are the rate coefficients of the channels of the IO self reaction ($k_{10.2.a}$, $k_{10.2.b}$, $k_{10.2.c}$, $k_{10.2.d}$), the rate coefficient for R10.7, R10.10 and R10.12 ($k_{\text{OIO}+\text{X}}$), and the rate coefficient for R10.8, R10.9 and R10.11 ($k_{\text{OIO}+\text{X}}$).

T10.1. Chemical mechanism used in this work for the investigation of the I₂/O₃ photochemical system.

Reaction	Rate coefficient	Ref.
$I_2+h\nu\rightarrow I(^2P_{1/2})+I(^2P_{3/2})$	$\sim 300\text{ s}^{-1}$	a
$I_2+h\nu\rightarrow 2I(^2P_{3/2})$	$\sim 800\text{ s}^{-1}$	
$I(^2P_{1/2})+O_2\rightarrow I(^2P_{3/2})+O_2(a^1\Delta_g)$	$2.6\times 10^{-11}\text{ cm}^3\text{ molecule}^{-1}\text{ s}^{-1}$	[161]
$O_3+O_2(a^1\Delta_g)\rightarrow 2O_2+O(^3P)$	$3.8\times 10^{-15}\text{ cm}^3\text{ molecule}^{-1}\text{ s}^{-1}$	[28]
$O_2+O+M\rightarrow O_3+M$	$5.9\times 10^{-34}\text{ cm}^6\text{ molecule}^{-2}\text{ s}^{-1}$	[28]
(R10.14) $I_2+O\rightarrow IO+I$	$1.4\times 10^{-10}\text{ cm}^3\text{ molecule}^{-1}\text{ s}^{-1}$	[29]
$IO+O\rightarrow O_2+I$	$1.4\times 10^{-10}\text{ cm}^3\text{ molecule}^{-1}\text{ s}^{-1}$	[29]
(R10.1) $I+O_3\rightarrow IO+O_2$	$1.3\times 10^{-12}\text{ cm}^3\text{ molecule}^{-1}\text{ s}^{-1}$	[29]
(R10.13) $IO+h\nu\rightarrow I+O(^3P)$	$\sim 2400\text{ s}^{-1}$	a
$IO(v''=0)+h\nu\rightarrow IO(v''=1,2)$		b
(R10.3) $IO(v'')+M\rightarrow IO(v''-1)+M$; $v''=1,2,\Sigma$ ^c	$2.2\times 10^{-15}\text{ cm}^3\text{ molecule}^{-1}\text{ s}^{-1}$	This work
$IO(v''-1)+M\rightarrow IO(v'')+M$; $v''=1,2,\Sigma$	$\varphi\times 2.2\times 10^{-15}\text{ cm}^3\text{ molecule}^{-1}\text{ s}^{-1}$ ^d	
(R10.2.a) $IO+IO\rightarrow I_2+O_2$	fitted (see F10.5 and T10.3)	
(R10.2.b) $IO+IO\rightarrow 2I+OIO$	fitted (see F10.5 and T10.3)	
(R10.2.c) $IO+IO\rightarrow I+OIO$	fitted (see F10.5 and T10.3)	
(R10.2.d) $IO+IO\rightarrow I_2O_2$	fitted (see F10.5 and T10.3)	
(R10.7) $(OIO)_n+OIO\rightarrow(OIO)_{n+1}$; $n=1,2,3,4$	fitted k_{OIO+X} (see F10.20 and T10.3)	
(R10.8) $(OIO)_n+IO\rightarrow(OIO)_nIO$; $n=1,2,3,4$	fitted k_{IO+X} (see F10.20 and T10.3)	
(R10.9) $(OIO)_n(IO)_m+IO\rightarrow(OIO)_n(IO)_{m+1}$ $n=1,2,3,4$; $m=1,2$	the same as for R10.8 (k_{IO+X})	
(R10.10) $(OIO)_n(IO)_m+OIO\rightarrow(OIO)_{n+1}(IO)_m$ $n=1,2,3,4$; $m=1,2$	the same as for R10.7 (k_{OIO+X})	
(R10.11) $(IO)_n+OIO\rightarrow(IO)_{n+1}IO$; $n=1,2,3,4$	the same as for R10.8 (k_{IO+X})	
(R10.12) $(IO)_n+OIO\rightarrow(IO)_{n+1}IO$; $n=1,2,3,4$	the same as for R10.7 (k_{OIO+X})	

^{a)} Determined for the experimental conditions of this work in separated photolysis experiments with mixtures of (I₂ and N₂/O₂). The photolysis rate refers to the maximum of the flash photolysis pulse ($t\sim 90\text{ }\mu\text{s}$). ^{b)} Estimated for each experiment by fitting simplified model to reduced datasets. May include both photolytic and chemical sources associated to excited state chemistry. ^{c)} Σ represents the rest of vibrational excited states of IO considered as a single species. ^{d)} In thermal equilibrium, the activation rate coefficient between levels $v''+1$ and v'' is given by the deactivation rate coefficient multiplied by a factor $\varphi=f_B(v''+1)/f_B(v'')$, i.e. the ratio of Boltzmann factors for vibrational quantum numbers $v''+1$ and v'' .

Fitted curves for 15 hPa, 40 hPa and 400 hPa are shown in F10.2, F10.13 and F10.14 respectively. Simulated non-constrained curves of several oligomers are shown in F10.15. The fits show good agreement between the simulated and the observed concentration curves of I₂, I, IO and OIO curves within the experimental uncertainties. The pressure dependence of the rate coefficients obtained is shown in F10.6 and F10.16. The results are also summarised in T10.2. As no dependence on the buffer gas has been observed, the results for N₂ and O₂ have been averaged.

The overall rate coefficient of R10.2 for each pressure can be calculated by adding the rate coefficient of each channel obtained from the optimized simulations (F10.6). No pressure dependence of the $k_{10.2}$ values obtained in this manner can be discerned outside the error intervals. The weighted average of these values is $k_{10.2} = (7.5 \pm 1.0) \times 10^{-11} \text{ cm}^3 \text{ molecule}^{-1} \text{ s}^{-1}$, in good agreement with the value of $k_{10.2}$ obtained by steady state analysis reported in the previous section. The agreement of the values obtained by simple kinetic analysis and optimized complex simulation can be explained by the small influence of R10.8, R10.9 and R10.11 at the time where IO reaches its maximum. In a sensitivity study, unconstrained simulations of the I₂/hν/O₃ system with and without these reactions, and subsequent analysis of the calculated [IO] curves with the steady state approach, have shown an effect of these reactions on the $k_{10.2}$ value obtained by this method of less than 6%. The weighted average of the values obtained by both approaches is $k_{10.2} = (7.6 \pm 1.1) \times 10^{-11} \text{ cm}^3 \text{ molecule}^{-1} \text{ s}^{-1}$.

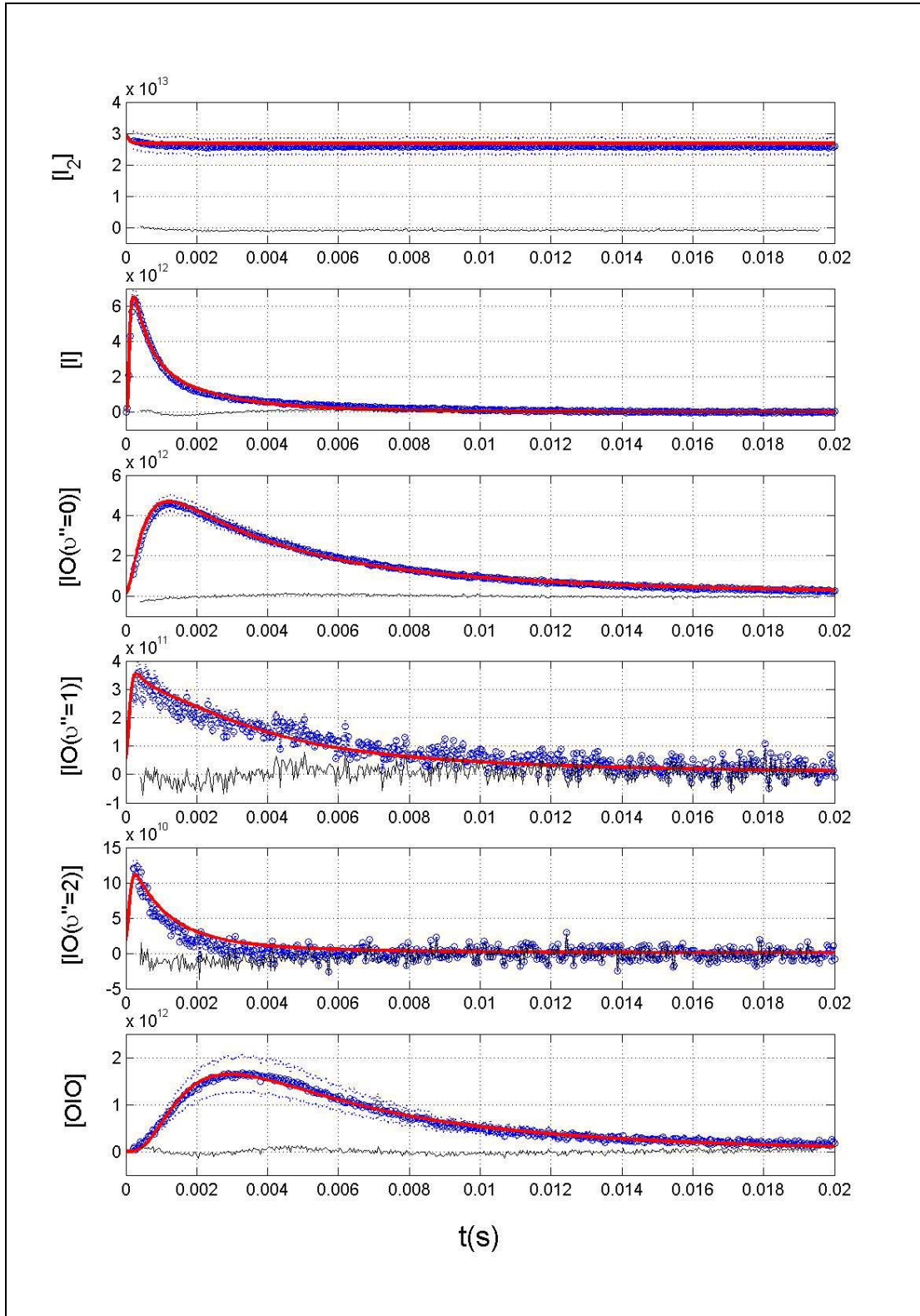
The rate coefficients of the channels of reaction R10.2 obtained from the optimized simulations are in agreement with those obtained from simple kinetic analysis (F10.6). The preferred values are those obtained from optimized simulations, because they are consistent with the complete data recordings and the channel R10.2.a is explicitly taken into account. The values of $k_{10.2.a}$ and $k_{10.2.b}$ take low and practically

constant values within the uncertainty region in the whole pressure range. On the other hand, the decrease of $k_{10.2.c}$ and $k_{10.2.b}+0.5k_{10.2.c}$ is accompanied by an increase in the rate coefficient of $k_{10.2.d}$. Taking into account that the products I+OIO of channel R10.2.c are unlikely to result from the excited complex IOOI*, these results indicate that the most likely symmetry of the dimer is IOIO.

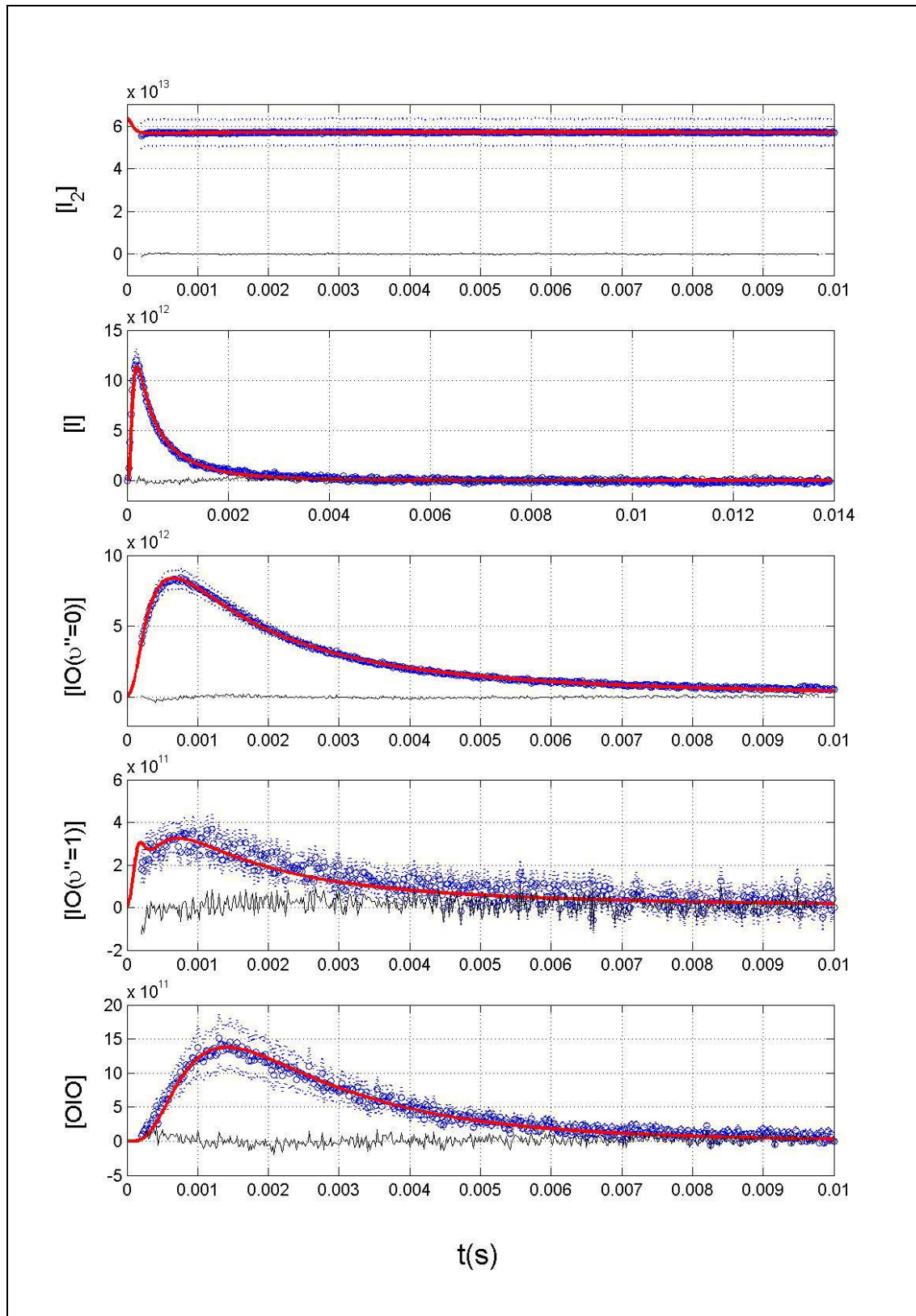
T10.2. Rate coefficients ($\text{cm}^3\text{molecule}^{-1}\text{s}^{-1}$) obtained with the proposed mechanism ^a

P (hPa)	$k_{10.2}$ $\times 10^{10}$	$k_{10.2.a}/k_{10.2}$	$k_{10.2.b}/k_{10.2}$	$k_{10.2.c}/k_{10.2}$	$k_{10.2.d}/k_{10.2}$	$k_{\text{OIO}+\text{X}}$ $\times 10^{10}$	$k_{\text{IO}+\text{X}}$ $\times 10^{10}$
10	0.71±0.06	0.05±0.02	0.07±0.02	0.74±0.10	0.14±0.07	0.57±0.05	0.19±0.06
15	0.73±0.10	0.05±0.02	0.04±0.03	0.75±0.10	0.17±0.13	0.90±0.23	0.16±0.30
20	0.72±0.09	0.05±0.02	0.02±0.04	0.81±0.13	0.14±0.10	0.70±0.09	0.34±0.04
30	0.72±0.05	0.05±0.02	0.05±0.05	0.77±0.12	0.13±0.09	0.89±0.09	0.39±0.03
40	0.76±0.17	0.04±0.02	0.07±0.08	0.74±0.15	0.18±0.17	0.90±0.09	0.43±0.13
100	0.76±0.14	0.06±0.03	0.10±0.07	0.59±0.11	0.29±0.15	1.00±0.11	0.46±0.13
150	0.73±0.09	0.07±0.01	0.11±0.03	0.52±0.09	0.33±0.09	1.01±0.30	0.56±0.06
200	0.79±0.06	0.04±0.02	0.11±0.05	0.54±0.09	0.36±0.11	1.06±0.10	0.49±0.03
250	0.78±0.07	0.06±0.04	0.11±0.09	0.52±0.09	0.36±0.13	1.26±0.10	0.53±0.02
300	0.70±0.09	0.04±0.03	0.07±0.05	0.49±0.09	0.39±0.14	1.32±0.25	0.55±0.09
350	0.75±0.09	0.05±0.03	0.09±0.07	0.47±0.07	0.41±0.13	1.23±0.10	0.48±0.12
400	0.76±0.09	0.07±0.04	0.08±0.06	0.45±0.09	0.44±0.13	1.21±0.11	0.44±0.13

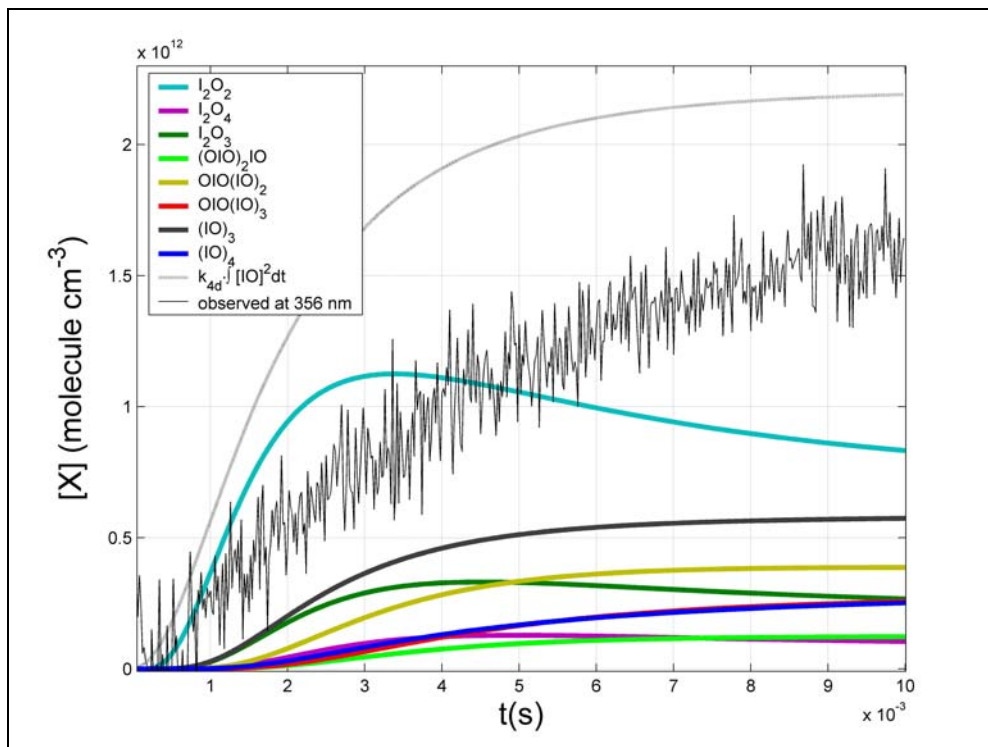
^a)38 datasets have been analysed. For each pressure there are a minimum of 3 and a maximum of 5 datasets. Error estimations comprise random error in the 1σ level and systematic errors arising from uncertainties in the concentrations of the precursors, inhomogeneity in the cross axis and the absorption cross sections.



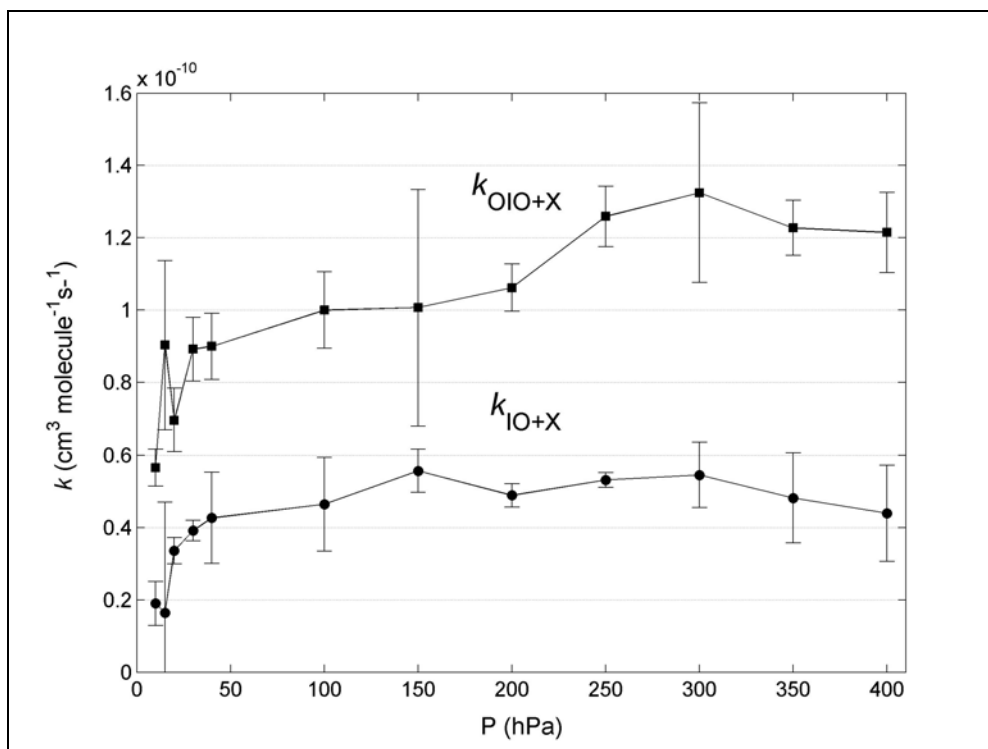
F10.13. Measured and simulated concentration versus time curves (in molecule·cm⁻³) for an experimental run at 20 hPa with $[O_3] = 6 \times 10^{14}$ molecule cm⁻³ and $[I_2] = 2 \times 10^{13}$ molecule cm⁻³ (blue circles). The rest as for F10.2.



F10.14. Group of concentration versus time curves (in molecule·cm⁻³) for a typical experimental run at 400 hPa with $[O_3] = 2 \times 10^{15}$ molecule cm⁻³ and $[I_2] = 6.3 \times 10^{13}$ molecule cm⁻³ (blue circles). The rest as for F10.2



F10.15. Time trace of a broad band absorption recorded in the UV, compared to the time behaviours of higher iodine oxides and clusters of iodine oxides generated by simulation with optimal parameters. This species has not been included to constrain the fit which yields the optimal parameters, because of the ambiguous assignment and uncertain absorption cross sections. The cumulative integral of the IO time behaviour is also shown for comparison.



F10.16. Pressure dependence of the second order rate coefficients of reactions R10.8, R10.9 and R10.11 ($k_{\text{IO}+\text{X}}$, X=any iodine oxide) and R10.7, R10.10 and R10.12 ($k_{\text{OIO}+\text{X}}$) obtained by complex kinetic simulation.

10.4.2.3. Sensitivity studies

It has been checked that the parameters related to the IO self reaction returned by the fit are unique. To this end the optimised values have been varied by an arbitrary amount and fixed at the modified value in the model, one at a time. The fitting to the simulated curves has been subsequently run with one free parameter less. The fits are measurably worse whenever the optimised values are varied by amounts larger than the error intervals shown in F10.6. The strong interdependence between I, IO and OIO facilitates the measurability of the changes in the quality of the fit and illustrates how important it is to monitor as many species as possible. The influence of using fixed values reported in the literature was also checked. In general, the use of values of $k_{10.2}$ larger than $0.9 \times 10^{-10} \text{ cm}^3 \text{ molecule}^{-1} \text{ s}^{-1}$ leads to significant conflict between the simulated and the observed curves (the simulated IO curve is measurably underestimated). Similarly, the branching reported by Vipond et al. [174] and Joseph et al. [83] was impossible to reconcile with the time behaviours recorded within this study, and especially with the iodine atom curve, which in this case was overestimated by a factor of two in the time interval where iodine recycling occurs.

Using the proposed mechanism (T10.1) as reference, further possible reactions and their influence on the optimal parameters have been investigated

Photolysis of O₃

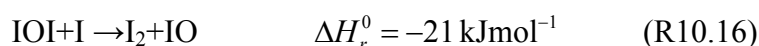
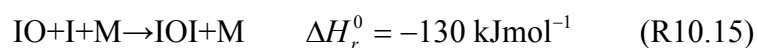
In the first place, the role of any O₃ photodissociation has been investigated by using a photolysis frequency, derived from the upper limit of the extent of O₃ photolysis determined experimentally. The inclusion of this process implies a slight correction of the photolysis rate of IO (T10.1, R10.13), in order to better fit the initial concentration of IO, thus indicating that both processes are essentially not separable in the data available. On the other hand, these processes are irrelevant for the study of the removal

of IO and OIO, because O(³P) is rapidly consumed in an excess of I₂ (R10.14) The only requirement is a good empirical estimation of the initial amount of IO.

Iodine atom reactions

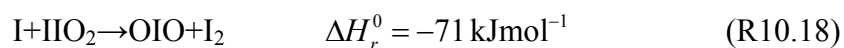
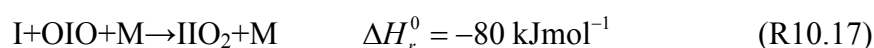
Iodine atoms are expected to react quickly with O₃ and therefore further sinks for iodine atoms like reactions R10.5-R10.6 have been judged in principle to be unimportant and have not been included in the proposed model. In addition, no substantial I₂ formation is observed at the mixing ratios used in these investigations. However, reactions R10.5 are exothermic according to Misra and Marshall [84] and expected to be fast, and therefore they could have some influence at the beginning of the photochemical process, where the concentrations of I are still high. Therefore, it is worthwhile to check what influence could have these reactions on the rate coefficient and the branching of the IO self reaction determined with the base model.

IO catalysed I-atom recombination cycle [171] could have an influence on the concentration curve of IO in the time interval where the concentration of I is still high:



By including R10.15 with a free rate coefficient, values of about $10^{-11} \text{ cm}^3 \text{ molecule}^{-1} \text{ s}^{-1}$ are obtained, but no significant improvement of the correlation coefficients is observed. At this rate, reaction R10.16 is negligible as a result of the low production of IOI in reaction R10.15. The fits are significantly worse if the rate coefficients reported for these reactions at 1013 hPa are considered [79].

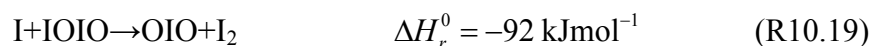
A similar cycle for OIO would be:



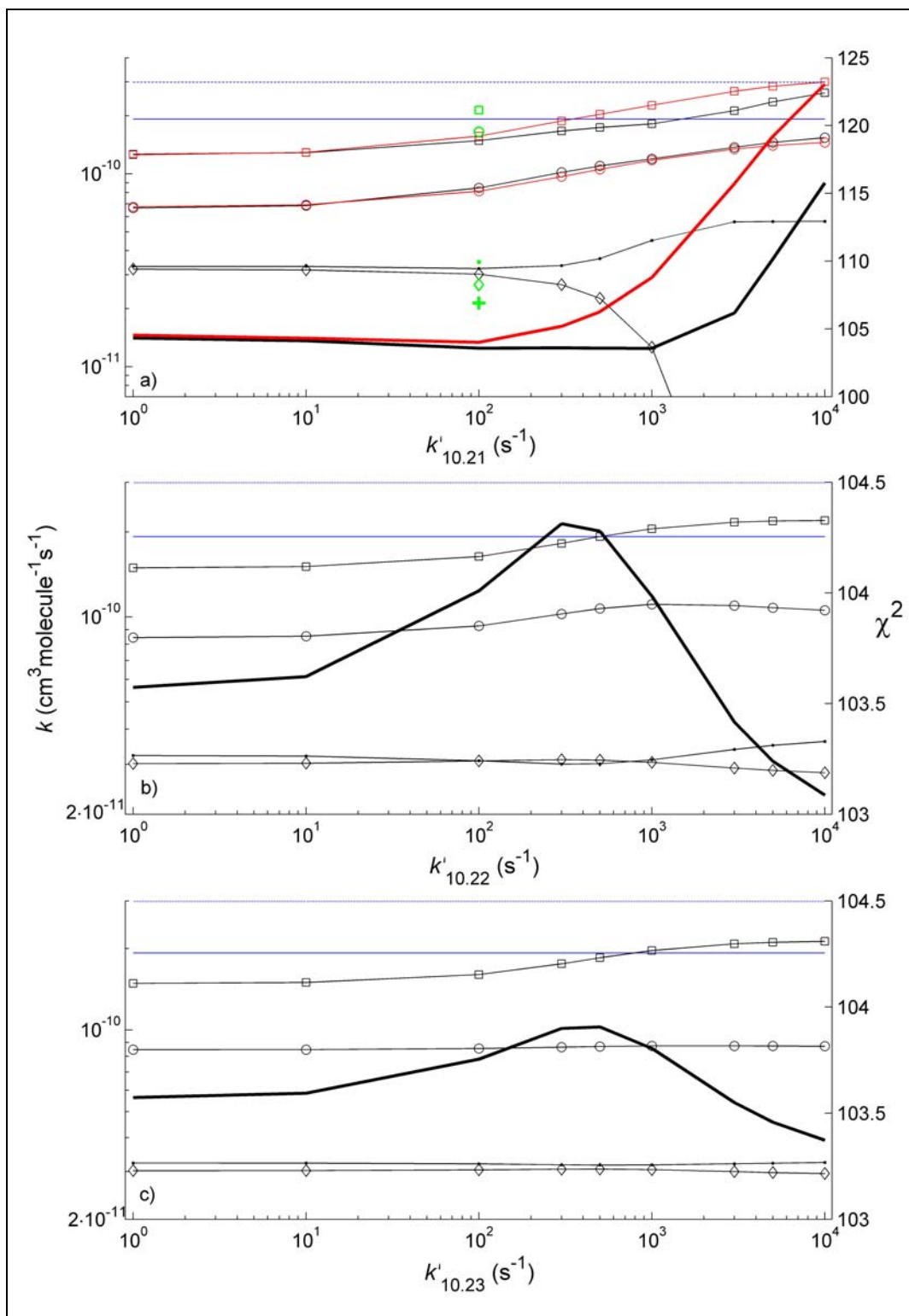
The Y-shaped molecule IIO₂ is the most stable I₂O₂ isomer, with a predicted life time

with respect to the reverse of R10.17 of 4 s at ambient conditions [84]. Reaction R10.18 could have a direct influence in the branching of reaction R10.2. By considering the cycle R10.17-R10.18 with the rate coefficients reported in the literature [83], and allowing IIO₂ to react with OIO and IO, no significant changes in the parameters determined with the proposed model are observed, which in all cases keep within the error bars reported.

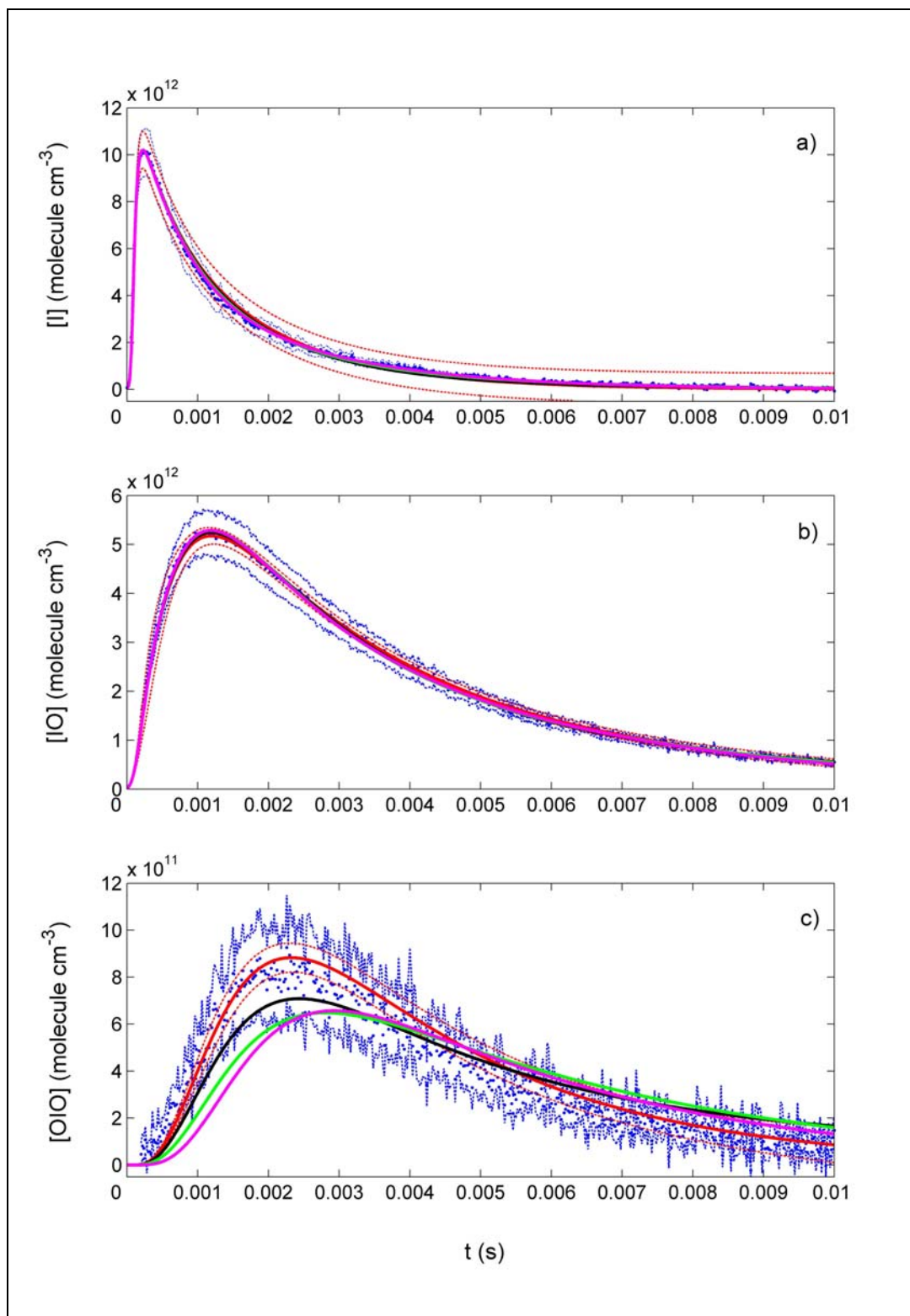
Further iodine abstraction reactions involving the other I₂O₂ isomers produced via reaction R10.2 could also affect the apparent branching of R10.2:



The results obtained indicate that the stabilised IO dimer is most likely the asymmetric one. Therefore, only the influence of reaction R10.19 in the mechanism has been checked. Firstly, by including this reaction with a free rate coefficient, values of about $10^{-11} \text{ cm}^3 \text{ molecule}^{-1} \text{ s}^{-1}$ are obtained, without significant improvement of the correlation between simulations and observation. By using fixed values of this rate coefficient, it has been observed that for $k_{10.19} \sim 10^{-10} \text{ cm}^3 \text{ molecule}^{-1} \text{ s}^{-1}$ the fits are significantly worse and that the upper limit for no measurable changes in the fit quality is indeed $10^{-11} \text{ cm}^3 \text{ molecule}^{-1} \text{ s}^{-1}$. The changes of the branching ratios caused by including this reaction at the upper limit rate coefficient are less than 10%. The value of $k_{\text{OIO}+\text{X}}$ is somewhat higher (about 15%), in response to the reduction in the amount of IOIO and the increase in the species which has to be removed (OIO). These variations are however inside the error intervals.



F10.17. Optimal values of rate coefficients (left axis, thin lines with symbols) and χ^2 values (right axis, thick lines) for different values of the dissociation rate coefficients $k'_{10.21}$ ' (panel a), $k'_{10.22}$ ' (panel b) and $k'_{10.23}$ ' (panel c). Each panel corresponds to the variation of one dissociation coefficient, while the other two were fixed at 100 s^{-1} . Red lines and symbols correspond to fits where $k_{10.2.c}$ (diamonds), $k_{10.2.d}$ (points), k_{10+X} (circles) and k_{O10+X} (squares) were allowed to vary. Black lines and symbols: only k_{10+X} and k_{O10+X} were allowed to vary. Green symbols: R10.11 and R.9.12 were not considered. The blue lines indicate the collision frequency factors [50, 151] for OIO calculated assuming a density for I_2O_4 of $2.57 \text{ g}\cdot\text{cm}^{-3}$ (dashed line) [210] and $4.97 \text{ g}\cdot\text{cm}^{-3}$ (solid line) [211, 212]. The experimental data used in the fits was recorded at 400 hPa (see F10.17).



F10.18. Experimental data (blue points) and optimized fits for 400 hPa. Blue dashed lines indicate the uncertainty of the experimental data. Red lines are concentrations obtained with the proposed model using the optimal values shown in figure 6. Red dashed lines indicate the estimated uncertainty of the optimized simulation, extrapolated from local first order sensitivity coefficients [50]. Black, green and magenta lines correspond to optimized fits for $k_{10,21}'=100 \text{ s}^{-1}$, 500 s^{-1} and 1000 s^{-1} respectively.

Dissociation, re-dissociation, and further reactions of the IO dimer

An attempt has been made to fit the experimental data with a model containing reversible reactions R10.7-R10.12. The simulated concentrations, the free parameters and the quality of the fits are sensitive to the values assumed for the reverse rate coefficients of these reactions. A strong dependence of the reverse rate coefficients on cluster size is expected [50, 110], and in fact all attempts to fit the observed data with “global” reverse rate coefficients $k_{XOIO \rightarrow X+OIO}$ and $k_{XIO \rightarrow X+IO}$ failed. The optimized aerosol model parameters of Burkholder et al. [110] indicate that the clusters containing three or more monomer molecules would be stable on the time scale studied in the present work. The dissociation of I_2O_2 , I_2O_3 and I_2O_4 have therefore been considered explicitly:



The inclusion of rapid dissociation of IOIO [84] in the chemical mechanism results in a significant regeneration of I and OIO. As a consequence, a different multidimensional χ^2 surface is obtained. In particular, local minima of the new χ^2 are found at different points of the 6-dimensional parameter space. The fitting algorithm searches for these points, i.e. varies some of the free parameters in order to find the new minima. This is illustrated in figure F10.17, where the results of a series of optimized simulations for different values of $k_{10.21}'$, $k_{10.22}'$ and $k_{10.23}'$ are plotted along with the corresponding values of χ^2 . In first place, the branching of the IO self reaction is fixed to the values obtained in the present study by simple kinetic modelling and only k_{IO+X} and k_{OIO+X} are allowed to vary (F10.17.a, red curves). The resulting χ^2 surface is flat for $k_{10.21}' \leq 100 \text{ s}^{-1}$, while beyond 100 s^{-1} an increase of χ^2 is observed (thick red line, $k_{10.22}'$

and $k_{10,23}'$ are fixed). Therefore, a well defined lower limit for the lifetime of IOIO is found.

On the other hand, if $k_{10,2,c}$ and $k_{10,2,d}$ are allowed to vary, the optimization algorithm finds a prolongation of the flat landscape (F.9.17.a, thick black line) for dissociation rates up to 3000 s^{-1} (0.3 ms lifetime) by increasing $k_{10,2,c}$ and decreasing $k_{10,2,d}$ ($k_{10,2,a}$ and $k_{10,2,b}$ do not change significantly). This is a consequence of the relatively weak constraint imposed by the OIO observed curves, whose weight is determined by the $\sim 23\%$ uncertainty of the absorption cross section. In terms of reproduction of the shape of the OIO curve these fits are significantly poorer than those obtained for $k_{10,21}' \leq 100\text{ s}^{-1}$ (F10.18.c), while the other observed species are similarly well reproduced (F10.18.a and F10.18.b). The weighting function does not take into account the high accuracy of the optical density curve (i.e. the shape of the concentration curve), whose uncertainty is about 5%. Therefore, it has been considered that the most consistent set of parameters is that obtained for $k_{10,21}' \leq 100\text{ s}^{-1}$, and as a consequence a lower limit for the lifetime of I₂O₂ of about 10 ms is suggested.

By contrast, the values of $k_{10,2,c}$ and $k_{10,2,d}$ and χ^2 are relatively insensitive to variations in $k_{10,22}'$ and $k_{10,23}'$ (F10.17.b and F10.17.c). The increase of the dissociation rate coefficients is mainly compensated by an increase of the forward rate constant $k_{\text{OIO}+\text{X}}$ and to a minor extent of $k_{\text{IO}+\text{X}}$. Increasing values of $k_{10,22}'$ and $k_{10,23}'$ are compensated by values of $k_{\text{OIO}+\text{X}}$ closer to the collision frequency factor for OIO+OIO (blue lines in figure 11). A small increase of χ^2 is observed for dissociation rate coefficients larger than 10 s^{-1} , but χ^2 falls again for $k_{10,22}'$ and $k_{10,23}' > 1000\text{ s}^{-1}$. Divergence of $k_{10,2,c}$ and $k_{10,2,d}$ starts to be important for $k_{10,22}' > 1000\text{ s}^{-1}$, suggesting a lower limit for the lifetime of I₂O₃ of about 1 ms. In summary, the evidence indicating a slow dissociation of I₂O₃ and I₂O₄ is much weaker than in case of I₂O₂. As a consequence, it

can be concluded that the values of $k_{\text{OIO}+\text{X}}$ and $k_{\text{IO}+\text{X}}$ obtained with the proposed mechanism (Table 3) are lower limits. Nevertheless, F10.17 shows that upper limits for both rate coefficients can also be estimated by performing optimized simulations combining $k_{10.21}'=100 \text{ s}^{-1}$, $k_{10.22}'=1000 \text{ s}^{-1}$ and $k_{10.23}'=10000 \text{ s}^{-1}$. These calculations yielded $k_{\text{OIO}+\text{X}} < (2.9 \pm 0.3) \times 10^{-10} \text{ cm}^3 \text{ molecule}^{-1} \text{ s}^{-1}$ and $k_{\text{IO}+\text{X}} < (1.0 \pm 0.2) \times 10^{-10} \text{ cm}^3 \text{ molecule}^{-1} \text{ s}^{-1}$ at 400 hPa. The introduction in the mechanism of a 10-fold slower dissociation for the oligomers containing 3 monomer molecules did not change these upper limits significantly.

Reactions R10.11 and R10.12

Reactions R10.11 and R10.12 have been included in the mechanism as a logical consequence of the potentially longer lifetime of the IO dimer. The quality of the fits is slightly improved by including these reactions (see F.9.17.a). The common rate coefficient for R10.7, R10.10 and R10.12 (i.e. $k_{\text{OIO}+\text{X}}$) obtained with the proposed mechanism is 30% smaller than the corresponding result if only R10.7 and R10.10 are considered (green symbols in F10.17.a). Similarly, the common rate coefficient for R10.8, R10.9 and R10.11 (i.e. $k_{\text{IO}+\text{X}}$) is about 40% smaller with respect to the result obtained for R10.8 and R10.9 only. The kinetic parameters of R10.2 change slightly by the inclusion of these reactions.

Reactions of IO and OIO with O₃

The reaction of IO with O₃ is very exothermic and could be a potential candidate for the additional sink of IO observed. However, its rate coefficient would have to be of about $5 \times 10^{-14} \text{ cm}^3 \text{ molecule}^{-1} \text{ s}^{-1}$ to account for this sink completely. The analysis of the χ^2 surface of the optimized simulations is insensitive to this reaction for rate coefficients smaller than $10^{-14} \text{ cm}^3 \text{ molecule}^{-1} \text{ s}^{-1}$. These values are significantly larger than the estimations previously reported [110, 209] and can be seen as rough upper limits. On the

other hand, an upper limit for the rate coefficient of the O₃+OIO reaction of 5×10^{-14} cm³ molec⁻¹ s⁻¹ has been estimated.

10.5. Discussion

10.5.1. Excited IO species

At the lowest pressures, the concentrations of vibrationally excited IO are sufficiently large that their collisional quenching contributes to the rate of production of IO($v''=0$). For these experiments, chemical removal of the non-equilibrium concentration of vibrationally excited IO, e.g. by reaction with IO($v''=0$), cannot be ruled out. Although the amount of IO($X^2\Pi_{3/2}, v''=2$) does not show a strong anti-correlation with [IO($v''=0$)], it was not possible to separate the contribution of physical quenching of IO($v''=2$) from that of potential chemical removal processes.

The identity of the short lived absorber 'X' (F9.1.e and F9.1.f) is intriguing. The observed spectrum appears somewhat similar to the spectrum observed in the matrix by Maier and Bothur [150], but the possibility of the absorption being caused by IOO has been excluded at this time, because photolysis experiments of I₂/O₂ mixtures at room temperature (i.e. the same mixtures excluding O₃) do not provide any evidence for the short lived transient. Spectroscopic vibrational analysis has shown that the absorption does not originate from excited vibrational state IO($X^2\Pi_{3/2}, v''>0$) [124, 126]. A plausible explanation of the absorption labelled as 'X' is the $A^2\Pi_{1/2} \leftarrow X^2\Pi_{1/2}$ sub-band system. The vibrational ground state of $X^2\Pi_{1/2}$ has an energy slightly larger than that of IO($X^2\Pi_{3/2}, v''=3$), and IO($X^2\Pi_{3/2}$) with v'' up to 6 has been observed in this system (see e.g. F8.2). Therefore, there is enough energy in the system to form $X^2\Pi_{1/2}$. According to *ab initio* calculations by Roszak et al. [146], the $A^2\Pi_{1/2}$ state does not form any potential well. By using the reflection method [130], the graphical imaging of the ground state vibrational wave function corresponding to $X^2\Pi_{1/2}$ into the $A^2\Pi_{1/2}$ potential calculated by

Roszak et al. [146] yields a featureless spectrum, which peaks at about 373 nm and has a similar shape to the broad band spectrum of 'X' [126]

$\text{IO}(X^2\Pi_{1/2})$ is a metastable state, and therefore it is likely that its main fate is to react with other species in excess in a pseudo first order process rather than being quenched. In fact, no clear dependence on pressure of this species has been observed, while it decays exponentially (F9.1.f). Nevertheless, the ground state energy of $\text{IO}(X^2\Pi_{1/2})$ roughly coincides with that of $\text{IO}(X^2\Pi_{3/2}, v''=3)$, and the concentration of $\text{IO}(X^2\Pi_{3/2}, v''>1)$ is small even at the lowest pressure considered in the present work.

10.5.2. Overall rate of the IO self reaction

In general, the determination of $k_{10.2}$ in systems with ozone has been normally avoided by other workers because of the iodine atom recycling through the IO self reaction, which creates a source of IO coupled to its decay. If the amount of ozone in the experiment is high enough to cause instantaneous consumption of I (pseudo steady state approximation), it is possible to fit second order decays to the observed IO concentration in a large section of the measured curve and to obtain an effective $k_{10.2}$ ($k_{10.2\text{eff}} = k_{10.2} \times (1 - \alpha) < k_{10.2}$), which only accounts for non iodine atom products. This approach has been used by some authors [53, 80, 171] to determine the iodine atom yield of the IO self reaction. On the other hand, Stickel et al. [163] reported a value of $k_{10.2} = (0.66 \pm 0.20) \times 10^{-10} \text{ cm}^3 \text{ molecule}^{-1} \text{ s}^{-1}$ at 1013 hPa, which is also thought to be rather a $k_{10.2\text{eff}}$ value because in their study the specific branching of the IO self reaction was not taken into account. By contrast, the recycling of iodine atoms has been taken into account and systematic errors in the iodine atom curve have been conservatively quantified. However, although a pressure independent value is obtained, it is still significantly lower than the IUPAC recommendation. An effort has been made to identify a potential source of IO which could be active in the I_2/O_3 system and not in the

N₂O/I₂ system, causing this difference:

- a) Molecular product(s) of R10.2 react with O₃ at a similar rate to that of atomic iodine in R10.1, and yield IO and/or I.
- b) The IO dimer thermally decomposes to IO+IO and/or I+OIO at a very high rate, while in a system without ozone and with I atoms in large excess reaction R10.19 competes successfully with dissociation in such a way that the IO consumption rate is not reduced.

Hypothesis a) has been discarded due to the poor quality of the fits obtained by including such reactions in the modelling. In the case of OIO, it has been shown that the pseudo-first order decay rate coefficient obtained (section 10.4.1.3) is not directly proportional to [O₃]. Several arguments have been found against hypothesis b). First of all, unexpected values for the branching are obtained by fitting the experimental data to a scheme containing these reactions. Moreover, simulation of the I₂/O₃ system including dissociation at $\sim 1000 \text{ s}^{-1}$ gives small values of $k_{10.2\text{eff}}$. Finally, simulation of the N₂O/I₂ chemistry in the range of conditions reported in the literature demonstrates that reactions R10.19 or R10.20 proceeding at the collision rate ($\sim 2 \times 10^{-13} \text{ cm}^3 \text{ molecule}^{-1} \text{ s}^{-1}$) would not be fast enough to compete with re-dissociation at 1000 s^{-1} , and therefore if re-dissociation occurred at that rate it would cause the measured values of $k_{10.2}$ to be significantly smaller than the values reported in the literature.

Recently, the pressure dependence of $k_{10.2\text{eff}}$ obtained by fitting second order to the IO decay have been reported by J. Crowley and T. Dillon in the framework of the European project THALOS [53]. At the highest pressures investigated, the value of $k_{10.2\text{eff}}$ is approximately equal to the value of $k_{10.2}$ that reported here. The reason for such coincidence can not be identified clearly. However, it could be that as a result of the significantly higher I₂ concentration employed in their studies (5×10^{14} - 10^{15} molecule

cm⁻³) for a similar [O₃] concentration (10¹⁵ molecule cm⁻³), the higher concentration of iodine atoms obtained slows down the growth of higher iodine oxides by iodine abstraction from IOIO or I₂O₃, in such a way that the attachment of IO to nascent polymers and clusters is masked in an apparent second order.

T10.3. Determinations of the IO Self-Reaction Rate Coefficient at 295-298 K

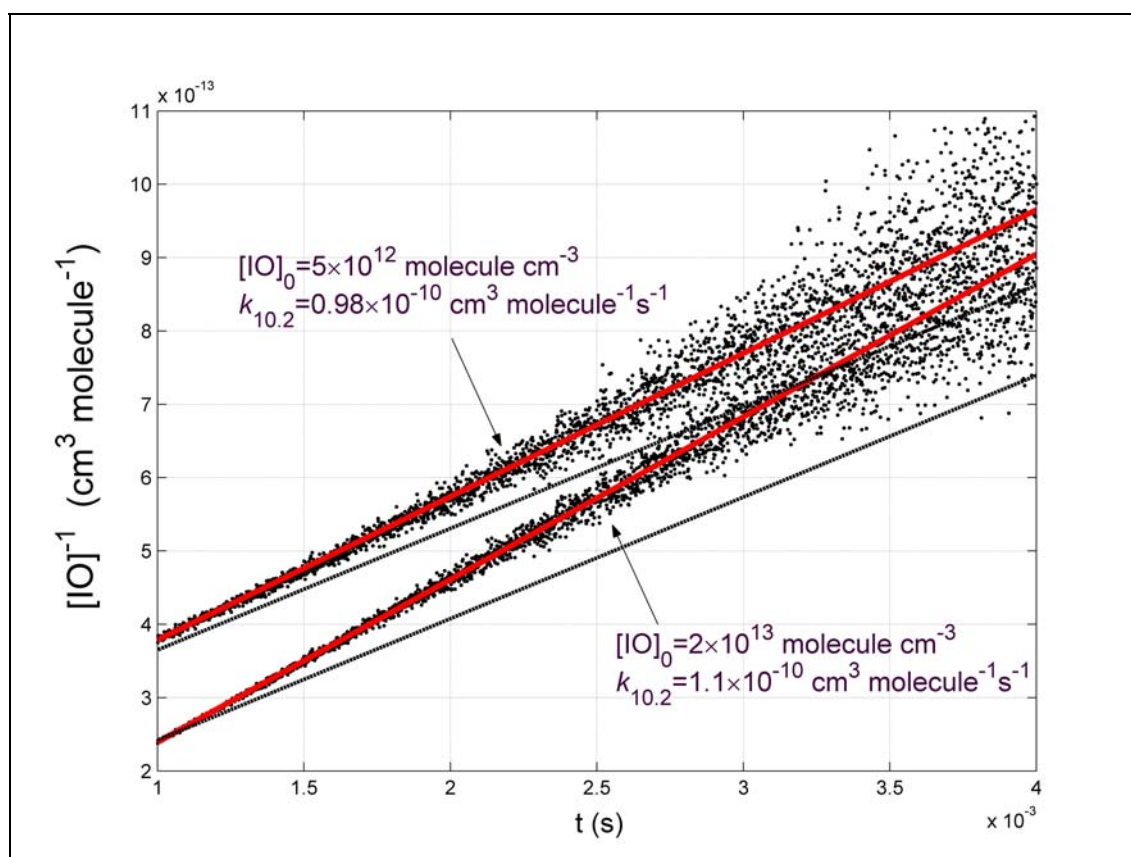
Ref.	System ^a	[IO] ₀ × 10 ⁻¹³ (molecule·cm ⁻³)	<i>P</i> (hPa)	Method ^b	<i>k</i> _{10.2} × 10 ¹⁰ ^c	<i>k</i> _{10.2} /σ _{IO} × 10 ⁻⁶ (cm/s)
Sander [80]	O ₂ /I ₂	2-20	28-933	<i>k</i> /σ 2 nd order	0.53 ± 0.03	1.8 ± 0.1
Stickel et al. [163]	O ₃ /I ₂ ; I ₂ /O ₃	Not instantaneous	1013	(σ, <i>k</i>) complex	0.66 ± 0.20	-
Laszlo et al. [170]	N ₂ O/I ₂	0.2-0.3	80-813	<i>k</i> /σ 2 nd order	0.80 ± 0.17	2.86
Harwood et al. [171]	N ₂ O/I ₂	0.5-2	813	<i>k</i> 2 nd order	0.99 ± 0.15	2.75
Vipond et al. [174]	O ₂ /CF ₃ I	~ 0.01	2.5-3	<i>k</i> complex	0.93 ± 0.10	-
Atkinson et al. [172]	N ₂ O/CF I	0.1-1.2	12.5; 40	<i>k</i> complex	1.0 ± 0.3	-
Ingham et al. [81]	O ₃ /I ₂	< 0.5	80	<i>k</i> /σ 2 nd order	0.9 ± 0.17	2.5 ± 0.6
Bloss et al. [79]	N ₂ O/I ₂	2-10	133-1013	<i>k</i> complex	0.82 ± 0.13	-
Atkinson et al. [29]	-	-	-	Review	0.99 ± 0.10	2.75
This work	I ₂ /O ₃	Not instantaneous	10-400	<i>k</i> , steady state, complex	0.76 ± 0.11	-

^a) The photochemical system is described by the two molecular precursors of IO. The first one indicates the molecule which releases free atoms after microwave discharge, photolysis or fast reaction. ^b) The method is described by the quantities determined and the type of kinetic modelling used. ^c) Unit: cm³ molecule⁻¹ s⁻¹

In systems where R10.14 is the only source of IO and where “instantaneous” formation is induced by using I₂ in great excess over O, second order decays of IO have been reported consistent with reaction R10.2 with rate coefficients between 0.8×10^{-10} and $10^{-10} \text{ cm}^3 \text{ molecule}^{-1} \text{ s}^{-1}$, independent of P , $[I_2]$ and $[IO]_0$ [79, 81, 170, 171] (see T10.3). It has been considered that these are the “cleanest” chemical systems for the measurement of $k_{10,2}$, because no other significant reactions of IO are occurring or they can be easily accounted for. The agreement between the values of $k_{10,2}/\sigma_{IO}(427.2 \text{ nm})$ reported in these chemical systems and the consensus about the absorption cross section of IO: ($\sigma_{IO}(427.2 \text{ nm}) = 3.6 \times 10^{-17} \text{ cm}^2 \text{ molecule}^{-1}$, [125, 171]) are the basis of the recommendation of the IUPAC Subcommittee on Gas Kinetic Data Evaluation for Atmospheric Chemistry [29]: $k_{10,2} = (0.99 \pm 0.10) \times 10^{-10} \text{ cm}^3 \text{ molecule}^{-1} \text{ s}^{-1}$. It must be observed, however, that the value of Bloss et al. [79] may not be useful in supporting the IUPAC argumentation, because it was not obtained by determination of $k_{10,2}/\sigma_{IO}(427.2 \text{ nm})$, but rather by fitting of simulated concentration curves, and it was measured at a significantly different spectral resolution from the other studies [81, 170, 171]. Sander [80] obtained a value of $(0.53 \pm 0.03) \times 10^{-10} \text{ cm}^3 \text{ molecule}^{-1} \text{ s}^{-1}$ in the O₂/I₂ system. However, his value for the I₂/O₃ system is also strongly reduced with respect to the most recent measurements of $k_{10,2,eff}$, indicating that the cause of such reduction is independent of the presence of O₃, and as a result it is disregarded in the IUPAC recommendation. On the other hand, the determination of Sander is still taken into account in the JPL Evaluation [28], which recommends a value of $k_{10,2} = 0.8 \times 10^{-10} \text{ cm}^3 \text{ molecule}^{-1} \text{ s}^{-1}$ consistent with the determination reported here.

Deviations of the IO decay from second order have been reported by Harwood et al. [171], who observed them for $T < 298 \text{ K}$ and found them to be consistent with the reaction of IO with one of the products of its self reaction. These deviations indicate

that there might be problems associated to the system $\text{N}_2\text{O}/\text{I}_2$, e.g. the large amount of free iodine atoms available for reaction with iodine oxides (reactions R10.5-R10.6) or reactions of IO with products of its own self reaction, including I. The reaction between IO and OIO has been disregarded up to now as a result of the independence of the IO decay on pressure observed. However, this reaction might be in the vicinity of its high pressure limit, as indicated by a RRKM calculation reported by Joseph et al. [83] and the experimental results reported here. F10.16 shows that the bimolecular rate coefficient for reactions R10.8 stabilises at about 50 hPa, where it reaches a value of about $5 \times 10^{-11} \text{ cm}^3 \text{ molecule}^{-1} \text{ s}^{-1}$.



F10.19. Second order fits (red solid lines) of simulated $[\text{IO}]^{-1}$ curves for the $\text{N}_2\text{O}/\text{I}_2$ system (black points). The simulated $[\text{IO}]$ profiles have been calculated for 1013 hPa and different initial $[\text{IO}]$ concentrations, by using in the mechanism a value of $k_{\text{IO}+\text{X}} = 5 \times 10^{-11} \text{ cm}^3 \text{ molecule}^{-1} \text{ s}^{-1}$ and the branching and the rate coefficient of R10.2 reported by Bloss et al. [79], which are consistent with the values reported here. A certain level of noise has been added to the simulated $[\text{IO}]$ curves, corresponding approximately to the noise of the $[\text{IO}]$ curves reported by Harwood et al. [171]. It can be seen that the inclusion of IO+OIO (R10.8, $n = 1$) does not change the second order behaviour of the curves, although it enhances the rate of consumption of IO with respect to the simulations performed without this reaction (dashed lines) from $\sim 0.8 \times 10^{-10}$ to $\sim 10^{-10} \text{ cm}^3 \text{ molecule}^{-1} \text{ s}^{-1}$. However, a dependence on $[\text{IO}]_0$ is observed, which has not been reported in experimental studies.

Within the present work, the N₂O/I₂ system has been simulated at 1013 hPa with the initial conditions employed by Harwood et al. [171] and considering reactions R10.7 ($n = 1, \dots, 4$), R10.8 ($n = 1$) and R10.11 ($n = 1$) with the rate coefficients shown in F10.16, and reactions R10.23-R10.24 with the values reported by Joseph et al. [83] and communicated personally by J. Plane (2005). By applying the conventional kinetic analysis to the simulated IO concentration curve (F10.19), it has been found that IO still decays to a good approximation in second order, while the apparent second order rate coefficient is enhanced to about $10^{-10} \text{ cm}^3 \text{ molecule}^{-1} \text{ s}^{-1}$. However, these simulations also indicate that if reactions R10.8 and R10.11 occur, the calculated $k_{10,2}$ would be dependent on $[\text{IO}]_0$ (20% increase between the lowest and the highest $[\text{IO}]_0$ considered by Harwood et al. [171], see F10.23), which has not been observed at room temperature [171].

The chemistry occurring in the N₂O/I₂ system is most likely much more complex than the models used up to now, and additionally experimental values of the rate coefficients of the potentially significant reactions R10.5-R10.6 are not available. However, these simulation exercises indicate that second order behaviour might not be in this case a sufficient criterion to validate a chemical mechanism, in agreement with the conclusion of Laszlo et al. [170]. In their analysis of the photochemistry of the O₂/I₂ system, values of $k_{10,2}$ closer to the values of Sander [80] (in the same system) than to the currently recommended value were obtained. Further, a dependence of $k_{10,2}$ on $[\text{I}_2]$ and $[\text{O}_2]$ was observed and it was attributed to a complex chemical behaviour related to the ozone produced in this system via third body recombination. In their opinion, such complexity is not always discernible as a deviation of $[\text{IO}]$ from second order kinetics and in fact both Sander [80] and Laszlo et al. [170] observed perfect second order decay of $[\text{IO}]$ in the O₂/I₂ system. A new experimental study of the N₂O/ $h\nu$ /I₂ system with a

multichannel approach like in the present work would contribute to solve these open questions.

Finally, there are two determinations of $k_{10,2}$ in the system $\text{N}_2\text{O}/\text{CF}_3\text{I}$. Atkinson et al. [172] investigated the $\text{IO}(2\leftarrow 0)$ ro-vibronic absorption band by CRDS, and observed second order in the IO decays. They derived a value $k_{10,2}=(1.0 \pm 0.3) \times 10^{-10} \text{ cm}^3 \text{ molecule}^{-1} \text{ s}^{-1}$. The uncertainty makes this value compatible with both a value closer to $0.8 \times 10^{-10} \text{ cm}^3 \text{ molecule}^{-1} \text{ s}^{-1}$ as proposed here and closer to $10^{-10} \text{ cm}^3 \text{ molecule}^{-1} \text{ s}^{-1}$ as proposed in the IUPAC review. Vipond et al. [174] employed a discharge flow tube, which is an experimental technique significantly different from the rest of optical absorption oriented setups. Their determination of $k_{10,2} = (0.93 \pm 0.19) \times 10^{-10} \text{ cm}^3 \text{ molecule}^{-1} \text{ s}^{-1}$ does not rely on the knowledge of the absorption cross section of IO but rather in the knowledge of the rate of the IO+NO reaction. The uncertainty of this value is also rather large and in fact the determination reported here lay inside the error interval. In this case the reaction of IO and OIO could play a role as well, although in this range of pressures its effect would be smaller

10.5.3. Branching of the IO self reaction

Table T10.4 contains a summary of the IO self reaction branching data published so far. The branching ratios and yields are also plotted as a function of pressure in F10.20. The IO self reaction is bimolecular and in principle can proceed through excited complexes of different symmetries [84, 174]. According to *ab initio* calculations [84], four I_2O_2 isomers are thermodynamically allowed from IO+IO. The formation of the most stable dimer (IIO_2) from the IO self reaction would require extensive rearrangement of bonds. The upper limit of 5% for the yield of I_2 obtained by Sander [80], consistent with the result reported here, indicates that collisions on the OIIO^* potential energy surface are minor. The intermediates IOOI^* and IOIO^* would end up

in the reaction products 2I+O₂ (R10.2.b) and I+OIO (R10.2.c) respectively, although they could also be collisionally stabilized (R10.2.d).

The results of the present study show that collisions on the IO/OI surface (R10.2.b) are minor (~ 10%). No pressure dependence of this channel can be distinguished. This indicates that IOOI* cannot be stabilized in this range of pressures. On the other hand, most collisions take place on the IO/IO surface, as expected from the interaction of two strong dipoles. This conclusion is consistent with the tendency of the halogen monoxides to react with each other via an alternating excited complex XOYO*, when proceeding from chlorine via bromine to iodine. The weight of channel R10.2.c is overtaken by channel R10.2.d as pressure increases, thus indicating the stabilization of IOIO*. Rapid dissociation of IOIO has been found to be hardly compatible with the data recorded in the present study and with the most recent results of $k_{10.2}$ reported in the literature.

In the calculations performed by Misra and Marshall [84], it was assumed that the contributions of R10.2.a and R10.2.b are small. They suggested that a pressure independent channel R10.2.c would dominate over R10.2.d, which is consistent with the pressure independence of the overall rate coefficient. The results reported by Vipond et al. [174] ($k_{10.2,c}/k_{10.2} = 0.44 \pm 0.20$ at 1.9-2.2 Torr), Joseph et al. [83] ($k_{10.2,c}/k_{10.2} = 0.31 \pm 0.10$ at 40 Torr) and Bloss et al. [79] ($k_{10.2,c}/k_{10.2} = 0.38 \pm 0.08$ at 760 Torr) seem to be consistent with a pressure independent branching ratio for channel R10.2.c. However, these three studies disagree with Misra and Marshall about the importance of channels R10.2.b and R10.2.d. On the other hand, the pressure dependence of $(1-\alpha)$ observed by Sander [80] and Harwood et al. [171] and the experimental results of the present study are inconsistent with a pressure independent branching. Saunders and Plane [85] have suggested that the I-OIO bond strength determined *ab initio* [84] could be

underestimated by about 20 kJ mol^{-1} , thus explaining the divergence between theoretical predictions and experimental results.

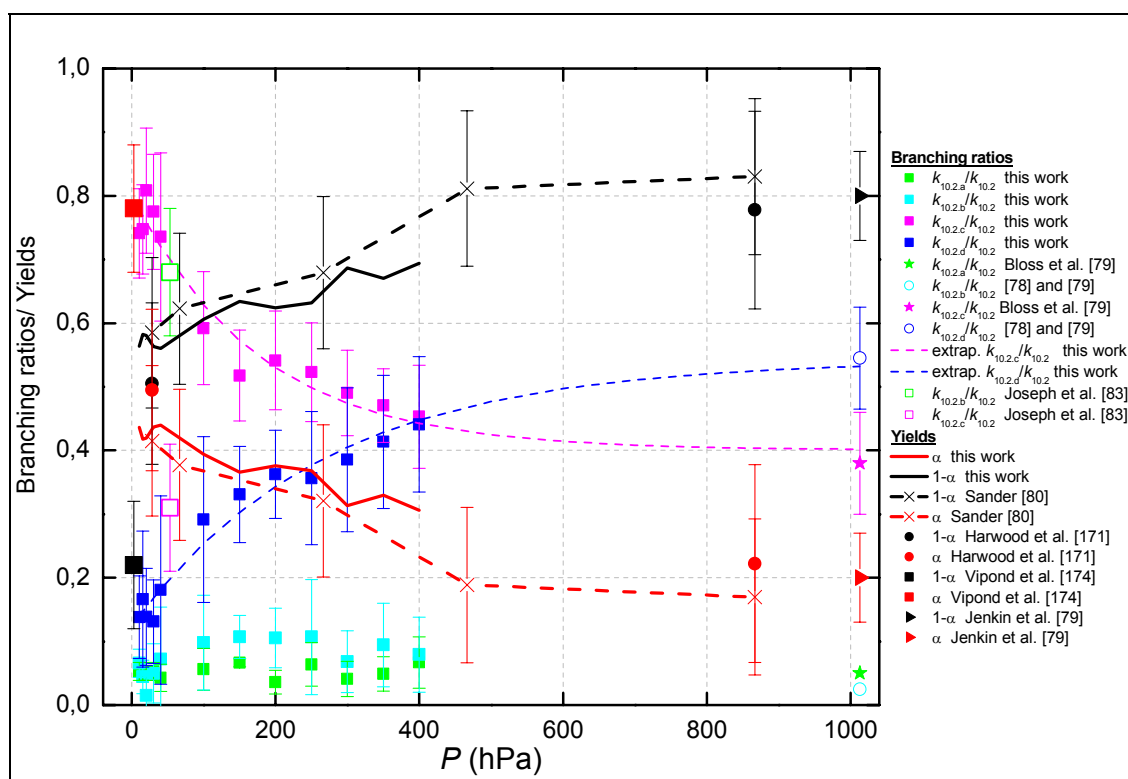
The value of $k_{10.2,c}/k_{10.2}$ measured by Bloss et al. at 760 Torr (1013 hPa) [79] is consistent with the extrapolation of the determination of the present study towards atmospheric pressure (F10.27) by using an empirical exponential decay of the form $f(P) = A + Be^{-cP}$ (where A , B and C are constants). However, it must be noted that reaction R10.25 may also be a source of OIO in the $\text{N}_2\text{O}/\text{I}_2$ system, and thus the value of $k_{10.2,c}/k_{10.2}$ reported by Bloss et al. [79] could be an overestimate. From the work of Jenkin et al. [78], an iodine atom yield $\alpha=0.2$ can be deduced, and thus the value of $k_{10.2,d}/k_{10.2} \sim 0.5$ at atmospheric pressure can be estimated. This value is also consistent with the extrapolation of the results of this study by using an exponential growth of the form $f(P) = A - Be^{-cP}$.

In summary, the results of the present study together with those of Harwood et al. [170], Sander [80] and Bloss et al. [79] offer a consistent picture about the mechanism of the IO self reaction: under ambient conditions, IO+IO proceeds most likely by energy transfer through bimolecular channels, whose end products are all thermodynamically allowed. Those channels related to the asymmetric excited complex are favoured by the dipole interaction. The IOIO* complex can be stabilized under pressures within the atmospheric range, and the IOIO isomer is somewhat more stable than predicted by *ab initio* calculations, in such a way that indirect evidence for its formation can be obtained in a time scale of at least one hundred milliseconds. Future experiments at low temperatures may help to distinguish a termolecular channel –like in the case of ClO+ClO and BrO+BrO– and to gain more information about the properties of the IO dimer.

T10.4. Determinations of the IO Self-Reaction Branching Ratios at 295-298 K

Reference	Species Monitored	<i>P</i> (hPa)	<i>k</i> _{10.2.a} / <i>k</i> _{10.2}	<i>k</i> _{10.2.b} / <i>k</i> _{10.2}	<i>k</i> _{10.2.c} / <i>k</i> _{10.2}	<i>k</i> _{10.2.d} / <i>k</i> _{10.2}	α	$\alpha - 1$
Jenkin et al. [78]	I ₂ , O ₃	1013	0	-	-	-	0.20 ± 0.07^{a,b}	0.80 ± 0.07
Sander [80]	IO, I ₂	28 867	< 0.05	-	-	-	0.42 ± 0.12 0.17 ± 0.12	0.58 ± 0.12 0.83 ± 0.12
Harwood et al. [171]	IO, I ₂	28 ^c 867	< 0.30	-	-	-	0.50 ± 0.16 0.12 ± 0.16	0.51 ± 0.1 0.78 ± 0.16
Vipond et al. [174]	IO, I	2.5-3	-	> 0.56 ± 0.2	< 0.44 ± 0.2	-	0.78 ± 0.10	0.22 ± 0.10
Bloss et al. [79]	IO, I ₂ , OIO	> 800	< 0.05	0.11 ± 0.04	0.38 ± 0.08	0.46 ± 0.06	0.3	> 0.65
Joseph et al. [83]	OIO	53	-	> 0.68	0.31 ± 0.10	-	> 0.83	< 0.17
This work	IO, I ₂ , I, OIO	10 400	0.05	0.09 ± 0.06	0.74 ± 0.10 0.45 ± 0.10	0.14 ± 0.08 0.44 ± 0.13	0.44 ± 0.11 0.28 ± 0.14	0.56 ± 0.11 0.72 ± 0.14

^{a)} The branching ratios directly deduced from experimentally determined quantities are indicated in bold case. ^{b)} Jenkin et al. [78] determined the quantum yield for O₃ removal (1.25 ± 0.11). From this quantity, they derived the ratio of the rate coefficient of the iodine producing channels to that of the non iodine producing channels (0.25 ± 0.11). At that time no evidence for channel R10.2.c had been found, and therefore the authors [78] postulated that $k_{10.2.b}/k_{10.2.d} = 0.25$. The detection of OIO as a product of the IO self reaction confirmed the existence of this channel, and the updated ratio must include the contribution of one half of R10.2.c. The iodine atom yield has been derived directly from the ratio reported in this reference [78]. ^{c)} The range of pressures is not indicated in the text [171]. It has been deduced that the range refers to the same range considered by Sander [80].



F10.20. Literature values for the pressure dependence of branching ratios and yields and extrapolation of the results of the present study to ambient conditions.

T10.5. Branching ratios for the bimolecular channels of the reactions between halogen monoxides [29].

	ClO+ClO	ClO+BrO	ClO+IO	BrO+BrO	BrO+IO	IO+IO
OXYO* XOOY*	40% Cl ₂ +O ₂	10% BrCl+O ₂	20% ICl+O ₂	10% Br ₂ +O ₂	-	5% I ₂ +O ₂
XOOY*	40% Cl+ClO ₂	40% Br+ClO ₂	25% Cl+I+O ₂	85% 2Br+O ₂	-	10% (60%) 2I+O ₂
XOYO*	20% Cl+OCIO	50% Br+OCIO	55% I+OCIO	a) ₋	80% Br+OIO	30% I+OIO 55% IOIO (40%)
k (cm ³ molecule ⁻¹ s ⁻¹)	1.6·10 ⁻¹⁴	1.4·10 ⁻¹¹	1.2·10 ⁻¹¹	3.2·10 ⁻¹²	8.5·10 ⁻¹¹	7.5·10 ⁻¹¹

a) Only BrO+BrO does not fit into the series. The channel producing OBrO would be favoured by dipole interaction, but seems to be thermodynamically closed ($\Delta H_r^0 \approx 36 \text{ kJmol}^{-1}$ [29])

Vipond et al. [174] reported a yield of iodine atoms from the self reaction of $\alpha = 0.78 \pm 0.10$ at 1.9-2.2 Torr (2.5-3 hPa), roughly 2 times larger than the value at 10 hPa reported here. As the pressure in this case would be too low to enable the stabilization of the IO dimer, this value implies that other iodine producing channels apart from R10.2.c must be active. If the channel R10.2.c were very dominant, the iodine atom yield would be about 0.5, as the results of this and other studies indicate [53, 80, 171]. The chemical system O₂/CF₃I in a discharge flow tube set up is extremely complex due to the interaction of NO and CF₃ with IO and to further sinks of IO attributed to wall losses. The authors dedicatedly addressed this issue by determining the required rate coefficients and considering the corresponding reactions in a numerical model of the chemistry. This is critical to avoid overestimation of the amount of IO consumed via reaction R10.2 and the overestimation of iodine produced in reaction R10.2. The reason for the discrepancy is not easy to identify, but it should be noted that unaccounted losses of the iodine atoms produced by reaction of IO and NO in the interval between injection of NO and detection of I by resonance fluorescence (4 ms) would lead to an underestimation of the amount of IO, and to a subsequent overestimation of the iodine atom yield. These potentially unaccounted losses might be related to the cycle R10.23-R10.24 (reaction R10.23 would proceed at $\sim 6 \times 10^{-11}$ molecule \times cm³, rate coefficient communicated by J. Plane, 2005) or to other cycles of the type R10.5-R10.6. However, sinks for I atoms are in general pressure dependence and expected to be slow at 3 hPa. On the other hand, the reaction OIO+IO would have the opposite effect.

Joseph et al. [83] reported a branching ratio for channel R10.2.c at 40 Torr (52 hPa) of $k_{10.2.c}/k_{10.2} = (0.31 \pm 0.10)$ and, assuming that channels R10.2.a and R10.2.d are not active, they derived $k_{10.2.b}/k_{10.2} = 0.68$. By taking into account the difference in the absorption cross sections employed to scale the OIO transient absorption ($\sim 15\%$ larger

than the results reported here [83,125]) and the overall rate coefficient (Joseph et al. [83] use the value of Bloss et al. [79]), a value of $k_{10.2.c}/k_{10.2} \sim 0.45$ is obtained ($k_{10.2.b}/k_{10.2} = 0.55$), still far from the value at 40 hPa of about 0.7 reported here. It has been found that at 40 hPa there is a non negligible production of the IO dimer, which has been quantified as about 0.2. This would reduce the value of $k_{10.2.b}/k_{10.2}$ reported by Joseph et al. [83] to 0.25. The use of the results of the latter study in simulations of the I₂/O₃ system does not allow reproducing properly the curves of I, IO and OIO data recorded at 40 hPa, even if the different OIO cross section is taken into account. As a result of the large branching ratio of channel R10.2.c, the simulated curves overestimate the amounts of I and IO significantly. Further, the simulated peak concentration of OIO is almost three times smaller than observed. This disagreement might be the result of a small overestimation of the excimer laser fluence, leading to an overestimation of the initial amount of IO produced from the photolysis of N₂O. This would cause a significant underestimation of $k_{10.2.c}/k_{10.2}$, because in steady state of OIO this ratio depends on [IO]⁻².

10.5.4. Fate of OIO and link to the higher oxides

To date only one attempt to fit the complex kinetic behaviour of OIO measured in laboratory studies has been published. Joseph et al. [83] studied it at 52 hPa and 298 K in the N₂O/CF₃I system and concluded that the OIO decay is mainly caused by reaction R10.23. The present study constitutes the first systematic investigation of the OIO temporal behaviour reported in the literature under a variety of conditions. The presence of ozone enables the induction of processes of potential atmospheric relevance. By quickly removing iodine atoms, the loss of OIO is more clearly linked with the formation of higher iodine oxides.

Burkholder et al. [110] succeeded in reproducing the particle production in a Teflon bag experiment by assuming OIO homogeneous nucleation and using parameterized thermodynamics to model the backward rate coefficients. They used forward coefficients derived from kinetic theory [151] ($\geq 3 \times 10^{-10} \text{ cm}^3 \text{ molecule}^{-1} \text{ s}^{-1}$) and did not consider participation of IO in the cluster formation. The present study has shown that attachment of IO to other species, and in particular the reaction $\text{IO} + \text{OIO} \rightarrow \text{I}_2\text{O}_3$ (R10.8, $n = 1$), must be included in the mechanism in order to reproduce the observed IO and OIO concentrations and to obtain reasonable values for $k_{\text{OIO}+\text{X}}$ ($n < 4$), which otherwise would be larger than $5 \times 10^{-10} \text{ cm}^3 \text{ molecule}^{-1} \text{ s}^{-1}$. A recent modelling study by Pirjola et al. [111] shows good correlation between observed and modelled particle size distributions in chamber experiments [104] by including reaction R10.8 $n = 1$ and considering I_2O_3 in the first cluster size section. However, their model apparently does not consist of a binary nucleation or co-polymerization of IO and OIO. The good performance of the proposed model (T10.1) in reproducing the experimental data also depends on the polymerization of IO units.

As a consequence of the introduction of reactions R10.8, R10.9 and R10.11 in the chemical model, the optimal values of $k_{\text{OIO}+\text{X}}$ are smaller than $3 \times 10^{-10} \text{ cm}^3 \text{ molecule}^{-1} \text{ s}^{-1}$ (see F10.17, panels b and c). The optimal values obtained for $k_{\text{IO}+\text{X}}$ are a factor of 2 or 3 smaller than those obtained for $k_{\text{OIO}+\text{X}}$. On the other hand, the IO and OIO collision frequency factors are very similar. This could indicate that the kinetic theory does not account for the rate coefficients of forward reactions in the first steps of the nucleation process. The assumption of spherical geometry is probably inadequate for polymeric structures, where steric constraints might play a role. However, the ability to reproduce the sinks of IO and OIO with only two rate coefficients for all reactions encompassed in R10.7-R10.12 might result from the fact that $\text{IO} + \text{OIO}$ (R10.8, $n = 1$)

and OIO+OIO (R10.7, $n = 1$) are rate determining. The rate coefficients obtained in particular for these two reactions are smaller than the capture rate coefficients from the dipole-dipole interaction [83, 85]. This also suggests the existence of steric constraints, although the possibility of different short dissociation lifetimes of the polymeric adducts can not be discarded.

From the results of the continuous, I₂-photosensitized ozone destruction experiments carried out by Jenkin et al. [78], an iodine atom yield $\alpha = 0.2$ from reaction (2) can be deduced by assuming that the only fate of I and O₃ is reaction (1). This suggests that the lifetime of the IO dimer could be even longer than the lower limit of 10 ms reported here. This would be also consistent with the tentative assignments of IOIO reported in the literature [79, 80], and with the assignment of the absorber labelled as ‘Y’ in the present work (F9.2). The participation of this species in gas to particle conversion has been hypothesized in a number of previous publications [103, 111] In laboratory studies, this depends most likely on the amount of radicals generated. Reactions R10.11 and R10.12 might be significant with respect to thermal decomposition at very high concentrations of IO and OIO.

10.5.5. Higher iodine oxides

The simulated concentration versus time profiles of the more important oligomers generated are shown in F10.15, together with the experimentally determined time trace of ‘Z’ and the cumulative integral of the $([IO](t))^2$ (E9.1 with $C = k_{10.2,d}$). The concentration versus time curves are similar and an unambiguous kinetic assignment of ‘Z’ is not possible. An overlap of different absorptions with similar kinetic behaviour could be also responsible for the absorption labelled as ‘Z’. The concentration versus time profile of I₂O₂ obtained by complex kinetic simulation differs from E9.3, because the sinks R10.11 and R10.12 have been included. However, the difference in shape of

the concentration curves in the first 3 ms is small, because it is dominated by the second order rate of formation due to the IO self reaction. As the critical difference between the concentration curves 'Y' and 'Z' occurs in the first milliseconds as well (see F9.1.d), it does not make a big difference to consider one curve or the other in the separation of the absorber 'Y'. Thus, the tentative assignment of 'Y' to I₂O₂ remains valid. Time resolved measurements of IR spectra and/or Photo-ionisation-Time of Flight Mass Spectrometry could help to remove the ambiguity in the assignment.

Several previous studies have reported the observation of iodine oxides in the form of aerosol or solid deposits as products of the gas phase I₂/O₃ chemistry [31]. Harwood et al. [171] report spectroscopic evidence of aerosol formation in the I₂/O₃ photochemical system (which could be reduced by reducing [O₃]) whereas no aerosol production in the N₂O/I₂ system. Jenkin et al. [78] observed that in their system the O₃ removal rate progressively decreased during photolysis, being that consistent with alternative reactions of iodine atoms at low ozone concentrations. In the chemical system studied by Joseph et al. [83], significant amounts of I₂ are regenerated, while they state that in the presence of ozone particles are more readily formed. These results are consistent with the observation of different amount of deposit depending on the initial ratio [I₂]/[O₃] in the experiments conducted within the present study. It can be concluded that ozone helps to convert iodine to higher oxides rather than to molecular iodine, by preventing iodine abstraction cycles of the type R10.5-R10.6.

The mechanism proposed (T10.1) indicates that higher iodine oxides will form with stoichiometric ratio O/I ≤ 2. However, in a previous study performed in the IUP-UB, a white solid deposit was collected and identified as I₂O₅ [149] Saunders and Plane [85] have also collected particles with I₂O₅ stoichiometry. In the present study, performed with significantly different mixing ratios of precursors, a pale yellow powder

has been observed, which would be consistent with I_4O_9 [114, 115, 173, 213]. Recently Ristovski et al. [113] have reported a O/I ratio of 2 for particles produced in the photolysis of CH_2I_2 in the presence of ozone, consistent with I_2O_4 . This suggests that the stoichiometry of the solid products might depend on the concentration of precursors employed. Assuming that successive reaction of iodine oxides with ozone leads to I_2O_5 [85], the amount of iodine and ozone employed might determine if these oxidation steps, or rather polymerization, dominate the production of higher iodine oxides. However, the short lifetime predicted for I_2O_4 would slow down dramatically the formation of I_2O_5 .

To date there are no laboratory studies reporting simultaneous measurements of gas phase iodine oxides, polymers and particle production. Further investigations are required in order to achieve a spectroscopic assignment of the higher order oxides. Kinetic studies of the thermal decomposition of I_2O_2 , I_2O_3 and I_2O_4 and of the polymerization mechanism would require the implementation of methods capable of simultaneous time resolved monitoring of the gas phase and the nascent polymers.

10.5.6. Atmospheric relevance

The present study confirms the results reported by Bloss et al. [79] for the branching of the IO self reaction at atmospheric conditions. The iodine atom yield takes a value of about 0.2, so that the ozone destroying potential of the iodine chemistry depends rather on the fate of the molecular products. Recent studies indicate that OIO is relatively photostable, with a quantum yield smaller than 0.1 at 562 nm [83] and 0.24 at 532 nm [77]. Thus, the only channel which could enhance significantly the iodine atom yield of the IO self reaction is the dissociation of IOIO to I+OIO.

The life time of IOIO with respect to dissociation is most likely larger than 10 ms. This figure is large for the typical experimental time scales employed in laboratory

studies, but it still would make thermal dissociation the main sink for IOIO in the atmosphere, as a result of the low concentrations of IO and OIO [36-43] (see T10.5). The reactions R10.11 ($n = 1$) and R10.12 ($n = 1$) could be atmospheric sinks for IOIO in ‘hot spots’ [110] only if the lifetime of IOIO with respect to dissociation is larger than about 1 s. Additionally, as a result of the low I-OIO bonding energy (from 50 to 80 kJ mol⁻¹) [84, 85], the threshold for photo-dissociation of IOIO is situated in the near IR. The unidentified UV absorbers tentatively assigned to I₂O₂ (see Chapter 9 and references [79, 80,125]) absorb inside the actinic window, and therefore photolysis of I₂O₂ could be another sink for this species:



The photolysis rate for I₂O₂ at 0 km and 16° SZA (T10.6), obtained under the assumption ‘Y’ = I₂O₂, in the present work (see Appendix D) is of the same order of magnitude than the first order rate coefficients of the first polymerisation steps in R10.11 and R10.12.

T10.6. First order rate coefficients for consumption of OIO and I₂O₂ in the atmosphere, calculated by considering the maximum mixing ratios of IO and OIO measured in Mace Head during the NAMBLEX campaign by Saiz-López et al. [38]

	$k_{\text{IO}+\text{X}} \times [\text{IO}]$ (s ⁻¹)		$k_{\text{OIO}+\text{X}} \times [\text{OIO}]$ (s ⁻¹)		$k_{10.21}$ (s ⁻¹)	$k_{\text{IOIO}+h\nu}$ (s ⁻¹)	$k_{\text{OIO}+h\nu}$ (s ⁻¹)
	Day	Night	Day	Night		Day	Day
For measured Mixing ratios ^a	0.009	0.004	< 0.012 ^c	0.03	< 10 ^d	0.024 ^e	0.042 ^f
For local Mixing ratios ^b	0.109	0.047	< 0.15	0.375			

^{a)} The measurements were performed with long path DOAS. ^{b)} It was estimated that the intertidal zones where the emissions of I₂ and iodocarbons take place comprised only 8% of the path. Therefore to estimate the local concentrations a factor 12.5 must be considered. ^{c)} During the day OIO was under the detection limit (4 pmol × mol⁻¹). ^{d)} According to the experience accumulated in laboratory studies [79, 80, 85, 171] and the results of the present study, the IO-dimer is stable on a time scale of more than ~100 ms. ^{e)} Under the assumption ‘Y’ = IOIO (See Chapter 9) ^{f)} Assuming a quantum yield 0.1 across the whole visible spectrum (see Appendix D).

Jenkin et al. [78] carried out I₂-photosensitised ozone destruction experiments, where long photolysis times were used. They obtained a quantum yield for ozone destruction of 1.25 per iodine atom, from which an iodine atom yield of the IO self reaction of 0.2 can be deduced by assuming that the only fate of I and O₃ is R10.1. This yield is consistent with the results reported here and those of Sander [80] and Harwood et al. [171]. This agreement between the results obtained in continuous and flash photolysis experiments could be interpreted as a very slow thermal dissociation of IOIO. The only information available about the thermal stability of IOIO has been obtained by *ab initio* calculations. If IOIO dissociates as readily as these studies predict, the effective iodine atom yield of the IO self reaction would increase to up to 0.6.

The effective quantum yield for O₃ removal per iodine atom in the atmosphere would be as a consequence of about 2.5 (a factor 2.4 smaller than the corresponding quantum yield for bromine), and the IO self reaction would have a larger impact on ozone destruction. On the other hand, if IOIO were photostable, the main consequence of the IO self reaction would be rather the partitioning of a larger fraction of iodine to aerosol by nucleation processes or by heterogeneous uptake of IOIO [45, 46]. In conclusion, the thermal stability of IOIO remains as a major uncertainty of the iodine chemistry, and new laboratory studies are required to elucidate this question.

The decay of OIO observed in the laboratory can be satisfactorily explained by a mechanism comprising addition steps. A fully consistent description of the chemistry requires consideration of at least one further nucleating species (IO). In the atmosphere, photo-oxidation of biogenic iodine containing species leads to the formation of IO and OIO, which in the absence of other important sinks could polymerise or react in the gas phase to form condensable species. According to the first possibility, IO and OIO would act as monomers and built chains, as suggested in the present study. The iodine oxide

polymers could keep on growing heterogeneously in a supersaturated mixture of the iodine containing monomers and/or further condensable species [214]. There is, however, an impediment for the homogeneous homomolecular OIO nucleation, derived from the low thermal stability of I₂O₄ predicted *ab initio*. Similar to IOIO, I₂O₄ is predicted to decay thermally in less than 1 ms under atmospheric conditions [85]. If both dimers were unstable, the nucleation would proceed completely via the stable species I₂O₃. In the second mechanism, IO and OIO would react in the gas phase to produce other condensable species, e.g. I₂O₅, which would act as monomers.

Two recently published studies deal with the modelling of particle formation in the coastal MBL. Saiz-López et al. [103] consider a heteromolecular nucleation mechanism where the smallest “particles” formed can be either I₂O₂, I₂O₃ or I₂O₄ and suggest that the rate of formation of these species can be competitive with OIO photolysis when the concentration of iodine oxides is high, making the rate of new particle formation only slightly sensitive to the OIO photolysis rate. On the other hand, the model suggests that the impact of the iodine chemistry on the ozone budget is small. Both results are related to the key assumption of thermal stability of IOIO, which is critical as well to reproduce the particle formation. Pechtl et al. [116] consider in their model the parameterization of the homomolecular homogeneous OIO nucleation of Burkholder et al. [110] and ternary H₂SO₄-H₂O-NH₃ nucleation. In this study, I₂O₂ is assumed to be thermally unstable, in such a way that the IO self reaction proceeds effectively at 80% through the I+OIO channel. As the iodine driven new particle production in this study is based only on OIO nucleation, the amount of particles predicted by the model must be sensitive to additional OIO sinks like OIO photolysis or NO_x. A significant difference between both studies is the inclusion of ternary H₂SO₄-H₂O-NH₃ nucleation in the model of Pechtl et al. This lack of this source of particles in

the model of Saiz Lopez et al. is compensated by the assumption of IOIO thermal stability. It is worthwhile to note here that I_2O_4 has been predicted to be thermally unstable as well, so that in principle there is not a strong argument to favour OIO nucleation against IO nucleation.

10.6. Summary and conclusion

The temporal behaviours corresponding to the more relevant absorbers of the I_2/O_3 gas phase photochemistry have been simultaneously recorded under different conditions by using synchronised molecular absorption spectroscopy and atomic resonance absorption spectroscopy. The raw data have been processed by using multivariate analysis techniques and absolutely scaled by using the absorption cross sections reported in a previous publication [125]. Parameters relevant for the gas phase chemistry have been determined by applying conventional kinetic analysis. Additionally, state-of-the-art techniques for numerical integration of ODEs and for non-linear fitting have been used in order to simulate the chemistry of the system and fit the parameters under investigation. A chemical mechanism has been proposed, which succeeds in the reproduction of the observed data at a variety of chemical conditions. By fitting the simulated curves obtained with this mechanism to the observed concentration versus time curves, the complete branching of the IO self reaction at 298 K and the rate coefficients for the first steps of the IO-OIO nucleation mechanism have been obtained. To knowledge of the author the present study constitutes the first attempt to obtain a complete kinetic description of the I_2O_3 photochemistry.

The overall rate coefficient of the IO self reaction at 298 K has been found to be pressure independent, but smaller than the current IUPAC recommendation [29]. This result suggests that an unaccounted source of IO might persist in this system, but also might indicate that unaccounted sinks are hidden in the second order behaviours observed in the I_2/N_2O system, like for example the reaction of IO and OIO, which

according to RRKM calculations [83] reaches its high pressure limit in the range of pressures considered in this study. A new investigation of the N₂O/I₂ with a multichannel approach would be convenient to elucidate this question.

The branching of the IO self reaction determined suggests that the IO self reaction proceeds principally through an IOIO* excited complex, which is increasingly stabilised as the pressure grows up, and becomes the most important product at atmospheric pressure. Other channels arising from different symmetries of the excited complex seem to have minor importance. The analysis of data collected for this study, chemical simulations and comparison to previously published results all seem to indicate that the stabilised asymmetric dimer does not thermally decompose on a time scale smaller than hundreds of milliseconds, being during this time available for other interactions. The results obtained indicate that IO and OIO may undergo homogeneous nucleation, and that it is likely that IOIO takes part in this process under the chemical conditions employed. They also suggest that if the thermal stability of the IO and OIO dimers is not long enough under atmospheric conditions to enable other sinks to compete, the species I₂O₃ could be potentially responsible for the nucleation phenomena observed in the atmosphere rather than I₂O₄. Other reactions like iodine abstraction reactions (at the mixing ratios considered) or reactions of ozone with secondary products have been found to be of minor importance.

There are no laboratory studies in the literature reporting simultaneous measurements of iodine oxides and particle production, which would enable to correlate quantitatively IO, OIO and eventually IOIO with higher oxides and aerosol. Further investigations are required to unequivocally identify higher order oxides and study their temporal behaviour, e.g. by recording time resolved IR spectra of these molecules. Kinetic studies of the polymerization-nucleation process would require the

implementation of methods capable of time resolved synchronised monitoring of the gas phase and the nascent polymers, e.g. coupling optical absorption spectroscopy to time resolved FTIRS or Time of Flight Mass Spectrometry.

This work has been partially funded by the German Space Agency (contract 50EP9207 ‘SCHIAMACHY’ and project LVA 01/003), the European Union (contract EVK2-CT2001-00104 ‘THALOS’), the EU-ACCENT Network of Excellence and the University and the State of Bremen.

DANKSAGUNG / AKNOWLEDGEMENTS / AGRADECIMIENTOS

Zuerst möchte ich mich ganz herzlich bei Peter Spietz bedanken. Sein bedingungsloser Glaube an meine Fähigkeiten hat es mir ermöglicht, dass ich in Deutschland meine Doktorarbeit schreiben konnte. In vier Jahren Zusammenarbeit haben wir eine sehr gute Mannschaft aufgebaut und jedes unserer wissenschaftlichen Ziele erreicht. Alles, was Labor und Werkstatt angeht, habe ich von ihm gelernt. Peters Neugier und technischen Kenntnisse sorgten unaufhörlich für intellektuelle Anregungen. Ich habe auch das Glück, seine Freundschaft zu genießen, und hoffe –trotz unserer häufigen Auseinandersetzungen ;-)- dieses Glück für immer behalten zu können.

I also thank Professor John Burrows for his enthusiastic personal support. He has been always open for discussion and he has taught me many things about science. In the difficult position of maintaining equilibrium between productivity and rigour, he always encouraged me to think freely, while trying to constrain my ‘wild theories’ within sensible limits. I’m very proud of having received his help in writing the paper on absorption cross sections of iodine oxides. Those days I learned a lot and I enjoyed for hours his stimulating discussions and his humour.

Agradezco a M^a Dolores Andrés Hernández (Lola) su ayuda como química de guardia y experimentalista veterana, sus consejos como emigrante de larga duración y, también, por qué no, sus regañinas fraternas. Pero lo que más le agradezco es su actitud vital, que ha sido para mi un ejemplo durante estos cuatro años. Su forma de superar los momentos difíciles a base de reirse de todos, incluida ella misma, con su fina ironía, me ha ayudado en muchas ocasiones a salir de mis recurrentes depresiones. Es una suerte tenerla en la oficina de enfrente.

Ich wollte mich auch bei Lars Reichert, Deniz Kartal, Folkard Wittrock, Hilke Oetjen, Bilgehan Gür und Professor Jörn Bleck-Neuhaus bedanken.

Outside the Institute of Environmental Physics of the University of Bremen, I would like to acknowledge Professor John Plane and Alfonso Sáiz López for helpful discussions and collaboration.

Mis amigos en Bremen han hecho que todo fuera mucho más llevadero. Cada uno merecerían una medalla a la paciencia por aguantarme en mis malos momentos. Pero sobre todo hemos vivido juntos momentos muy felices. Hemos viajado, nos hemos hinchado de comer y de beber, hemos aprendido casi de todo, nos hemos sumergido en la cultura del Norte de Alemania, hemos bailado, reído y cantado. A todos mis 'Klaus': Britta, Elena, Santiago, Anna, Higinio, Fabian, Eva, Nina, Begoña, Pablo, Joandré, Simon, Anke, Peter...

No hay palabras suficientemente hermosas para agradecer a mis padres todo aquello de lo que se compone mi existencia. La intensidad y la plenitud de mi vida y el futuro que se abre ante mi de par en par se deben a su amor sin medida. Gracias a ellos están conmigo Alicia y Carmen, mis infatigables compañeras de viaje, sin las cuales nunca habría conseguido llegar hasta aquí.

Es mucho también lo que debo a mis abuelas, Lola y Concha, y a la tita Maina, que me enseñaron a hablar, a andar, a cantar, que están siempre presentes en los recuerdos más felices de mi infancia y mi juventud, y que han sufrido mucho con mi prolongada ausencia. Mis abuelos Mariano y Pepe ya no están con nosotros, pero no puedo dejar de recordar aquí todo el cariño que pusieron en mí y el entusiasmo con el que seguían mis progresos en mis estudios. Creo que estarían orgullosos de su nieto.

Gracias, a Paco, Loli, Pablo, Natalia, M^a Luisa, Mariano, Mari Paz, Emilio, Carmen, y a toda mi gran familia por acogerme con cariño cuando vuelvo a casa.

Gracias Cati, por aquellos años tan hermosos en los que empezó a fraguarse lo que hoy somos. Tu amistad es uno de mis mejores tesoros.

Gracias a la Comunidad (Pepe, Tere, Mariano, Chari, Inés, Jesús, Cristina, Juan, Luz, y los retoños Cristina y Darío). Sois mi ejemplo de vida y la voz de mi conciencia.

APPENDIX

A. STATISTICAL INDEPENDENCE AND COST FUNCTIONS

Definitions of statistical independence can be found in [186, 197]. Given a set of scalar random variables, these variables are mutually independent if their joint probability distribution function $f_{\mathbf{x}}$ can be factorised into the marginal pdfs of each of the variables. Uncorrelatedness is a necessary condition for statistical independence and is equivalent to it *only* for variables with Gaussian distribution. Thus, independence is a stronger constraint than uncorrelatedness.

Information Theory provides the arguments to build cost functions, which are able to quantify the quality of linear combinations of mixed signals in terms of the factorisation of their joint probability distribution function (pdf). Mutual information is the natural measure of the dependence between random variables. The mutual information \mathfrak{I} between n scalar random variables $s_i, i = 1, \dots, n$, is given by:

$$\mathfrak{I}(s_1 \dots s_n) = \sum_{i=1}^n H(s_i) - H(\mathbf{s}) \quad (\text{EA.1})$$

where $H(s_i) = -\int_{-\infty}^{+\infty} f_i(s_i) \log f_i(s_i) ds_i$ is the differential entropy of a given variable s_i and $H(\mathbf{s}) = -\int_{\mathbf{x}} f_{\mathbf{x}}(\mathbf{s}) \log f_{\mathbf{x}}(\mathbf{s}) d\mathbf{s}$ is the entropy of the random vector \mathbf{s} . $\mathfrak{I}(s_1, \dots, s_n)$ is always non negative and zero if and only if the variables are statistically independent.

A number of equivalent approaches can be followed in order to formulate ICA. The so-called *infomax* approach is based on the maximisation of the information flow of a neural network with non-linear outputs, or, in other words, the maximisation of mutual information between the observations and the sources transformed by a non linear function (see Bell et al. [202]). The Maximum Likelihood Estimation approach uses the log-likelihood as cost function. Likelihood here means the probability of a data set as a function of the parameters of the model (the mixing matrix and the pdf of the source

vector). Further details on this approach can be found in [186]. The negentropy approach is based on the minimisation of an approximation to mutual information $\mathfrak{I}(s_1 \dots s_n)$ between linear combinations $s_j = (\mathbf{b}^\dagger)^T \mathbf{y}$ with respect to the weights \mathbf{b} (see Hyvärinen [203]). Because of its simplicity, this is the approach considered in the present work.

An important property of mutual information is that for an invertible linear transformation $\mathbf{s} = \mathbf{B}^\dagger \mathbf{y}$ it is possible to write EA.1 in the form:

$$\mathfrak{I}(\mathbf{s}) = \sum_{i=1}^n H(s_i) - H(\mathbf{y}) - \log |\det \mathbf{B}^\dagger|$$

If the components are constrained to be uncorrelated and normalised to unit variance, and the observed data \mathbf{y} are also uncorrelated (i.e. $E[\mathbf{y}\mathbf{y}^T] = \mathbf{I}$, what can be achieved by PCA pre-processing), then the minimisation of $I(\mathbf{s})$ with respect to \mathbf{B}^\dagger is equivalent to the minimisation of the individual differential entropies $H(s_i)$. To calculate exactly the differential entropy $H(s)$ of a random scalar variable, s , it is necessary to know its pdf, which is in general unknown. Nevertheless, an approximation of the pdf can be obtained using the Maximum Entropy Method ([203]). Considering such approximation, the differential entropy can be approximated as follows:

$$H(s) \approx -\int f(s) \log f(s) ds \approx H(v) - \frac{1}{2} \sum_{k=1}^m E[G_k(s)]^2 \quad (\text{EA.2})$$

where $H(v) = \frac{1}{2}(1 + \log(2\pi))$ is the entropy of the standardised gaussian distribution, and $\{G_k, k = 1, \dots, m\}$ is a set of functions which are intended to ‘measure’ characteristics of the distribution of s . Differential entropy is also referred to as negentropy.

EA.2 can be seen as a ‘one-unit’ cost function, in the sense of one-by-one extraction of components. It shows how maximisation of independence (minimisation of mutual information) of estimated components is equivalent to maximisation of non-

gaussianity, characterised by the second term in EA.2). As $H(v)$ is constant, the second term itself can be considered as a ICA cost function, denoted as J_G :

$$J_G(\mathbf{b}^\dagger) = \sum_{k=1}^m \mathbb{E}[G_k((\mathbf{b}^\dagger)^T \mathbf{y})]^2$$

where s has been substituted by $(\mathbf{b}^\dagger)^T \mathbf{y}$.

To choose the set of functions G_k , several criteria must be considered. The functions must allow easy practical estimation of $\mathbb{E}[G_k(s)] = \int f(s)G_k(s)ds$, be as insensitive as possible to outliers, not increase faster than they would quadratically to assure that $f(s)$ is integrable, and ‘measure’ characteristics of the distribution of s that are informative in the calculation of $H(s)$, like symmetry and bimodality. If $f(s)$ were known, the optimal function would be $-\log f(s)$. Thus, it is a common practice to look for log-densities of some well known distributions. In case that prior knowledge about the pdf is available, the choice of the optimal function would be the negative logarithm of a guess of the pdf.

A single function G can be used to build a cost function (Hyvärinen [188]) with the form:

$$J_G(\mathbf{b}^\dagger) \propto \{\mathbb{E}[G((\mathbf{b}^\dagger)^T \mathbf{y})] - \mathbb{E}[G(v)]\}^2 \quad (\text{EA.3})$$

where G is any non-quadratic function and v is a variable with a standardised gaussian distribution.

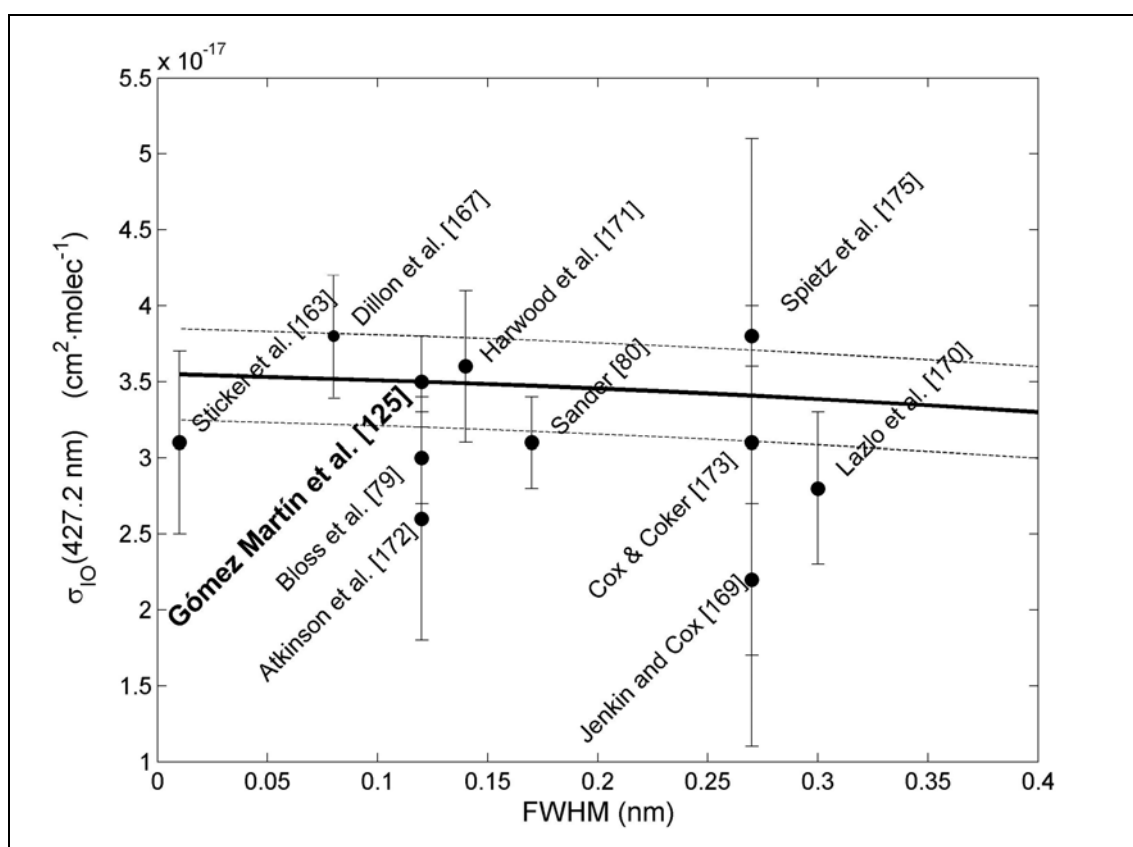
B. NOTATION IN PCA AND ICA

t	variable label (time)
λ	sampling label (wavelength)
N	dimension of the random vector \mathbf{y} (or \mathbf{a})
M	size of the sample of the random vector \mathbf{y} (or \mathbf{a})
n	number of sources
$I_0(t, \lambda)$	incoming intensity
$I(t, \lambda)$	transmitted intensity
L	path length through the reaction vessel
$A(t, \lambda)$	optical density in a MTRMAS dataset
\mathbf{a}	vector of optical density as observational random vector, with components $a_i, i=1 \dots N$
\mathbf{a}_j	pure optical density vector associated to the absorber $j, j=1 \dots n$
\mathbf{C}	mixing matrix of concentration times path length
$\boldsymbol{\sigma}$	vector of cross sections as source signals
σ_j	component j of $\boldsymbol{\sigma}$, cross section of the absorber j
\mathbf{M}^\dagger	generalised inverse of matrix \mathbf{M}
\mathbf{M}^T	transpose of matrix \mathbf{M}
\mathbf{I}	identity matrix
\mathbf{y}	observational random vector
$\bar{\mathbf{y}}$	centered observational vector
\mathbf{B}	mixing matrix
$(\mathbf{b}^\dagger)^T$	row of the generalised inverse of \mathbf{B}
\mathbf{s}	vector of source signals or components
s_j	component j of \mathbf{s} , or source signal j .
$\boldsymbol{\varepsilon}$	noise term
\mathbf{P}	estimator of the mixing matrix \mathbf{B} in PCA
\mathbf{p}_j	column j of \mathbf{P}
$\tilde{\mathbf{P}}$	mixing matrix for the retained principal components
\mathbf{Q}	estimator of \mathbf{B}^\dagger in PCA
\mathbf{q}_j^T	row j of \mathbf{Q}
\mathbf{z}	estimator of the principal components
$\tilde{\mathbf{z}}$	retained principal components

\mathbf{M}	estimator of the mixing matrix \mathbf{B} in ICA
\mathbf{m}_j	column j of \mathbf{M}
\mathbf{W}	estimator of \mathbf{B}^\dagger
\mathbf{w}_j^T	row j of \mathbf{W}
\mathbf{x}	estimator of the independent components
$\hat{\Sigma}$	estimator of the covariance matrix of \mathbf{y}
\mathbf{U}	total mixing matrix
\mathbf{u}_j	column j of \mathbf{A}
\mathbf{V}	generalised inverse of the total mixing matrix \mathbf{U}
\mathbf{v}_j^T	row j of \mathbf{V}
\mathfrak{I}	mutual information
H	differential entropy
f	probability distribution function
G	measuring function
J_G	cost function
$E[\cdot]$	expectation operator
s_j	standard deviation of $\sigma(\lambda)$
$\bar{\sigma}_j$	centered cross section
$\hat{\sigma}_j$	standardised cross section

C. ABSORPTION CROSS SECTIONS OF IODINE OXIDES

Three years ago there was a considerable uncertainty in the absorption cross sections of IO and OIO and, as a consequence, in the corresponding atmospheric concentrations and photolysis rates. The results reported by different authors [79, 80, 163, 167, 170, 171] for the absorption cross section at the band head and/or at the maximum of the ($4\leftarrow 0$) band of IO, denoted here as $\sigma_{\text{IO}(4\leftarrow 0)}$, show a relatively large scatter (FC.1). In the case of OIO, there was only one determination [79].



FC.1: Published results for the IO ground state absorption cross section. The slightly inclined solid line shows the effect of instrument resolution on the IO($4\leftarrow 0$) band as determined by Spietz et al. [122]. The most recent determinations are also included [125, 166].

In the context of the THALOS project [53], an effort has been done to reduce these uncertainties, and as a result new determinations of $\sigma_{\text{IO}}(\lambda)$ [125, 166] and $\sigma_{\text{OIO}}(\lambda)$

[77, 83, 125, 126] have been reported. The cross sections employed in the present work [124, 125] for the absolute scaling of the absorption versus time curves were determined in the same laboratory and using the same experimental set-up (see Chapter 3). The author of the present work collaborated as well in the determination of these absorption cross sections, which was the central topic of the doctor thesis of P. Spietz [124]

The approach considered in that investigation was the “conservation of iodine” [124], consist in equating the initial concentration of I atoms (contained in the initial I₂) to the concentration of I atoms, present in molecules or as atoms, after the photolysis flash at each time step t_i of the reaction:

$$2 [I_2]_0 = 2[I_2](t_i) + [I](t_i) + [IO](t_i) + [IO(v''=1)](t_i) + [IO(v''>1)](t_i) + [OIO](t_i) + [X](t_i) + [Y](t_i) + [Z](t_i) + \dots \quad (\text{EC.1})$$

The concentration of each absorber ‘M’ can be expressed as a function of the corresponding absorption cross section by using the Beer-Lambert Law:

$$[M](t_i) = \frac{a_M(\lambda_M, t_i)}{L \cdot \sigma_M(\lambda_M)} \quad (\text{EC.2})$$

where a_M is the optical density of the absorber M and λ_M is the wavelength used to determine the σ of the absorber M (M= IO(X²Π_{3/2}, v''=0), IO(X²Π_{3/2}, v''=1), IO(X²Π_{3/2}, v'' > 1), OIO, ‘X’...). If EC.2 is substituted in the equations EC.1, these can be arranged in the following way:

$$\{2([I_2]_0 - [I_2](t_i)) - [I](t_i)\} \cdot L = \frac{a_{IO}(\lambda_{IO}, t_i)}{\sigma_{IO}(\lambda_{IO})} + \frac{a_{IO(v''=1)}(\lambda_{IO(v''=1)}, t_i)}{\sigma_{IO(v''=1)}(\lambda_{IO(v''=1)})} + \frac{a_{IO(v''>1)}(\lambda_{IO(v''>1)}, t_i)}{\sigma_{IO(v''>1)}(\lambda_{IO(v''>1)})} + \frac{a_{OIO}(\lambda_{OIO}, t_i)}{\sigma_{OIO}(\lambda_{OIO})} + \frac{a_X(\lambda_X, t_i)}{\sigma_X(\lambda_X)} + \frac{a_Y(\lambda_Y, t_i)}{\sigma_Y(\lambda_Y)} + \frac{a_Z(\lambda_Z, t_i)}{\sigma_Z(\lambda_Z)} + \varepsilon(t_i) \quad (\text{EC.3})$$

where $\varepsilon(t_i)$ represents the error in predicting the observations in the left hand side with the proposed model. Multiple Linear Regression (MLR) was used to determine the σ s. Note that separated and instrument independent optical densities a_M are required (Chapters 8 and 9). The results obtained are shown in TC.1.

An important advantage of this approach is its independence of mechanistic hypotheses, kinetic reference data and multi-parametric non-linear fitting. The only reference parameter required is the absorption cross section of I_2 , which was checked in an independent study [127]. A second advantage is that the approach enables simultaneous and consistent determination of cross sections of all different species observed in the experiment. A third advantage is the increased coverage in time with respect to conventional approaches based in instantaneous stoichiometric conversion. With the iodine conservation approach it is possible to use also observations from later times within the course of reaction, provided that the later products of the reaction are included. The quality of the results obtained is improved by an increased averaging effect.

TC.1: Absorption cross sections of iodine oxides as reported by Spietz [124] and Gómez Martín et al. [125].

Molecule	$\lambda(\text{vac})$ [nm]	σ^a [cm ² molecule ⁻¹]	σ [cm ² molecule ⁻¹]	<i>FWHM</i> [nm]
IO	427.19 ± 0.05 (4←0)	(MIntAS correction before iodine conservation)	(3.5 ± 0.3)·10⁻¹⁷	0.12 ^b
IO($\nu''=1$)	449.3 ± 0.2 (3←1)	(2.1 ± 1.3)	> (3.9 ± 2.4)·10 ⁻¹⁷ (4.5 ± 0.5)·10⁻¹⁷ d	0.35 ^b 0.12 ^{b,d}
IO($\nu''>1$)	484.9 ± 0.2 (1←2)	(0.5 ± 0.4)	> (0.9 ± 0.7)·10 ⁻¹⁷ (6.0 ± 0.5)·10⁻¹⁷ d	0.35 ^b 0.12 ^{b,d}
OIO	549.3 ± 0.1 (5,1,0←0,0,0)	(1.1 ± 0.3)	(1.3 ± 0.3)·10⁻¹⁷	0.35 ^b
‘Z’	356 ± 0.2 continuum		> (8.8 ± 1.2)·10 ⁻¹⁹ c	1.3
‘Y’ (I ₂ O ₂)	322 ± 0.2 continuum		(1 to 8)·10 ⁻¹⁸ c	1.3
‘X’	373.2 ± 0.2 continuum		(0.5 to 2)·10 ⁻¹⁸ c	1.3

The measured OD for IO(4←0) was MIntAS-corrected for effects of resolution and binning to an effective *FWHM* of 0.12 nm before usage of the method of iodine conservation. IO($\nu''=1$), IO($\nu''>1$), and OIO were corrected afterwards with the appropriate scaling factors (T7.1). For I₂O₂ and ‘Z’ no resolution or binning dependent correction has been applied as they are continuous smooth absorptions. Note that for I₂O₂ only an estimated value can be given. The uncertainties are one standard deviation for each set of results. ^{a)} Result from iodine conservation with MIntAS correction to be applied afterwards by scaling. ^{b)} *FWHM* of MIntAS corrected cross section. ^{c)} cm² iodine atom⁻¹. ^{d)} Based on the cross section for (4←0) at 0.12 nm *FWHM* and the Franck-Condon factors by Rao et al. [139].

D. PHOTOLYSIS RATES OF IODINE OXIDES

The spectra determined by the procedure explained in Chapter 9 and published by Spietz et al. [126], and the absolute scaling published by Spietz [124] and Gómez Martín et al. [125] (Appendix C), have been used *within the present work* to determine the photolysis rates of all species studied for a latitude of 40° at summer solstice as a function of altitude and zenith solar angle (SZA). Actinic fluxes at 1.3nm *FWHM* resolution have been calculated with the radiative transfer model SCIATRAN [215] (for an introduction to the model see [216] and references therein) for a typical water surface albedo of 0.1, assuming a cloud free sky and a total ozone column of 330 DU. The use of unity quantum yield for IO and IO* can be inferred from LIF [145] and CRDS [144] studies showing that dissociation from all ro-vibronic states in the upper electronic state occurs very rapidly. Moreover, Ingham et al. [81] measured a quantum yield close to unity for IO at 355nm. For all broad band absorbers a unity quantum yield has been assumed. For OIO an upper limit of 0.1 has been considered based in the results obtained by Joseph et al. [87] (562 nm). The results obtained are shown in TD.1.

The photolysis rates calculated for IO are in qualitative agreement with the values obtained by Laszlo et al. [170], Harwood et al. [171] and Bloss et al. [79]. They are somewhat smaller than those of Laszlo et al. and Harwood et al., most likely as a result of the lower underlying continuum exhibited by the wavelength dependent absorption cross section used here [126]. Additionally, the spectra of Laszlo et al. and Harwood et al. contain IO($v'' > 0$) bands. In general, the values reported here are in better agreement with those of Bloss et al. [79], whose spectrum presents the smallest difference to the spectrum reported by Spietz et al. [126] in the continuum. In this case the smaller cross section of [79] at 428.2 nm (used to scale the IO spectrum) could explain the slightly larger photolysis rates obtained here. The partitioning of reactive

iodine (IO_x) between I and IO is determined by the photolysis rate of IO and the rate coefficient of R10.1, and a smaller photolysis rate implies a greater partitioning of IO_x as IO in the atmosphere. This implies a larger ozone destroying potential of the iodine chemistry if subsequent reactions of IO produce free I atoms without concomitant $\text{O}(^3\text{P})$ formation.

TD.1. Atmospheric photolysis rates (40°N , summer solstice, cloud free sky, albedo 0.1 and total ozone column of 330 DU) for relevant iodine oxides as a function of height and solar zenith angle.

SZA	Photolysis Rate (s^{-1})				
	0 Km	5 Km	10 Km	20 Km	30 Km
16°	0.18 ^a	0.22	0.23	0.23	0.23
	0.11 ^b	0.14	0.14	0.14	0.14
	0.016 ^c	0.022	0.023	0.023	0.022
	0.042 ^d	0.048	0.049	0.049	0.048
	0.024 ^e	0.037	0.041	0.041	0.039
	0.032 ^f	0.040	0.040	0.029	0.025
40°	0.15	0.21	0.22	0.23	0.22
	0.10	0.13	0.14	0.14	0.13
	0.013	0.020	0.022	0.022	0.021
	0.03	0.046	0.048	0.048	0.047
	0.018	0.031	0.035	0.037	0.036
	0.030	0.042	0.045	e0.038	0.024
60°	0.11	0.18	0.20	0.21	0.21
	0.08	0.12	0.13	0.13	0.13
	0.009	0.016	0.019	0.020	0.020
	0.029	0.042	0.045	0.046	0.045
	0.010	0.020	0.025	0.030	0.030
	0.021	0.037	0.042	0.042	0.04
80°	0.03	0.09	0.13	0.17	0.18
	0.02	0.07	0.09	0.11	0.11
	0.003	0.006	0.010	0.015	0.016
	0.009	0.027	0.033	0.038	0.039
	0.002	0.005	0.008	0.014	0.016
	0.006	0.014	0.021	0.030	0.036

^{a)} IO; ^{b)} IO*; ^{c)} 'X'; ^{d)} upper limit for OIO; ^{e)} lower limit for I_2O_2 ; ^{f)} lower limit for 'Z' (it is assumed that 'Z' contains 2 iodine atoms).

In the case of $\text{IO}(v'' > 0)$, photolysis cannot compete with collisional quenching. For the MBL the quenching rate derived from these experiments is $\sim 5 \times 10^4 \text{ s}^{-1}$, while in the lower stratosphere is $\sim 3 \times 10^4 \text{ s}^{-1}$.

Most estimations reported in the literature for the photolysis rate of OIO [81, 79] have been obtained by considering a unity quantum yield. The current understanding is

that OIO is relatively photostable, although an upper limit for the quantum yield of about 0.1 is still high enough to make photolysis a main fate of OIO in the day time.

For the higher iodine oxides only upper limits can be estimated due to the partial spectral coverage. Nevertheless, the actinic flux under 300 nm is small enough to consider these low limits as realistic approximations.

E. REFERENCES

- [1] S. E. Schwartz and P. Warneck, **Units for use in atmospheric chemistry (IUPAC Recommendations 1995)**, *Pure & Appl. Chem.*, 1995, 67, 1377-1406.
- [2] L. Rosenfeld, **Discovery and early uses of iodine**, *J. Chem. Ed.*, 2000, 77, 984-987
- [3] A. Clow, **The Chemical Revolution: A Contribution of Social Technology**, *Gordon and Breach*, London, 1970.
- [4] J. Wisniak, **Bernard Courtois. The discoverer of iodine**, *Educ. Quím.*, 2002, 3, 206-213.
- [5] R.A. Smith, **Air and rain: The beginnings of a chemical climatology**. Longmans, Green London, 1872.
- [6] G. A. Chatin, **Recherche de l'iode dans l'air, les eaux, le sol et les produits alimentaires des Alpes de la France et du Piémont**, *C. R. Hebd. Seances Acad. Sci.*, 1852, 34, 51-54
- [7] M. Marchand, **Sur la composition physique et chimique des eaux naturelles**, *C. R. Hebd. Seances Acad. Sci.*, 1852, 34, 54-56
- [8] F.M. MacNabb, **Thyroid Hormones**, Prentice Hall, 1992.
- [9] B. de Benoist, M. Andersson, I. Egli, B. Takkouche and H. Allen (Editors), **Iodine status worldwide: WHO Global Database on Iodine Deficiency**. Department of Nutrition for Health and Development, World Health Organization, Geneva, 2004.
- [10] J.S. Edmonds and M. Morita, **The determination of iodine species in environmental and biological samples**, *Pure & Appl. Chem.*, 1998, 70, 8, 1567-1584.
- [11] R.A. Duce, J. T. Wasson, J. W. Winchester and F. Burns, **Atmospheric Iodine, Bromine and Chlorine**, *J. Geophys. Res.*, 1963, 68, 3943-3947.
- [12] J.L. Moyers and R.A. Duce, **Gaseous and particulate iodine in the marine atmosphere**, *J. Geophys. Res.*, 1972, 77, 5229-5238.
- [13] J.E. Lovelock, K.J. Maggs and R.J. Wade, **Halogenated hydrocarbons in and over the Atlantic**, *Nature*, 1973, 241, 194.
- [14] O.C. Zafiriou, **Photochemistry of halogens in the marine sphere**, *J. Geophys. Res.*, 1974, 79, 2730-2732

- [15] A.C. Chamberlain, A.E.J. Eggleton, W.J. Megaw and J.B. Morris, **Behaviour of iodine vapour in air**, *Discuss. Farad. Soc.*, 1960, 30, 162-169.
- [16] Agency for toxic substances and disease registry, U.S. Department of Health and Human services, Public Health service, **Toxicological profile for iodine**, <http://www.atsdr.cdc.gov/toxprofiles/tp158.html>
- [17] R.B. Firestone, **Table of Isotopes**, CD- ROM Edition, Version 1.0, Wiley-Interscience, 1996.
- [18] D.R. Lide (Ed.), **Handbook of chemistry and Physics**, 73rd edition, CRC Press, Boca Raton, USA, 1992-1993.
- [19] M.J. Clark and F.B. Smith, **Wet and dry deposition of Chernobyl releases**, *Nature*, 1988, 332, 245-249,
- [20] J.M. Molina and F.S. Rowland, **Stratospheric sink for chlorofluoromethanes: chlorine-atom catalyzed destruction of ozone**, *Nature*, 1974, 249, 810-814.
- [21] R.S. Stolarski and R. J. Cicerone, **Stratospheric chlorine: A possible sink for ozone**, *Can. J. Chem.*, 1974, 52, 1610
- [22] S.C. Wofsy, M.B. McElroy and Y.L. Yung, **The chemistry of atmospheric bromine**, *Geophys. Res. Lett.*, 21, 1994, 285-288.
- [23] W.L. Chameides, and D.D. Davis: **Iodine: Its possible role in tropospheric photochemistry**, *J. Geophys. Res.*, 1980, 85, 7383-7398,.
- [24] R.B. Chatfield, and P.J. Crutzen: **Are there interactions of iodine and sulphur species in marine air photochemistry?**, *J. Geophys. Res.*, 1990, 95D, 22319-22341
- [25] S. Solomon, R.R. García and A. R. Ravishankara: **On the role of iodine in ozone depletion**, *J. Geophys. Res.*, 99, 1994, 20491-20499
- [26] R.P. Wayne, G. Poulet, P. Biggs, J.P. Burrows, R.A. Cox, P.J. Crutzen, G.D. Hayman, M.E. Jenkin, G. Le Bras, G.K. Moortgat, U. Platt, R.N. Schindler, **Halogen Oxides: Radicals, Sources and Reservoirs in the Laboratory and in the Atmosphere**. *Atm. Environ.*, 1995, 29, 2677-2881.
- [27] Y. Mirokhin, G. Mallard, D.M. Blakeslee, F. Westley, J. Herron, D. Frizzell and R. Hampson, **The NIST Chemical Kinetics Database**, *NIST Standard Reference Database 17, Standard Reference Data Program, National Institute of Standards and Technology*, Gaithersburg, 1998
- [28] W.B. DeMore, S.P. Sander, D.M. Goldan, R.F. Hampson, M.J. Kurylo, C.J. Howard, A.R. Ravishankara, C.E. Kolb, M.J. Molina, **Chemical Kinetics and**

- Photochemical Data for use in Stratospheric Modeling**, Jet Propulsion Laboratory, Evaluation number 14, 2003
- [29] R. Atkinson, D. L. Baulch, R. A. Cox (Chairman), J. N. Crowley, R. F. Hampson Jr, R. G. Hynes, M. E. Jenkin, J. A. Kerr, M. J. Rossi and J. Troe (IUPAC Subcommittee on Gas Kinetic Data Evaluation for Atmospheric Chemistry), **Summary of Evaluated Kinetic and Photochemical Data for Atmospheric Chemistry**, Web Version February 2006 (prepared by R.G. Hynes, S.M. Saunders, G.D. Carver and R.A. Cox, Centre for Atmospheric Science, University of Cambridge, UK)
- [30] H.Keller-Rudek, G. K. Moortgat, **MPI-Mainz-UV-VIS Spectral Atlas of Gaseous Molecules**, www.atmosphere.mpg.de/spectral-atlas-mainz, Status: December 2005.
- [31] M.W. Chase, **NIST-JANAF thermochemical tables for the iodine oxides**, *J. Phys. Chem. Ref. Dat.*, 1996, 25, 5, 1297-1340.
- [32] S. Himmelmann, J. Orphal, H. Bovensmann, A. Richter, A. Ladstaetter-Weissenmayer and J.P. Burrows, **First observation of the OIO molecule by time-resolved flash photolysis absorption spectroscopy**, *Chem. Phys. Lett.*, 1996, 251, 330-334.
- [33] H.K. Roscoe and K.C. Clemitshaw, **Measurement Techniques in Gas-Phase Tropospheric Chemistry: A Selective View of the Past, Present, and Future**, *Science*, 1997, 276, 1065-1072
- [34] L. J. Carpenter, W. T. Sturges, S. A. Penkett, P. S. Liss, B. Alicke, K. Hebestreit, and U. Platt, **Short-lived alkyl iodides and bromides at Mace Head, Ireland: Links to biogenic sources and halogen oxide production**, *J. Geophys. Res.*, 1999, 104(D1), 1679-1689.
- [35] G. McFiggans, H. Coe, R. Burgess, J. Allan, M. Cubison, M. R. Alfarra, R. Saunders, A. Saiz-Lopez, J. M. C. Plane, D. Wevill, L. Carpenter, A. R. Rickard and P. S. Monks, **Direct evidence for coastal iodine particles from Laminaria macroalgae – linkage to emissions of molecular iodine**, *Atm. Chem. Phys.*, 2004, 4, 701-713.
- [36] A. Saiz-López and J.M.C. Plane, **Novel iodine chemistry in the marine boundary layer**, *Geophys. Res. Lett.*, 2004, 31, L04112
- [37] C. Peters, S. Pechtl, J. Stutz, K. Hebestreit, G. Hönninger, K. G. Heumann, A. Schwarz, J. Winterlik and U. Platt, **Reactive and organic halogen species in**

- three different European coastal environments**, *Atm. Chem. Phys.*, 2005, 5, 3357-3375.
- [38] A. Saiz-Lopez, J. A. Shillito, H. Coe and J. M. C. Plane, **Measurements and modelling of I₂, IO, OIO, BrO and NO₃ in the mid-latitude marine boundary layer**, *Atm. Chem. Phys.*, 2006, 6, 1513-1528.
- [39] M. Bitter, S.M. Ball, I.M. Povey and R.L. Jones, **A broad band cavity ringdown spectrometer for in-situ measurements of atmospheric trace gases**, *Atm. Chem. Phys.*, 2005, 5, 2547-2560.
- [40] F. Wittrock, R. Müller, A. Richter, H. Bovensmann, and J.P. Burrows, **Observations of Iodine monoxide above Spitsbergen**, *Geophys. Res. Lett.*, 2000, 27, 1471-1474.
- [41] B. Alicke, K. Hebestreit, J. Stutz, and U. Platt, **Iodine oxide in the marine boundary layer**, *Nature*, 1999, 397, 572- 573
- [42] B.J. Allan, G. McFiggans, J. M. C. Plane, and H. Coe, **Observation of iodine oxide in the remote marine boundary layer**, *J. Geophys. Res.*, 2000, 105, 14363-14370
- [43] B.J. Allan, J. M. C. Plane, and G. McFiggans, **Observations of OIO in the remote marine boundary layer**, *Geophys. Res. Lett.*, 2001, 28, 1945-1948.
- [44] R Vogt, R. Sander, R. Von Glasow and P.J. Crutzen, **Iodine Chemistry and its Role in Halogen Activation and Ozone Loss in the Marine Boundary Layer: A Model Study**, *J. Atm. Chem.*, 1999, 32, 375-395.
- [45] G. McFiggans, J.M.C. Plane, B.J. Allan, L.J. Carpenter, H. Coe and C. O'Dowd, **A modelling study of iodine chemistry in the marine boundary layer**, *J. Geophys. Res.*, 2000, 105(D11), 14371-14385
- [46] R. von Glasow and P.J. Crutzen, **Tropospheric halogen chemistry**, in *Treatise on Geochemistry*, 4, 2, 21-64, Elsevier, 2003.
- [47] L. J. Carpenter, **Iodine In the marine Boundary Layer**, *Chemical Reviews*, 2003, 103 (12), 4953-4962
- [48] J.M.C. Plane and A. Saiz-López, **Recent applications of differential Optical Absorption Spectroscopy: halogen chemistry in the lower Troposphere**, *J. Phys. IV France*, 2004, 121, 223-238
- [49] C.D. O'Dowd and T. Hoffmann, **Coastal new particle formation: a review of the current state-of-the-art**, *Environ. Chem*, 2005, 2, 245-255.

- [50] J.S. Seinfeld and S.N. Pandis, **Atmospheric Chemistry and Physics**, Wiley-Interscience, New York, 1998
- [51] D. E. Heard, K. A. Read, J. Methven, S. Al-Haider, W. J. Bloss, G. P. Johnson, M. J. Pilling, P. W. Seakins, S. C. Smith, R. Sommariva, J. C. Stanton, T. J. Still, B. Brooks, G. De Leeuw, A. V. Jackson, J. B. McQuaid, R. Morgan, M. H. Smith, L. J. Carpenter, N. Carslaw, J. Hamilton, J. R. Hopkins, J. D. Lee, A. C. Lewis, R. M. Purvis, D. J. Wevill, N. Brough, T. Green, G. Mills, S. A. Penkett, J. M. C. Plane, A. Saiz-Lopez, D. Worton, P. S. Monks, Z. Fleming, A. R. Rickard, M. Alfarra, J. D. Allan, K. Bower, H. Coe, M. Cubison, M. Flynn, G. McFiggans, M. Gallagher, E. G. Norton, C. D. O'Dowd, J. Shillito, D. Topping, G. Vaughan, P. Williams, M. Bitter, S. M. Ball, R. L. Jones, I. M. Povey, S. O'Doherty, P. G. Simmonds, A. Allen, R. P. Kinnersley, D. C. S. Beddows, M. Dall'Osto, R. M. Harrison, R. J. Donovan, M. R. Heal, S. G. Jennings, C. Noone and G. Spain, **The North Atlantic Marine Boundary Layer Experiment (NAMBLEX). Overview of the campaign held at Mace Head, Ireland, in summer 2002**, *Atm. Chem. Phys.*, 2006, 6, 2241-2272.
- [52] U. Platt and R. von Glasow, **Halogens in the Troposphere – HitT**, *Geophys. Res. Abs.*, 2005, 7, 07581
- [53] R.A. Cox, J.P. Burrows, J.N. Crowley, P.S. Liss, J.M.C. Plane, J.A. Pyle and M.J. Rossi, **Final Report of the EC Fifth Framework Project THALOZ, ‘Tropospheric Halogens: Effect on ozone’**, Project EVK2-CT-2001-00104, 2005.
- [54] B.J. Finlayson-Pitts and J.N. Pitts, **Chemistry of the Upper and Lower Atmosphere : Theory, Experiments, and Applications**, Academic Press, San Diego, 2000
- [55] C. Shall and K.G. Heumann, **GC determination of volatile organoiodine and organobromine compounds in arctic seawater and air samples**, *Fres. J. Anal. Chem.*, 1993, 346, 717-722
- [56] O.V. Rattigan, D.E Shallcross and R.A. Cox, **UV absorption cross-sections and atmospheric photolysis rates of CF₃I, CH₃I, C₂H₅I and CH₂ICl**, *Far. Trans.*, 1997, 93, 2839-2846

- [57] J. Mössinger, D.E. Shallcross and R.A. Cox, **UV-visible absorption cross-sections and atmospheric lifetimes of CH₂Br₂, CH₂I₂, and CH₂BrI**, *J. Chem. Soc.- Far. Trans.*, 1998, 94 (10), 1391-1396
- [58] S. Klick and K. Abrahamsson, **Biogenic volatile iodated hydrocarbons in the ocean**, *J. Geophys. Res.*, 1992, 97, 12683-12687.
- [59] H.B. Singh, L.J. Salas and R.E. Stiles, **Methyl halides in and over the Eastern Pacific (40°N-32°S)**. *J. Geophys. Res.*, 1983a. **88**(C6): p. 3684-3690.
- [60] R.M. Moore and O.C. Zafiriou, **Photochemical production of methyl iodide in seawater** *J. Geophys. Res.*, 1994, 99(D8) , p.16415-16420
- [61] L.J. Carpenter, **Ocean-atmosphere exchange and chemical complexity: transformations and impact of reactive halogen species**, oral presentation at the Workshop of the “Atmospheric Composition Change European Network of Excellence” (ACCENT) in Urbino (Italy), 2005
- [62] L.J. Carpenter, T. Anders, J. Hopkins, C. Jones, C. Palmer, D. Wevill and G. McFiggans, **Influence of oceanic iodine on atmospheric chemistry** , oral presentation at the Workshop of the “Atmospheric Composition Change European Network of Excellence” (ACCENT) in Urbino (Italy), 2005
- [63] Y. Miyake and S. Tsungoai, **Evaporation of iodine from the ocean**, *J. Geophys. Res.*, 1963, 68, 3989-3994
- [64] J.A.Garland and H. Curtis, **Emission of iodine from the sea surface in the presence of ozone**. *J. Geophys. Res.* 1981, 86(C4)
- [65] F.R. Livens, D. Fowler and A.D. Horril, **Wet and dry deposition of I-131, Cs-134 and Cs-137 at an upland site in northern England**, *J. Environ. Rad.*, 1992, 16, 243-254
- [66] R. Vogt, P.J. Crutzen and R. Sander, **A mechanism for halogen release from sea-salt aerosol in the remote marine boundary layer**, *Nature*, 1996, 383, 327–330
- [67] C.D. O’Dowd, J.L. Jimenez, R. Bahreini, R.C. Flagan, J. H. Seinfeld, M. Kulmala, L. Pirjola, and T. Hoffmann, **Particle formation in the marine atmosphere controlled by biogenic iodine emissions**, *Nature*, 2002, 417, 632-636
- [68] R.J. Salawitch, **Observations and Budgets of Minor constituents related to atmospheric ozone: an overview**, oral presentation at the Quadrennial Ozone Symposium in Kos (Greece), 2004.

- [69] P. O. Wennberg, J.W. Brault, T.F. Hanisco, R.J. Salawitch, G.H. Mount **The atmospheric column abundance of IO: Implications for stratospheric ozone** *J. Geophys. Res.*, 1997, 102 (D7), 8887
- [70] I. Pundt, J.P. Pommereau, C. Phillips and E. Lateltin, **Upper Limit of Iodine Oxide in the Lower Stratosphere**, *J. Atm. Chem.*, 1998, 30 (N1), 173-185
- [71] H. Bösch, C. Camy-Peyret, M. P. Chipperfield, R. Fitzenberger, H. Harder, U. Platt and K. Pfeilsticker, **Upper limits of stratospheric IO and OIO inferred from center-to-limb-darkening-corrected balloon-borne solar occultation visible spectra: Implications for total gaseous iodine and stratospheric ozone** *J. Geophys. Res.*, 2003, V. 108, D15, 4455
- [72] A.A. Turnipseed, M.K. Gilles, J.B. Burkholder and A.R. Ravishankara, **Kinetics of the IO radical.1. Reaction of IO with ClO**, *J. Phys. Chem.*, 1997, 101 (N 30), 5517-5525
- [73] M.K. Gilles, A.A. Turnipseed, J.B. Burkholder, A.R. Ravishankara and S. Solomon, **Kinetics of the IO radical.1. Reaction of IO with BrO**. *J. Phys. Chem.* 1997, 101 (N 30), 5526-5534
- [74] David M. Rowley, William J. Bloss, R. Anthony Cox and Roderic L. Jones, **Kinetics and Products of the IO + BrO Reaction**, *J. Phys. Chem. A*, 2001, 105 (N33)
- [75] Y. Bedjanian, G. Le Bras, and G. Poulet, **Kinetics and Mechanism of the IO+ClO Reaction**, *J. Phys. Chem. A* 1997, 101, 4088-4096
- [76] Y. Bedjanian, G. Le Bras, and G. Poulet, **Kinetics and Mechanism of the IO+BrO Reaction**, *J. Phys. Chem. A*, 1998, 102, 10501
- [77] M. E. Tucceri, D. Hölscher, A. Rodriguez, T. J. Dillon and J. N. Crowley, **Absorption cross section and photolysis of OIO**, *Phys. Chem. Chem. Phys.*, 2006, 8, 834 – 846
- [78] M.E. Jenkin, R.A. Cox and D.E. Candeland, **Photochemical aspects of tropospheric iodine behaviour**, *J. Atmos. Chem.* 1985, 2, 359–375.
- [79] W.J. Bloss, D.M. Rowley, R.A. Cox and R.L. Jones, **Kinetics and products of the IO Self-Reaction**. *J. Phys. Chem. A*, 2001, 105, 7840-7854.
- [80] S. P. Sander. **Kinetics and Mechanism of the IO+IO Reaction**. *J. Phys. Chem.*, 1986, 90, 2194-2199.

- [81] T. Ingham, M. Cameron and J.N. Crowley, **Photodissociation of IO (355 nm) and OIO (532 nm): Quantum yields for O(³P) and I(²P_J) Production**, *J. Phys. Chem. A*, 104 (2000), 8001-8010.
- [82] S.H. Ashworth, B.J. Allan and J.M.C. Plane. **High resolution spectroscopy of the OIO radical: implications for the ozone depleting potential of iodine**, *Geophys. Res. Lett.*, 2002 29,10,10.1029/2001GL013851
- [83] D.M. Joseph, S.H. Ashworth and J.M.C. Plane, **The absorption cross-section and photochemistry of OIO**, *J. Photochem. Photobiol. A*, 2005, 176, 68-77
- [84] A. Misra and P Marshall, **Computational investigations of iodine oxides**. *J. Phys. Chem.*, 1998, 102, 9056-9060.
- [85] R.W. Saunders and J.M.C. Plane, **Formation pathways and composition of iodine oxide ultrafine particles**, *Environ. Chem*, 2005, 2, 299-303.
- [86] L. Kaleschke, A. Richter, J. Burrows, O. Afe, G. Heygster, J. Notholt, A. M. Rankin, H. K. Roscoe, J. Hollwedel, T. Wagner, H.-W. Jacobi., **Frost flowers on sea ice as a source of sea salt and their influence on tropospheric halogen chemistry**, *Geophys. Res. Lett.*, 2004, 31, L16114
- [87] J. M. C. Plane, D. M. Joseph, B. J. Allan, S. H. Ashworth, and J. S. Francisco, **An Experimental and Theoretical Study of the Reactions OIO + NO and OIO + OH**, *J. Phys. Chem. A.*, 2006; 110(1); 93-100.
- [88] R.M. Chambers, A.C. Heard, R.P. Wayne, **Inorganic gas-phase reactions of the nitrate radical – I₂+NO₃ and I+NO₃**, *J. Phys. Chem. A*, 1992, 96, 3321-3331.
- [89] Y. Kanaya, Y. Yokouchi, J. Matsumoto, K. Nakamura, S. Kato, H. Tanimoto, H. Furutani, K., Toyota and H. Akimoto, **Implications of iodine chemistry for daytime HO₂ levels at Rishiri Island**, *Geophys. Res. Lett.*, 2002, 29, 1212
- [90] W. J. Bloss, J. D. Lee, G. P. Johnson, R. Sommariva, D. E. Heard, A. Saiz-Lopez, J. M. C. Plane, G. McFiggans, H. Coe, M. Flynn, P. Williams, A. R. Rickard, and Z. L. Fleming, **Impact of halogen monoxide chemistry upon boundary layer OH and HO₂ concentrations at a coastal site**, *Geophys. Res. Lett.*, 2005, 32, L06814
- [91] R. Sommariva, W. J. Bloss, N. Brough, N. Carslaw, M. Flynn, A.-L. Haggerstone, D. E. Heard, J. R. Hopkins, J. D. Lee, A. C. Lewis, G. McFiggans, P. S. Monks, S. A. Penkett, M. J. Pilling, J. M. C. Plane, K. A.

- Read, A. Saiz-Lopez, A. R. Rickard, and P. I. Williams **OH and HO₂ chemistry during NAMBLEX: roles of oxygenates, halogen oxides and heterogeneous uptake**, *Atm. Chem. Phys. Disc.*, 2005, 5, 10947-10996
- [92] D.M. Rowley, J.C. Mössinger, R.A. Cox and R.L. Jones, **The UV-Visible Absorption Cross Sections and Atmospheric Photolysis Rate of HOI**, *J. Atm. Chem.*, 1999, 34, 137-151.
- [93] T. Gravestock, M. A. Blitz and D. E. Heard, **Kinetics study of the reaction of iodine monoxide radicals with dimethyl sulphide**, *Phys. Chem. Chem. Phys.*, 2005, 7, 2173-2181
- [94] C.S. Martens, **Ion ratio variations with particle size in Puerto Rican aerosols**, *J. Geophys. Res.*, 1973, 78 (36), 8867-8871.
- [95] R.A. Cox, W.J. Bloss, R.L. Jones and D.M. Rowley. **OIO and the atmospheric cycle of iodine**. *Geophys. Res. Lett.*, 1999, 26, 13, 1857.
- [96] A.R. Baker, D. Thompson, M. L. A. M. Campos, S. J. Perry, and T. D. Jickells, **Iodine concentration and availability in atmospheric aerosol**, *Atmos. Environ.*, 2000, 34, 4331-4336
- [97] H. Cauer, **Some problems of atmospheric chemistry**, *Compendium Meteorol.*, 1951, 1126-1138.
- [98] J. Mössinger and R.A. Cox, **Heterogeneous Reaction of HOI with Sodium Halide Salts**, *J. Phys. Chem. A*, 201, 105, 5165
- [99] O'Dowd, C.D., Geever, M., Hill, M.K., Jennings, S.G., & Smith, M.H. **New particle formation and spatial scales in the clean marine coastal environment**, *Geophys. Res. Letts.*, 1998, 25, 1661-1664
- [100] O'Dowd, C.D., G.M. McFiggans, L. Pirjola, D.J. Creasey, C. Hoell, M.H. Smith, B.J. Allan, J.M.C. Plane, D.E. Heard, J.D. Lee, M.J. Pilling and M. Kulmala, **On the photochemical production of new particles in the coastal boundary layer**, *Geophys. Res. Letts.*, 1999, 26, 1707-1710
- [101] O'Dowd, C.D., K. Hämeri, J.M. Mäkelä, L. Pirjola, M. Kulmala, S.G. Jennings, H. Berresheim, H.-C. Hansson, G. de Leeuw, A. G. Allen, C. N. Hewitt, A. Jackson, Y. Viisanen, T. Hoffmann, **A dedicated study of new particle formation and fate in the coastal environment (PARFORCE): Overview of objectives and initial achievements**. *J. Geophys. Res.*, 2002, 107 (D19) 8108.

- [102] H. Coe, J. D. Allan, M. R. Alfarra, K. N. Bower, M. J. Flynn, G. B. McFiggans, D. O. Topping, P. I. Williams, C. D. O'Dowd, M. Dall'Osto, D. C. S. Beddows and R. M. Harrison, **Chemical and physical characteristics of aerosol particles at a remote coastal location, Mace Head, Ireland, during NAMBLEX**, *Atm. Chem. Phys.*, 2006, 6, 3289-3301.
- [103] A. Saiz-Lopez, J. M. C. Plane, G. McFiggans, P. I. Williams, S. M. Ball, M. Bitter, R. L. Jones, C. Hongwei, and T. Hoffmann, **Modelling molecular iodine emissions in a coastal marine environment: the link to new particle formation**, *Atmos. Chem. Phys.*, 2006, 6, 883-895.
- [104] K. Sellegri, Y.J. Yoon, S.G. Jennings, C.D. O'Dowd, L. Pirjola, S. Cautenet, H. Chen and T. Hoffmann, **Quantification of coastal new ultra-fine particles formation from *in situ* and chamber measurements during the BIOFLUX campaign**, *Environ. Chem.*, 2005, 2, 260-270.
- [105] R.J. Flanagan, M. Geever and C.D. O'Dowd, **Direct Measurements of new particle fluxes in the costal environment**, *Environ. Chem.*, 2005, 2, 256-259
- [106] J.M. Mäkelä, T. Hoffmann, C. Holzke, M. Väkevä, T. Suni, T. Mattila, P.P. Aalto, U. Tapper E.I. Kauppinen and C.D. O'Dowd, **Biogenic iodine emissions and identification of end-products in coastal ultra-fine particles during nucleation bursts**, *J. Geophys. Res.*, 2002, 107(D19).
- [107] C.E. Kolb, **Atmospheric chemistry: Iodine's air of importance**, *Nature*, 2002, 417, 597-598.
- [108] T. Hoffmann, C.D. O'Dowd, and J. H. Seinfeld, **Iodine oxide homogeneous nucleation: An explanation for coastal new particle production**, *Geophys. Res. Lett.*, 28, 1949-1952, 2001.
- [109] J.L. Jimenez, R. Bahreini, D.R. Cocker III, H. Zhuang, V. Varutbangkul, R.C. Flagan, J.H. Seinfeld, C.D. O'Dowd and T. Hoffmann, **New particle formation from photooxidation of diiodomethane (CH₂I₂)**, *J. Geophys. Res.*, 2002, 108, D10, 4318,
- [110] J. B. Burkholder, J. Curtius, A. R. Ravishankara and E. R. Lovejoy, **Laboratory studies of the homogeneous nucleation of iodine oxides**, *Atmos. Chem. Phys.*, 2004, 4, 19-34.
- [111] L. Pirjola, C.D. O'Dowd, Y.J. Yoon and K. Sellegri, **Modelling iodine particle formation and growth from seaweed in a chamber**, *Environ. Chem.*, 2005, 2, 271-281

- [112] C.J. Palmer, T. L. anders, L.J. Carpenter, F.C. Küpper and G.B. McFiggans, **Iodine and halocarbon response of *Laminaria Digitata* to oxidative stress and links to atmospheric new particle production**, *Environ. Chem*, 2005, 2, 282-290.
- [113] Z. D. Ristovski, C. Fletcher, B. D'Anna, G. R. Johnson and J. T. Bostrom **Characterization of iodine particles with Volatilization-Humidification Tandem Differential Mobility Analyser (VH-TDMA), Raman and SEM techniques**, *Atm. Chem. Phys. Discuss.*, 2006, 1481-1508.
- [114] A.C. Vikis and R. MacFarlane, **Reaction of Iodine with Ozone in the gas phase**, *J. Phys. Chem*, 1985, 89, 812-815
- [115] S. Sunder, J.C. Wren and A.C. Vikis, **Raman spectra of I₄O₉ formed by the reaction of iodine with ozone**, *J. Ram. Spec.*, 1985, 16, 424-426.
- [116] S. Pechtl, E. R. Lovejoy, J. B. Burkholder, and R. von Glasow, **Modeling the possible role of iodine oxides in atmospheric new particle formation**, *Atmos. Chem. Phys.*, 2006, 6, 505-523.
- [117] G. McFiggans, **Marine aerosols and iodine emissions**, *Nature*, 433, 2005
- [118] C.D. O'Dowd, J.L. Jimenez, R. Bahreini, R.C. Flagan, J. H. Seinfeld, M. Kulmala, L. Pirjola, and T. Hoffmann, **Marine aerosols and iodine emissions**, *Nature*, 433, 2005
- [119] U. Platt, in **Air Monitoring by Spectroscopic Techniques**, Chemical Analysis Series 127, Wiley, New York, 1994, chap. 2.
- [120] P. Spietz, U. Gross, E. Smalins, J. Orphal and J.P. Burrows. **Estimation of the emission temperature of an electrodeless discharge lamp and determination of the oscillator strength for the I(²P_{3/2}) 183.038 nm resonance transition**. *Spectrochim. Acta Part B*, 56, 2465-2478, 2001.
- [121] P. Spietz, S. Himmelmann, U. Gross, J. Orphal, and J.P. Burrows: **Study of iodine oxides and iodine chemistry using flash photolysis and time resolved absorption spectroscopy**, *Ann. Geophys. Supp. II*, 16, C722, 1998
- [122] P. Spietz, J.C. Gómez Martín and J.P. Burrows, **Quantitative treatment of insufficiently resolved and/or coarsely binned optical multichannel recordings in molecule absorption spectroscopy**, *Spectrochim. Acta A*, 2006, 64, 722-735.
- [123] J.C. Gómez Martín, P. Spietz, J. Orphal and J.P. Burrows, **Principal and Independent Components Analysis in the context of Multichannel Time-**

- resolved Absorption Spectroscopy**, *Spectrochim. Acta A*, 2004, 60 ,2673-2693.
- [124] P. Spietz, **Absorptionsquerschnitte von in der Photolyse von J₂ und O₃ und in der Atmosphäre relevanten Jodverbindungen**, Dissertation zur Erlangung des Grades Doktor der Naturwissenschaften am Fachbereich Physik der Universität Bremen Bremen, März 2005
- [125] J.C. Gómez Martín, P. Spietz and J. P. Burrows, **Spectroscopic Studies of the I₂/O₃ photochemistry Part 1: Determination of the absolute absorption cross sections of iodine oxides of atmospheric relevance**, *J. Photochem. Photobiol. A*, 2005, 176, 15-38.
- [126] P. Spietz, J.C. Gómez Martín and J.P. Burrows, **Spectroscopic Studies of the I₂/O₃ photochemistry Part 2: Improved Spectra of Iodine Oxides and Analysis of the IO Absorption Spectrum**, *J. Photochem. Photobiol. A*, 2005, 176, 50-67.
- [127] P. Spietz, J. C. Gómez Martín and J. P. Burrows, **Effects of column density on I₂ spectroscopy and a determination of I₂ absorption cross section at 500 nm**, *Atm. Chem. Phys.* 2006, 6, 2177-2191.
- [128] B.H. Bransden and C.J. Joachain, **Physics of Atoms and Molecules**, *Longman Scientific and Technical*, Hong Kong 1991
- [129] W. Demtröder, **Molekülphysik, Theoretische Grundlagen und Experimentelle Methoden**, Oldenburg Verlag, Munchen, 2003.
- [130] G. Herzberg, **Molecular spectra and molecular structure I. Spectra of Diatomic molecules**, Krieger Publishing, Malabar, Florida, 1989.
- [131] G. Herzberg, **Molecular spectra and molecular structure II. Infrared and Raman spectra of polyatomic molecules**, Krieger Publishing, Malabar, Florida, 1989.
- [132] G. Herzberg, **Molecular spectra and molecular structure III. Electronic spectra and electronic structure of polyatomic molecules**, Krieger Publishing, Malabar, Florida, 1989.
- [133] E.W. Weisstein, **Mathworld**, <http://mathworld.wolfram.com/>, 02/02/2006
- [134] R.A. Durie and D.A. Ramsay, **Absorption Spectra of the Halogen Monoxides**. *Can. J. Phys.*, 36, 35-53, 1958.
- [135] R.A. Durie, F. Legay and D.A. Ramsay. **An emission system of the IO molecule**. *Can. J. Phys.*, 1960, 38, 444-452.

- [136] J.B. Bekooy, W. Leo Meerts and A. Dymanus, **High-Resolution Laser-rf Spectroscopy on the $A^2\Pi_{3/2}-X^2\Pi_{3/2}$ System of Iodine Oxide (IO)**, *J. Mol. Spec.*, 1983, 102, 320-343.
- [137] K. Nakamoto, **Infrared and Raman spectra of inorganic and coordination compounds**, *John Wiley & Sons*, New York, 1986.
- [138] J. T. Vanderslice, E. A. Mason, W. G. Maisch and E. R. Lippincott, **Ground state of hydrogen by the Rydberg-Klein-Rees method**, *J. Mol. Spec.*, 1959, 3, 17-29.
- [139] M.L.P. Rao, D.V.K. Rao and P.T. Rao, **Dissociation energies, r-centroids and Franck-Condon factors of the IO molecule**, *Phys. Lett.*, 50A(5), 341-342, 1974.
- [140] W.M. Vaidya, **The Flame Spectra of Some Aliphatic Halides-Part I. (1) Methyl Iodide**, *Proc. Ind. Acad. Sci.*, 6A, 122, 1937.
- [141] E.H. Coleman, A.G. Gaydon and W.M. Vaidya, **Spectrum of Iodine Oxide (IO) in flames**, *Nature (London)*, 162, 108-109, 1948.
- [142] M.K. Gilles, M.L. Polak and W.C. Lineberger, **Photoelectron spectroscopy of the halogen oxide anions FO^- , ClO^- , BrO^- , IO^- , $OCIO^-$ and OIO^-** , *J. Chem. Phys.*, 1992, 96 (11), 8012-8021.
- [143] C.E. Miller and E.A. Cohen, **Rotational spectroscopy of IO $X^2\Pi_i$** , *J. Chem. Phys.*, 2003, 115 (10), 6459-6470
- [144] S. M. Newman, W.H. Howie, I.C. Lane, M.R. Upson and A.J. Orr-Ewing, **Predissociation of the state $A^2\Pi_{3/2}$ of IO studied by cavity ring-down spectroscopy**, *J. Chem. Soc., Far. Trans.*, 1998, 94, 2681-2688
- [145] G. Inoue, M. Suzuki and N. Washida, **Laser induced fluorescence of IO radicals and rate constant for the reaction $IO+NO$** , *J. Chem. Phys.*, 1983, 79, 10, 4730-4735.
- [146] S. Roszak, M. Krauss, A.B. Alekseyev, H.-P. Liebermann, R.J. Buenker, **Spin-Orbit Configuration Interaction Calculation of the Potential Energy Curves of Iodine Oxide**, *J. Phys. Chem. A*, 2000, 104, 2999-3003.
- [147] IUP database: <http://www.iup.uni-bremen.de/gruppen/molspec/index.html>
- [148] C.E. Miller and E.A. Cohen, **The rotational spectrum of iodine dioxide, OIO**, *J. Chem. Phys.*, 2003, 118 (10), 6309-6317.

- [149] S. Himmelmann, **Untersuchung von Halogenoxiden mittels Blitzlichphotolyse**, Dissertation zur Erlangung des Grades Dr. rer. nat. der Universität Bremen, Cuvillier Verlag Göttingen, 1997
- [150] G. Maier and A. Bothur, **Matrix isolation of iodine superoxide and iodine dioxide**. *Chem. Ber./Rec.*, 1997, 130,179-181.
- [151] K.J. Laidler, **Chemical Kinetics**, Harper Collins Publishers, New York, 1987.
- [152] W.H. Press, S. A. Teukolsky, W. T. Vetterling and B. P. Flannery, **Numerical Recipes in C. The Art of Scientific Computing**. Second Edition, Cambridge University Press, Cambridge, 1992
- [153] **Documentation for MathWorks Products**, Release 14 with Service Pack 3, www.mathworks.com, 2005
- [154] A.M. Malleson, H.M. Kellet, R.G. Myhill and W.P. Sweetenham (Eds.), **FACSIMILE**, *AERE Harwell Publications*, Oxfordshire, 1990.
- [155] F.W. Sears and G.L. Salinger, **Thermodynamics, kinetic theory, and statistical thermodynamics**, 3rd Ed., Addison-Wesley, 1986
- [156] R. De Avillez Pereira, D.L. Baulch, M.J. Pilling, S.H. Robertson and G. Zeng, **Temperature and Pressure Dependence of the Multichannel Rate Coefficients for the CH₃ + OH System** *J. Phys. Chem. A.*, 1997; 101(50); 9681-9693.
- [157] M.E. Tucceri, T. J. Dillon and J. N. Crowley, **A laser photolysis–resonance fluorescence study of the reactions: I+O₃→IO+O₂, O+I₂→IO+I, and I+NO₂+M→INO₂+M at 298 K**, *Phys. Chem. Chem. Phys.*, 2005 , 7, 1657–1663.
- [158] E. Rabinowitch and W. Wood, **Dissociation of excited iodine molecules**, *J. Chem. Phys.*, 1936, 4, 358–362.
- [159] L. Brewer and J. Tellinghuisen, **Quantum yield for unimolecular dissociation of I₂ in visible absorption**, *J. Chem. Phys.*, 1972, 56, 3929–3938.
- [160] A.D. Palla, D.L. Carol and J.T. Verdeyen, **Post-Discharge Modelling of Recent ElectricOIL Experiments**, 36th AIAA Plasmadynamics and Lasers conference, Toronto, Ontario, Canada, 6-9 June 2005.
- [161] A.T. Young and P.L. Houston, **The I(²P_{1/2})+O₂↔ I(²P_{3/2})+O₂(¹Δ) equilibrium**, *J. Chem. Phys.*, 1983, 78, 2317-2326.
- [162] T.G. Slanger and P.C. Cosby, **O₂ Spectroscopy bellow 5.1 eV**, *J. Phys. Chem.*, 1988, 92, 267-282.

- [163] R. E. Stickel, A. J. Hynes, J. D. Bradshaw, W. L. Chameides and D. D. Davies, **Absorption Cross Sections and Kinetic Considerations of the IO Radical As Determined by Laser Flash Photolysis/Laser Absorption Spectroscopy**, *J. Phys. Chem.*, 92, 1862-1864, 1988.
- [164] Y. Matsumi, F. J. Comes, G. Hancock, A. Hofzumahaus, A. J. Hynes, M. Kawasaki, and A. R. Ravishankara, **Quantum yields for production of O(¹D) in the ultraviolet photolysis of ozone: Recommendation based on evaluation of laboratory data**, *J. Geophys. Res.*, 2002, 107(D3), 4024
- [165] K. Takahashi, M. Kishigami, N. Taniguchi, Y. Matsumi, and M. Kawasaki, **Photofragment excitation spectrum for O(¹D) from the photodissociation of jet-cooled ozone in the wavelength range 305–329 nm**, *J. Chem. Phys.*, 1997, 106, 6390-6397
- [166] M.A.A. Clyne and H.W. Cruse, **Rates of elementary reactions involving the BrO(X²Π) and IO(X²Π) Radicals**. *Trans. Farad. Soc.*, 1970, 66, 2227-2236.
- [167] T.J. Dillon, M.E. Tucceri, D. Hölscher and J.N. Crowley, **Absorption cross-section of IO at 427.2 nm and 298 K.**, *J. Photochem. Photobiol. A*, 2005, 176 (1-3), 14 December 2005, Pages 3-14
- [168] M.J. Kurylo, W. Braun and A. Kaldor, **A laser enhanced reaction technique for the measurement of V-T deactivation rates: deactivation of vibrationally excited O₃[†]**, *Chem. Phys. Lett.*, 1974, 27, 249-253.
- [169] M.E. Jenkin and R.A. Cox, **Kinetics study of the Reactions IO+NO₂+M→IONO₂+M, IO+IO→products and I+O₃→IO+O₂**, *J. Phys. Chem.*, 1985, 89, 192-199.
- [170] Lazlo, M.J. Kurylo and R.E. Huie, **Absorption cross sections, kinetics of formation and self reaction of the IO radical produced via the laser photolysis of N₂O/I₂/N₂ mixtures**. *J. Phys. Chem.*, 1995, 99, 11701-11707.
- [171] M.H. Harwood, J.B. Burkholder, M. Hunter, R.W. Fox and A.R. Ravishankara, **Absorption cross sections and self-reaction kinetics of the IO Radical**. *J. Phys. Chem. A*, 101, 853-863, 1997.
- [172] D.B. Atkinson, J.W. Hudgens and A.J. Orr-Ewing, **Kinetic studies of the reactions of IO radicals determined by cavity ring-down spectroscopy**. *J. Phys. Chem.*, 1999, 103, 6173-6180.

- [173] R.A. Cox and G.B. Coker, **Absorption cross section and Kinetics of IO in the Photolysis of CH₃I in the presence of Ozone**. *J. Phys. Chem.*, 1983, 87, 4478-4484.
- [174] A. Vipond, C. E. Canosa-Mas, M. L. Flugge, D. J. Gray, D. E. Shallcross, D. Shaha and R. P. Wayne, **A discharge-flow study of the self-reaction of IO** , *Phys. Chem. Chem.Phys.*, 2002, 4, 3648-3658.
- [175] P. Spietz, S. Himmelmann, U. Gross, J. Orphal, and J.P. Burrows: **Study of iodine oxides and iodine chemistry using flash photolysis and time resolved absorption spectroscopy**, *Annaes Geophysicae Supp. II*, 1998, 16, C722.
- [176] T-W. Lee, A.J. Bell and R. Orglmeister. **Blind Source Separation of real world signals**. *Proceedings of IEEE International Conference on Neural Networks 1997*, IEEE, Houston, 1997, 2129.
- [177] T-P Jung, C. Humphries, T-W Lee, S. Makeig, M.J. McKeown, V. Iragui and T.J. Sejnowski. **Extended ICA removes artefacts from electroencephalographic recordings**. *Adv. Neu. Inf. Process. Sys.*, 10 (1998), 894.
- [178] M. Feng and K.D Kammeyer, **Application of source separation algorithms for mobile communication environments** . *Proceedings of IEEE International Workshop on Independent Component Analysis and Blind Separation of Signals 1999*, IEEE, Aussoise, 1999.
- [179] H. Von Storch and T.J. Zwiers, **Statistical Analysis in Climate Research**. Cambridge University Press. Cambridge, 1998, Chapter 13 .
- [180] F. Aires and A. Chédin. **Independent Component Analysis of multivariate time series: Application to the tropical SST variability**. *J. Geophys. Res.*, 105 (2000), N. D13, 17,437.
- [181] C.W. Brown, P.F. Lynch, R.J. Obremski and D.S. Lavery, **Matrix Representations and Criteria for Selecting Analytical Wavelengths for Multicomponent Spectroscopic Analysis**, *Anal. Chem.*, 54, 1472-1479, 1982.
- [182] F.Aires, W.B. Rossow, N.A. Scott and A. Chédin. **Remote sensing from the infrared atmospheric sounding interferometer instrument, 1, Compression, denoising and first-guess retrieval algorithms**. *J. Geophys. Res.*, 107(D22) (2002), 4619, doi:10.1029/2001JD000955.

- [183] I.T. Jolliffe. **Principal Component Analysis**. Springer Verlag. New York, 2002.
- [184] R.J. Bolton and W.J. Krzanowski. **A characterization of Principal Components for Projection Pursuit**. *The American Statistician*, 1999, 53(2), 108.
- [185] Hyvärinen and E. Oja, **Independent Component Analysis: Algorithms and Applications**. *Neur. Net.*, 2000, 13(4-5), 411.
- [186] J.F. Cardoso, **Blind signal separation: statistical principles**, *Proceedings of the IEEE 1998*, R.-W. Liu and L. Tong editors, 1998, vol. 90, n.8, p 2009.
- [187] Hyvärinen. **Survey on Independent Component Analysis**. *Neur. Comp. Sur.*, 1999, 2, 94.
- [188] Hyvärinen, **Fast and robust fixed-point algorithms for Independent Component Analysis**. *IEEE Trans. Neur. Net.* 10(3) (1999), 626.
- [189] A.J. Bell and T.J. Sejnowski, **An information-maximisation approach to Blind Separation and Blind Deconvolution**, *Neur. Comp.*, 1995, 7, 1129.
- [190] Hyvärinen, **New approximations of differential entropy for Independent Component Analysis and Projection Pursuit**. *Proceedings of the Neural Information Processing Systems Conference 1997*, MIT press, 1998, 273.
- [191] P.D. Allison, **Multiple regression**. Thousand Oaks, CA: Pine Forge Press, 1999
- [192] Dahlquist, A. Björk, N. Anderson, **Numerical methods**, Prentice-Hall, Englewood cliffs, New Jersey, 1974
- [193] G. Porter, **Flash Photolysis and Spectroscopy. A New Method for the Study of Free Radical Reactions**, *Proc. R. Soc. A*, 1950, 200 (1061), 284-300.
- [194] R.T. Watson, S.P. Sander and Y.L. Yung, **Pressure and Temperature Dependence Kinetics Study of the $\text{NO} + \text{BrO} \rightarrow \text{NO}_2 + \text{Br}$ Reaction. Implications for Stratospheric Bromine Photochemistry**, *J. Phys. Chem.*, 1979, 83 (N23), 2936-2944
- [195] J. U. White, **Long optical paths of large aperture**, *J. Opt. Soc. Am.*, 1942, 32, 285-291
- [196] J. Tellinghuisen. **Resolution of the visible-infrared absorption spectrum of I_2 into three contributing transitions**. *J. Chem. Phys.*, 1973, 58, 2821-2834

- [197] Saiz-Lopez, R. W. Saunders, D. M. Joseph, S. H. Ashworth and J. M. C. Plane, **Absolute absorption cross-section and photolysis rate of I₂**, *Atmos. Chem. Phys.*, **4**, 1443-1450, 2004.
- [198] S. Voigt, J. Orphal, K. Bogumil, and J. P. Burrows: **The Temperature Dependence (203-293 K) of the Absorption Cross-Sections of O₃ in the 230–850 nm region Measured by Fourier-Transform Spectroscopy**, *J.Photochem. Photobiol. A*, 2001, 143, 1–9,.
- [199] B. Gür, **Temperature dependent absorption cross sections of O₃ and NO₂ in the 240-790 nm range determined by using GOME-2 satellite spectrometers**, Dissertation zur Erlangung des akademisches Grades eines Doktors der Naturwissenschaften (Dr. Rer. Nat.) am Fachbereich Physik der Universität Bremen, February 2006
- [200] D.M. Rowley, M.H. Harwood, R.A. Freshwater and R.L. Jones, **A Novel Flash Photolysis/UV Absorption System Employing Charge-Coupled Device (CCD) Detection: A Study of the BrO + BrO Reaction at 298 K**, *J. Phys. Chem.*, 1996, 100, 3020-3029
- [201] U. Gross, A. Ubelis, P. Spietz and J. P. Burrows, **Iodine and mercury resonance lamps for kinetic experiments and their spectra in the far ultraviolet**, *J. Phys. D: Appl. Phys.*, 2000, 33, 1588-1591.
- [202] A.D. Polyanin, **Handbook of Linear Partial Differential Equations for Engineers and Scientists**, *Chapman & Hall/CRC*, 2002,
- [203] M.E. Jenkin, R.A. Cox, A. Mellouki, G. Le Bras, G. Poulet, **Kinetics of the reaction of iodine atoms with HO₂ radicals**, *J. Phys. Chem.*, 1990, 94, 2927
- [204] Wahner, G.S. Tyndall and A.R. Ravishankara. **Absorption cross sections for OCIO as a function of temperature in the wavelength range 240-480 nm**. *J. Phys. Chem.*, 1987, 91, 2734.
- [205] D.Maric, J.P.Burrows, R. Meller and G.K. Moortgat. **A study of the UV-visible absorption spectrum of molecular chlorine**. *J. Photochem. Photobiol. A*, 1993, 70, 205
- [206] A.F. Holleman and E. Wiberg, **Lehrbuch der Anorganischen Chemie**, Walter de Gruyter, 101. Auflage, Berlin, 1995.
- [207] L. F. Shampine and M. W. Reichelt, **The Matlab ODE Suite**, *SIAM J. Sci. Comput.*, 1997, 18, 1-22.

-
- [208] H. Dostal and R. Raff, **Über die Kinetik einer thermischen Polykondensation**, *Z. Physikal. Chem. B*, 1936, 32, 2, 117-129.
- [209] I.K. Larin, D. V. Nevozhai, A.I. Spasskii, E.M. Trofimova and L.E. Turkin, **Measurement of rate constants for the reaction of iodine monoxide with ozone**, *Kinet. Catal.*, 1999, 40, 487-495.
- [210] H. Fjellvåg and A. Kjekshus, **The crystal structure of I₂O₄ and its relations to other iodine-oxygen-containing compounds**, *Act. Chem. Scand.* 1994, 48, 815-822.
- [211] G. Daehlie and A. Kjekshus, **Iodine oxides, Part I**, *Acta Chem. Scand.*, 1964, 18, 144-156.
- [212] K. Selte and A. Kjekshus, **Iodine oxides. Part III. The crystal structure of I₂O₅**. *Acta Chem. Scand.*, 1970, 24, 1912-1924.
- [213] A.F. Holleman and E. Wiberg, **Lehrbuch der Anorganischen Chemie**, Walter de Gruyter, 101 Auflage, Berlin, 1995.
- [214] H. Reiss, **Homogeneous Gas Phase Polymerization**, *Acc. Chem. Res.*, 1997, 30, 297-305.
- [215] V. Rozanov, A. Rozanov, R. de Beek, M. Buchwitz, D. Diebel, K.U. Eichmann, C. Haite, R. Hoogen, J. Kauss, T. Kurosu, J. Murray, R.J.D. Spurr, M. Vountas and J.P. Burrows, **SCIATRAN 2.0.15**, <http://www.iup.uni-bremen.de/sciatran/index.html>, Release date: August 3rd, 2005.
- [216] M. Buchwitz, K.U. Eichmann, A. Rozanov and J.P. Burrows, **User's Guide for the Software Package SCIATRAN (Radiative Transfer Model and Retrieval Algorithm), Version 2.0**, <http://www.iup.uni-bremen.de/sciatran/index.html>, 2004.

